Characteristics, Applications, and Properties of Carbon-Dioxide-Laser-Induced Long-Period Fiber Gratings

A Thesis
Presented to
The Academic Faculty

by

Brent L. Bachim

In Partial Fulfillment
of the Requirements for the Degree
Doctor of Philosophy

School of Electrical and Computer Engineering
Georgia Institute of Technology
August 2005

Characteristics, Applications, and Properties of Carbon-Dioxide-Laser-Induced Long-Period Fiber Gratings

Approved by:

Professor Thomas K. Gaylord, Chair
School of Electrical and Computer Engineering
Georgia Institute of Technology

Professor Ali Adibi
School of Electrical and Computer Engineering
Georgia Institute of Technology

Professor John A. Buck
School of Electrical and Computer Engineering
Georgia Institute of Technology

Professor Gee-Kung Chang
School of Electrical and Computer Engineering
Georgia Institute of Technology

Professor R. Stephen Weis
Department of Engineering
Texas Christian University

Date Approved: June 15, 2005

To my parents,

Terry and Betty

ACKNOWLEDGEMENTS

I have anticipated writing the *Acknowledgements* section for some time now. This is not because the section marks the end of a long and tortuous path. Rather, it is because so many people have helped me along that path and I have looked forward to thanking them in this more permanent form.

It has been a privilege to have Prof. Gaylord as an advisor. He is the epitome of hard work, dedication, and energy and I only hope that I can incorporate some portion of those qualities in my future career. It is when I look back five years ago to when I entered graduate school that I realize how much I have learned under Prof. Gaylord's guidance. I thank him particularly for giving me latitude to pursue my (sometimes questionable) research schemes and for his constant, unwavering support.

I owe a great deal to Prof. R. Stephen Weis for giving me a start in research while I was still an undergraduate at Texas Christian University. Few other individuals display such an exemplary dedication to the education and development of their students and I thank him immensely for providing continuous encouragement and support over the time that I have been fortunate to know him.

I thank the other members of my committee, Prof. John Buck, Prof. Gee-Kung Chang, and Prof. Ali Adibi, for their thoughtful considerations and questions. Like all good teachers and researchers, they prompted me to consider new and different aspects of my research. I also thank Prof. Elias Glytsis for all of his assistance, guidance, and for many fruitful conversations.

Without the assistance and support of my colleagues in the Optics Group, I doubt even a minuscule amount of this thesis would have been completed. It has been a distinct pleasure to work with such talented and genuinely good people. Special thanks go to Mr. Mohammad Braiwish, who was instrumental in developing the fabrication apparatus, conducted the prototype device research, and provided hours of thoughtful discourse as we

toiled together on our many and varied tasks. I thank Dr. Carole Montarou for teaching me the finer points of microscopy, for our many discussions on optical characterization, and for her contagious enthusiasm. Mr. Oluwafemi Ogunsola (soon to be Dr.) fabricated the waveguides used for the coupler and provided illumination on the complicated issues surrounding optical interconnects. More importantly, I thank him for his general goodwill and kindly consideration. The camaraderie offered by Dr. Gregory Kilby, Mr. Jon Maikisch, Mr. Justin Stay, Dr. Ricardo Villalaz, Mr. Arthur Wu, and Dr. Shun-Der Wu is also greatly appreciated.

There are a number of people outside of Georgia Tech that provided invaluable assistance throughout all stages of this research. I thank Dr. Donald Davis for teaching me how to fabricate long-period fiber gratings using a carbon-dioxide laser and for providing such a solid footing from which I could begin my work. Similarly, Dr. Gregory VanWiggeren's initial work on the flexure response of long-period fiber gratings motivated all of the investigations that followed. Dr. Stephen Mettler provided substantial assistance with the refractive-index profile measurements and also made sure that I had access to the OFS laboratories. I thank him for both. Dr. Victor Grubsky and Dr. William Morey, of Sabeus Photonics, generously provided the ultraviolet-induced long-period fiber grating that was used in many of the investigations.

Finally, my entire family deserves my utmost gratitude for the love and support they have given me over the years. I am fortunate to have grown up surrounded by such a wonderful family. I especially thank my brothers, Blaine and Lance, for helping me to laugh (a true necessity) and ensuring that I keep a proper perspective on life. In addition, I thank my sister, Andrea, for her concern, wisdom, and support. What I owe my parents, Terry and Betty, can never be described in full—I would consider it something in this life if I can even approach being such a loving, caring, and supportive parent as they both have been. Perhaps, in this case, the simplest words are the best: Thank you from the bottom of my heart.

Proceeding through graduate school reinforces, both continuously and without ambiguity, how little you actually know. The greatest lesson that you then learn from the journey

is that you can succeed in spite of this unavoidable limitation, but only if you have the help of others. Sir Isaac Newton wrote, "If I have seen further it is by standing on the shoulders of giants." I do not claim that I have seen further than other men or women, only that I know the view from atop the giants.

Brent L. Bachim

Georgia Institute of Technology

June 15, 2005

TABLE OF CONTENTS

LIST OF TABLES

LIST OF FIGURES

LIST OF SYMBOLS OR ABBREVIATIONS

ABS	Acrylonitrile-Butadiene-Styrene.
AFTS	Automated Flexure Testing System.
BDP	Brightfield-Darkfield-Polarized.
BPM	Beam Propogation Method.
CCD	Charge-Coupled Device.
CCW	Counterclockwise.
CMT	Coupled Mode Theory.
CO_2	Carbon-Dioxide.
CPM	Complex Plane Method.
CT	Computed Tomography.
CW	Clockwise.
CWDM	Coarse Wavelength Division Multiplexing.
DGD	Differential Group Delay.
DIC	Differential Interference Contrast.
DOE	Diffractive Optical Element.
FBG	Fiber Bragg Grating.
FFT	Fast Fourier Transform.
GPIB	General Purpose Instrumentation Bus.
JME	Jones Matrix Eigenanalysis.
λ	wavelength.
Λ	grating period.
LP	Linearly Polarized.
LPFG	Long-Period Fiber Grating.
LWD	Long-Working Distance.
MIOPT	Microinterferometric Optical Phase Tomography.
MMF	Multi-Mode Fiber.
N	number of grating periods.

NIR Near-Infrared.

OSA Optical Spectrum Analyzer.

OTF Optical Tunable Filter.

PDL Polarization-Dependent Loss.

PMD Polarization Mode Dispersion.

PMF Polarization-Maintaining Fiber.

PSI Phase-Shifting Interferometry.

PSP Principal States of Polarization.

Si Silicon.

SiO_2 Silicon-Dioxide.

SMF Single-Mode Fiber.

SOP State-of-Polarization.

TE Transverse Electric.

TM Transverse Magnetic.

UV Ultraviolet.

VAT Variable Attenuation Tuning.

VOA Variable Optical Attenuator.

WT Wavelength Tuning.

SUMMARY

Optical fiber-based devices, including fiber gratings, play an important role in optical communications and optical sensor applications. One type of fiber grating, the long-period fiber grating (LPFG), is used to perform such crucial operations as gain flattening of erbium-doped fiber amplifiers and dispersion compensation in optical communications. The ability of LPFGs to manipulate light traveling in optical fibers and their sensitivity to various external perturbations make them well-suited for creating optical fiber-based devices.

LPFGs are typically fabricated by exposing photosensitive optical fiber to ultraviolet light. However, LPFGs can be fabricated by a variety of other techniques, including exposure to carbon-dioxide (CO_2) laser light. The physical process by which the refractive-index change is induced in an optical fiber during exposure to CO_2 laser light gives CO_2-laser-induced LPFGs unique properties when compared to more traditional LPFGs fabricated by exposure to UV light. CO_2-laser-induced LPFGs respond differently to external perturbations and useful behavior has been observed, including variable attenuation tuning at a constant wavelength and wavelength tuning at constant amplitude with applied flexure.

In order to manipulate, harness, and enhance the unique features of CO_2-laser-induced LPFGs, it is necessary to understand their physical properties and optical characteristics. The main objectives of the research presented in this thesis are to quantify experimentally the optical performance of CO_2-laser-induced LPFGs with respect to flexure, torsion, and variable incident polarization, to characterize grating cross-sectional refractive-index profiles, and to demonstrate applications of CO_2-laser-induced LPFGs that exploit their unique properties. The research presented in this thesis represents a detailed study and consideration of the consequences of the asymmetric refractive-index change on LPFG performance and how the unique features can be used to create novel devices for important applications.

As part of the investigation of the effects of asymmetry, the fabrication and basic

transmission characteristics of CO_2-laser-induced LPFGs are examined. The polarization-dependent transmission characteristics, specifically polarization-dependent loss and polarization mode dispersion, of CO_2-laser-induced LPFGs are investigated. The unique behavior of the gratings in response to applied flexure and applied torsion is also explored. The potential advantages resulting from the presence of the asymmetric index profile in CO_2-laser-induced LPFGs are clearly illustrated by variable optical attenuator, optical tunable filter, and fiber-to-waveguide coupler devices. A new cross-sectional refractive-index profiling technique is presented that enables measurement of profiles containing small and irregular index variations. The profiling technique is used to measure the cross-sectional refractive-index profiles of optical fiber exposed to CO_2 laser light. Future areas of research concerning CO_2-laser-induced LPFGs are identified and discussed.

CHAPTER 1

INTRODUCTION

Optical fiber-based devices play an important role in optical communications and optical sensor applications. Within optical communication networks, optical fiber-based devices perform such critical operations as coupling, wavelength-selective filtering, and switching [7]. Optical fiber sensors possess several advantages over other sensor technologies, including immunity to electromagnetic interference, high sensitivity, and large bandwidth [8]. Recent applications for optical fiber sensors include monitoring in smart structures, seismic measurements, and spectroscopy [9, 10].

Fiber gratings form one technology base available for creating optical fiber-based communication and sensing devices. Fiber Bragg gratings (FBGs), the most common type of fiber grating, consist of a periodic variation in the refractive index of an optical fiber, with the period being on the order of hundreds of nanometers. FBGs couple light from a forward-propagating core-guided mode to a backwards-propagating core-guided mode near a resonant wavelength, in effect acting as wavelength-selective mirrors [11]. Additional types of fiber gratings include tilted gratings and chiral gratings.

One other additional type of fiber grating, the long-period fiber grating (LPFG) has been used for flattening the gain spectrum of erbium-doped fiber amplifiers, for monitoring power levels transmitted in fiber, for compensating dispersion, and for many other applications [12–14]. The ability of LPFGs to manipulate selectively light traveling in optical fibers and their sensitivity to various external perturbations make them well-suited for creating optical fiber-based devices.

LPFGs are typically fabricated by exposing photosensitive optical fiber to ultraviolet (UV) light either through an amplitude mask or period-by-period to create a grating structure. However, LPFGs can be fabricated by a variety of other techniques, including exposure to carbon-dioxide (CO_2) laser light [15]. The physical process by which the refractive-index

change is induced in an optical fiber during exposure to CO_2 laser light gives these LPFGs unique properties when compared to more traditional LPFGs fabricated by exposure to UV light. As such, CO_2-laser-induced LPFGs respond differently to external perturbations and useful behavior has been observed, including variable attenuation tuning at a constant wavelength and wavelength tuning at constant amplitude with applied flexure [3].

In order to manipulate, harness, and enhance the unique features of CO_2-laser-induced LPFGs, it is necessary to understand their physical properties and optical characteristics. Therefore, the primary goal of this research is to further the understanding of CO_2-laser-induced LPFGs by quantifying their physical properties and optical characteristics while exploring potential applications. Prior to discussing the specific research objectives, previous research concerning LPFGs, in general, and CO_2-laser-induced LPFGs specifically is discussed.

1.1 Background

1.1.1 Long-Period Fiber Gratings (LPFGs)

1.1.1.1 General Properties and Characteristics

In the most basic form, an LPFG consists of a periodic spatial variation (along the fiber longitudinal axis) in the refractive index of an optical fiber. The periodic variation creates a grating structure that couples light from a forward-propagating core-guided mode to forward-propagating cladding-guide modes near certain resonant wavelengths [12]. Grating periods for LPFGs, when used for wavelength filtering in commercial telecommunications bands, are commonly in the hundreds of micrometers. Coupling occurs, for LPFGs written in single-mode fiber (SMF), when phase-matching between the fundamental core mode and a particular cladding mode is achieved; the presence of the grating creates the condition for phase-matching between modes [16]. The phase-matching condition required for coupling is given by

$$\beta_{01} - \beta_{mn} = \frac{2\pi}{\Lambda} = K, \tag{1.1}$$

with β_{01} being the propagation constant of the fundamental linearly polarized (LP_{01}) core-guided mode, β_{mn} being the propagation constant of the LP_{mn} cladding-guided mode, Λ

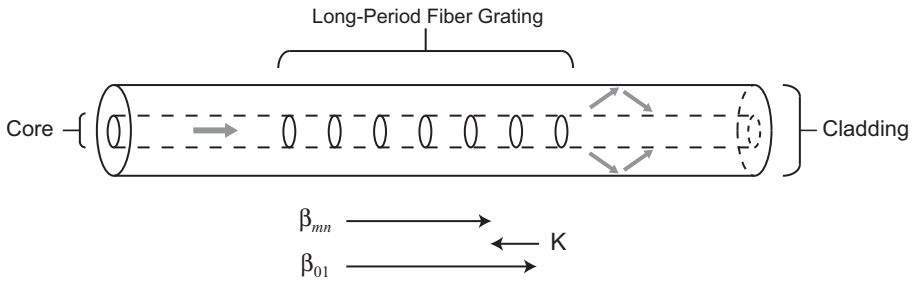

Figure 1.1: Illustration of coupling between a core-guided and a cladding-guided mode due to the LPFG structure. The grating acts to match the phases of the two modes to permit coupling.

being the grating period, and K being the grating vector magnitude. An alternative form of the phase-matching condition is given by

$$\Lambda(n_{01} - n_{mn}) = \lambda_{res}, \tag{1.2}$$

where n_{01} is the effective index of the core-guided mode, n_{mn} is the effective index of the LP_{mn} cladding-guided mode, and λ_{res} is the center wavelength of the transmission resonance. The phase-matching condition required for coupling is illustrated by the vectors in Fig. 1.1.

The light coupled into cladding-guided modes is, most typically, absorbed in the fiber buffer or radiates away from the fiber. Thus, this type of fiber grating acts as a wavelength-selective transmission filter. The wavelength transmission response of a typical LPFG is shown in Fig. 1.2. Over a wide wavelength range (hundreds of nanometers), an LPFG couples to a number of distinct cladding modes at various wavelengths. Phase-matching is a necessary, but not sufficient, condition for coupling between the core-guided and the cladding-guided modes. Cladding-modes exist in at least a three-layer cylindrical waveguide and share similarities with the modes present in multi-mode fiber (MMF) (which supports hundreds of modes). For significant coupling to occur between the core-guided mode and a cladding-guided mode, there must also be an overlap between the mode profiles. This requirement explains why, over large wavelength ranges, coupling occurs to only a finite number of distinct cladding modes. Also, the mode overlap requirement explains why LPFGs with azimuthally symmetric index profiles couple to only symmetric cladding modes.

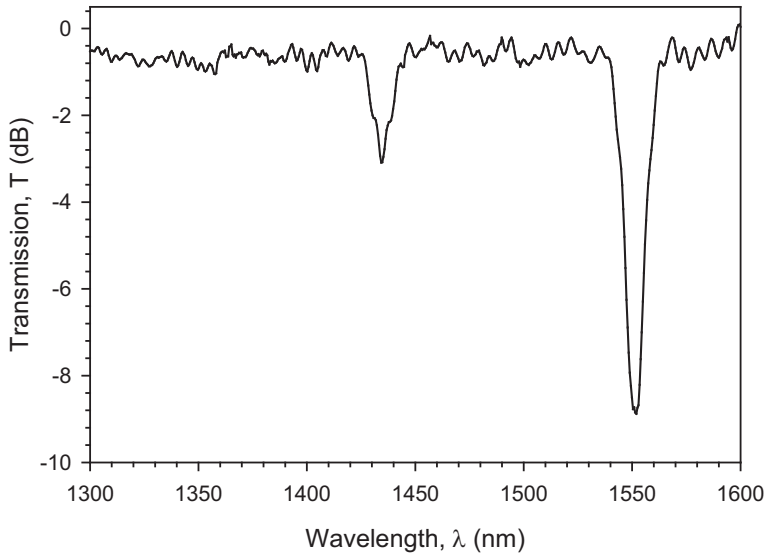

Figure 1.2: Transmission response of a typical LPFG

While the wavelengths at which coupling occurs can be determined from Eq. (1.2), predicting the actual amount of power coupled and, therefore, the wavelength transmission response requires the use of additional analysis techniques. Primary among them is coupled-mode theory (CMT), which uses modes of an unperturbed waveguide to represent modes in a perturbed waveguide through a set of coupling coefficients [17]. CMT has been successfully used to model LPFG transmission wavelength response for ultraviolet-induced (UV-induced) LPFGs [18].

LPFGs for coupling core modes to cladding modes were first demonstrated by Vengsarkar *et al.* in 1996 [12]. The gratings were written by exposing hydrogen-loaded germanosilicate optical fibers to UV laser light through an amplitude mask. Exposure to UV light through the mask induced a periodic spatial refractive-index change in the core of the doped optical fiber. Basic transmission and reflection characteristics of the gratings were measured and it was found that they acted as wavelength-specific transmission filters, similar to FBGs, but possessed broader bandwidths and very low backreflection (less than $-90dB$). The effects of temperature and strain on transmission were also examined. Early applications of LPFGs included band-rejection in Raman amplifiers and static gain flattening of erbium-doped fiber amplifiers [12, 19, 20]. Additional application of LPFGs to temperature, axial

strain, and refractive-index sensing were explored [21].

1.1.1.2 Fabrication Techniques

A number of techniques have been developed for fabricating LPFGs in addition to exposing photosensitive optical fibers to UV light. Electric arc discharge and focused infrared femtosecond laser pulses have both been used to write LFPGs on a period-by-period basis [22, 23]. LPFGs have also been created by ion implantation (bombardment) through a metal amplitude mask [24]. Hollow-core optical fiber filled with a liquid crystal solution can be periodically poled (spatially) by applying voltage to electrodes to create an LPFG structure [25]. Pressing on an optical fiber with a grooved plate is another method by which an LPFG can be temporarily created [26]. A temporary LPFG can also be created using acoustical (vibrational) modulation of a length of optical fiber [13]. Fabrication techniques involving exposing optical fiber to CO_2 laser light are discussed in Sec. 1.1.2.1.

1.1.1.3 Applications

Initial investigations involving LPFGs indicated that they could be useful in a variety of application areas. Both active and passive LPFG-based devices have been reported in the literature, of which only a small number are mentioned here. In addition to wavelength-specific transmission properties, the high sensitivity of cladding modes to surrounding refractive index values makes LPFGs suitable for environmental measurements [27]. Sensor applications in addition to the ones listed in Sec. 1.1.1.1 include bend sensing, torsion sensing, and chemical sensing [28, 29]. A pair of cascaded (in-series) LPFGs was used to create an in-fiber interferometer that functions as a high sensitivity refractometer [30]. All-optical switching using LPFGs is possible by manipulating nonlinear effects [31]. Two coupling schemes, one for fiber-to-fiber coupling and one for coupling light from a laser diode into an optical fiber, employ LPFGs [32, 33]. A wavelength-selective polarizing filter was created by writing an LPFG in a polarization-maintaining fiber (PMF) [34].

1.1.2 CO_2-Laser-Induced LPFGs

In addition to the fabrication techniques mentioned in the previous section, LPFGs can also be created by periodic (spatial) exposure of standard telecommunications optical fiber to CO_2 laser light. Previous research conducted on CO_2-laser-induced LPFGs is examined in this section.

1.1.2.1 Fabrication

Fabrication of LPFGs by exposure to focused CO_2 laser light was demonstrated in 1998 by Davis *et al.* [15]. Grating writing occurred through one-sided, period-by-period exposure rather than through an amplitude mask, as is commonly done for UV-induced LPFGs. To write a single period of a grating (induce a refractive-index change), CO_2 laser light at a wavelength of $10.6\mu m$ was focused to a spot on a section of optical fiber using a spherical lens. Opening and closing a shutter positioned in front of the lens controlled the amount of time the fiber was exposed to laser light. The next period of the grating was written by first translating the fiber a specified distance (the grating period, Λ) and then exposing the new section of fiber to laser light. Grating formation during fabrication was monitored using a broadband light source and an optical spectrum analyzer [2]. In the initial work, hydrogen loading was found to enhance the writing sensitivity, but was not required for grating formation. Later adjustments to the fabrication apparatus introduced a cylindrical lens, in place of the spherical lens, to focus light to a line (instead of a spot) perpendicular to the fiber axis. Adoption of the cylindrical lens reduced alignment sensitivity [2]. CO_2-laser-induced LPFGs were fabricated using the same exposure time for each grating period and at a constant period spacing.

Variations on the initial CO_2 laser LPFG fabrication method have been reported in the literature. Two different configurations exist that use high-frequency CO_2 laser pulses (around a $5kHz$ repetition rate) to create LPFGs. The first variation on the method simply involves the substitution of a pulsed CO_2 laser for the continuous-wave laser used by Davis, with the rest of the apparatus remaining similar [2, 35]. The second variation also involves substituting a pulsed CO_2 laser for the continuous-wave version. In addition, laser light

is focused to a small spot ($50\mu m$ diameter) on the fiber surface [36]. The small spot is then scanned transversely over the fiber surface to create a single grating period. Both fabrication methods employing pulsed CO_2 lasers yielded LPFGs with transmission spectra similar in form to the gratings fabricated by Davis.

Another reported method for fabricating LPFGs using a CO_2 laser involves heating a small diameter fiber and then pulling it to create narrowed taper regions. Conducting the tapering repeatedly along the length of a fiber yields an LPFG, though by different means than the other fabrication methods that use high-frequency pulsed CO_2 lasers as mentioned above [37].

While LPFGs can be successfully written with a CO_2 laser, some level of variability is observed during the fabrication process. Davis reported observing a wide range of grating strengths for similar exposure conditions [2]. For the same fabrication conditions (incident power, wavelength, fiber, exposure time), there can be significant variation in the resulting grating transmission spectra, especially the peak transmission loss at resonance. The reasons for the observed variability are not fully understood. Issues related to variability hinder efforts to fabricate CO_2-laser-induced LPFGs possessing more complicated structures, such as chirped period gratings or apodized gratings. Chirping and apodization of grating profiles have been demonstrated in UV-induced LPFGs, but not in CO_2-laser-induced LPFGs.

1.1.2.2 Fabrication Mechanisms

A large amount of the research concerning CO_2-laser-induced LPFGs and exposure of optical fiber to CO_2-laser-light has concentrated on the mechanisms responsible for inducing a refractive-index change. At the CO_2 laser wavelengths employed during fabrication, the absorption coefficient of the optical fiber glass is relatively large. As energy from the laser is absorbed in the glass during exposure, the local temperature of the glass rises. The elevation in temperature (heating) enables changes in the glass refractive index [15]. Preferential heating of the side of the fiber toward the laser beam occurs because of one-sided exposure and leads to an azimuthally asymmetric refractive-index change over the fiber transverse cross-section [1]. The one-sided nature of the absorption can be seen in Fig. 1.3,

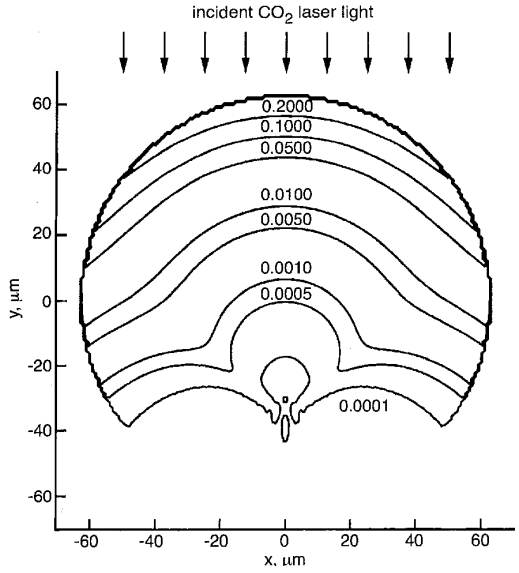

Figure 1.3: Calculated intensities (relative to unity) over a fiber transverse cross-section for incident CO_2 laser light. The fiber diameter is $125\mu m$ with a complex refractive index of $2.22 - j0.1$ [1].

which shows the calculated intensities over a fiber transverse cross-section upon exposure to transverse-electric linearly polarized light at a wavelength of $10.6\mu m$. The intensity of the light is much higher on the side of the fiber where the CO_2-laser light is incident (top of figure) than on the opposite side (bottom of figure). Also evident from the intensity profile is the fact that absorption occurs primarily in the cladding, which leads to a refractive-index change over the entire fiber transverse cross-section and not just in the core, as is the case for UV-induced LPFGs. While substantial one-sided absorption results in preferential heating, thermodynamic models indicate that the temperature difference across the fiber cross-section is less than 1% after $50ms$ of exposure [38]. If the rapid rise to steady-state temperature is correct (having not been verified experimentally), it is not readily obvious why the induced index change from one-sided exposure should be asymmetric.

Relaxation of internal stresses, both elastic and viscoelastic, in optical fibers during exposure to CO_2 laser light has been identified as a primary mechanism governing changes in the refractive index. Modeling temperature levels in optical fiber during exposure indicates that the softening temperature of silica is reached, which facilitates the relaxation of internal

stresses [2, 39]. LPFGs fabricated in optical fiber drawn under high tension exhibit significant changes in refractive index upon exposure to laser light. The major changes result from the release of the large initial elastic stresses frozen in high-stress fiber during cooling after drawing [40, 41]. More recently, relaxation of viscoelastic strain has been identified as a possible mechanism for refractive-index change and it is thought this effect is significant for optical fiber drawn at both low and high tension [42–44]. For hydrogen-loaded optical fibers exposed to moderate intensity CO_2 laser light, the formation of oxygen-hydrogen bonds accounts for observed refractive-index changes [45].

As in the case of UV-induced refractive-index changes, a variety of mechanisms appear to be responsible for the index changes in optical fiber exposed to CO_2 laser light. Which mechanism is dominant, if any, in the fabrication process depends on a large number of factors, including the peak temperature reached during exposure, exposure duration, incident power levels, laser wavelength, stress levels present in the fiber, and surface conditions. The significance of each of these factors in creating an index change is not clear for a particular fabrication approach. Also, the accuracy of the heating models has not been verified experimentally, so it is not explicitly known what temperature the optical fiber reaches during exposure to laser light, how long steady-state temperature is maintained, and what exactly occurs during the cooling process. Fabrication mechanisms is still an area requiring further investigation.

1.1.2.3 Transmission and Reflection Spectral Characteristics

The transmission characteristics of CO_2-laser-induced LPFGs for unpolarized incident light are similar to those of UV-induced LPFGs. A transmission spectrum of a typical CO_2-laser-induced LPFG is shown in Fig. 1.4. Coupling to various cladding modes at several distinct resonant wavelengths can be observed in the transmission spectrum shown in the figure. Consistent with grating functionality, back-reflection of CO_2-laser-induced LPFGs is quite low (less than $-70dB$) [2].

Mode profiles emerging from CO_2-laser-induced LPFGs have been observed through the use of a cladding mode measurement apparatus [2,46]. Davis calculated the effective indices

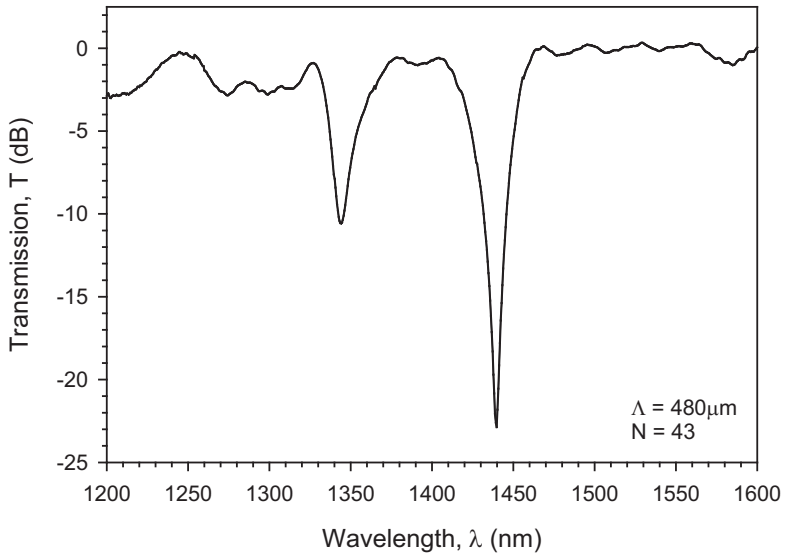

Figure 1.4: Example transmission spectrum of a CO_2-laser-induced LPFG exhibiting low broadband loss. The grating has a period (Λ) of $480\mu m$ and a total of 43 periods (N).

and field intensity profiles of several cladding modes by solving the wave equation for light propagating in a three-layer cylindrical waveguide. Using Eq. (1.2) and the effective index values, the resonant coupling wavelengths were subsequently determined. Figure 1.5 shows good agreement between observed and calculated mode intensity profiles for a $480\mu m$-period CO_2-laser-induced LPFG [2].

1.1.2.4 Polarization-Dependent Transmission Characteristics

Polarization-dependent transmission has been observed in the spectra of CO_2-laser-induced LPFGs. Davis *et al.* reported a maximum polarization-dependent loss (PDL) of $1.7dB$ for an LPFG with an attenuation of $-23.9dB$ at the same wavelength [46]. No resonant peak splitting was observed [2]. Later studies of LPFG polarization-dependent transmission characteristics reported similar peak PDL levels, but a resonant peak splitting of approximately $1nm$ was observed [47]. Ryu *et al.* attributed the presence of PDL to the measured asymmetric stress profile resulting from one-sided exposure of optical fiber to CO_2 laser light. Their stress profile measurements also indicated that the asymmetry present in the cladding was greater than that found in the core [47]. The azimuthally asymmetric refractive-index

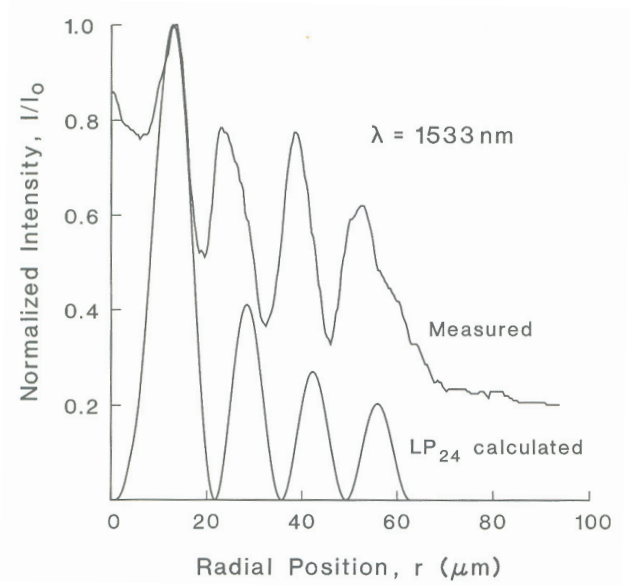

Figure 1.5: Calculated mode field intensity pattern for the LP_{24} cladding mode compared to measured, normalized intensity profile for a CO_2-laser-induced LPFG [2].

change [1] introduces birefringence within the grating structure and leads to a polarization-dependent phase-matching condition.

Symmetrically exposing a section of fiber (using a concave mirror) to laser light while writing a grating period has been shown to remove most PDL effects [48]. Symmetric exposure to laser light eliminates the aspect of preferential heating associated with one-sided exposure.

While the effect of asymmetry in the stress profile is known, other aspects of the polarization-dependent transmission characteristics of CO_2-laser-induced LPFGs have not been studied. No detailed examination of asymmetry and its effect on the phase-matching condition exists; most of the developed theory concerns UV-induced LPFGs. No direct comparison of PDL and birefringence levels in similar UV-induced and CO_2-laser-induced LPFGs has been performed. The introduction of polarization mode dispersion (PMD) in CO_2-laser-induced LPFGs resulting from birefringence is also an issue that has not been examined.

1.1.2.5 Response to Flexure

As a result of the azimuthally asymmetric refractive-index change induced from one-sided exposure, CO_2-laser-induced LPFGs exhibit behavior different from traditional UV-induced LPFGs when subjected to flexure (bending). The change in the transmission spectra of CO_2-laser-induced LPFGs with applied curvature was found to be dependent upon the axial (longitudinal) rotational orientation of the grating relative to the plane of curvature or, equivalently, the direction of bending.

The axial rotational orientation dependence of bending in CO_2-laser-induced LPFGs was first demonstrated by VanWiggeren *et al.* [1] They observed that the change in transmission resonance resulting from bending was different depending on the axial rotational orientation of the grating relative to the plane of curvature; the change in the transmission spectrum is different if a grating is first rotated about its longitudinal axis and then bent rather than if it were not rotated and only bent. Figure 1.6 illustrates the concept of axial rotational orientation relative to the plane of curvature. From symmetry considerations, the change in transmission with bending is the same for the 90^o and the 270^o axial rotational orientations. The orientations exhibiting similar transmission responses upon flexure are thought to correspond to the 90^o and 270^o axial rotational orientations (the side of the optical fiber where laser light was incident being perpendicular to the plane of curvature). An even symmetry in the transmission response is observed about axial rotational orientations of 0^o and 180^o. The axial rotational orientation dependence and the symmetry conditions observed are a consequence of the azimuthally asymmetric refractive-index change induced by one-sided exposure.

Variable attenuation tuning (VAT) at a constant wavelength and resonant wavelength tuning (WT) at constant amplitude behaviors were observed for CO_2-laser-induced LPFGs subjected to bending over curvature range from $0m^{-1}$ to $5m^{-1}$ [3]. The two different behaviors were sometimes observed in the same grating but at different axial rotational orientations relative to the plane of curvature. Figure 1.8 shows both types of tuning behavior for various applied curvatures. In this case, VAT and WT were observed in two separate CO_2-laser-induced LPFGs (LPFG No. 1 and LPFG No. 2).

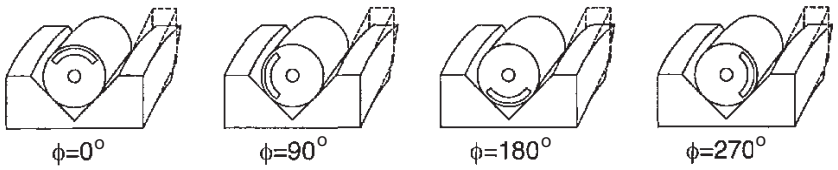

Figure 1.6: Four possible axial rotational orientations of a CO_2-laser-induced LPFG relative to the plane of curvature. Bending is up and down, therefore, the plane of curvature is vertical. The curved stripe designates the side of the fiber that faced the laser during fabrication. The change in transmission spectrum is the same for the 90° and 270° orientations [1].

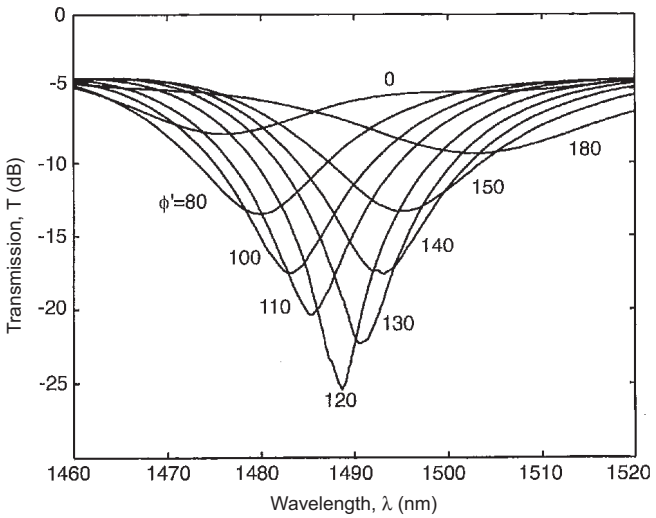

Figure 1.7: Transmission curves of a CO_2-laser-induced LPFG at constant curvature ($2.1m^{-1}$) for various axial rotational orientations, $\phi^{'}$. Note the observed symmetry around $\phi^{'} = 120^{o}$. For this measurement, the relationship between $\phi^{'}$ and ϕ is unknown since the side of the fiber the facing the laser during fabrication is unknown [1].

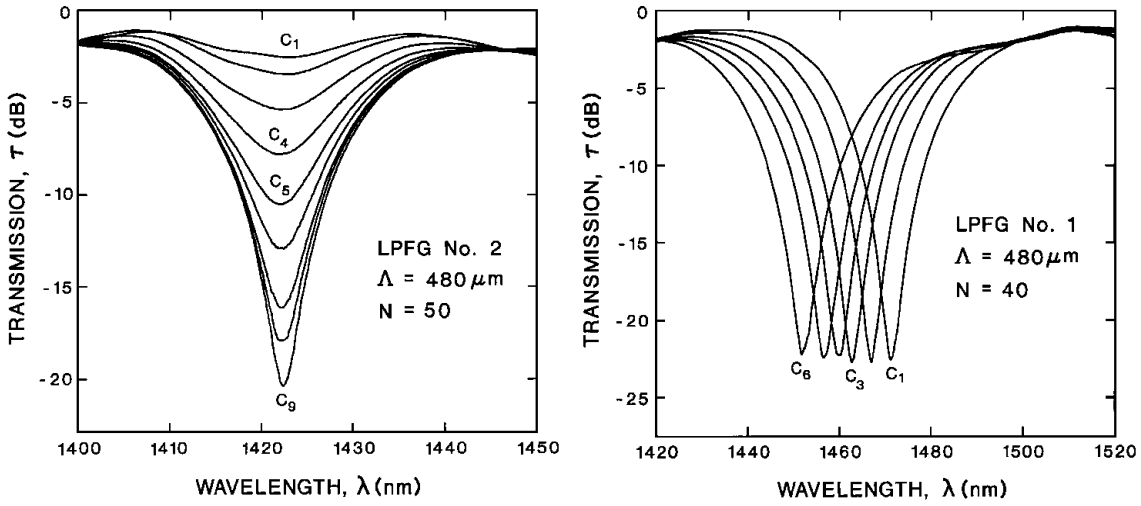

Figure 1.8: (a) Variable attenuation tuning with applied curvature, from $C_1 = 0.00m^{-1}$ to $C_9 = 1.61m^{-1}$. (b) Wavelength tuning with applied curvature, from $C_1 = 2.23m^{-1}$ to $C_6 = 3.85m^{-1}$ [3].

Bending response measurements conducted for LFPGs fabricated using a pulsed CO_2 laser yielded results similar to those reported by VanWiggeren *et al.* using LPFGs fabricated with a standard (non-pulsed) CO_2 laser [1, 49]. However, VAT and WT with bending were not reported for high-frequency (several kHz) CO_2-laser-induced LPFGs.

The observed VAT and WT behavior in flexed CO_2-laser-induced LPFGs would be useful for devices operating in the $1550nm$ telecommunications wavelength band. Nonetheless, such behavior has not been observed in that band and it is not evident what grating parameters (period, attenuation levels, curvature ranges, axial rotational orientations) lead to VAT and WT behavior. Attempts to model changes in LPFG transmission with applied flexure have been limited to UV-induced LPFGs [50].

1.1.2.6 Applications

The VAT and WT behavior observed in flexed CO_2-laser-induced LPFGs has direct applications in optical telecommunications networks [3]. Flexed LPFGs can be used as variable optical attenuators or as dynamic gain equalizers. Resonant WT can be used directly for performing dynamic wavelength-selective filtering in coarse wavelength division multiplexing (CWDM) systems. Using CO_2-laser-induced LPFGs for such applications has been suggested, but prototype devices have not been demonstrated previously.

A tunable gain equalizer device was realized using LPFGs written with high-frequency CO_2 laser pulses that were subjected to variable transverse loading [51]. Similar to UV-induced LPFGs, CO_2-laser-induced LPFGs may also be used for strain, transverse load, torsion, bending, and temperature sensing applications [49].

1.1.2.7 Characterization of Refractive-Index and Stress Profiles

With the variety of unique characteristics observed in CO_2-laser-induced LPFGs, several attempts have been made to measure the change in the refractive-index profile resulting from exposure to CO_2 laser light. Index profile measurements are important for investigating fabrication mechanisms, understanding grating performance, and in modeling efforts. Profile measurements conducted by Davis, using transverse interferometric profiling, clearly indicated that the index change was asymmetric [2,15]. However, the measurement method employed assumed azimuthally symmetric samples, which CO_2-laser-induced LPFGs are not. While care was taken to orient grating samples to achieve the most symmetric profile, the exact asymmetric refractive-index profile could not be obtained from the one-dimensional measurement.

While not directly characterizing refractive index, Ryu *et al.* did measure the asymmetric axial stress profile of an optical fiber exposed to CO_2 laser light [47]. From the stress profile the modal birefringence resulting from asymmetry was calculated.

No actual measurement of the two-dimensional transverse cross-sectional refractive-index profile of optical fiber exposed to CO_2 laser light has been reported. This is due, in part, to the lack of a suitable two-dimensional measurement technique that possesses sufficient index resolution and accuracy.

1.2 Research Objectives

From the previous research conducted on CO_2-laser-induced LPFGs, it is evident that they possess useful characteristics that can be harnessed to create novel devices. It is also clear that the asymmetry induced in an optical fiber resulting from one-sided exposure to CO_2 laser light impacts performance. Previous research has examined only limited aspects of the effect of asymmetry. In order to manipulate, harness, and enhance the unique features

of CO_2-laser-induced LPFGs, it is necessary to understand their physical properties and optical characteristics. The main objectives of the research presented in this thesis are to experimentally quantify the optical performance of CO_2-laser-induced LPFGs with respect to flexure, torsion, and variable incident polarization, to characterize grating cross-sectional refractive-index profiles, and to demonstrate applications of CO_2-laser-induced LPFGs that exploit their unique properties. The azimuthally asymmetric refractive-index change generated in CO_2-laser-induced LPFGs during fabrication gives these gratings unique features, especially as compared to more traditional UV-induced LPFGs. The research presented in this thesis represents a detailed study and consideration of the consequences of the asymmetric refractive-index change on LPFG performance and how the gratings unique features can be used to create devices for important applications. CO_2-laser-induced LPFG optical transmission characteristics, applications, physical properties, and related issues investigated in this research and representing original contributions include:

1. The improvement of CO_2-laser-induced LPFG fabrication yield achieved through changes in the fabrication apparatus and procedure.

2. The first detailed measurements of CO_2-laser-induced LPFG polarization-dependent transmission characteristics, including both PDL and PMD.

3. The extension of existing LPFG PDL theory to encompass LPFGs other than UV-induced, including CO_2-laser-induced LPFGs.

4. The first demonstration of variable attenuation tuning and wavelength tuning in the important $1550nm$ telecommunications band by controlled flexure of CO_2-laser-induced LPFG and the first direct comparison of the flexure response of a CO_2-laser-induced LPFG (azimuthally asymmetric) with a UV-induced LPFG (azimuthally symmetric).

5. The measurement of the torsion response of CO_2-laser-induced LPFGs.

6. The first development of CO_2-laser-induced LPFG-based prototype variable optical attenuators and optical tunable filters.

7. The first demonstration of a CO_2-laser-induced LPFG-based optical fiber-to-waveguide coupler.

8. The development of a new cross-sectional refractive-index profiling technique, micro-interferometric optical phase tomography (MIOPT), that enables measurement of optical fiber samples possessing small and azimuthally asymmetric refractive-index variations.

9. The first cross-sectional refractive-index profile measurements of azimuthally asymmetric optical fibers and azimuthally symmetric optical fibers conducted using the new profiling technique.

10. The first cross-sectional refractive-index profile measurements of CO_2-laser-induced LPFGs.

1.3 Thesis Overview

The research objectives and contributions described above are examined in detailed within the following chapters.

Chapter 2 concerns CO_2-laser-induced LPFG fabrication and basic transmission characteristics. The fabrication apparatus and procedure are briefly described. Improvement of fabrication yield to allow LPFGs with specific transmission characteristics to be obtained rapidly is also discussed. Finally, several basic CO_2-laser-induced LPFG transmission curves, for unpolarized incident light, are given.

Chapters 3 and 4 discuss the impact of the azimuthally asymmetric refractive-index change present in CO_2-laser-induced LPFGs on grating transmission. Polarization-dependent transmission is considered in Chapter 3, with measurements of CO_2-laser-induced LPFG PDL and PMD reported and discussed. Direct comparisons between CO_2-laser-induced LPFG polarization-dependent transmission and UV-induced LPFG polarization-dependent transmission are presented. The response of CO_2-laser-induced LPFGs to physical manipulation is examined in Chapter 4. Both the response to applied flexure and the response to applied torsion are considered.

Example applications in which the use of azimuthally asymmetric refractive-index profile present in CO_2-laser-induced LPFGs confers certain advantages are discussed in Chapter 5. The concept of prototype variable optical attenuator and optical tunable filter devices based on controlled flexure of CO_2-laser-induced LPFGs is presented and example results from constructed prototype devices are given. An example of a CO_2-laser-induced LPFG-based optical fiber-to-waveguide coupler is also investigated. Simulation results for a weak directional coupler are first given and then the measurement configuration and measurement results are presented.

Refractive-index profile measurements of CO_2-laser-induced LPFGs are presented in Chapter 6. A new refractive-index profiling technique that enables measurements of the azimuthally asymmetric refractive-index change induced in CO_2-laser-induced LPFG is described. Profile measurements of azimuthally symmetric and asymmetric optical fibers are presented that demonstrate the profiling technique's capabilities.

Finally, Chapter 7 summarizes the research presented in the thesis. Potential future research areas are discussed.

CHAPTER 2

FABRICATION AND BASIC TRANSMISSION CHARACTERISTICS

The one-sided exposure of optical fiber to a carbon-dioxide (CO_2) laser beam impacts the performance of the resulting CO_2-laser-induced long-period fiber gratings (LPFGs). In this chapter, the fabrication apparatus and procedure that yield CO_2-laser-induced LPFGs with asymmetric refractive-index profiles are discussed. Examples of CO_2-laser-induced LPFG basic transmission spectra for various grating periods are given. Changes made to the apparatus and in the procedure to increase the likelihood of fabricating LPFGs with specific transmission characteristics are presented.

2.1 Fabrication

2.1.1 Fabrication Apparatus

A diagram of the apparatus used for fabricating LPFGs by controlled exposure to CO_2 laser light is shown in Fig. 2.1. Light emerging from a CO_2 laser is reflected by a broadband, silver-coated mirror so as to be precisely aligned with the subsequent arrangement of optical elements. A beamsplitter reflects approximately 10% of the incident light reflected from the mirror to an optical power meter or CO_2 spectrum analyzer to permit measurement of the laser power level or wavelength (respectively). After passing through the polarization optical elements (polarizer and waveplates), the laser beam is incident upon an electronically controlled shutter. The shutter opens and closes to control the amount of time a section of fiber is exposed to laser light for creating one grating period. A cylindrical lens focuses the incident light passing through the shutter (when open) to a line that is perpendicular to the fiber longitudinal axis. The optical fiber, into which an LPFG is written, is positioned at the lens focal length at the center of the focused perpendicular line and is held in alignment by a precision fixture. A photograph of an optical fiber in the alignment fixture is shown

in Fig. 2.2. One end section of the fiber is secured to a motorized linear translation stage while a small weight is attached to the other end section (positioned on a pulley) to keep the fiber taut during fabrication.

The status of the LPFG during fabrication is monitored by two separate methods in the apparatus. A broadband optical source and an optical spectrum analyzer (OSA) are used to monitor grating transmission spectrum evolution during fabrication. A charge-coupled device (CCD) camera/microscope arrangement, positioned above the fiber in the alignment fixture, facilitates visual observations of any damage or visible change in fiber condition during exposure.

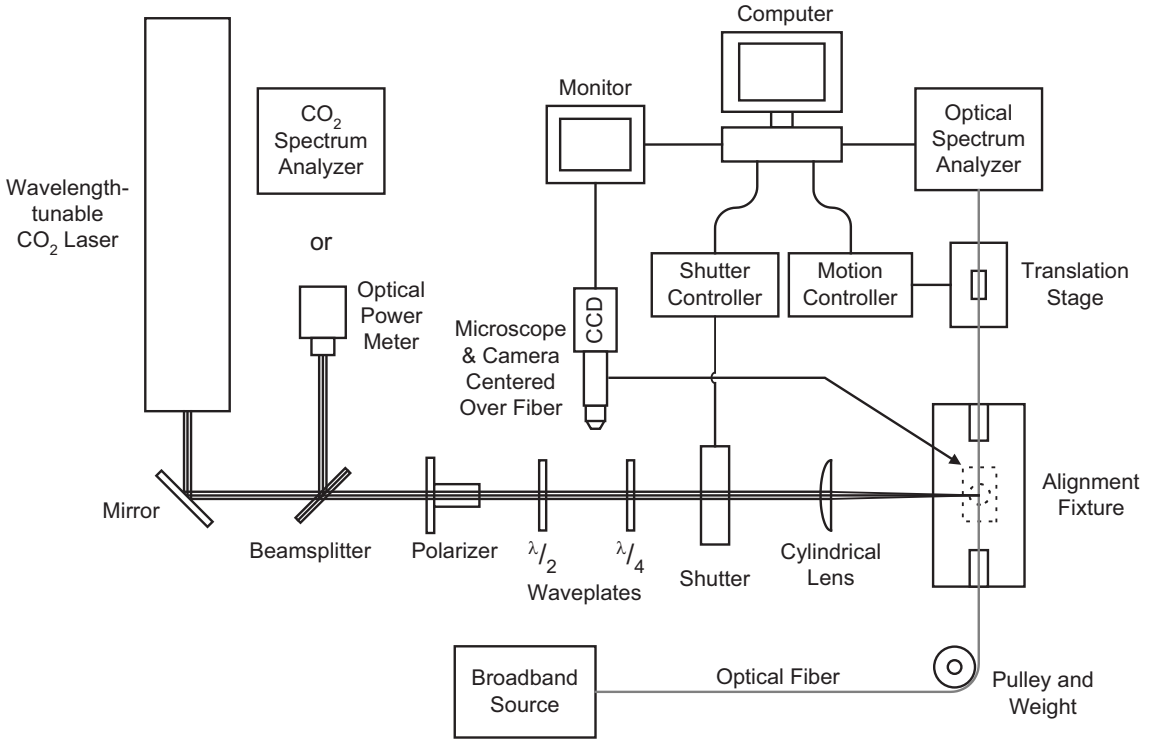

Figure 2.1: Diagram of the apparatus used to fabricate CO_2-laser-induced LPFGs.

The initial CO_2-laser-induced LPFG fabrication apparatus described by Davis [2] has been enhanced to permit additional control and monitoring during the grating fabrication process. Use of the power-stabilized, wavelength-tunable CO_2 laser ensures that the incident laser power does not fluctuate significantly and that a suitable wavelength can be selected and maintained during fabrication [5]. The CO_2 spectrum analyzer is used to verify that the correct laser wavelength has been selected. The addition of polarization-control optics,

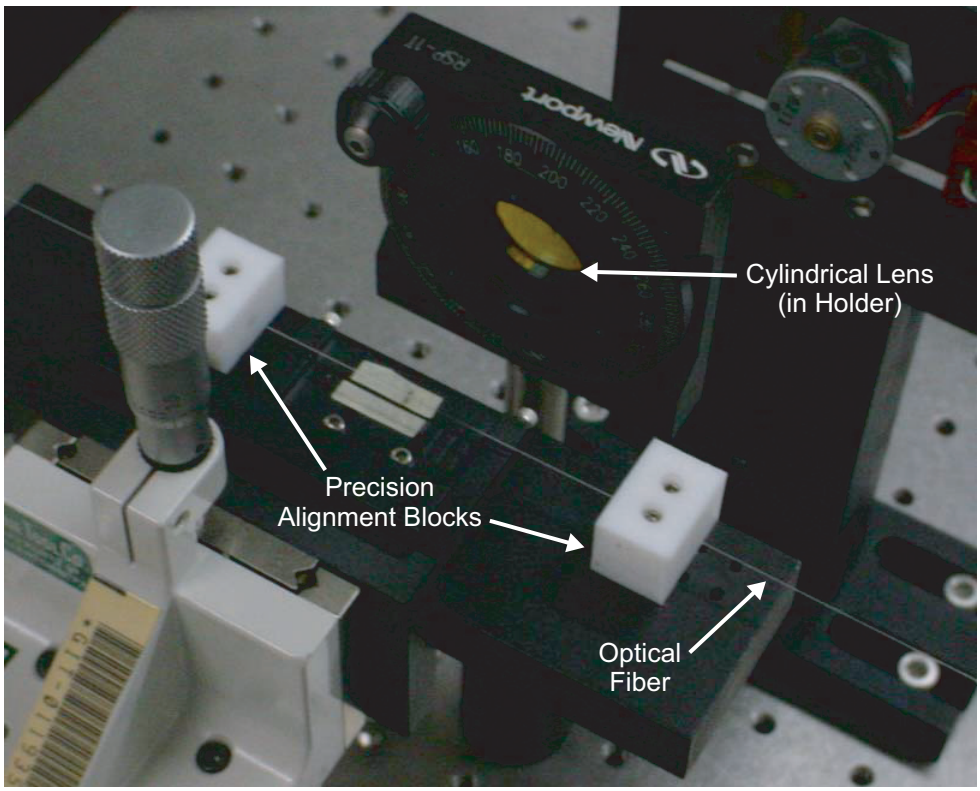

Figure 2.2: Picture of the precision alignment fixture for holding the optical fiber during fabrication.

specifically a polarizer, a quarter-wave retardation plate, and a half-wave retardation plate, enables the polarization state of the CO_2 laser beam to be controlled. Monitoring of the LPFG transmission spectrum during fabrication was improved by the use of a relatively high power edge-emitting LED source. The higher-power source permitted high attenuation levels at peak resonance to be measured. A further, detailed description of the fabrication apparatus is available in the literature [5, 6].

It is evident from the arrangement shown in Fig. 2.2 that the focused CO_2 laser light is incident on only one side of the optical fiber that is held in the alignment fixture. Some of the consequences of the preferential heating and absorption associated with the one-sided exposure are examined in later chapters.

2.1.2 Fabrication Procedure

The actual process of writing an LPFG in an optical fiber using a CO_2 laser begins with inserting the fiber into the alignment fixture, securing the fiber to the linear translation

stage, removing a short section of fiber buffer (usually about $40mm$) with a mechanical fiber stripper and gently cleaning the stripped section with isopropyl alcohol and wipes. A portion of the optical fiber outside of the alignment fixture is then positioned over the pulley and the small weight attached. Once the start of the stripped section of the fiber is positioned near the lens focal line, a small mark is placed on the fiber with a black marker to indicate the start of the grating structure. The mark is used in subsequent testing to assist in positioning and centering the LPFG.

A single grating period is written by opening the shutter for a specified time period. Subsequent grating periods are written by translating the fiber a specified length (the grating period, Λ) and opening the shutter again. After each period is written, the transmission spectrum of the grating is measured and recorded using the OSA. If desired, images of the optical fiber are taken with the CCD/microscope arrangement during exposure and stored for later examination. The individual-period writing process is repeated until the specified number of total periods have been written or a desired transmission spectrum is observed. The exposure, translation, and monitoring processes are completely controlled from a central computer using a custom LabVIEW program [52]. A further, detailed description of the fabrication procedure is available in the literature [5, 6]. The total number of periods that can be written in an individual grating is limited by the travel limit of the linear stage.

After the grating is completely written, another black mark is added to indicate the location of the end of the LPFG and a small tape tab is placed near the beginning of the grating and oriented in the direction of the incident laser beam. Each fabricated CO_2-laser-induced LPFG is assigned a unique identification number to identify it in later studies. The transmission spectrum, measured after each period, is stored in a data file along with the grating fabrication parameters (see Sec. 2.2).

The tab placed on the fiber after writing each grating is used to indicate which side of the fiber the laser beam was incident upon during fabrication. The tab is useful for experiments that examine the effect of index asymmetry induced in the grating, however, the orientation of the tab is only approximate, typically $\pm 15^{o}$. If the orientation of the fiber relative to the incident laser beam must be known with higher precision, a supplementary technique

should be used. A suitable and rapid qualitative imaging technique that is beneficial for establishing orientation is discussed in Appendix B.

2.1.3 Improvement of Fabrication Yield

The issue of fabrication variability has been discussed previously by both Davis and Braiwish [2, 5]. They state that for the same incident power level, exposure time, number of periods, LPFGs with different peak attenuation levels can result. Suggested reasons for the fabrication variability include variation of fiber properties with length, variable surface conditions, and varying environmental conditions, but it is not known what combination of factors lead to the observed variability. With the fabrication apparatus and procedure described above, significant variation still occurred during grating fabrication. Rather than conduct a detailed investigation to identify the source(s) of the observed variability, an attempt to improve the fabrication yield of CO_2-laser-induced LPFGs, that is, to increase the number of fabricated gratings with significant and useful attenuation levels at resonance, was made by altering the fabrication parameters and procedure. While it is possible some of the factors that contributed to fabrication variability were addressed while attempting to improve the yield, the effort concerns obtaining specific/desired grating transmission characteristics rapidly. The ability to create CO_2-laser-induced LPFGs with specific transmission characteristics is important for investigating their characteristics, properties, and potential applications.

Changes made to the fabrication arrangement include selecting a suitable laser wavelength, changing the laser beam polarization state from vertical linearly polarized (LP) to horizontal LP, and changing shutter exposure from a single open/close cycle per period to multiple cycles per period. Alterations made in the fabrication procedure include improved monitoring of transmission spectra during fabrication and modification of the fabrication control program to permit changes in exposure conditions during the actual writing process. The individual changes listed above improved fabrication yield and their individual impact on yield is discussed below.

Ensuring that a suitable laser wavelength is used for fabrication proved critical to improving yield; to induce a refractive-index change during exposure, there must be sufficient power at the correct wavelength. The importance of the lasing wavelength was demonstrated by attempting to fabricate LPFGs at two different wavelengths, $9.3\mu m$ [9R(20) line] and $10.6\mu m$ [10P(20) line]. The two wavelengths offer peak power levels within the individual CO_2 bands [5]. It was initially believed that $9.3\mu m$ would be a suitable wavelength because of the fiber cladding material's strong absorption at that wavelength (an absorption coefficient for silica of $3.05\mu m^{-1}$ at $9.3\mu m$ versus 0.03-$0.533\mu m^{-1}$ at $10.6\mu m$) [53, 54]. Fourteen attempts were made to write LPFGs in optical fiber, seven at the $9.3\mu m$ wavelength and seven at the $10.6\mu m$ wavelength. Other fabrication parameters were kept constant (full laser output power of approximately $10W$ was used). All of the fabrication attempts at $10.6\mu m$ yielded gratings with peak attenuation ranging from 10 to $20dB$, while no LPFG could be written for the $9.3\mu m$ laser wavelength. The difference in grating yield between the two wavelengths is believed to be due to the high reflectance (0.426) at $9.3\mu m$; even though the glass absorption is high, the reflectance at that particular wavelength is as well and this causes a large portion of the incident laser light to be reflected instead of absorbed. A wavelength of $10.6\mu m$ is better suited for writing because, while the material absorption is not as high as at $9.3\mu m$, the amount of light reflected is much lower (reflectance of 0.132). As a result of the study, all later CO_2-laser-induced LPFGs were fabricated at the $10.6\mu m$ wavelength. Use of a power-stabilized, wavelength-tunable CO_2 laser ensures that all available power will be at the wavelength most suitable for inducing a refractive index change in exposed optical fiber.

In addition to the laser wavelength, the polarization state of the light incident on the optical fiber influences fabrication yield. Changing the polarization state of the incident laser beam from transverse magnetic (TM) incident (vertical LP) to transverse electric (TE) incident (horizontal LP) improves fabrication yield significantly by reducing the frequency of erratic gratings. The polarization state of the light emerging from the laser is TM but can be rotated from TM LP to TE LP using the half-wave retardation plate. The yield improvement resulting from the polarization change is indicated in Fig. 2.3, where the

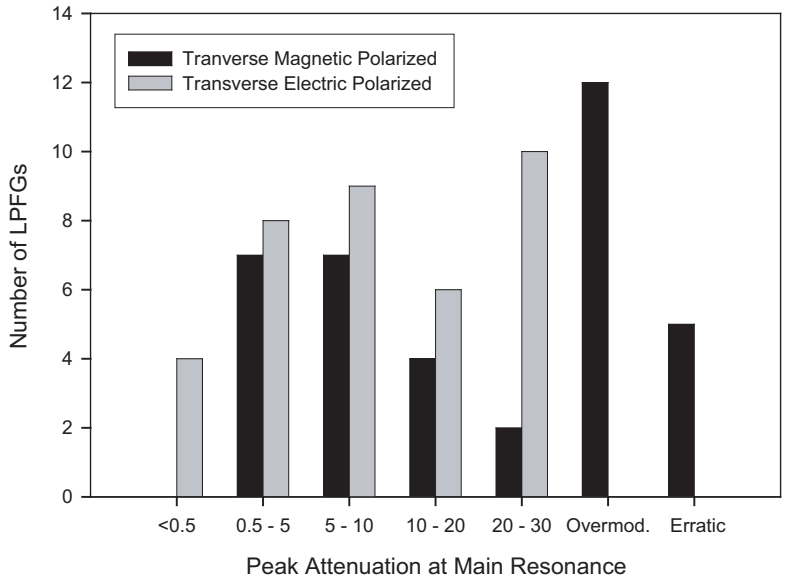

Figure 2.3: Comparison of CO_2-laser-induced LPFGs fabricated with transverse-magnetic (TM) and transverse-electric (TE) linearly polarized (LP) light. Gratings fabricated with TM LP light exhibited more variation.

peak attenuation at the main cladding-mode resonance (nearest a wavelength of $1550nm$) is compared for gratings fabricated with TM LP or TE LP light. The designation overmodulated refers to a rapid increase and then decrease in attenuation at the main cladding-mode resonance as light is initially coupled out of and then back into the fiber core. Erratic classification is similar to overmodulated, but the process occurs in far fewer periods and significant broadband loss in grating transmission spectra occurs. Other fabrication parameters of the gratings, summarized in Table 2.1, are similar with exception of the incident power level and exposure time. The number of fabricated CO_2-laser-induced LPFGs with desirable attenuation levels is larger for TE LP light while gratings fabricated with TM LP light exhibit more variation, especially overmodulated and erratic.

One possible explanation for the observed difference in fabrication yield for the two polarization states is the differing absorption profiles associated with the incident polarization states. The dissimilarity in the profiles is evident in comparing the field intensity contour plots of Fig. 2.4 and Fig. 2.5. For both of the plots, light with a wavelength of $10.6\mu m$ is incident from the top of the figure on an SMF fiber; only the polarization state of the

Table 2.1: CO_2-Laser-Induced LPFG Fabrication Parameters for Incident Polarization State Comparison

	Trans. Magnetic LP	**Trans. Electric LP**
Total Number of LPFGs	37	37
Average Number of Periods	41	40
Average Incident Power (10% split)	$0.784W$	$0.902W$
Average Exposure Time per Period	$273ms$	$411ms$
Grating Period	$640\mu m$	$640\mu m$
Laser Wavelength	$10.6\mu m$	$10.6\mu m$

incident light changes. The closer spacing of the contour lines for the TM case indicates stronger initial absorption at the fiber surface. In the TE case, the absorption is more gradual and uniform over the profile (less variation along the sides). The explanation is consistent with the lower power level and shorter exposure time found sufficient for creating LPFGs with TM LP light. The stronger initial absorption and shorter exposure time leave the system more susceptible to quick environmental fluctuations and slight changes in fiber position that could contribute to observed variations.

Based on the results obtained from the incident polarization state comparison, it was surmised that a longer exposure time might also improve fabrication yield. However, leaving the shutter open for times longer than approximately $450ms$ produced little improvement in yield. A series of rapid and short shutter exposures for each period, instead of a single exposure per period, was then attempted. For each period, the shutter was opened and closed rapidly, usually with a period of $50ms$ and a duty cycle of about 75%. The cycling was repeated over a hundred times for each grating period. The use of multiple shutter exposures each grating period extended the amount of time necessary to write a given period, but allowed the temperature in the fiber to increase toward steady-state in a more controlled manner. The exposed section of fiber is also held at elevated temperatures longer, which lowers the chance of a quick fluctuation influencing the resulting glass temperature. Changing to multiple exposures per period from a single exposure per period did improve fabrication yield, but produces only a modest impact as compared to the incident

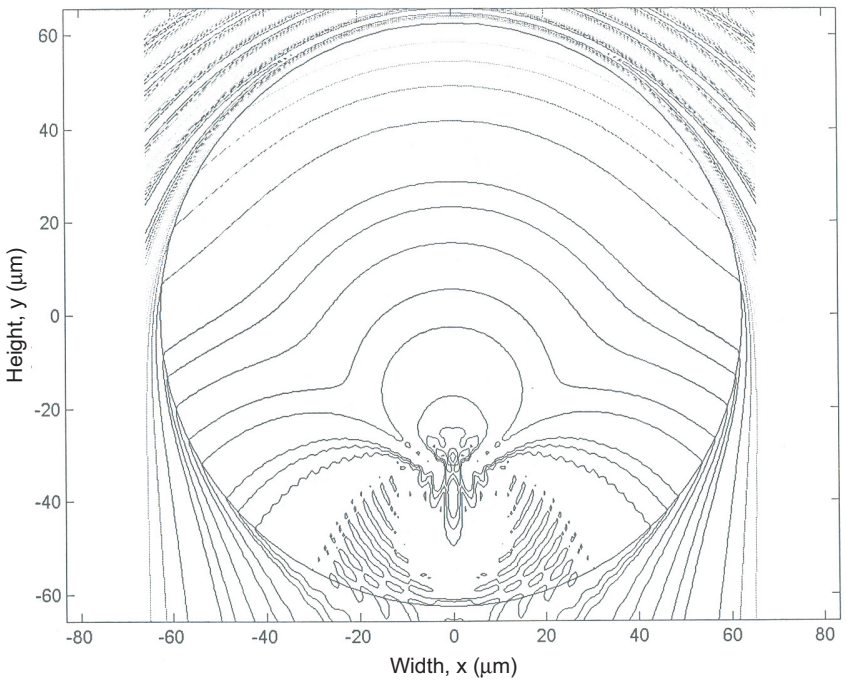

Figure 2.4: Contour line plot of field intensity in a $125\mu m$ diameter cylinder for $10.6\mu m$-wavelength TE LP light. The cylinder (n = 2.22-j0.1) is surrounded by air (n = 1.0) [4].

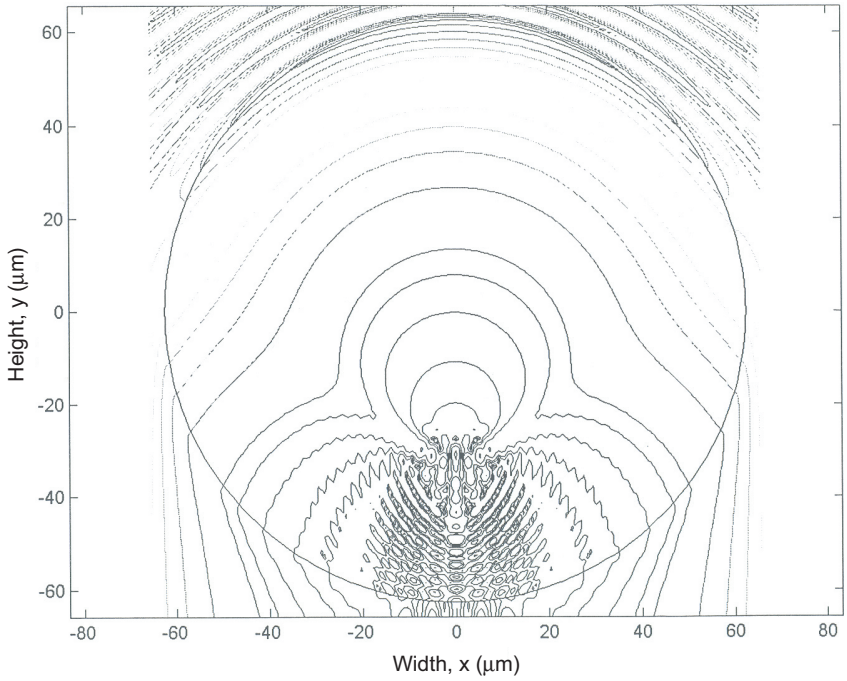

Figure 2.5: Contour line plot of field intensity in a $125\mu m$ diameter cylinder for $10.6\mu m$-wavelength TM LP light. The cylinder (index of 2.22-j0.1) is surrounded by air (n = 1.0) [4].

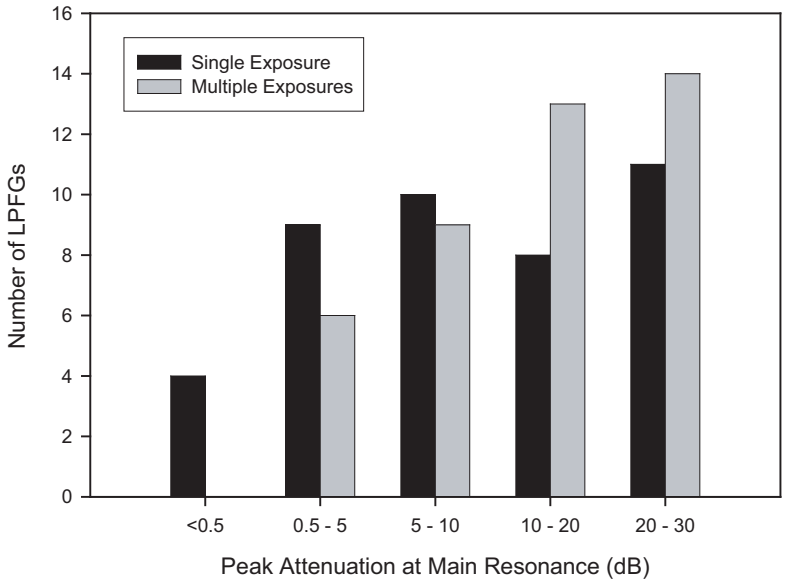

Figure 2.6: Comparison of CO_2-laser-induced LPFGs fabricated with a single exposure per period and multiple, short exposures per period. Multiple exposures per period produced a slightly higher yield of LPFGs with higher attenuation at resonance.

polarization state and wavelength changes. A comparison of LPFGs resulting from the two different forms of exposure is shown in Fig. 2.6. Again, the other fabrication parameters, shown in Table 2.2, were kept similar while conducting the comparison.

The alterations discussed above all involved changes to the incident laser beam, namely, how and in what state the laser beam is incident upon the fiber. While the alteration

Table 2.2: CO_2-Laser-Induced LPFG Fabrication Parameters for Exposure Comparison

	Single	**Multiple**
Total Number of LPFGs	42	42
Average Number of Periods	40	39
Average Incident Power (10% split)	$0.900W$	$0.854W$
Average Exposure Duty Cycle	100%	72.3%
Average Time Period of Exposure	$400ms$	$50ms$
Number of Exposures per Period	1	160
Grating Period	$640\mu m$	$640\mu m$
Laser Wavelength	$10.6\mu m$	$10.6\mu m$

of specific fabrication parameters did improve fabrication yield, variation between CO_2-laser-induced LPFGs fabricated with the same parameters still occurred. An additional modification, this time to the fabrication procedure itself, was then made to improve the yield further. The change combines an improvement in monitoring LPFG transmission spectra with the ability to alter exposure parameters during fabrication to adjust the writing process.

The addition of a relatively high-power, broadband source for use in monitoring LPFG transmission spectra during fabrication assisted in creating gratings with specific, desired characteristics. Combined with the OSA, transmission spectra attenuation levels in excess of $25 dB$ could be readily detected. The high-resolution monitoring afforded by the source and OSA permitted fabrication to be halted early, if a desired spectrum was observed, and allowed detailed observations to be made so that the fabrication parameters could be appropriately adjusted.

The CO_2-laser-induced LPFG fabrication program was altered to allow parameters such as exposure time, number of exposures, and the total number of periods to be changed during fabrication. For instance, after the first few periods of a grating were written, if the induced index change was not deemed to be sufficient to reach a final desired attenuation level at resonance, the number of exposures per period could be increased or more periods added. The alterations to the programs made it easier to create gratings with specific transmission characteristics with a reasonable number of total periods.

Careful monitoring, both of the tranmission spectrum and of the fiber image, proved to be crucial for obtaining LPFGs with specific transmission characteristics. Often, simple visual observation of the fiber for the first few grating periods was sufficient to predict the final peak attenuation at resonance. As an example, several images of an optical fiber, captured before and after exposure to laser light, using the CCD/microscope arrangement, are shown in Fig. 2.7. The visual change in the light pattern reflected from exposed optical fiber typically provided a qualitative indication of the level of index modulation. In future versions of the fabrication system, the combination of visual and transmission spectrum monitoring (with the OSA) could serve as a form of feedback to completely automate the

LPFG fabrication process and improve yield further.

Ensuring a laser wavelength of $10.6\mu m$, changing the incident light polarization state from TM LP to TE LP, and changing from single exposure per grating period to multiple and shorter exposures all helped in creating CO_2-laser-induced LFPGs with more predictable transmission characteristics. Improvement in monitoring transmission spectra during fabrication and changing fabrication parameters during the writing process were both important for creating LPFGs with specific transmission characteristics. Although the changes certainly contributed to improving yields, fabrication variation still occurred. Example transmission spectra of CO_2-laser-induced LPFGs fabricated with the described apparatus and procedure are shown in the next section.

2.2 Example Basic Transmission Characteristics

Following the investigation into improving fabrication yield, several hundred LPFGs were fabricated with various period spacings. Periods of $480\mu m$, $565\mu m$, $597\mu m$, $640\mu m$, and $650\mu m$ were commonly selected for use since they produce cladding-mode coupling resonances within the important $1550nm$ telecommunications wavelength band. Several example transmission spectra, observed for broadband unpolarized incident light, of CO_2-laser-induced LPFGs are shown below. Examples of both undermodulated and overmodulated LPFGs are given. The undermodulated and overmodulated designation is applied with reference to a specific cladding-mode resonant wavelength, usually whichever one is closest to a wavelength of $1550nm$. The evolution of transmission spectra during fabrication is also shown. Before each grating is written, the spectrum measured at the OSA is normalized to remove any power variation over the wavelength range due to the broadband source emission spectrum.

Gratings with various period spacings and modulation levels are useful for different applications, as will be demonstrated in subsequent chapters. A list of the symbols used to identify LPFG parameters is given in Table 2.3. Although not all of the parameters are provided for each grating referred to in the following chapters, the listed parameters are

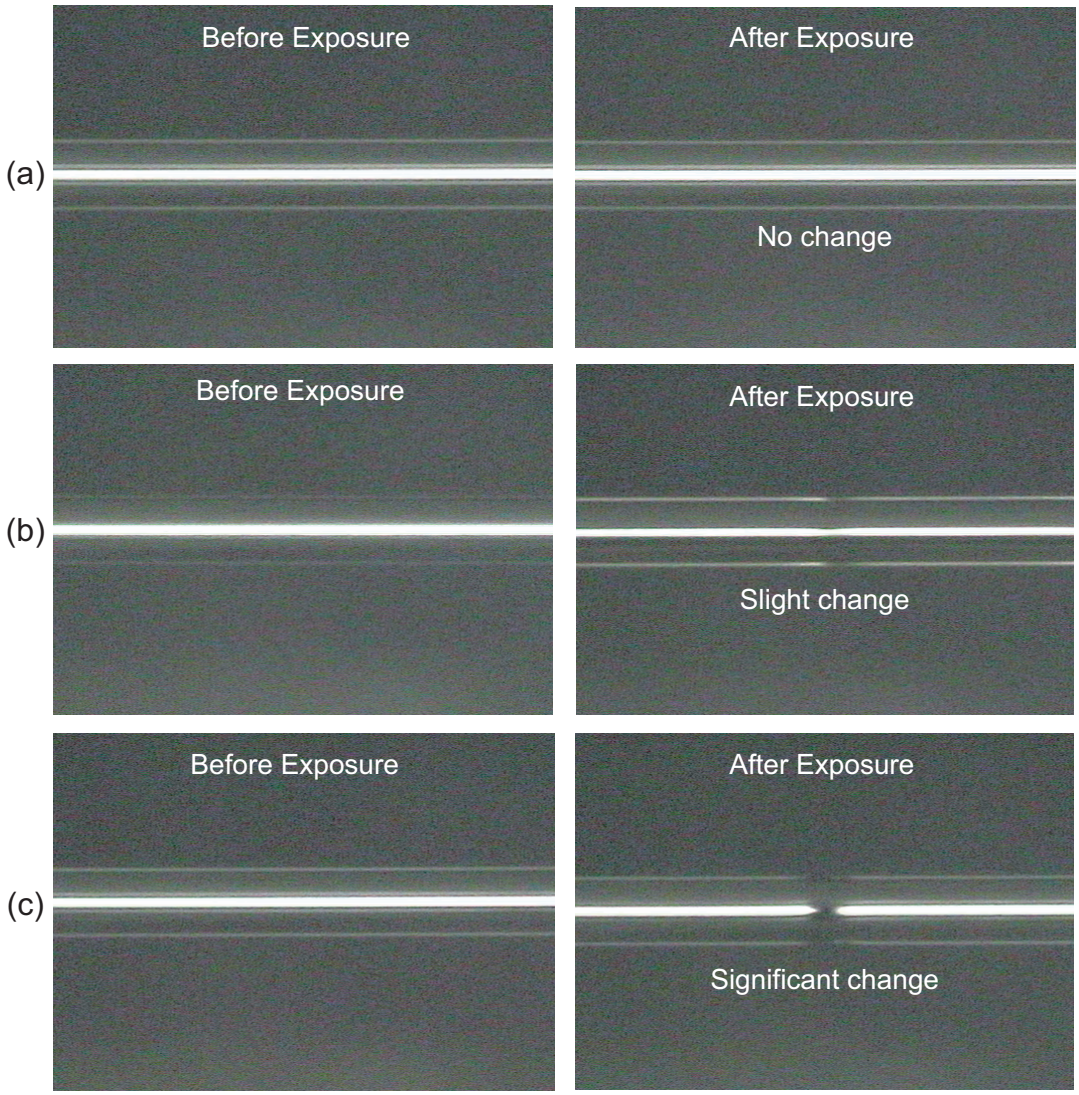

Figure 2.7: Photographs of an optical fiber before and after exposure to CO_2 laser light. The photographs were taken with the CCD/microscope arrangement and show light reflected from the top and bottom surfaces of the bare glass fiber. (a) No observable visual change produces LPFGs with little attenuation at resonance, (b) Slight visible change produces LPFGs with moderate to strong attenuation at resonance. (c) Significant visible changes produce overmodulated, erratic, and lossy LPFGs.

Table 2.3: Definition and Symbols of CO_2-Laser-Induced LPFG Fabrication Parameters

Grating Period Spacing	Λ
Total Number of Periods	N
Number of Exposures per Period	n
Total Exposure Time Period (each cycle)	T_t
Time Shutter is Open per Exposure	T_p
Power Level (10% split)	P

recorded following fabrication. Each CO_2-laser-induced LPFG is also given a unique identifier based on the date of fabrication and its order number that day (LPFG MMDDYYNN). Appendix A contains a table of fabrication parameters for the CO_2-laser-induced LPFGs referred to within the thesis. Unless otherwise stated, the transmission spectra shown in this and the following chapters are for unpolarized incident light (with exception of Chapter 3). Also, the terms *attenuation* and *transmission loss* are used interchangeably, with *attenuation* being the positive equivalent of the (negative) *transmission loss*.

All of the CO_2-laser-induced LPFGs discussed in the thesis are fabricated in Corning SMF-28 single-mode fiber with a uniform exposure envelope and with no period chirp. It should be noted that even though the exposure envelope is uniform, the induced refractive-index change may still vary over the length of a CO_2-laser-induced LPFG as a result of variability. Similarly, attempts to apply or implement period chirp, apodization, and grating concatenation during fabrication were attempted on a limited scale but, due to variability, were unsuccessful.

2.2.1 Undermodulated Gratings

Undermodulated LPFGs are characterized by the gradual growth of the main resonance with increasing number of periods as light is coupled from the core to the cladding. The light in the cladding-mode at the end of the grating is then lost as it radiates out of the fiber or is absorbed in the buffer. Transmission spectra of three undermodulated CO_2-laser-induced LPFGs, one with a $640\mu m$-period, one with a $650\mu m$-period, and one with a $565\mu m$-period are shown in Figs. 2.8-2.10. The attenuation at the primary cladding-mode resonant wavelength ($1542.4nm$) is $20dB$ for the $640\mu m$-period grating. The attenuation

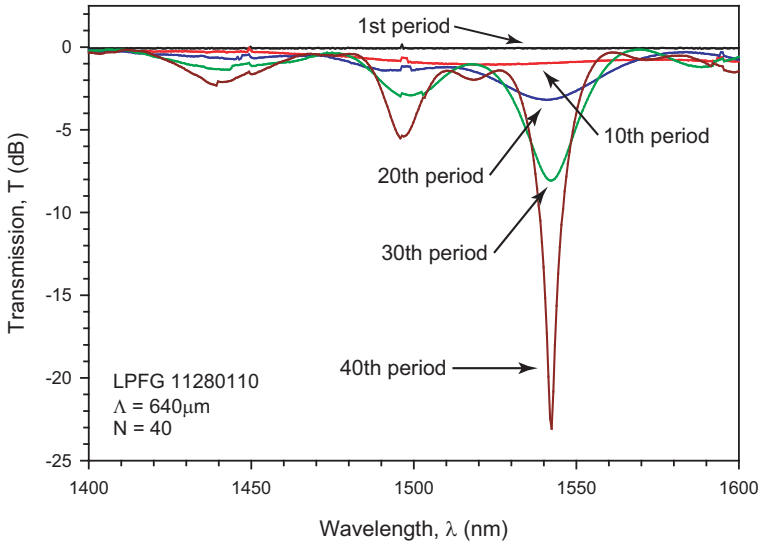

Figure 2.8: Transmission spectrum of a $640\mu m$-period CO_2-laser-induced LPFG. By the 40th period, the primary cladding mode resonance exhibits significant attenuation.

at the primary cladding-mode resonant wavelength ($1551.9nm$) is $7.5dB$ for the $650\mu m$-period grating. For the $565\mu m$-period grating, the attenuation is $23.9dB$ for the resonant wavelength of $1506.4nm$.

2.2.2 Overmodulated Gratings

Overmodulated LPFGs are characterized by the rapid growth and then decrease of the attenuation level at the main resonance as additional periods are added. The increase and then decrease of attenuation at resonance indicates that light is initially coupled from a core-guided mode to cladding-guided modes, but a portion of the light in the cladding modes then couples back into the fiber core over the grating length. The transmission spectrum of a $597\mu m$-period overmodulated CO_2-laser-induced LPFG is shown in Fig. 2.11. The $597\mu m$-period grating becomes overmodulated after the 27th period (peak attenuation of $29dB$ at $1557.9nm$) and has a final attenuation level of $4.7dB$ around $1558.2nm$.

2.3 Summary

The fabrication apparatus and procedure for writing CO_2-laser-induced LPFGs have been discussed, in part, to highlight the one-sided nature of the exposure. Fabrication variability

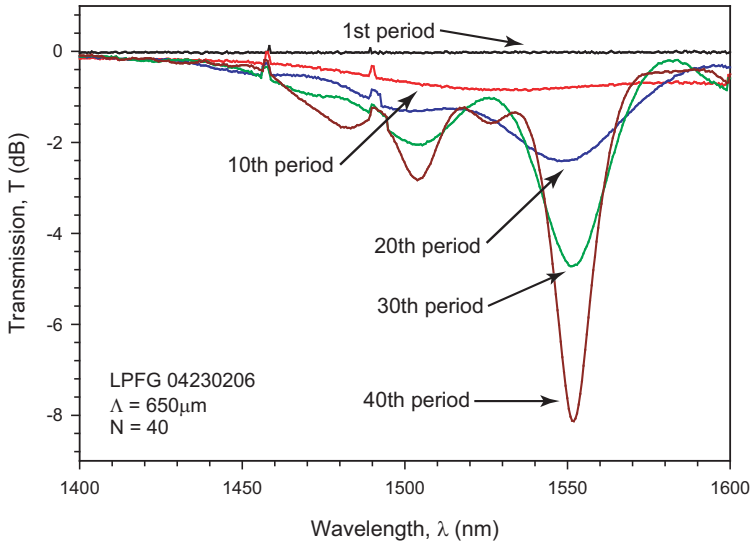

Figure 2.9: Transmission spectrum of a 650μm-period CO_2-laser-induced LPFG.

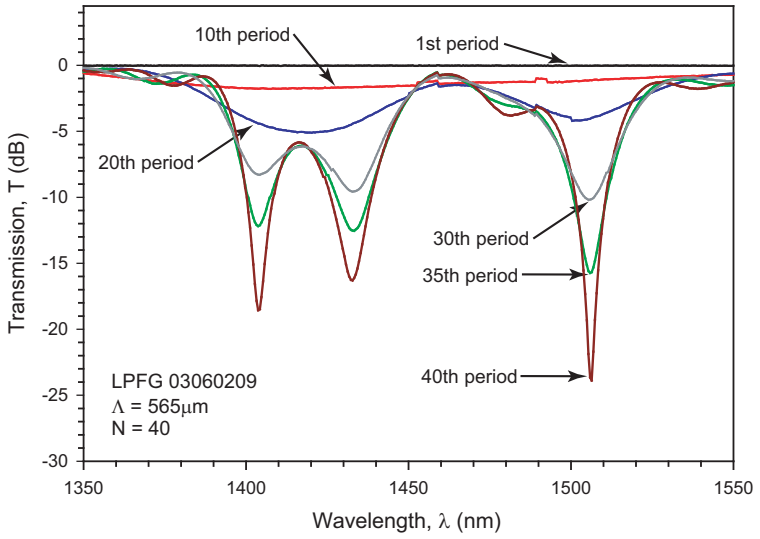

Figure 2.10: Transmission spectrum of a 565μm-period CO_2-laser-induced LPFG.

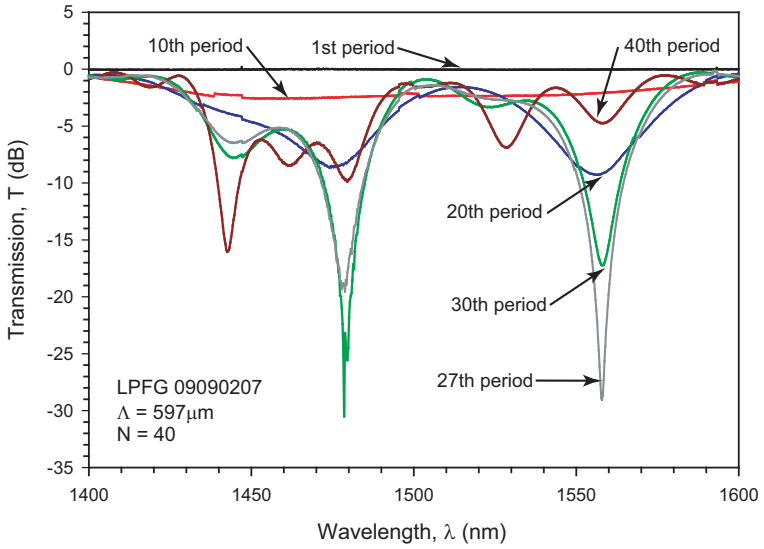

Figure 2.11: Transmission spectrum of an overmodulated 597μm-period CO_2-laser-induced LPFG. The evolution of the grating spectrum during fabrication is shown, with the attenuation level near the 1550nm resonance increasing and then decreasing as more periods are added. The grating becomes overmodulated after the 27th period.

was discussed briefly and improvement in fabrication yield through changes in the fabrication parameters and procedure was demonstrated. Several example transmission spectra of CO_2-laser-induced LPFGs with various periods were given. The effects of one-sided exposure/absorption and the resulting azimuthally asymmetric refractive-index profile are examined in subsequent chapters.

CHAPTER 3

POLARIZATION-DEPENDENT TRANSMISSION CHARACTERISTICS

The azimuthally asymmetric refractive-index change induced in an optical fiber by one-sided exposure to carbon-dioxide (CO_2) laser light introduces optical anisotropy [55] within the long-period fiber grating (LPFG) structure, which manifests as linear birefringence. The presence of birefringence can dramatically alter the transmission characteristics of CO_2-laser-induced LPFGs, especially with regard to polarization-dependent transmission. In this section, two important aspects of polarization-dependent transmission are examined: polarization-dependent loss (PDL) and polarization mode dispersion (PMD).

The basic theory of the origins of PDL in LPFGs is examined in Sec. 3.1, with particular emphasis on extending the existing theory to include CO_2-laser-induced LPFGs. Measurement results of polarization-dependent transmission spectra and PDL illustrate the influence of the asymmetric refractive-index change. In Sec. 3.2, PMD present in LPFGs is discussed and measurement results are presented. The effects of the asymmetric refractive-index change on CO_2-laser-induced LPFG polarization-dependent transmission are summarized in Sec. 3.3.

3.1 Polarization-Dependent Loss

In this section, birefringence and PDL in LPFGs are discussed, in general terms, and the explanation of PDL in UV-induced LPFGs is extended to include CO_2-laser-induced LPFGs [56]. A review of the origins of PDL in LPFGs is presented to highlight the role of linear birefringence in generating grating PDL. Three categories of LPFGs are identified based on the location(s) of birefringence over the optical fiber cross-section: (1) core-only birefringence, (2) cladding-only birefringence, and (3) both core and cladding birefringence. It is established that CO_2-laser-induced LPFGs belong in the cladding-only birefringence

category. Each of these different forms contributes to PDL in LPFGs, but the relationship between birefringence and factors that determine PDL vary between them. This variation is discussed in terms of modal birefringence, resonant wavelength separation, and the grating phase-matching condition. Approximations that are valid in the equations relating resonant wavelength separation to modal birefringence are identified for each category of LPFG. For example, the approximations made for the more traditional UV-induced LPFGs are not correct for CO_2-laser-induced LPFGs. Several conclusions, regarding decreasing/increasing grating PDL and measuring birefringence in these gratings, are derived by examining the expressions for each category. Additionally, PDL-related measurement results are presented for a CO_2-laser-induced LPFG and a UV-induced LPFG possessing similar transmission spectra for unpolarized incident light. The PDL and resonant wavelength separation measured for the two gratings highlights the significant differences that can exist between different types of LPFGs.

3.1.1 Origins of PDL in LPFGs

PDL in the transmission spectrum of an LPFG originates from birefringence present in the grating structure. Birefringence, in most cases, arises from a general variation in the azimuthal index profile in an optical fiber. Due to the birefringence, the grating transmission characteristics, resonant wavelength and coupling strength, depend on the state-of-polarization (SOP) of light incident on the grating and it is this dependence on polarization that generates PDL in LPFGs.

Birefringence alters the grating transmission characteristics in two distinct ways. First, the resonant wavelength of the grating, defined by the phase-matching condition, depends on the SOP of light incident on the grating. Second, the peak refractive-index modulation is different for each SOP. The variation in index modulation with polarization implies that for each SOP the amount of light coupled to the relevant cladding mode changes. This leads to a variation in attenuation in the grating transmission spectra with polarization. As a result of these two phenomenon, each incident SOP possesses a particular resonant wavelength

and transmission spectrum (with associated bandwidth and wavelength-dependent attenuation). At any wavelength, it is the absolute difference between maximum and minimum transmitted power over all SOPs that defines the PDL. The change in PDL with wavelength is referred to as wavelength-dependent PDL.

From the above description of PDL in LPFGs, it is evident that the dependence is not directly related to loss (absorption) as the term is commonly used in reference to materials. Instead, the birefringence leads to polarization-dependent coupling of core-guided modes to cladding modes. Since the cladding modes are then absorbed or radiate out of the fiber, with respect to transmission the polarization-dependent coupling does appear as PDL. It is widely accepted to refer to the polarization-dependent coupling as PDL, despite the discrepancy.

The variation of the resonant wavelength and attenuation over all SOPs determines the PDL of an LPFG. For all possible incident SOPs around a particular coupling resonance, there exists a maximum and minimum resonant wavelength. The difference between the maximum and minimum resonant wavelengths is defined as the resonant wavelength separation. Associated with the maximum and minimum resonant wavelengths are transmission spectra, each with a peak attenuation, established by the coupling characteristics for that SOP (peak index modulation, number of periods, and envelope profile) [12]. For low to moderate levels of birefringence, the transmission spectra of the resonant wavelengths still overlap. The absolute difference between the associated transmission spectra then yields the wavelength-dependent PDL of a grating. This produces a distinctive peak-trough-peak appearance, due to the intersection of the spectra, in the LPFG wavelength-dependent PDL [57].

The sources of birefringence that generate PDL can be either intrinsic to the optical fiber into which an LPFG is written, induced by the mechanism that creates the refractive-index change (as is the case with CO_2-laser-induced LPFGs), result from some applied external mechanism, or result from a combination of any of the first three. Intrinsic birefringence is a fundamental property of an optical fiber and can either be low (standard telecommunications fiber) or high (polarization-maintaining fiber) depending on the fiber type. The

location and type of birefringence induced in an LPFG during writing depends upon the fabrication technique employed; the same argument holds for birefringence resulting from applied external mechanisms.

Birefringence existing within an optical fiber or fiber grating can be linear, circular, or elliptical. However, linear birefringence is the most common type present in LPFGs as circular or elliptical birefringence usually require external manipulation (twisting, rotating exposure, induced optical activity). The form of linear birefringence present in CO_2-laser-induced LPFGs is examined in the next section.

3.1.1.1 Categories of Linearly Birefringent LPFGs

Independent of the fabrication technique used to write an LPFG and the sources of linear birefringence, three categories of LPFGs can be delineated based on the location(s) of the birefringence over the optical fiber cross-section: (1) core-only birefringence, (2) cladding-only birefringence, and (3) both core and cladding birefringence. As the designations suggest, the first category consists of LPFGs that have birefringence only in the core of an optical fiber, the second category have birefringence only in the fiber cladding, and the third category have birefringence in both the core and cladding. Figure 3.1 illustrates the location of birefringence for each of the three categories. The third category represents the most general situation in LPFGs, but in several practical cases the restrictions of the first two categories are valid. The three categories encompass existing LPFGs fabricated in optical fiber. Which category an LPFG belongs in can be established by measuring the transverse cross-sectional refractive-index or stress profile in the grating region using, for example, computed tomography methods [47, 58]. In some cases, the location of birefringence is evident from the fiber geometry alone (such as PMF). The significance of categorizing LPFGs in this way will be evident when the equations governing birefringence and resonant wavelength separation are considered below. The discussion in this section is limited to linear birefringence as it is the form most commonly found in LPFGs; circular birefringence results primarily from twisting of optical fibers and is a special case that is examined in Sec. 4.2.

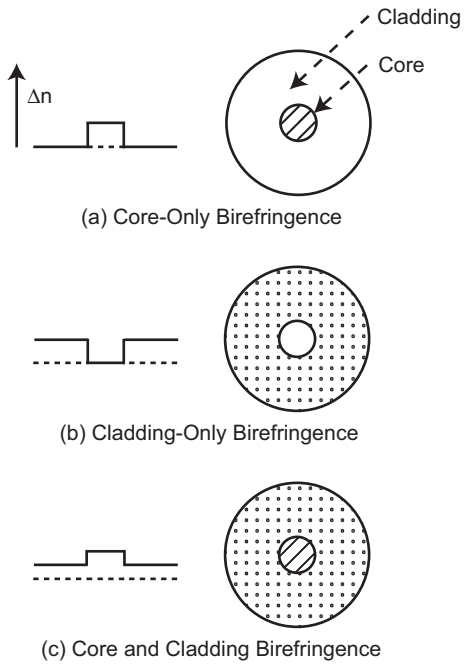

Figure 3.1: Illustration of the three categories of birefringent LPFGs: (a) core-only birefringence, (b) cladding-only birefringence, and (c) both core and cladding birefringence. The hatched areas indicate regions of birefringence.

LPFGs written in low-intrinsic birefringence optical fiber using a fabrication technique that induces an index change over the entire optical fiber cross-section tend to belong in the cladding-only birefringence category. Recent measurements of axial stress in optical fibers exposed to CO_2 laser light establish that CO_2-laser-induced LPFGs belong in this category [47], with the asymmetry resulting from the preferential heating associated with one-sided exposure. When the index change is over the entire fiber cross-section, both the core and cladding may be birefringent. However, for an azimuthally asymmetric refractive-index profile that is not rapidly varying over the cross-section, the index change in the core region can be considered azimuthally symmetric since the core of a SMF covers only a small portion of the overall fiber cross-section. The birefringence in the core is much smaller than that in the cladding, therefore, the core birefringence can be neglected and the cladding is the only portion of the fiber cross-section that is birefringent. This condition is the opposite of core-only birefringence.

Ultraviolet-induced (UV-induced) LPFGs fabricated in low-intrinsic birefringence, photosensitive optical fiber are the primary example of LPFGs that belong in the core-only

birefringence category. Due to the restriction of photosensitive dopants to the fiber core, the index change is limited to this region; this implies that the induced birefringence is confined to the core as well. As mentioned previously, birefringence in this type of UV-induced LPFG has been studied extensively and the induced birefringence for this type of grating can also be attributed to one-sided exposure, which creates a larger index change on the side of the core where the UV beam is incident [59], and/or the polarization state of the incident writing beam [60].

The third category signifies the general case where birefringence is present in both the core and cladding, with the core- or cladding-only birefringence conditions forming limiting cases. Birefringence in both regions of a fiber can be due to either the intrinsic fiber properties (such as in certain PMFs) and/or the induced index change. For example, UV-induced LPFGs fabricated in stress-induced PMF possess birefringence in both the core and cladding due to the intrinsic properties of the PMF (not due strictly to UV exposure). The stress members present in the cladding introduce birefringence in both the PMF core and cladding. LPFGs fabricated in etched optical fibers by ion implantation [24] belong in this category as well since, for certain ion energy levels, the induced refractive-index change covers the core and a portion of the cladding.

3.1.2 Resonant Wavelength Separation and Phase-Matching Condition

LPFGs belonging to any of the three different categories all exhibit PDL in their grating transmission spectra. However, the relationship between birefringence and one of the factors that determines PDL, the resonant wavelength separation, differs for each category. The different forms of the relationship are due to approximations that can be made for core-only and cladding-only birefringence. This section discusses which approximations are valid for each category of LPFG and how the approximations impact the relationship between resonant wavelength separation and birefringence. Consequences of these approximations, with regard to altering grating PDL and measuring modal birefringence, are also given. The discussion begins with a consideration of the general grating phase-matching condition for

LPFGs before examining each category individually. It is shown that the same approximations are not valid for both CO_2-laser-induced LPFGs and UV-induced due to their differing locations of asymmetry.

For an ideal LPFG with no birefringence, the phase-matching condition describing the center wavelength of the transmission resonance in an LPFG may be expressed as

$$\lambda_{res} = \Lambda(n_{01} - n_{mn}) = \Lambda(\Delta n), \tag{3.1}$$

where λ_{res} is the resonant wavelength, Λ is the grating period, n_{01} is the effective guided-mode index of the LP_{01} core-guided mode, and n_{mn} is the effective guided-mode index of the LP_{mn} cladding-guided mode [12].

The condition established by Eq. (3.1) is correct for non-birefringent gratings only; if a grating is birefringent then the resonant wavelength will depend upon the SOP of the light incident on the LPFG. For each SOP, there exists a specific resonant wavelength derived from the effective indices of the core-guided and cladding-guided mode for that polarization state. Again, the variation in indices with SOP is due to birefringence. The actual refractive index that each SOP experiences is related to the effective index [61, 62] and, therefore, the variation in refractive index (birefringence) with polarization is related to the variation in the effective guided-mode index.

For all possible input SOPs, a minimum and maximum wavelength (λ_{res}^{min} and λ_{res}^{max}) exist that correspond to a minimum and maximum effective guided-mode index difference (Δn^{min} and Δn^{max})

$$\lambda_{res}^{min} = \Lambda(\Delta n^{min}), \tag{3.2}$$

$$\lambda_{res}^{max} = \Lambda(\Delta n^{max}). \tag{3.3}$$

The wavelength separation between the minimum and maximum resonant wavelengths is then given by

$$\Delta\lambda_{res} = \lambda_{res}^{max} - \lambda_{res}^{min} = \Lambda(\Delta n^{max} - \Delta n^{min}), \tag{3.4}$$

where $\Delta\lambda_{res}$ is the largest resonant wavelength separation for a particular cladding-mode resonance.

From Eq. (3.4), it is apparent that the resonant wavelength separation is related to the change in effective indices (due to birefringence) with polarization through the Δn^{min} and Δn^{max} terms, but it is not immediately clear how the birefringence in the core and cladding relate individually to the resonant wavelength separation since the Δn terms represent an index *difference*. However, approximations can be made in Eq. (3.4), depending on the type of LPFG and the category to which it belongs, that simplify the relationship between the resonant wavelength separation and birefringence. The approximations valid for each category are examined below.

For LPFGs in the first category, the birefringence is limited to the fiber core. The assumption can then be made that the cladding mode effective index (n_{mn}) is independent of the incident polarization state (i.e. constant) [57]. Then, the minimum and maximum Δn terms only involve the variation in the LP_{01} effective indices and Eq. (3.4) reduces to

$$\Delta\lambda_{res} \approx \Lambda(n_{01}^{max} - n_{01}^{min}), \tag{3.5}$$

where n_{01}^{max} and n_{01}^{min} are the maximum and minimum effective indices for the LP_{01} core-guided mode, respectively, over all polarization states. The approximation and equation for this category have the same form as that commonly cited for UV-induced LPFGs written in low intrinsic birefringence optical fiber [57]. The $n_{01}^{max} - n_{01}^{min}$ term in Eq. (3.5) represents the modal birefringence [62, 63] in the fiber core.

The first category contained gratings with birefringence in the core only. By contrast, LPFGs in the second category have a birefringent cladding and non-birefringent core; this category includes CO_2-laser-induced LPFGs. If the induced index change is over the entire cross-section and mostly azimuthally symmetric (not rapidly varying) in the core region, the effective indices of the core-guided mode (n_{01}) can be considered constant. Equation (3.4) then reduces to

$$\Delta\lambda_{res} \approx \Lambda(n_{mn}^{max} - n_{mn}^{min}), \tag{3.6}$$

where n_{mn}^{max} and n_{mn}^{min} are the maximum and minimum effective indices for the LP_{mn} cladding-guided mode, respectively, over all polarization states. Equation (3.6) has a form similar to that of Eq. (3.5), but now the modal birefringence of the cladding-guided mode

is represented by the $n_{mn}^{max} - n_{mn}^{min}$ term and the core-guided mode is not birefringent. As the polarization state of the light incident on this category of grating changes, it is the variation in the cladding-guided mode effective indices that determines the degree of resonant wavelength separation.

The third category of birefringent LPFGs, where both the core and cladding are affected, represents a more complex situation than the core-only and cladding-only birefringence categories. The relationship between resonant wavelength separation and the effective index difference can not be directly simplified by neglecting birefringence in a particular location over the optical fiber cross-section. Therefore, the relationship between birefringence and resonant wavelength separation as described by Eq. (3.4) applies; it is the *combination* of birefringence in the core and cladding that determines the separation and not the individual birefringence as in the situations of core-only and cladding-only birefringence. The quantity $\Delta n^{max} - \Delta n^{min}$ in Eq. (3.4) cannot be directly interpreted as modal birefringence since it is not merely the difference between two effective indices, as in Eq. (3.5) and Eq. (3.6), but is the difference between the largest effective guided-mode index difference (between core and cladding modes) and the smallest effective guided mode index difference (between core and cladding modes) for all input SOPs. General comments about LPFGs exhibiting core and cladding birefringence, beyond the ones already given, are difficult to make since the form and combination of birefringence is dependent on the type of optical fiber a grating is written into and the fabrication method; distinct combinations of core and cladding birefringence yield distinct resonant wavelength separation and PDL behavior.

Several conclusions can be drawn from the resonant wavelength expressions, Eqs. (3.4) - (3.6), for each category. For LPFGs with core-only or cladding-only birefringence, if the approximate birefringence of the relevant region is known then the resonant wavelength separation can be easily calculated. Here, resonant wavelength separation serves as an indirect measure of PDL, with a larger wavelength separation indicating a larger peak PDL value and larger wavelength range affected by PDL (resulting from a larger separation of the associated transmission spectra). Conversely, it is possible to measure modal birefringence from the resonant wavelength separation for LPFGs in the first two categories. Equations (3.5)

and (3.6) also suggest that PDL can be increased or decreased by directly increasing or decreasing the relevant birefringence. For LPFGs in the second category, the core-guided modes are not birefringent. This implies that in CO_2-laser-induced LPFGs the core-guided modes at the output of the grating do not exhibit modal birefringence. The situation is more complicated for LPFGs in the third category, but a certain flexibility exists since a correct combination of core and cladding birefringence could be used to increase or decrease PDL. For example, it is theoretically possible to cancel the effect of core birefringence by introducing an offsetting birefringence in the cladding. This might be difficult to implement in practice because it would require the ability to establish individually the core and cladding birefringences, but might be achieved by combining an elliptical core PMF (core-only birefringence) with grating fabrication using a CO_2 laser. Increasing PDL through a combination of core and cladding birefringence, however, has already been demonstrated in LPFGs written into stress-induced PMF so as to create wavelength-selective polarizing elements [34]. The performance of wavelength-selective polarizing elements might be improved by combining the birefringence present in CO_2-laser-induced LPFGs with PMF.

Resonant wavelength separation is only one factor that determines the PDL in an LPFG. The amount of light coupled to a cladding mode (attenuation) and the bandwidth of the transmission curve associated with a particular SOP is the other factor influencing PDL. While resonant wavelength separation is readily derived from the phase-matching condition, establishing the actual wavelength-dependent PDL is more difficult. Ishii *et al.* presented a model for calculating wavelength-dependent PDL using an approximate loss formula, but this approach requires knowledge of, among other factors, the transmission bandwidth [57]. As stated above, for low to moderate levels of birefringence (which includes most LPFGs not fabricated in PMF) the wavelength-dependent PDL is well characterized by the difference between the transmission curves associated with the minimum and maximum resonant wavelengths. If the refractive-index modulation associated with minimum and maximum cladding mode effective indices is known, then the transmission curves can be calculated using a variety of techniques, including coupled-mode theory. Once the transmission spectra are calculated, the wavelength-dependent PDL is then calculated by taking the absolute

value of the difference between the spectra. For LPFGs with higher levels of birefringence, the method given by Ishii *et al.* is more applicable [57].

From the above analysis and discussion, it is evident that CO_2-laser-induced LPFGs belong in the category of LPFGs that possess only cladding-mode birefringence. The presence of birefringence leads to polarization-dependent coupling of degenerate core-guided modes to non-degenerate cladding modes that possess different effective indices dependent upon the incident SOP. The variation in the cladding mode effective indices with incident polarization gives rise to a continuum of resonant wavelengths and associated transmission curves, with the minimum and maximum resonant wavelength separation indicative of the level of birefringence. Core-guided modes in CO_2-laser-induced LPFGs experience no birefringence and this has an impact on PMD, which is discussed in Sec. 3.2.

Although CO_2-laser-induced LPFGs and more traditional UV-induced LPFGs belong in different categories, the presence of birefringence in both still leads to wavelength-dependent PDL. Polarization-dependent transmission spectra and PDL of a CO_2-laser-induced LPFG and a UV-induced LPFGs are examined below to investigate the levels of birefringence present in each and how performance is impacted. The method used for measuring PDL in LPFGs is described first.

3.1.3 PDL Measurement Technique and Configuration

Several different techniques can be used to measure PDL in optical devices, with the three most common techniques being the Jones matrix method, the Mueller matrix method, and the polarization-scanning (power max/min) method. Any of the three methods are suitable for measuring PDL in fiber gratings [64]. However, due to a desire to track the power associated with the minimum and maximum resonant wavelength transmission curves and limitations of the measurement equipment (specifically the automatic gain control feature of the lightwave polarization analyzer), the polarization-scanning method was used for all LPFG PDL measurements. An additional advantage of the method is that the relative polarization Stokes parameters of the output light from the grating are recorded for the maximum and minimum transmitted powers since a lightwave polarization analyzer is used.

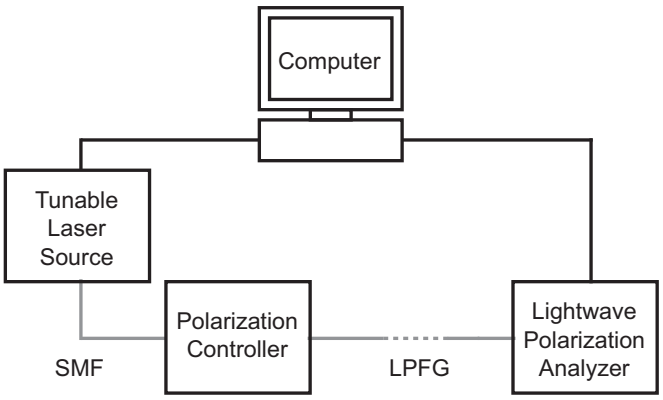

Figure 3.2: Configuration used for measuring PDL of LPFGs.

The measurement configuration used for conducting PDL measurements is shown in Fig. 3.2. A tunable laser source is used to select the measurement wavelength. Each LPFG being tested has its leads fusion-spliced to two short sections of connectorized single-mode fiber. The connectorized grating segment is then connected between a polarization controller and a lightwave polarization analyzer. Each LPFG being tested is also taped down to a glass slide to ensure they remain straight and stable during testing. If testing extended over a significant period of time (several hours), the temperature near the grating was monitored to ensure that no substantial fluctuation (less than $\pm 1^{o}C$) occured.

The polarization-scanning method used for PDL characterization involves measuring the output power from the device under test for varying input states of polarization. A desired wavelength testing range is selected to allow complete characterization of device wavelength-dependent PDL, with the maximum and minimum transmitted power for varying incident polarization then measured at discrete wavelengths within the range. The difference between maximum and minimum measured transmitted power for each test wavelength is the PDL at that wavelength. Variation of the incident input polarization state is achieved using a polarization controller set to scan for a selected duration. Scanning with the polarization controller for a sufficient period of time (from 30 seconds to one minute) randomly alters the polarization state to cover a significant portion of the Poincaré sphere. The scanning measurement is repeated at each discrete test wavelength. Maximum transmitted power, minimum transmitted power, their associated relative Stokes polarization parameters [65],

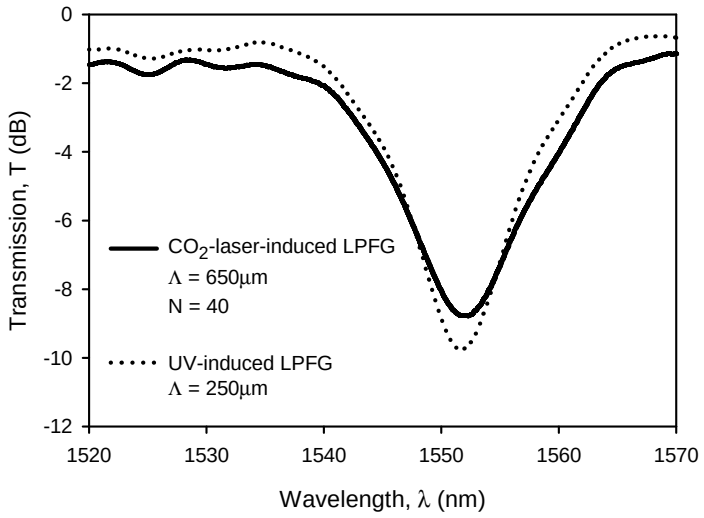

Figure 3.3: Transmission spectra for a CO_2-laser-induced LPFG (LPFG 04230206) and a UV-induced LPFG. The gratings possess similar transmission spectra. The number of periods of the UV-induced LPFG is not known.

and the calculated PDL are recorded for each test wavelength for subsequent examination.

3.1.4 Comparison of CO_2-Laser-Induced and UV-Induced LPFGs

As an illustration of some of the concepts discussed above and to highlight the significant differences that can exist between CO_2-laser-induced LPFGs and more traditional UV-induced LPFGs, the wavelength-dependent PDL, resonant wavelength separation, and modal birefringence of two representative LPFGs were measured. The gratings were fabricated so as to possess similar transmission spectra for unpolarized light. The transmission spectra of each LPFG, measured with a broadband light source and an OSA, are shown in Fig. 3.3 (referenced to $0dB$). The two gratings have nearly the same resonant wavelength, though the UV-induced LPFG has approximately $1dB$ higher attenuation at resonance. The differing periods of the gratings suggest that they couple to two different cladding modes.

Figure 3.4 shows the measured PDL of the CO_2-laser-induced LPFG and the UV-induced LPFG. Though the two LPFGs possess similar transmission spectra for unpolarized light, the peak PDL of the CO_2-laser-induced LPFG is $1.2dB$ versus less than $0.2dB$ for the UV-induced LPFG. Lower PDL is characteristic of commercially-available LPFGs designed for

use in optical networks. The higher PDL of the CO_2-laser-induced LPFG is a result of the induced azimuthally asymmetric refractive-index change resulting from preferential heating associated with one-sided exposure to laser light. Again, the peak-trough-peak nature of the grating PDL over the wavelength range is due to crossover of the transmission spectra associated with the minimum and maximum resonant wavelengths.

The spectra associated with the minimum and maximum transmitted power (also measured with the polarization-scanning technique) are shown in Fig. 3.5 and Fig. 3.6 for the CO_2-laser-induced LPFG and UV-induced LPFG, respectively. A narrower range of the resonant wavelength region is also shown in the figures, where the minimum transmission and maximum transmission resonant wavelengths in each case are clearly evident. The reason for the larger peak PDL of the CO_2-laser-induced LPFG is clear from the data in Fig. 3.5 and Fig. 3.6; the resonant wavelength separation ($\Delta\lambda_{res}$) is $1.1nm$ versus $0.05nm$ for the UV-induced LPFG. This result indicates the birefringence present in the cladding of the CO_2-laser-induced LPFG is much larger than the birefringence present in the core of the UV-induced LPFG. Because these two gratings exhibit either core-only or cladding-only birefringence, the modal birefringence present in each can be estimated from the resonant wavelength separation [from Eq. (3.5) and Eq. (3.6)]. For the CO_2-laser-induced LPFG, the estimated modal birefringence is $1.7\text{x}10^{-6}$, while for the UV-induced LPFG it is $2\text{x}10^{-7}$. Both values agree approximately with previously published measurements/calculations of modal birefringence despite differences in grating fabrication parameters [47, 66].

The wavelength-dependent PDL measured in the CO_2-laser-induced LPFG is consistent with visual observation of intensity variations in cladding modes emerging from a cleaved fiber endface located approximately $5mm$ after the grating. While imaging the fiber endface using an inspection microscope [15] and continuously altering the SOP of the light incident on the LPFG using a polarization controller, the intensity of the cladding mode changes. The cladding mode intensity variation possesses a noticeable wavelength dependence, with peak variations observed near peak PDL.

The low level of PDL found in the UV-induced LPFG makes it more suited for general filtering applications in optical telecommunications networks. The higher PDL level of

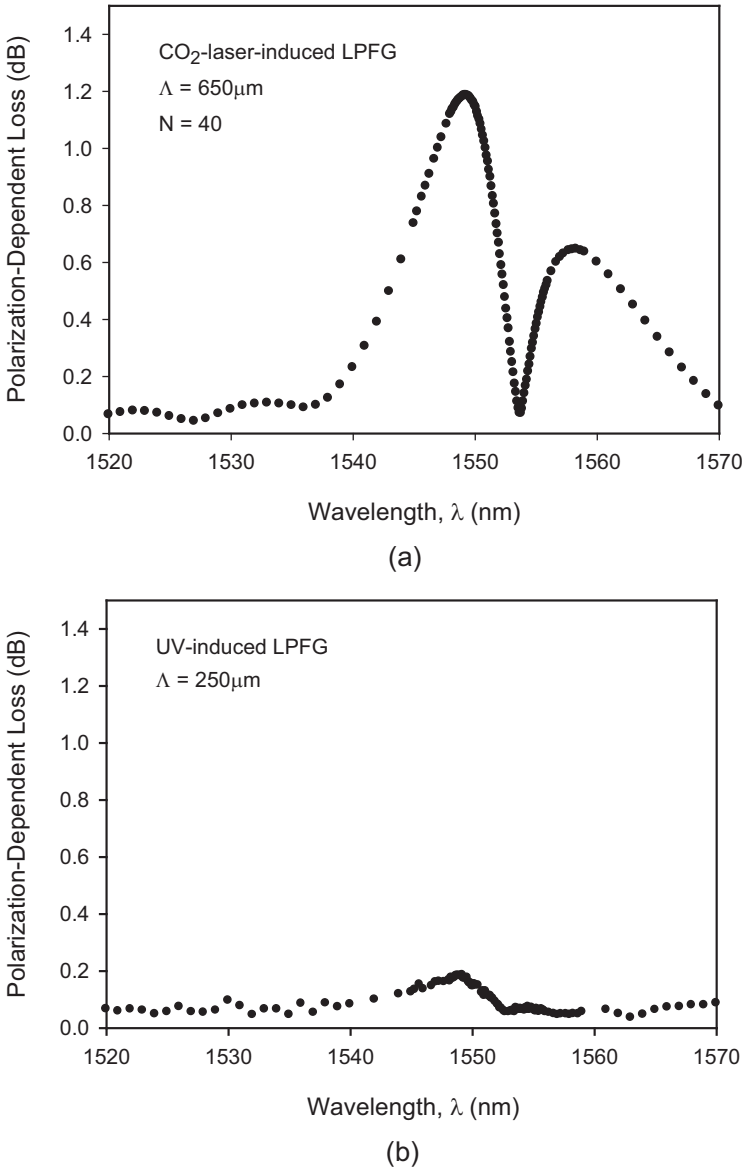

Figure 3.4: Measured PDL of the (a) CO_2-laser-induced LPFG and the (b) UV-induced LPFG.

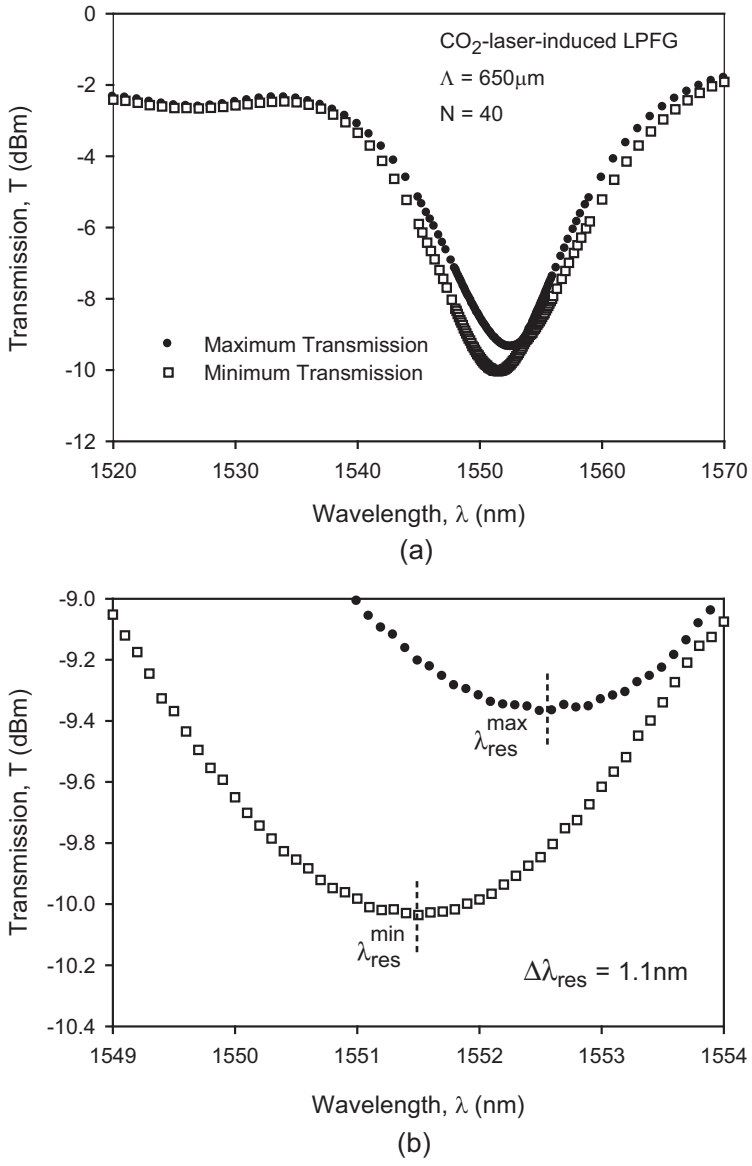

Figure 3.5: (a) Measured maximum and minimum transmitted power with randomly varying polarization of the CO_2-laser-induced LPFG (LPFG 04230206). (b) Narrower range of the same spectrum with the transmission curves of the maximum and minimum resonant wavelengths clearly visible.

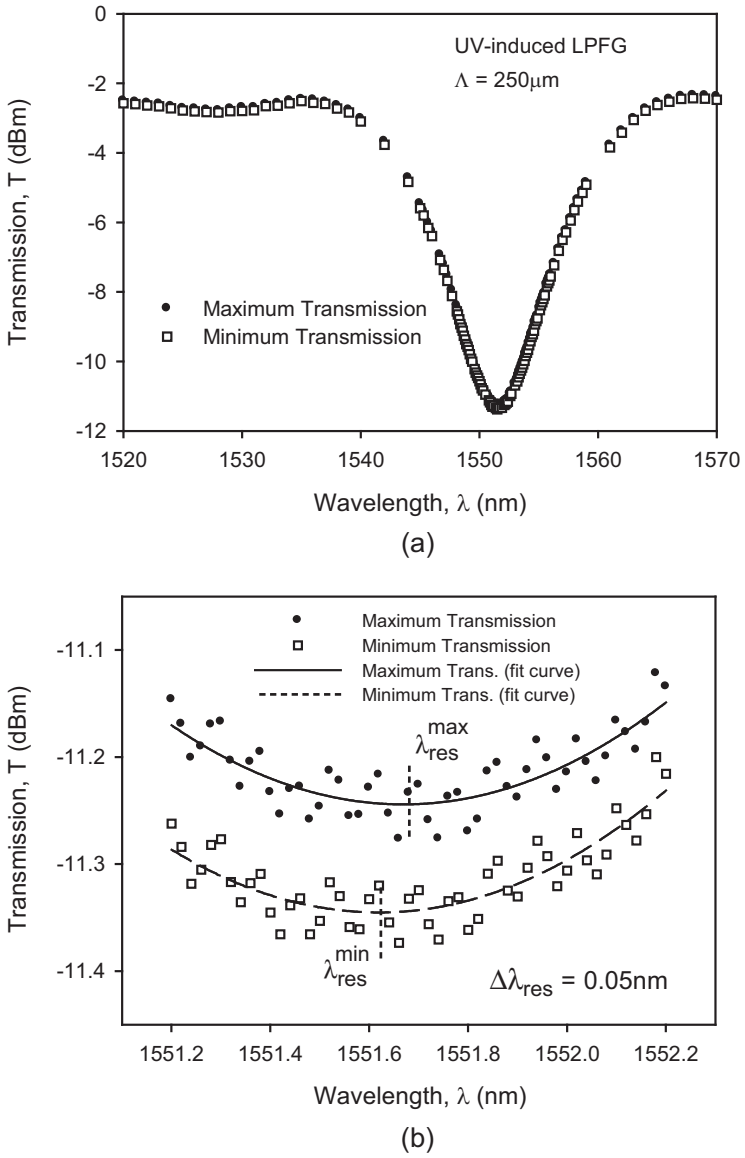

Figure 3.6: (a) Measured (average of 10 measurements) maximum and minimum transmitted power with randomly varying polarization of the UV-induced LPFG. (b) Narrower range of the same spectrum. A least-squares curve fit was applied to the measured data and the minimum of the fit curves was used to calculate the modal birefringence.

the CO_2-laser-induced LPFG could be useful for polarization-dependent filtering or PDL compensation applications [67].

3.1.4.1 Polarization States Associated with Transmitted Power

During the PDL measurements, the polarization state of the light associated with the maximum and minimum transmitted powers was recorded. Although the observed polarization states are referenced to a polarimeter internal to the lightwave polarization analyzer and not to the actual LPFG under test, examination of the evolution of the states over the wavelength range verifies certain behaviors anticipated from the theory discussed previously in this section and offers insight into the effects of birefringence. With the polarization state referenced to the internal lightwave polarization analyzer polarimeter, the measured states are related to the LPFG output states by some unknown transformation. The results presented below were measured for the same CO_2-laser-induced LPFG characterized above (LPFG 04230206).

The recorded polarization states are represented by normalized Stokes parameters [65] in Fig. 3.7 and Fig. 3.8. The states are categorized with respect to the maximum and minimum resonant wavelength shift transmission spectra [see Fig. 3.5(b)] and are distinguished by the respective designations $SOP_{\lambda max}$ and $SOP_{\lambda min}$. The separation of the measured states into the two categories corrects for polarization shifts/fluctuations related to the maximum and minimum transmitted power crossover point (zero PDL point). Figure 3.7 shows the associated polarization states over a $60nm$ wavelength range, with the states plotted in six wavelength groupings (five test wavelengths per each group) for the maximum and minimum resonant wavelength shift transmission spectra. The wavelength range covered in the plot includes the grating resonant wavelength (see Fig. 3.3). The solid and dashed lines in both of the figures indicate the surface of the normalized Poincaré sphere and are included for reference.

As is evident from Fig. 3.7, the polarization states associated with the maximum and minimum resonant wavelength shift at a given wavelength are orthogonal to each other. The orthogonal condition holds whether the given wavelength is near the LPFG resonant

wavelength or not, as is expected from basic waveguide modal theory. However, as the LPFG resonant wavelength is approached, the polarization states cluster together into two distinct, though still orthogonal, regions of the Poincaré sphere. The clustering near resonance is shown in more detail in Fig. 3.8.

In addition to the CO_2-laser-induced LPFG examined above, the output polarization states were recorded for the UV-induced LPFG (with basic transmission spectrum shown in Fig. 3.3) and for other CO_2-laser-induced LPFGs that possessed higher levels of PDL. For the UV-induced LPFG, the polarization states corresponding to the maximum and minimum resonant wavelength shift transmission spectra were widely scattered. A dispersed pattern for the orthogonal states serves as another indication of the of low levels of asymmetry (birefringence) within the UV-induced LPFG. For the CO_2-laser-induced LPFGs that possessed higher levels of PDL, even more clustering of the states was observed near resonance. The clustering mimics the behavior of a polarizer (which ideally possess infinite PDL), but is highly wavelength-dependent. The orthogonality and clustering near resonance is consistent with the theory governing PDL, as discussed in this section, and with the index asymmetry modeling conducted by Dossou *et al.* [68]

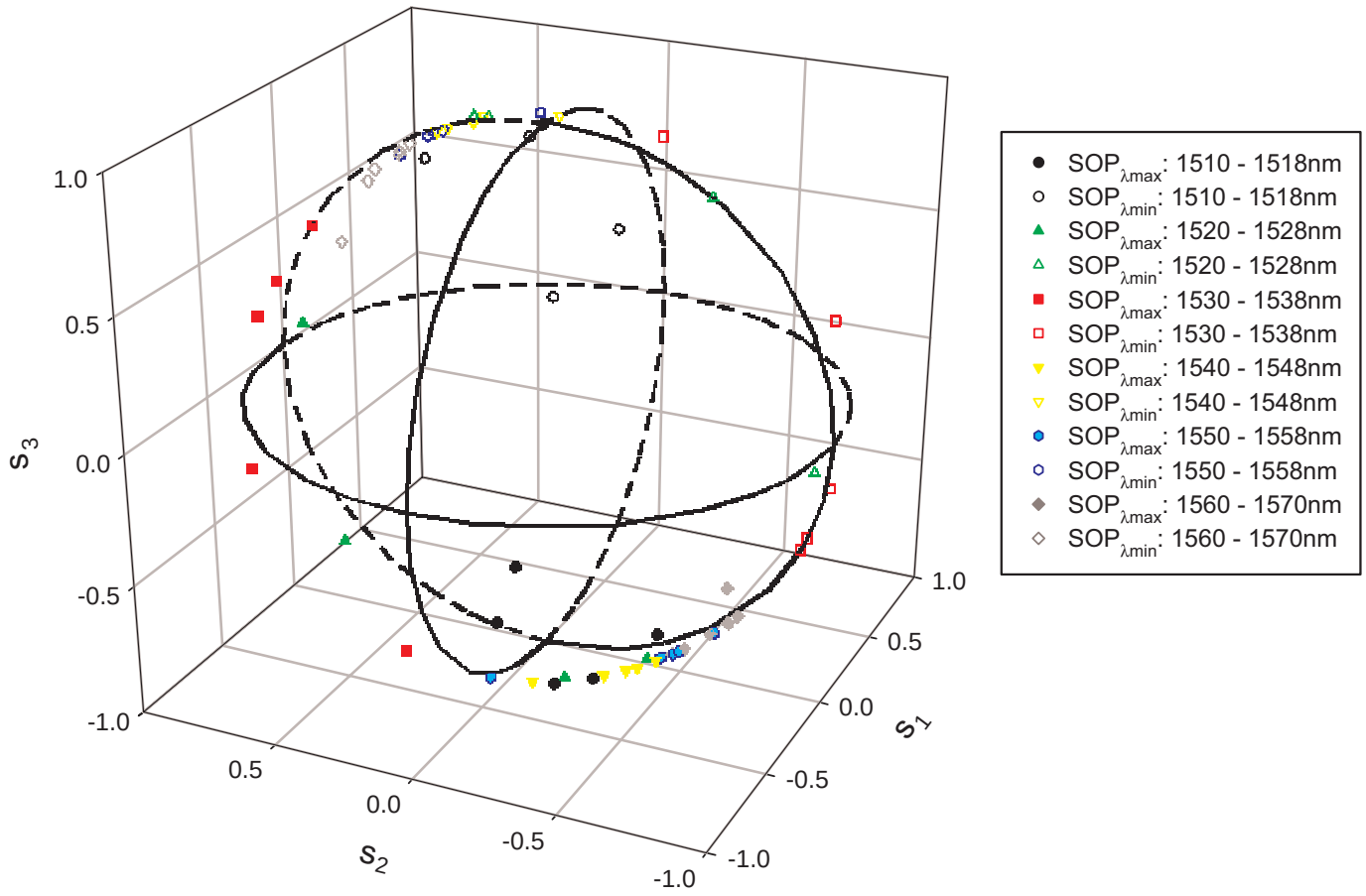

Figure 3.7: Polarization states associated with maximum and minimum resonant wavelength shift transmission spectra as measured with a lightwave polarization analyzer. The states are plotted as normalized Stokes parameters and are referenced internally to the analyzer (not to the actual CO_2-laser-induced LPFG output). $SOP_{\lambda max}$ and $SOP_{\lambda min}$ refer to the two related transmission spectra and the states are grouped into several wavelength ranges. The solid and dashed lines indicate the normalized Poincaré sphere.

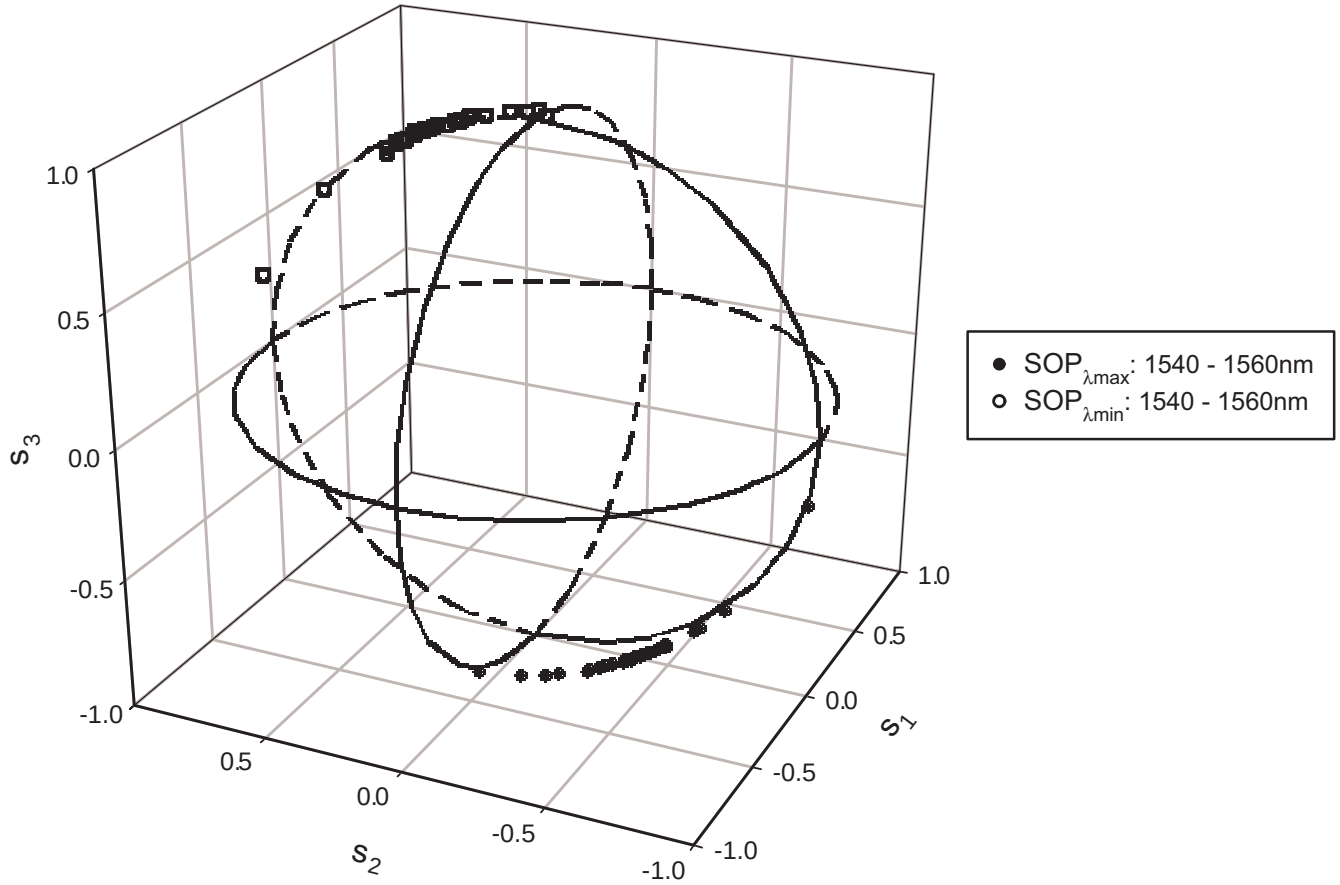

Figure 3.8: Polarization states associated with maximum and minimum resonant wavelength shift transmission spectra near the CO_2-laser-induced LPFG resonant wavelength. The observed polarization states become clustered as the grating resonant wavelength is approached.

3.2 Polarization Mode Dispersion

From the observations of PDL in CO_2-laser-induced LPFGs, it is known that birefringence levels are larger in that type of LPFG than in traditional LPFGs and that birefringence can have a significant impact on transmission characteristics and device performance. However, PDL is only one form of polarization-dependent transmission in LPFGs that is influenced by birefringence. In this section, another important polarization-related issue is examined: polarization mode dispersion (PMD).

PMD present in optical fiber devices such as LPFGs can significantly impact network performance [69]. The presence of linear birefringence due to the azimuthally asymmetric refractive-index change suggests that PMD might also be an issue in CO_2-laser-induced LPFGs. PMD levels in UV-induced LPFGs have been measured previously and are relatively low due to the small level of index asymmetry present in such gratings [12]. There has been no reported measurement of PMD in CO_2-laser-induced LPFGs, despite the fact that the index profile asymmetry is larger than in the UV case and its PDL is also noticeably larger.

In this section, the issue of PMD in CO_2-laser-induced LPFGs is considered. The form of PMD in optical devices, including LPFGs, is discussed first. Next, the technique and configuration used for measuring PMD in LPFGs are presented and measurement results given for the same CO_2-laser-induced and UV-induced LPFGs studied in Sec. 3.1. Finally, the measurement results are examined and discussed. Again, the emphasis is placed upon the impact of linear birefringence (as opposed to circular) since it is the form most commonly found in LPFGs not subjected to torsion.

3.2.1 PMD in Optical Devices and LPFGs

For most optical fiber devices, PMD is deterministic, as opposed to the statistical form found in optical fiber telecommunications links. Deterministic PMD is the temporal differential group delay (DGD) between two orthogonal core-guided modes [principal states of polarization (PSP)] at a specific wavelength [70]. Normally, orthogonal core-guided modes are degenerate and travel at the same propagation velocity. However, birefringence that affects

the core of an optical fiber removes the degeneracy of the modes. Non-degenerate, orthogonal core-guided modes travel at different propagation velocities and the difference gives rise to the DGD. Most often, the two orthogonal modes are associated with the birefringent axes (fast and slow) of individual optical fiber and fiber devices. An additional characteristic of DGD in optical fiber devices is that it remains mostly constant as wavelength changes (at least within individual telecommunications wavelength bands) [71].

LPFGs, as a type of optical fiber device, exhibit deterministic DGD. Even with LPFGs' characteristic wavelength transmission spectra, it is still expected that DGD does not vary significantly with wavelength. Birefringence present within grating structures gives rise to both PDL and PMD. While PDL is highly wavelength-dependent, the first-order PMD exhibited by LPFGs has no wavelength dependence (at least over the $1550nm$ telecommunications wavelength range). The wavelength-dependent PDL does introduce difficulties in measuring LPFG PMD levels.

3.2.2 PMD Measurement Technique and Configuration

A number of techniques exist for measuring deterministic DGD in optical devices. The most commonly employed, Jones matrix eigenanalysis (JME), assumes device PDL to be zero or constant over a narrow wavelength range when deriving DGD levels from output polarization state measurements [72]. Since CO_2-laser-induced LPFGs can possess relatively significant levels of wavelength-dependent PDL, the method cannot be used to measure accurately grating DGD near cladding mode coupling resonances. While it is possible to measure DGD away from resonance, since LPFGs couple light to multiple cladding modes at distinct wavelengths it is difficult to avoid all of the cladding mode resonances completely with the available measurement equipment. In addition, measuring DGD near the primary resonance (at $1550nm$) allows for direct comparison of PMD measurement results with PDL measurements results.

An alternative technique to the JME measurement method, the complex plane method (CPM), is capable of measuring DGD in devices possessing wavelength-dependent PDL [73]. The technique uses a complex number ratio of orthogonal mode amplitudes to solve an

equation governing the frequency evolution of an optical field emerging from a device-under-test. The optical field emerging from the device is still described by a frequency-dependent complex Jones matrix (as in the JME method),

$$\vec{E}_o(\omega) = \mathbf{T}(\omega)\vec{E}_i, \tag{3.7}$$

with $\vec{E}_o(\omega)$ being the output optical field, $\mathbf{T}(\omega)$ being complex Jones matrix of the device-under-test, and $\vec{E}_i$ being the input optical field. The frequency dependence of the output state of polarization (SOP) is known to be the source of PMD in fibers and optical devices [72]. The complex plane method solves Eq. (3.7) differently than in the Jones matrix eigenanalysis method and no assumption regarding PDL is made.

The frequency evolution of $\vec{E}_o(\omega)$ is solved by taking the frequency derivative of Eq. (3.7) and rewriting the field components in terms of a complex number ratio, χ [74]. The complex number ratio is then used to separate the frequency derivative of Eq. (3.7) into two differential equations that are solved to yield the device DGD [73]. Using the complex plane method, DGD is given by

$$DGD = Im\left[\sqrt{(n_{22} - n_{11})^2 + 4n_{12}n_{21}}\right], \tag{3.8}$$

where Im indicates the imaginary portion of the square-root term and n_{11}, n_{12}, n_{21}, and n_{22} are complex coefficients of the matrix $\mathbf{N}(\omega)$, which is related to $\mathbf{T}(\omega)$ by

$$\mathbf{N}(\omega) = \mathbf{T}'\mathbf{T}(\omega)^{-1}. \tag{3.9}$$

The coefficients are determined by solving a differential equation

$$\chi_0' = -n_{12}\chi_0^2 + (n_{22} - n_{11})\chi_0 + n_{21}, \tag{3.10}$$

where χ_0 is the ratio of the two orthogonal optical fields (principal states of polarization) at the test wavelength and χ_0' is the frequency derivative of χ_0 [73]. Solving Eq. (3.10) to find the coefficients n_{12} and n_{21} and the difference $(n_{22} - n_{11})$ requires measuring the output SOP ratio χ_0 and its frequency derivative for three different input polarizations at three separate wavelengths (the test wavelength and two near the test wavelength). From the

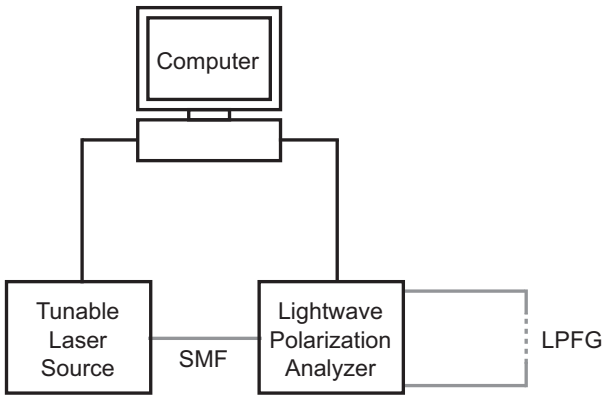

Figure 3.9: Configuration used for measuring differential group delay of LPFGs.

measurements, a set of linear equations can be generated and the coefficients determined using linear least-squares estimation [73].

The experimental configuration for measuring LPFG DGD is shown in Fig. 3.9. The configuration is the same for both CPM and JME. A tunable laser source is used to set the measurement wavelength and the source output is connected to a lightwave polarization analyzer with a single-mode fiber patchcord. Each LPFG being tested has its leads spliced to two short sections of connectorized single-mode fiber. The connectorized grating segment is then attached to the input and output ports of the lightwave polarization analyzer. Each tested LPFG is also taped down to a glass slide to ensure they remain straight and stable during measurement.

For each test wavelength, the laser is tuned to a slightly shorter wavelength ($\Delta\lambda_{test} = -0.2nm$) and the output polarization states are measured for three different input polarization states. The polarization state measurement process is repeated at the test wavelength and at a slightly longer wavelength ($\Delta\lambda_{test} = +0.2nm$). The measurements conducted on either side of the test wavelength are used to calculate the frequency derivative χ_0' required for solving Eq. (3.10). The complex plane method DGD measurement, when conducted over the entire wavelength span, was automated using a custom LabVIEW program [52].

3.2.3 PMD Measurement Results and Discussion

Measurements of DGD for both a UV-induced and a CO_2-laser-induced LPFG are shown in Fig. 3.10 and Fig. 3.11, respectively. Both gratings used for the PMD measurements

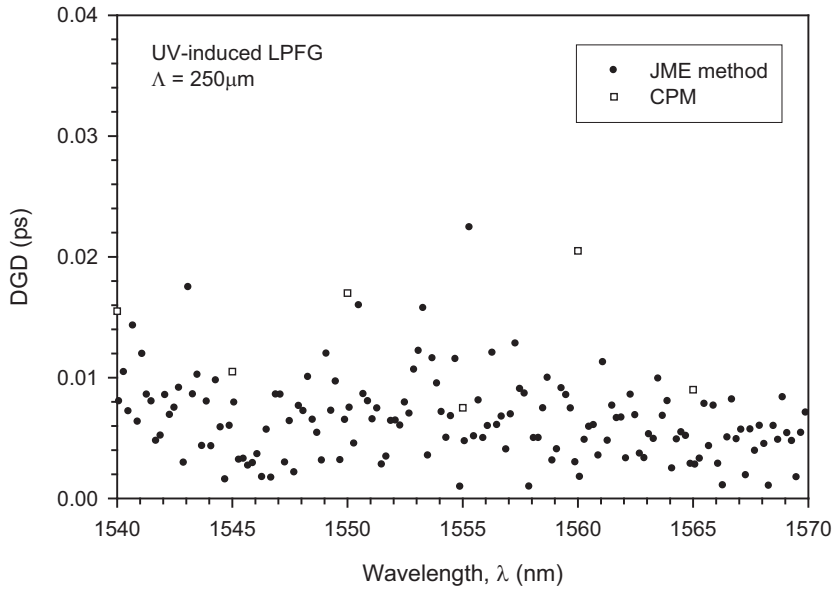

Figure 3.10: Measured DGD of a UV-induced LPFG using both the Jone matrix eigenanalysis (JME) method and the complex plane method (CPM).

are the same as the ones used in the PDL measurements in Sec. 3.1 and their transmission spectra for unpolarized light are shown in Fig. 3.3. DGD measurements were conducted at multiple wavelengths around the main grating resonance.

For the UV-induced LPFG, both the JME method and CPM were used to measure device DGD near resonance and the results from both tests agree closely, with $7fs$ resulting from the JME measurement versus $13fs$ obtained from the CPM measurement. The reported DGD values are the average of the measurements taken over the $30nm$ test wavelength range. The measured DGD of the grating agrees with the less than $10fs$ value previously reported in the literature for UV-induced LPFGs [12]. There is no distinct pattern of wavelength dependence in the measured DGD, which is consistent with the deterministic form of PMD found in most optical fiber devices. The close agreement between the CPM and the JME method measurements demonstrates that both are valid techniques for measuring DGD in the absence of PDL.

The CPM was used for measuring DGD of the CO_2-laser-induced LPFG in the wavelength region near resonance since the JME method yielded erroneous values for the same

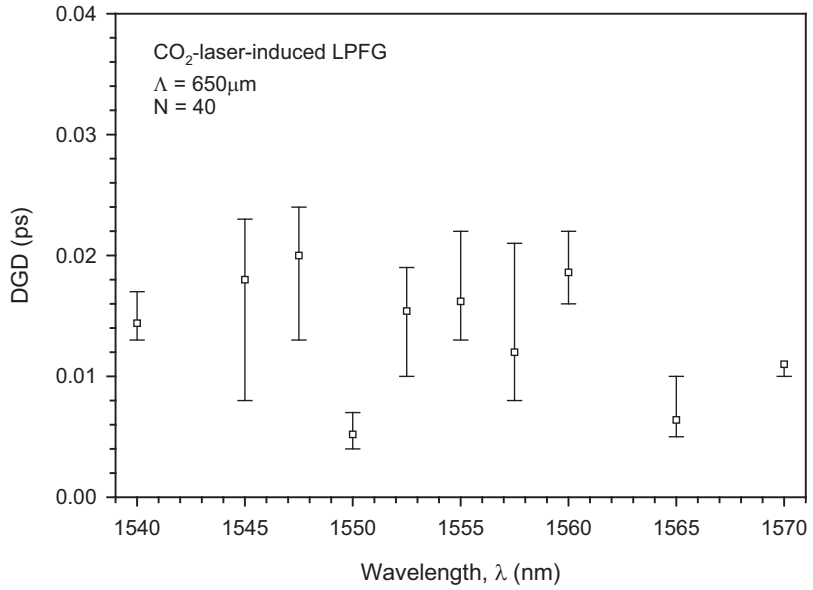

Figure 3.11: Measured DGD of a CO_2-laser-induced LPFG using the complex plane method. The symbols represent the average of three measurements taken at each test wavelength with the maximum and minimum values indicated by the error bars.

region. From the CPM measurements, the CO_2-laser-induced LPFG possesses an average DGD of $14fs$ (average of the measurements taken over the $30nm$ wavelength test range). Again, no distinct pattern of wavelength dependence for the DGD is observed. The JME method was used to examine grating DGD at a wavelength about $20nm$ away from the main resonance and an average DGD value of $6fs$ was measured.

3.2.3.1 Comments on PMD Measurement Results

The measured DGD of both the CO_2-laser-induced and UV-induced LPFG are similar, whether measured near to resonance or away from resonance and using both the CPM and the JME method. The DGD form of PMD of the two gratings is similar despite the higher measured levels of linear birefringence present in the CO_2-laser-induced LPFG (see Sec. 3.1). There are two possible explanations for this, both of which may be correct: (1) the DGDs of both gratings are below the noise floor of the measurement system, and (2) the birefringence present in the CO_2-laser-induced LPFG does not contribute to DGD.

The relatively short grating lengths (approximately $25mm$) and the low linear birefringence combine to produce low DGD levels, which can be difficult to quantify using most

PMD measurement methods. The measured DGD values are certainly near the resolution limits of the lightwave polarization analyzer employed in conducting the measurements [75]. It is more accurate to conclude from the measurement results that the actual DGDs of the tested LPFGs are less than the measured values instead of concluding that they are equal to them.

While it is true that low DGD levels in devices are difficult to measure, the modal birefringence of the CO_2-laser-induced LPFG is still an order of magnitude larger than that of the UV-induced LPFG. However, the index asymmetry present in a CO_2-laser-induced LPFG is known to be mostly in the cladding region and not in the core region [47]. Since the asymmetry and, therefore, the birefringence are concentrated in the cladding, the asymmetry has little effect on the actual propagation velocities of the orthogonal core-guided modes (principal states of polarization), whose propagation velocity difference *defines* first-order PMD. From the perspective of the core-guided mode, both the UV-induced and CO_2-laser-induced LPFG possess low birefringence with correspondingly low levels of DGD. In the UV-induced LPFG case, the birefringence in the core is simply very low. For the CO_2-laser-induced LPFG, the asymmetry is mostly in the cladding. The net result is that both types of LPFGs are expected to have low DGD.

Whether one or both of the above explanations are correct, it can be concluded from the measurements that the first-order PMD present in CO_2-laser-induced LPFGs does not adversely affect device performance. If a CO_2-laser-induced LPFG is considered separately and not as only one device in a telecommunications link system, then the DGD is certainly not significant for a digital communications link operating at $40Gb/s$, where 2 to $5ps$ average DGD can be tolerated [76, 77]. The measured DGD level is also below the restrictions imposed on commercial components that are used for $10Gb/s$ or faster systems ($0.05ps$ to $0.25ps$) [69]. Of course, if the CO_2-laser-induced LPFG is simply a device in a communications link containing many other devices and fiber segments, then the affect of the DGD present in a CO_2-laser-induced LPFG is more difficult to predict directly due to the statistical nature of system PMD.

It is of interest to consider when the DGD exhibited by CO_2-laser-induced LPFGs begins

to impact communication links. Basically, if the temporal width of a pulse incident on the LPFG approaches the DGD, then pulse propagation will start to be influenced [76]. With DGD levels present in CO_2-laser-induced LPFGs on the order of tens of femtoseconds (or less), pulses of sub-picosecond duration are affected. However, since the DGD is so low, the question exists as to whether ultrashort pulses even interact with typical LPFGs. Consider a $1ps$-duration pulse incident on an LPFG with a $640\mu m$ period and 40 total periods. The pulse has an approximate length of $200\mu m$, as calculated from

$$L_{pulse} = \frac{c\,T_{pulse}}{n_{01}}, \tag{3.11}$$

where L_{pulse} is the physical length of the pulse, c is the speed of light in a vacuum, T_{pulse} is the temporal duration of the pulse, and n_{01} is the effective index of the core-guided mode. Following a similar calculation, it takes the pulse approximately $125ps$ to travel through the LPFG. However, at any given time, the pulse only extends over at most one period of the grating as it travels through the structure. Sub-picosecond pulses are not influenced by the spectral transmission response of typical LPFGs but still might experience broadband loss and DGD as each individual period is encountered. By this reasoning, ultrashort pulses traveling through CO_2-laser-induced LPFGs are still impacted by DGD, resulting from birefringence present in the individual periods, but do not experience PDL since no coupling to cladding modes can occur. From the perspective of an ultrashort pulse, the LPFG is simply a concatenation of refractive-index changes separated by sections of unaltered fiber.

Although only a qualitative argument is given for ultrashort pulse propagation through LPFGs, similar reasoning has been applied to ultrashort pulses incident upon FBGs and was subsequently validated experimentally [78]. The argument is also consistent with research conducted on nonlinear pulse propagation in LPFGs, where the pulses employed all possessed temporal widths of at least several tens of picoseconds [31, 79].

3.3 Summary

In this chapter, the effect of the asymmetric refractive-index profile on the polarization-dependent transmission characteristics of CO_2-laser-induced LPFGs has been examined through consideration of PDL and PMD. The basic theory of PDL in typical LPFGs has

been extended to encompass other types of LPFGs, including CO_2-laser-induced LPFGs. Additionally, PDL-related measurement results were presented for a CO_2-laser-induced LPFG and a UV-induced LPFG possessing similar transmission spectra for unpolarized light. The PDL and resonant wavelength separation measured for the two gratings highlights the significant differences that can exist between different types of LPFGs.

PMD present in CO_2-laser-induced LPFGs has also been studied. After discussing PMD in optical fiber devices and LPFGs, measurement results were presented that demonstrate CO_2-laser-induced LPFGs possess low PMD levels. The impact of the LPFGs' PMD on telecommunications systems was also discussed.

Of the two polarization-dependent transmission characteristics examined, PDL has far more of an impact than PMD despite the fact that both originate from linear birefringence created by one-sided exposure to CO_2 laser light. If only one period were written into an optical fiber, PDL would not exist but (the small level of) PMD would.

CHAPTER 4

RESPONSE TO PHYSICAL MANIPULATION

Previous research concerning LPFGs in general, and carbon-dioxide-laser-induced long-period fiber gratings (CO_2-laser-induced LPFGs) specifically, indicates that physical manipulation of such gratings alters their transmission spectra in potentially useful ways. Asymmetry present in the induced refractive-index change of CO_2-laser-induced LPFGs causes them to behave differently than other LPFGs when subjected to physical manipulation. In this chapter, the change in CO_2-laser-induced LPFG transmission spectra for two different types of physical manipulation, bending and torsion, are considered.

The response of CO_2-laser-induced LPFGs to applied flexure is examined in Sec. 4.1 while the response to applied torsion is examined in Sec. 4.2. The results of subjecting CO_2-laser-induced LPFGs to physical manipulation are summarized in Sec. 4.3.

4.1 Response to Applied Flexure

Variable attenuation tuning (VAT) at constant wavelength, resonant wavelength tuning (WT) at constant attenuation, and the axial rotational orientation dependence on transmission have been observed previously in flexed CO_2-laser-induced LPFGs [1, 3] as was discussed in Chapter 1. VAT and WT behavior have only been observed around a wavelength of $1450nm$ and not in the important $1550nm$ telecommunications wavelength band. It is not evident which grating parameters (period, number of periods, coupling strength, axial rotational orientations) are necessary to generate VAT and WT behavior when CO_2-laser-induced LPFGs are flexed.

In this section, CO_2-laser-induced LPFG response to flexure is investigated further. A large number (greater than 50) of LPFGs were subjected to flexure testing to determine what grating parameters and flexure conditions produce tuning. To facilitate rapid and accurate testing of large numbers of LPFGs, an automated flexure testing system was

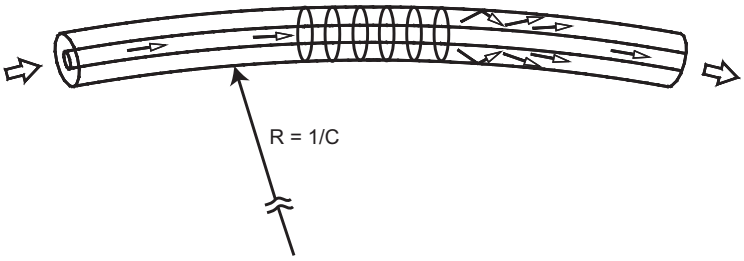

Figure 4.1: Illustration of a curved LPFG. R is the radius of curvature and its inverse is the curvature, C.

designed and developed. The testing system was used to identify CO_2-laser-induced LPFGs that exhibited VAT and WT in the $1550nm$ telecommunications wavelength band. A direct comparison of the response to flexure for a CO_2-laser-induced and a UV-induced LPFG that possess similar transmission spectra for unpolarized light was conducted. The comparison highlights differences in bending response of the two types of gratings and identifies potential advantages of each. The relationship between exposure conditions and symmetry observed in the CO_2-laser-induced LPFG transmission response to flexure was also verified.

Before discussing flexure of LPFGs in any significant detail, the associated nomenclature must be defined. Some of the concepts linked with flexing CO_2-laser-induced LPFGs are shown in Fig. 4.1 and in Fig. 1.6. Flexed gratings are bent to a radius of curvature (R), with the inverse of the radius of curvature being the curvature (C). The plane of curvature is defined as the plane containing the radius of curvature vector and, for all measurements reported in this section, is vertical. Axial rotational orientation (ϕ) is the designation for the angular separation between the plane of curvature and the side of the fiber facing the incident laser light during fabrication (see Fig. 1.6). An angle of 0^o corresponds to the incident side facing upward and being in the plane of curvature while 180^o corresponds to the incident side facing downward and being in the plane of curvature. The angles 90^o and 270^o then correspond to the incident side being perpendicular to the plane of curvature. The direction of rotation for axial orientation is always counterclockwise around the optical fiber longitudinal axis (from light input to output).

4.1.1 Automated Flexure Testing of Axially Rotated LPFGs

Previous investigations of CO_2-laser-induced LPFG response to flexure employed a manual testing apparatus [3]. Full characterization of LPFG transmission characteristics at a number of curvatures and at numerous axial rotational orientations takes a considerable amount of time. Since it was expected that a large number of LPFGs would be tested, an improved, automated flexure testing system was required. To accomplish the needed automated testing of LPFGs a computer-controlled testing system was designed that is capable of accurate flexure and frictionless axial rotation over a full 360^o [80]. The general flexure testing procedure along with the design and operation of the testing system are described below.

The general flexure testing procedure includes flexing an LPFG at one axial rotational orientation, axially rotating the grating to a new orientation, and then flexing the grating again. The procedure continues until all of the desired number of discrete rotational orientations have been tested. The system implements three separate processes to perform the testing procedure: platform deflection, weight removal/replacement, and rotating the optical fiber about its longitudinal axis.

Figure 4.2 illustrates the configuration by which a fiber grating is flexed. A $10mm$ diameter stainless steel dowel pin rests in the V-groove of a holder attached to a vertically mounted linear translation stage. The larger dowel pin and holder are translated upward to engage a $25.4mm \times 76.2mm$ smooth, flat plastic platform and press the platform against a set of four smaller stainless steel dowel pins ($4.8mm$ diameter). The smaller pins act as fixed points for continued deflection of the platform center thereby creating a curved surface for the fiber grating to rest upon. With this arrangement, accurate curvature values starting from $0m^{-1}$ are achievable using the precise positioning of the $0.074\mu m$-resolution stepper motor linear stage. Use of the computer-controlled linear stage and a smooth $1.59mm$ thick ABS plastic platform to flex the fiber grating avoids difficulties associated with hysteresis effects, such as those observed in piezo-ceramic devices.

The optical fiber grating under test rests upon the curved platform surface and is centered on the platform. Any variation in the tension on the fiber grating can alter the grating

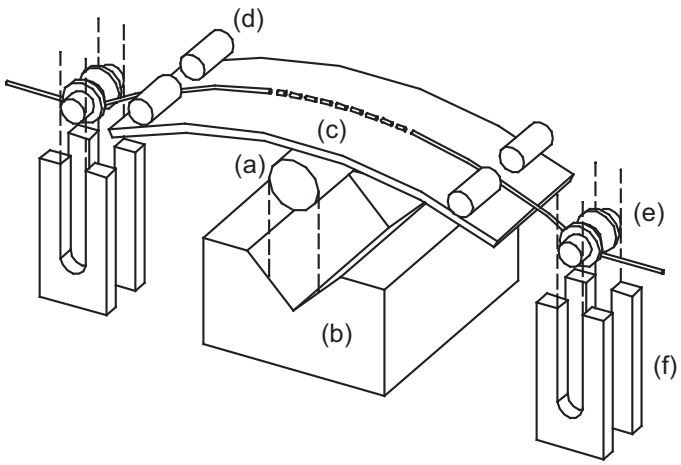

Figure 4.2: Controlled flexure of an LPFG. (a) Large diameter dowel pin for deflecting the platform. (b) V-groove holder for the large dowel pin. (c) Plastic platform (curved state) with optical fiber resting on top. (d) Small diameter dowel pins. (e) Small weights to hold the optical fiber against the platform. (f) Slots for guiding the weights. The dashed section of the optical fiber indicates the LPFG location on the platform.

properties and would be undesirable. Thus, two $2.4gm$ brass weights, one hanging at each end, are used to apply constant tension, to hold the fiber grating against the platform, and to ensure that the curvature of the platform and LPFG remain identical throughout the flexure testing range. A circular V-groove at the center of the weights reproducibly aligns the optical fiber on the plastic platform. Small cylinders located on ends of the weights are confined in the adjacent vertical slots. The pairs of vertical slots on each end of the platform guide the weights and assure that they remain in the same orientation with respect to the optical fiber.

The vertical slots also form part of the system used to remove the weights from the optical fiber so that the fiber can be rotated to a new axial rotational orientation. The weight removal/replacement subsystem and process is shown in Fig. 4.3. A pair of levers connect the slotted structures and the vertically mounted linear stage. Precision stainless steel shoulder screws, used for the connections, slide freely in the slots of the stainless steel levers. During flexure testing, the weights are confined in the vertical slots and rest on the optical fiber [Fig. 4.3(a)]. Upon completion of flexure testing for a particular axial rotational orientation, the linear stage moves downward, passing through the zero-curvature position [Fig. 4.3(b)]. The linear stage continues to move downward, forcing the slotted upright

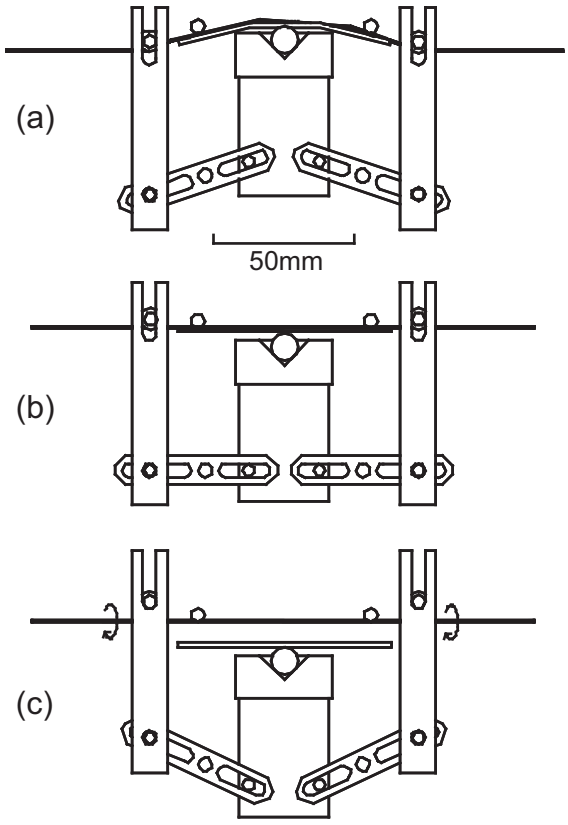

Figure 4.3: Weight removal cycle proceeds from (a) to (c). (a) Curved state with weights still on optical fiber. (b) Zero-curvature state. (c) Weights removed and optical fiber free to rotate. Weight replacement on the optical fiber follows the opposite process.

structures to move upward into contact with the weights thus lifting them off the optical fiber [Fig. 4.3(c)]. After removal of the weights the optical fiber is freely rotated to a new orientation. Replacement of the weights on the optical fiber follows the opposite process and when completed the next flexure testing cycle begins.

Rotation of the optical fiber while the weights are removed is accomplished using two computer-controlled rotation stages mounted on posts, one on each end of the central platform structure. The compact 0.001°-resolution rotation stages incorporate, in their central aperture, a device designed to hold the optical fiber during testing. The optical fiber holder consists of a modified fiber chuck, a key, and a chuck holder. The fiber chuck securely grips the optical fiber without introducing detrimental microbends. A flat area milled on the fiber chuck seats the key for insertion into the chuck holder. Each assembled holder is placed in the threaded central aperture of a rotation stage and held in location by two threaded rings.

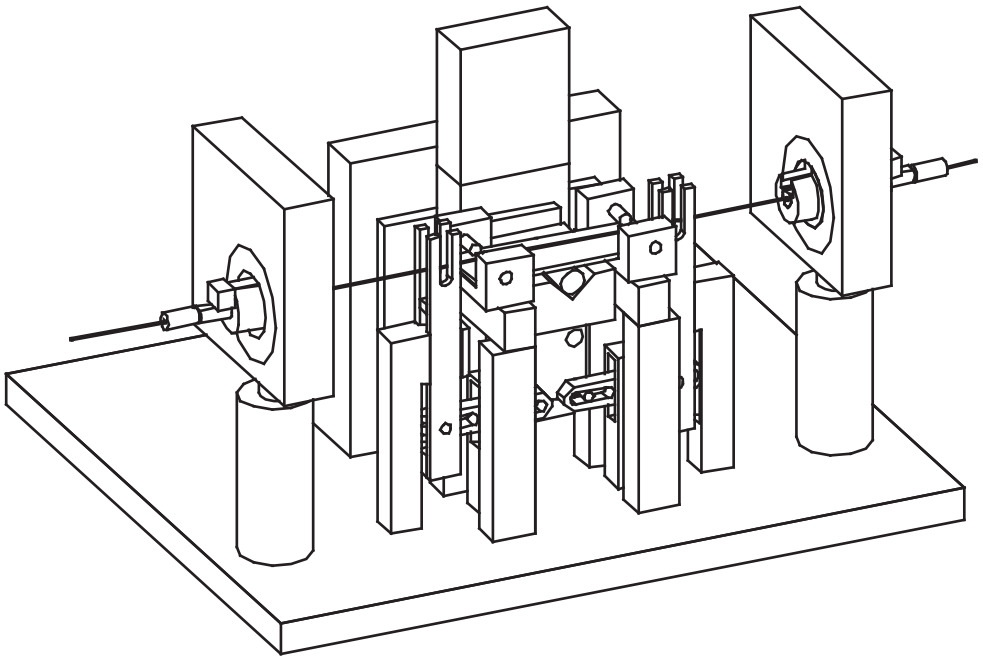

Figure 4.4: Assembled automated flexure testing system.

The arrangement holding the optical fiber in the stages guarantees the same orientation is maintained relative to the stage during rotation while holding the optical fiber securely during flexing.

Figure 4.4 shows the complete assembled flexure testing system. The optical fiber holder can be seen mounted in the rotation stages, which are located opposite each other. The linear stage is also shown mounted to an L-shaped bracket that enables a full $25.4mm$ vertical movement. The superstructure over the levers holds the small pins and provides a shelf for the plastic platform to rest against when the linear stage moves downward out of contact.

The two rotation stages and single linear stage used in the design operate under a central motion controller. Movement of the stages is synchronized and coordinated to permit simultaneous movement of both rotary stages. The motion controller incorporates a GPIB interface to facilitate programming and remote control from a computer. The changing fiber grating transmission properties during testing are monitored using a broadband source and computer-controlled optical spectrum analyzer. Wavelength transmission data measured by the optical spectrum analyzer is transmitted to the controlling computer and saved

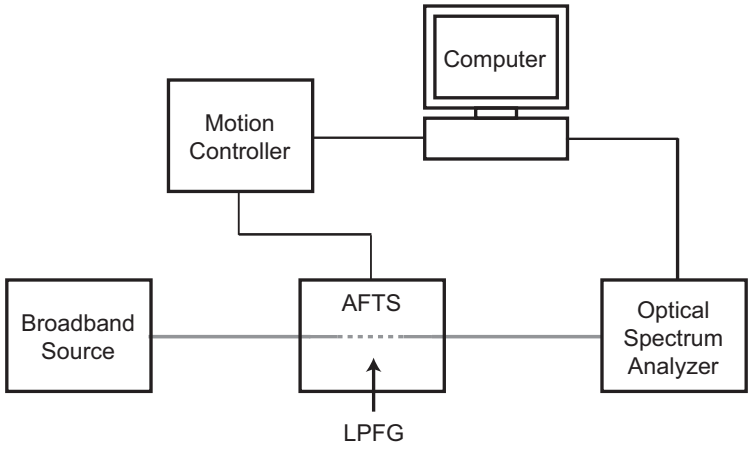

Figure 4.5: Instrument configuration used to measure the transmission spectra of LPFGs subjected to flexure at various axial rotational orientations using the automated flexure testing system.

for subsequent analysis. Once an optical fiber grating is secured and positioned in the testing fixture, the testing process and monitoring is completely automated through a single custom LabVIEW computer program [52]. The instrumentation configuration used for flexure testing of LPFGs is shown in Fig. 4.5.

Figure 4.6 shows an example LPFG transmission spectrum obtained using the described testing system. The measurements were made at a specific grating axial rotational orientation and over the full curvature testing range. Eight transmission spectra (of the 23 spectra measured at this orientation) are shown in the figure and designated as C_0, C_1, *etc.* The C_0 measurement corresponds to the zero-curvature (no deflection) starting position. Note that, in this case, flexing the fiber grating is necessary to observe any significant resonance. This is because the $597\mu m$-period CO_2-laser-induced LPFG being tested was overmodulated (see Chapter 2).

Use of the automated flexure testing system (AFTS) permitted a large number of LPFGs to be tested in a shorter period of time than comparable manual testing allowed. Flexure response measurement results, obtained with the AFTS, from two different investigations conducted on CO_2-laser-induced LPFGs are described below.

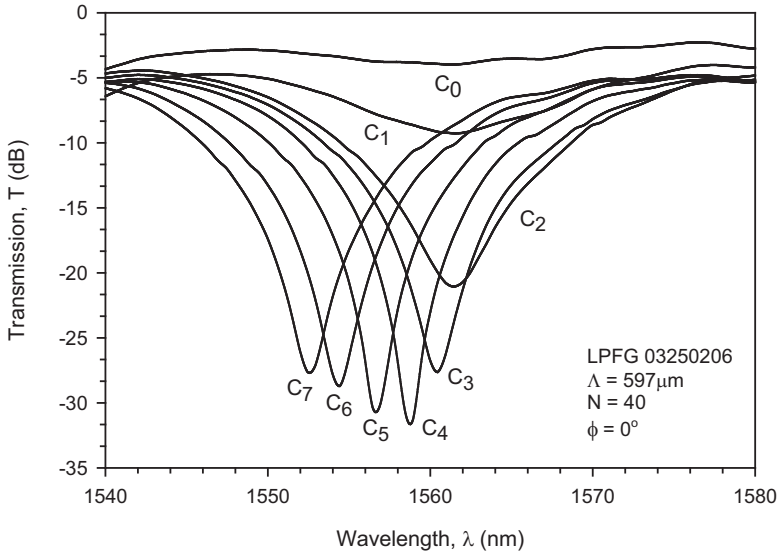

Figure 4.6: Example CO_2-laser-induced LPFG transmission spectra measured at a constant axial rotational orientation for various applied curvatures (C) using the AFTS. $C_0 = 0.0m^{-1}$, $C_1 = 1.0m^{-1}$, $C_2 = 2.1m^{-1}$, $C_3 = 2.5m^{-1}$, $C_4 = 2.9m^{-1}$, $C_5 = 3.3m^{-1}$, $C_6 = 3.7m^{-1}$, and $C_7 = 4.0m^{-1}$. The LPFG performs as a wavelength tunable filter for $C_3 \leq C \leq C_7$.

4.1.2 Comparison of UV-Induced and CO_2-Laser-Induced LPFGs

The response of typical LPFGs and CO_2-laser-induced LPFGs to applied flexure has been investigated previously [1, 3, 81]. However, no comparison has been conducted for LPFGs possessing similar transmission spectra for unpolarized light in order to directly compare and contrast their response to flexure. Therefore, a series of measurements of the change in transmission spectra in response to applied flexure were conducted for a CO_2-laser-induced and a UV-induced LPFG. The comparison highlights differences in bending response of the two types of gratings and identifies potential advantages of each [82]. The transmission spectra of the two LPFGs are shown in Fig. 3.3 for the zero-curvature (flat) state. The two gratings are the same as the ones used in the PDL and PMD studies presented in Chapter 3.

The change in LPFG transmission spectra in response to applied flexure was measured over a curvature range from $0m^{-1}$ to $4m^{-1}$ and over an axial rotational orientation range from 0^o to 345^o using the AFTS. Slight modifications were made to the AFTS optical fiber holders to accommodate the short lead lengths and fusion splice protectors of the UV-induced LPFG; the modifications limited the curvature testing range from $0.25m^{-1}$ to

$3.97m^{-1}$ for that grating.

The measured UV-induced LPFG transmission spectrum over the curvature range at four axial rotational orientations is shown in Fig. 4.7. The axial rotational orientation is arbitrary for the UV-induced LPFG since which side was facing the laser during fabrication is not known. Measured results for the CO_2-laser-induced LPFG for the same four orientations are shown in Fig. 4.8. The axial rotational orientation of 0^o corresponds to the fabrication tab, and therefore the incident side of the fiber, facing upward (see Fig. 1.6). The responses of the LPFGs at the particular orientations shown in Fig. 4.7 and Fig. 4.8 are representative of the responses observed at other orientations.

The two types of LPFGs, despite having similar transmission spectra at zero-curvature, respond quite differently when flexed at the various axial rotational orientations. The transmission spectrum of the UV-induced LPFG changes in the same pattern with increasing curvature no matter the axial rotational orientation; the attenuation of the cladding-mode resonance decreases and the resonant wavelength shifts towards a lower wavelength as the curvature increases. The unvarying response to applied flexure over all axial rotational orientations is consistent with the azimuthally symmetric refractive-index change found in UV-induced LPFGs.

Conversely, the change in the CO_2-laser-induced LPFGs transmission spectrum with applied flexure varied depending on the axial rotational orientation and is consistent with the inherent azimuthally asymmetric refractive-index change. The transmission response at the 90^o and 270^o axial rotational orientations is similar, indicating that the side of the fiber facing the laser during exposure (see Fig. 1.6) is consistent with the tab orientation. The CO_2-laser-induced LPFG even displays a small level of VAT behavior at the 180^o orientation. For both types of LPFGs, the resonance wavelength shifts and the attenuation decreases significantly (at least by half) at the higher curvature levels.

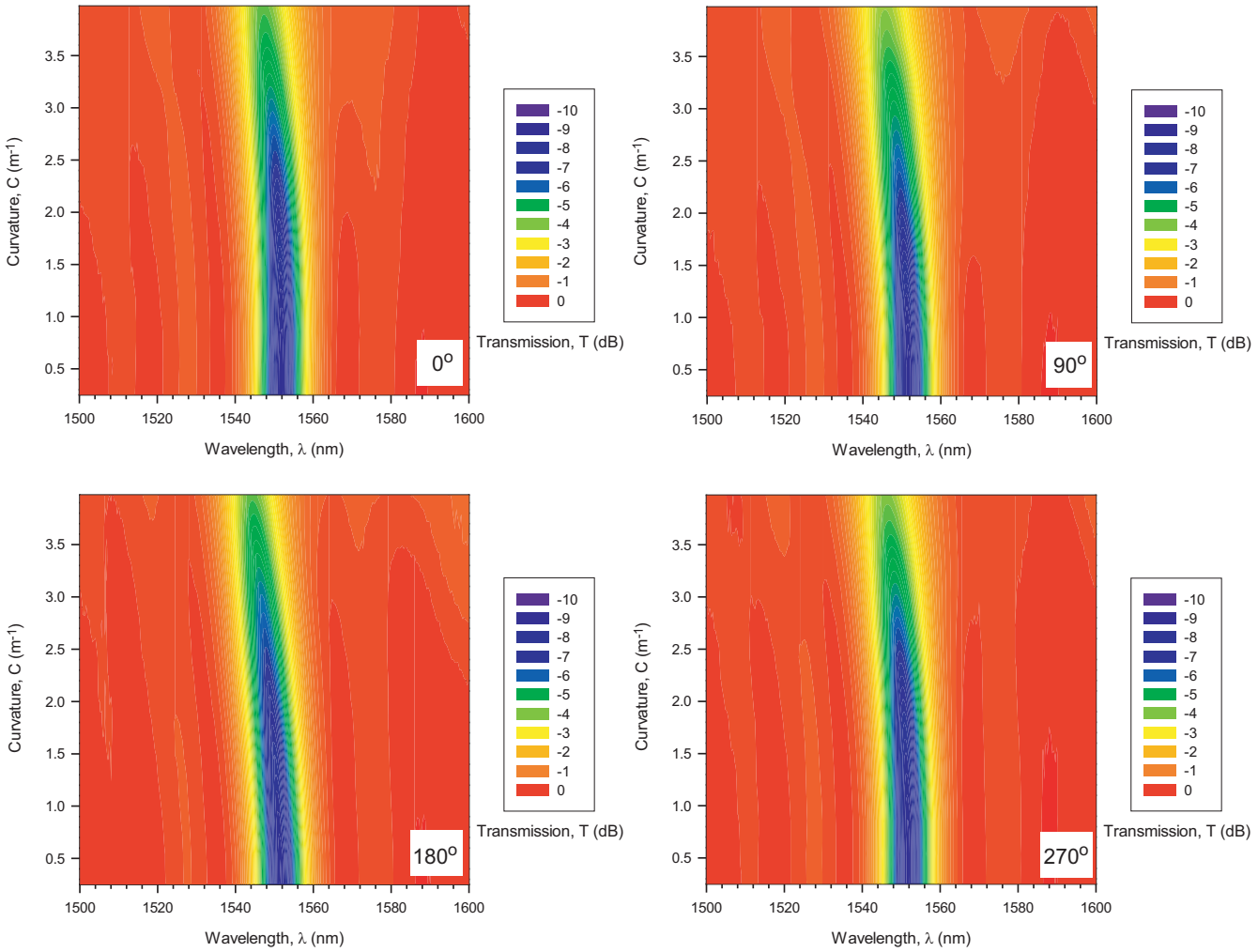

Figure 4.7: Pseudocolor surface plots of the transmission spectrum of a UV-induced LPFG at different curvatures for four different axial rotational orientations (0^o, 90^o, 180^o, and 270^o).

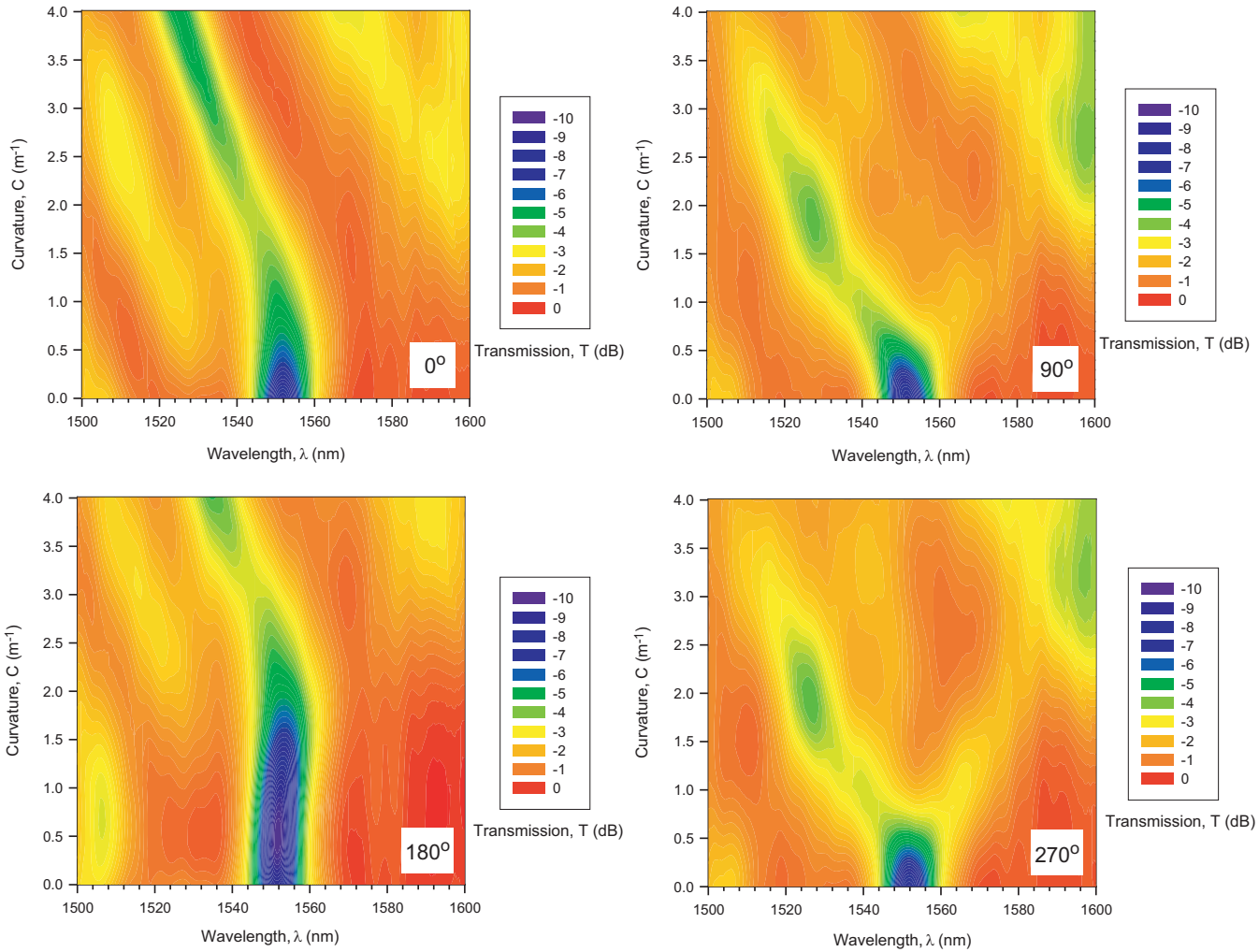

Figure 4.8: Pseudocolor surface plots of the transmission spectrum of a CO_2-laser-induced LPFG at various curvatures for four different axial rotational orientations (0^o, 90^o, 180^o, and 270^o).

The observed response to flexure for the two types of LPFGs suggests, in addition to the profile differences, that each possesses distinct advantages with respect to potential applications. UV-induced LPFGs offer stable performance and are relatively insensitive to bending; such characteristics make them ideal for use as fixed wavelength filters in optical telecommunications networks. CO_2-laser-induced LPFGs, conversely, appear to be more suited for dynamic operations where the filtering wavelength or attenuation level can be altered by relatively simple means. The variety of behavior seen in the transmission spectrum for the flexed CO_2-laser-induced LPFG at different axial rotational orientations can indicate the direction of bending, which is a useful feature for bend sensing applications.

4.1.3 Tuning Near $1550nm$

Controlled flexure of CO_2-laser-induced LPFGs at certain axial rotational orientations produces variable attenuation tuning (VAT) and wavelength tuning (WT). However, tuning behavior has not been observed in the important $1550nm$ telecommunications wavelength band and it is not evident what grating periods, modulation levels, or axial rotational orientations yield tuning in that wavelength range. Examples of VAT and WT occuring near the $1550nm$ wavelength that were observed during flexure testing of CO_2-laser-induced LPFGs are given below. Tuning was achieved using an overmodulated LPFG with a grating period different from that used possessed by previous CO_2-laser-induced LPFGs that exhibited tuning ($480\mu m$ [3]). In addition, it is verified that the symmetry observed in the transmission response to flexure at constant curvature is related to exposure conditions.

A large number of CO_2-laser-induced LPFGs were subjected to flexure testing in order to identify what combination of grating parameters (grating period, number of periods, modulation/attenuation level) produce VAT and WT in the $1550nm$ telecommunications wavelength band. Table 4.1 provides a summary of the various parameters evaluated during testing, with most combinations tested using the AFTS at some point during the investigation. CO_2-laser-induced LPFGs were tested over a curvature range from 0 to $4m^{-1}$ and over a full 360^o rotational range, typically testing at least every 15^o. If a particular LPFG exhibited VAT or WT behavior at a certain axial rotational orientation, the grating was

Table 4.1: Various Grating Parameters Evaluated During Flexure Testing

Grating Period Spacing	$480\mu m$, $565\mu m$, $597\mu m$, $640\mu m$, $650\mu m$
Total Number of Periods	30 to 50
Attenuation at Main Resonance (nearest to $1550nm$)	3 to $25dB$, both undermodulated and overmodulated

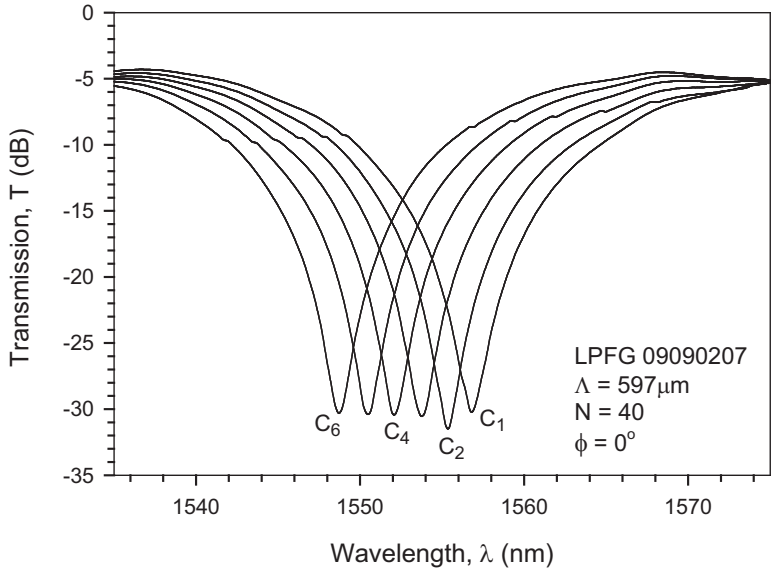

Figure 4.9: CO_2-laser-induced LPFG exhibiting wavelength tuning. The transmission spectrum response was measured at an axial rotational orientation ϕ=0° for various applied curvatures (C). $C_1 = 2.45m^{-1}$, $C_2 = 2.75m^{-1}$, $C_3 = 3.16m^{-1}$, $C_4 = 3.36m^{-1}$, $C_5 = 3.76m^{-1}$, and $C_6 = 3.97m^{-1}$.

tested again at additional orientations close to the initial one in an attempt to achieve better tuning performance (higher attenuation or wider tuning range).

Of the approximately 55 LPFGs subjected to flexure testing, overmodulated $597\mu m$-period LPFGs displayed the most consistent tuning activity in the $1550nm$ wavelength range. An example of WT observed in a flexed $597\mu m$-period CO_2-laser-induced LPFG is shown in Fig. 4.9 and the transmission response over a larger wavelength range is shown in Fig. 4.10. The axial rotational orientation of 0° corresponds to the incident side of the fiber facing upwards during bending (see Fig. 1.6). Wavelength tuning occurs over a range from 1548.5 to $1557nm$ at an attenuation of $30dB$ as shown in Fig. 4.11. The broadband loss is 3 to $4dB$ while the $20dB$ bandwidth is $2.4nm$ and the $3dB$ bandwidth is $20.6nm$.

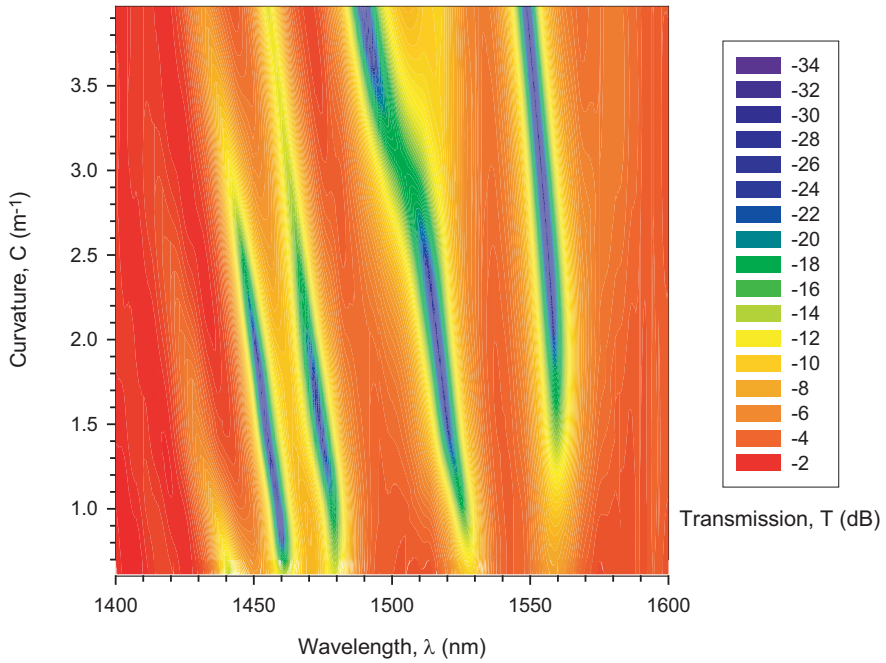

Figure 4.10: Pseudocolor surface plot of the transmission spectrum for the CO_2-laser-induced LPFG exhibiting wavelength tuning shown in Fig. 4.9 (LPFG 09090207). WT is indicated by the diagonal dark colored line around $1550nm$.

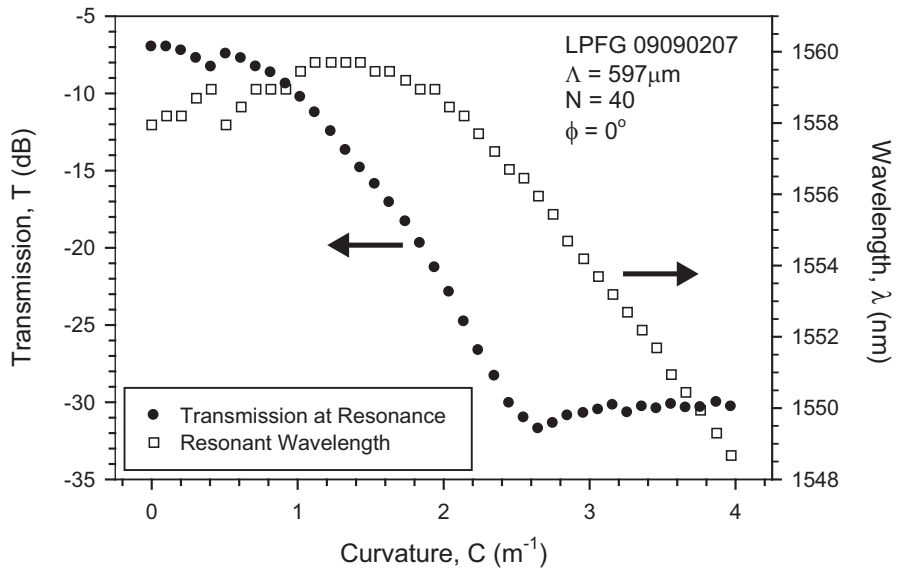

Figure 4.11: Plot of resonant wavelength and transmission at resonance versus curvature for the CO_2-laser-induced LPFG exhibiting wavelength tuning shown in Fig. 4.9.

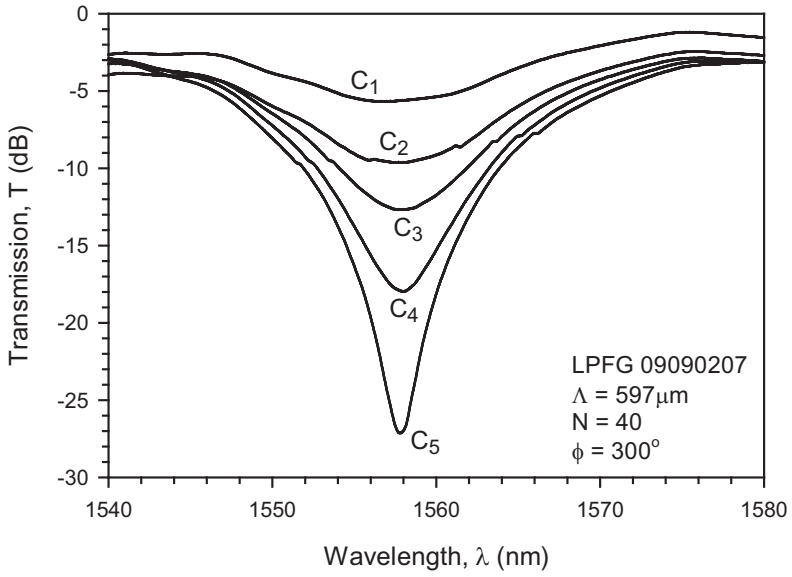

Figure 4.12: CO_2-laser-induced LPFG exhibiting variable attenuation tuning. The transmission spectrum response was measured at an axial rotational orientation ϕ=300° for various applied curvatures (C). $C_1 = 0.31m^{-1}$, $C_2 = 0.61m^{-1}$, $C_3 = 0.92m^{-1}$, $C_4 = 1.23m^{-1}$, and $C_5 = 1.53m^{-1}$.

An example of VAT observed in a flexed $597\mu m$-period CO_2-laser-induced LPFG is given in Fig. 4.12 [83] and the transmission response over a larger wavelength range is shown in Fig. 4.13. The transmission response shown in the two figures is from the same LPFG that exhibited WT; only the axial rotational orientation is different (0° versus 300°). Attenuation tuning occurs over a range from 5 to $28dB$ at a wavelength of $1558nm$ as shown in Fig. 4.14. The broadband loss is 1.5 to $2.5dB$ and the filter bandwidth varies depending upon the applied curvature.

Overmodulated CO_2-laser-induced LPFGs displayed both VAT and WT when flexed at certain axial rotational orientations. The combination of index asymmetry with overmodulation makes it possible for VAT and WT to occur. As the curvature of an overmodulated LPFG increases, less light is coupled back into the core and the curved LPFG eventually exhibits the transmission characteristics of an undermodulated grating. The change from overmodulated to undermodulated as curvature increases, combined with index asymmetry and a proper orientation, produces VAT as the attenuation at resonance increases with curvature. One potentially negative aspect of using overmodulated CO_2-laser-induced LPFGs

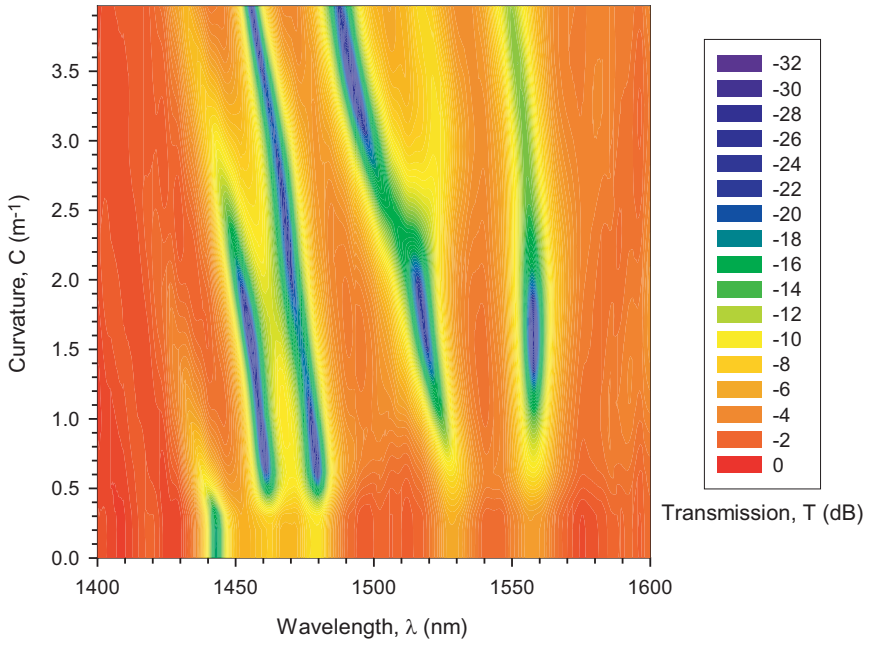

Figure 4.13: Pseudocolor surface plot of the transmission spectrum for the CO_2-laser-induced LPFG exhibiting variable attenuation tuning shown in Fig. 4.12 (LPFG 09090207).

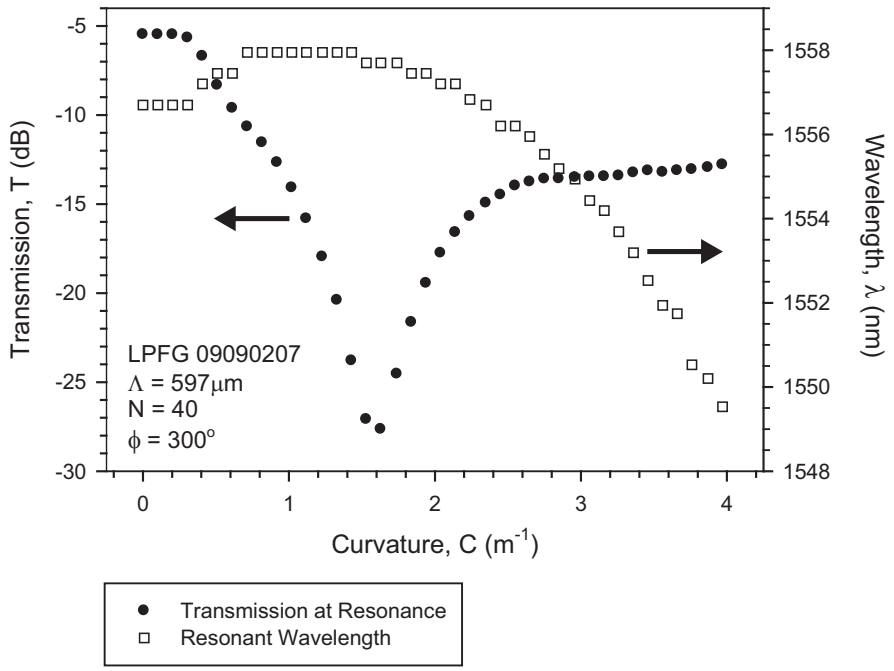

Figure 4.14: Plot of resonant wavelength and transmission at resonance versus curvature for the CO_2-laser-induced LPFG exhibiting variable attenuation tuning shown in Fig. 4.12.

is their typically higher broadband loss. Undermodulated LPFGs with strong attenuation at resonance could also be used, but those with moderate attenuation do not produce significantly large tuning ranges.

Why VAT and WT are associated with particular axial rotational orientations remains unknown. It is interesting to point out that WT occurs frequently at a 0^o orientation and that the low-high-low attenuation change of the cladding-mode resonance at $1550nm$ lasts longer over the curvature range than at other cladding-mode resonances. A detailed explanation of VAT and WT in CO_2-laser-induced LPFGs with applied flexure requires appropriate models to be developed. Issues surrounding the development of suitable models is discussed in Chapter 7.

As expected from previous measurements and symmetry arguments, the CO_2-laser-induced LPFG transmission spectra over the range of axial rotational orientations exhibits symmetry for a given constant curvature [1]. The symmetry of the response is evident in Fig. 4.15, where LPFG transmission spectra for different axial rotational orientations are plotted for a constant curvature of $1.63m^{-1}$. The response is clearly symmetric about the 0^o orientation, with the 0^o orientation corresponding to the incident side of the fiber being upward while 180^o and -180^o correspond to the incident side being downward. The observed symmetry confirms the statements by VanWiggeren *et al.* that the symmetry in the transmission response to applied flexure was due to the asymmetric refractive-index change and associated with orientation of the incident side of the fiber facing the laser during fabrication [1].

4.2 Response to Applied Torsion

Transmission spectra of certain types of fiber gratings change noticeably when subjected to torsion (twisting). Twisting a fiber containing tilted gratings produces variable polarization-dependent loss that can be used to compensate for polarization-dependent responsivity in certain classes of photodetectors [67]. For UV-induced LPFGs, twisting the fiber during fabrication reduces polarization-dependent loss [84]. Corrugated (periodically etched) LPFGs

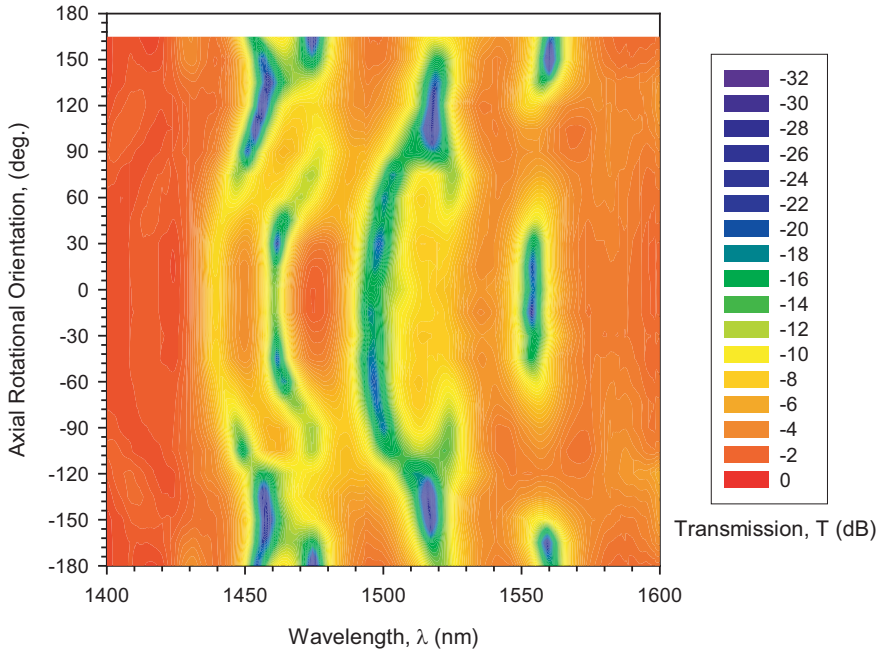

Figure 4.15: Pseudocolor surface plot of the CO_2-laser-induced LPFG transmission spectrum (LPFG 09090207) at constant curvature for a range of axial rotational orientations. The spectrum response is clearly symmetrical about the 0^o orientation. Axial rotational orientation is plotted from -180^o to 180^o (instead of 0^o to 360^o) to emphasize the symmetry.

have been used as torsion sensors because of their linear wavelength shift with increasing twist rate [85]. The resonant wavelengths of LPFGs fabricated with a high-frequency pulsed CO_2 laser also shift linearly with increasing applied torsion. In addition, they exhibit a unique wavelength shift dependence on twist direction [counterclockwise (CCW) versus clockwise (CW)] [86, 87].

The interesting and useful behavior observed for other fiber gratings suggests it is important to examine the effect of torsion on CO_2-laser-induced LPFGs. With the known asymmetric cross-sectional refractive index profile present in CO_2-laser-induced LPFGs and analogous to the observed response to flexure, it is anticipated that they will exhibit unique behavior when subjected to torsion. In this section, measurements of the response of CO_2-laser-induced LPFGs to applied torsion are presented and discussed. A twist-direction-dependent resonant wavelength shift occurs in the LPFG transmission spectrum as the amount of applied torsion increases from the initial untwisted state. However, as higher levels of twist are reached, the direction of resonant wavelength shift becomes independent

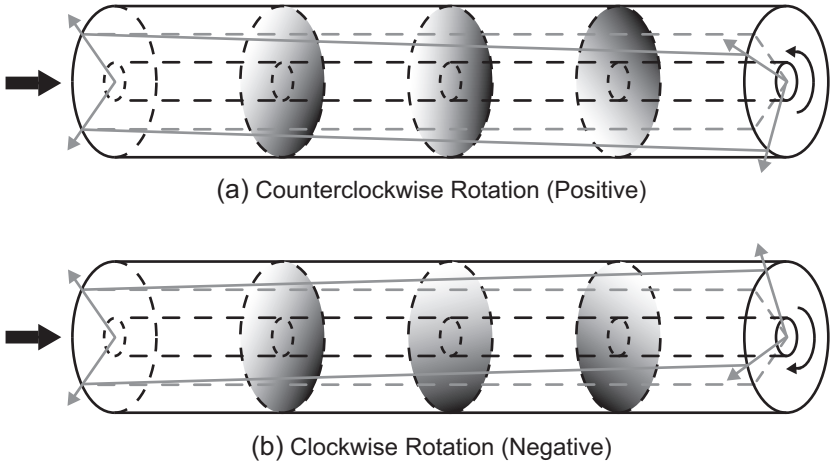

Figure 4.16: Diagram of a segment of a CO_2-laser-induced LPFG subjected to torsion (a) Counterclockwise rotation (positive twist) (b) Clockwise rotation (negative twist).

of the twist direction. Before discussing the measured torsion response in detail, torsion effects in optical fiber and LPFGs are briefly reviewed.

4.2.1 Torsion Effects in Optical Fibers and LPFGs

For a segment of optical fiber under slight tension (without slack), imparting a twist introduces shear strain and causes cross-sectional planes to rotate about the fiber longitudinal axis. If the applied torque is small (linear regime with no deformation), the cross-sectional planes remain parallel as they rotate and longitudinal lines on the surface of the fiber, which are straight in the untwisted state, become helical [88]. As the torque applied to a fiber increases, finite deformation of the fiber cross-section eventually occurs.

Consider the practical case of a segment of fiber fixed at both ends. If one end of the fiber is twisted with respect to the other, torque develops internally in the fiber. The *angle of twist* of one end of the segment of relative to the other is defined as the angle that a radial line rotates from the start of the segment to its end. Angle of twist is often cast as twist rate (τ), which is the angle of twist per unit length and is independent of the segment length. The fiber buffer is assumed to be removed in the following discussions so that the fiber can be treated as a single glass cylinder instead of a two-layer cylinder (both polymer and glass).

The optical effects of torsion on fiber manifest through alteration of the polarization

state of light traveling in the twisted fiber and the magnitude of the effect depends upon the amount of applied twist and the fiber characteristics. Three regimes of behavior have been identified that result from weak twist, moderate twist, and strong twist [89]. Optical fiber under weak twist behaves essentially as untwisted fiber. Any linear birefringence present in the fiber still dominates propagation; in standard single-mode fiber, which has low levels of linear birefringence, there is little effect on the propagation. Under moderate twist, the shear strains induced in the fiber by twisting yields circular birefringence. The circular birefringence combines with any linear birefringence present in the fiber segment to produce elliptical birefringence and an associated complex evolution of the light polarization state as the light propagates in the fiber. In the limit of strong twist, circular birefringence overshadows any linear birefringence that is present in the fiber. The resulting eigenmodes of the strongly twisted fiber are no longer linearly polarized, but become right-handed and left-handed circularly polarized [89, 90].

Change in the transmission spectra in response to applied torsion has been examined for several different types of LPFGs, including corrugated and UV-induced. Ivanov *et al.* applied finite deformation and nonlinear photoelasticity theory to explain the resonant wavelength shifts occuring in corrugated LPFGs when subjected to torsion [91]. Consistent with torsion in optical fibers, the electromagnetic field in many twisted LPFGs can be written as a superposition of circularly polarized modes. Their theory was verified by experimental measurements in both corrugated and UV-induced LPFGs. The shift in resonant wavelength with applied torsion is independent of the direction of twist (CCW or CW) in both UV-induced and corrugated LPFGs. Additional torsion response measurements conducted on UV-induced LPFGs for larger applied twist rates yielded similar results [92]. The resonant wavelength of twisted UV-induced LPFG consistently shifts to shorter wavelengths as the applied twist rate increases.

Corrugated LPFGs are created by etching and not as a result of any induced index change. Along similar lines, a relatively new type of LPFG, called a virtual LPFG, has been proposed. Virtual LPFGs are created by subjecting high-birefringence polarization-maintaining fiber to torsion [93]. The combination of the inherent linear birefringence

present in polarization-maintaining fiber and torsion produces a polarization-dependent effective-index change. The spectral response of the virtual LPFGs varies with the state of polarization of the incident light. Though a relatively high twist rate is applied to the polarization-maintaining fiber to create the virtual LPFG, the fiber is still considered to be in the regime of weak twist because of the high levels of intrinsic linear birefringence.

Recent torsion response measurements of CO_2-laser-induced LPFGs written with high-frequency laser pulses (see Chapter 1) demonstrated that the gratings behave differently than UV-induced or corrugated LPFGs. A distinct dependence of the response on the direction of twist was noted. Specifically, the direction of the resonant wavelength shift (towards shorter or longer wavelengths) differs depending on whether the LPFG is twisted CCW or CW. However, the amount of wavelength shift and the change in attenuation level were independent of the twist direction, meaning that their absolute values are the same for both twist directions. The CCW/CW dependence was attributed to the combination of linear birefringence resulting from one-sided exposure during fabrication and twist-induced circular birefringence [87]. Since CO_2-laser-induced LPFGs also possess linear birefringence due to induced asymmetry, twist-direction dependence of the resonant wavelength shift is anticipated.

4.2.2 Torsion Response Measurement Configuration and Procedure

The measurement configuration used for characterizing CO_2-laser-induced LPFG response to applied torsion is shown in Fig. 4.17. Two specially designed adapter plates, one secured to each of the automated rotation stages, contain fiber chucks that are used to securely hold the optical fiber containing the LPFG during testing. An LPFG is inserted through the chucks and positioned so that the fiber region containing the grating is centered between the stages. One chuck is then tightened so as to hold the fiber firmly in the chuck. While pulling one lead of the fiber containing the LPFG (in order to introduce a slight tension), the second fiber chuck is tightened. After the securing the fiber, the stages are then rotated to impart a desired twist rate (rotation per unit length, τ) on the grating being tested. The applied twist rate is calculated by dividing the total stage angular rotation (from an initial

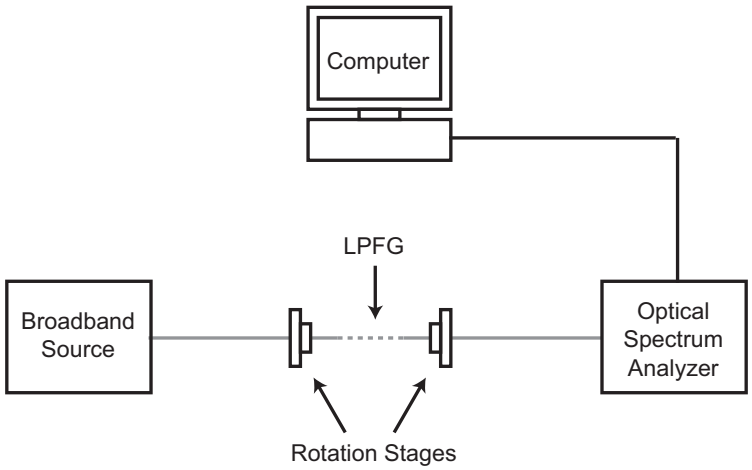

Figure 4.17: Measurement configuration used for characterizing LPFG transmission spectra in response to applied torsion.

unrotated state) by the length of fiber between the chucks. For the tests results presented here, the free length of fiber between the chucks/plates was either $36mm$ or $50mm$, with the LPFGs occupying an approximately $25mm$-long section in the center of the supported span for both cases.

The leads from the fiber segment containing the LPFGs are connected to a broadband light source and an optical spectrum analyzer to allow the transmission spectrum to be recorded for each applied twist rate. A custom LabVIEW program is used to control the automated rotation stages (through a motion controller) and to store spectral data transfered from the optical spectrum analyzer.

The range of twist rate examined during testing was limited by the tendency of the CO_2-laser-induced LPFGs to fracture as the total amount of applied twist between the ends of the grating approached 180^o (with a few notable exceptions). The fracturing of the glass fiber as the twist rate increases most likely results from micro-scratches on the fiber surface (created by mechanical stripping of the buffer) [94] or surface damage from exposure to laser light. For the test results reported in the following section, twist direction is designated following the right-hand rule (from light input to light output), with CCW being positive and CW being negative.

4.2.3 Torsion Response Measurement Results and Discussion

4.2.3.1 Twist Direction Dependence of Resonant Wavelength Shift

As can be expected from the torsion response tests conducted previously on UV-induced and corrugated LPFGs, the resonant wavelength and peak transmission loss of CO_2-laser-induced LPFGs change as the amount of applied torsion increases. However, a distinct dependence of the resonant wavelength shift on the torsion direction (CCW versus CW) was observed, as is shown by the plots in Fig. 4.18 of the transmission spectrum of a $640\mu m$-period CO_2-laser-induced LPFG for various twist rates . Figure 4.19 contains plots of the resonant wavelength and peak transmission loss versus twist rate for the same grating. The initial direction of resonant wavelength shift (towards longer or shorter wavelengths) depends upon whether CCW or CW twist is applied to the CO_2-laser-induced LPFG under test. However, as the applied CW twist rate continues to increase, the resonant wavelength stops shifting to longer wavelengths and begins to shift to shorter wavelengths. The initial twist-direction dependence of the resonant wavelength shift is consistent with measurement results reported for LPFGs fabricated by exposure to high-frequency CO_2 laser pulses [86], but reversal of the resonant wavelength shift direction at higher twist rates has not been reported previously. The lack of a previous observation of the reversal could possibly be due to a smaller testing range or the sensitivity to torsion of the examined cladding modes.

Ten additional $640\mu m$-period CO_2-laser-induced LPFGs were subjected to torsion response testing in order to corroborate the response shown in Fig. 4.18. Some variation in their response patterns was observed, though the $640\mu m$-period gratings tested predominantly followed the same response pattern as that shown in Fig. 4.19. As an example, the response of another $640\mu m$-period CO_2-laser-induced LPFG is given in Fig. 4.20. The trough-peak-trough pattern in the peak transmission loss near the untwisted state, shown in Fig. 4.19(b), is not necessarily present in the other $640\mu m$-period CO_2-laser-induced LPFG subjected to testing [Fig. 4.20(b)]. Any difference in the change in peak transmission loss with twist rate between the tested $640\mu m$-period gratings typically occurred around the untwisted state.

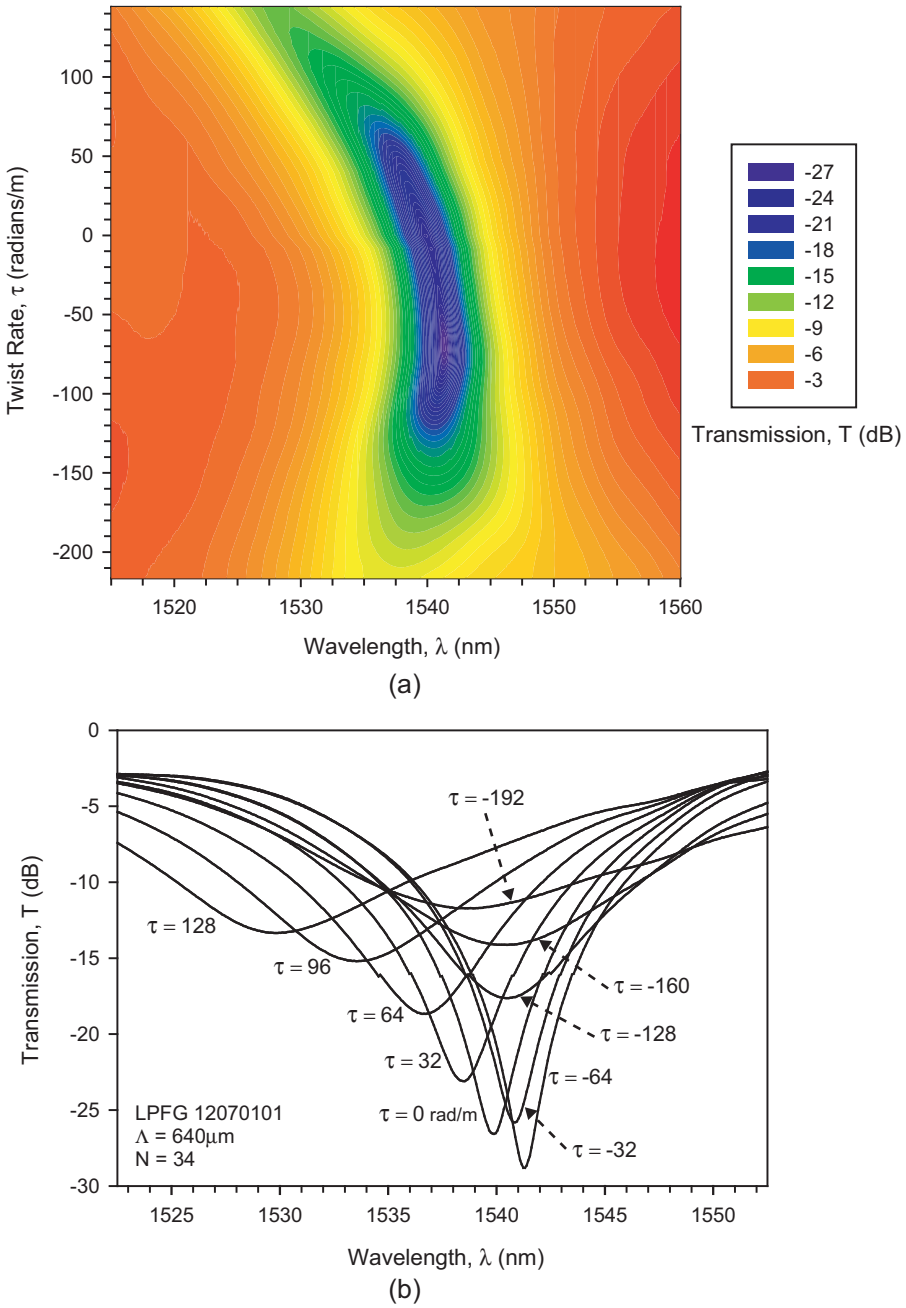

Figure 4.18: (a) Pseudocolor surface plot showing the change in the 640μm-period CO_2-laser-induced LPFG transmission spectrum for various levels of applied torsion (LPFG 12070101). (b) Selected transmission spectra of the same LPFG for several twist rates.

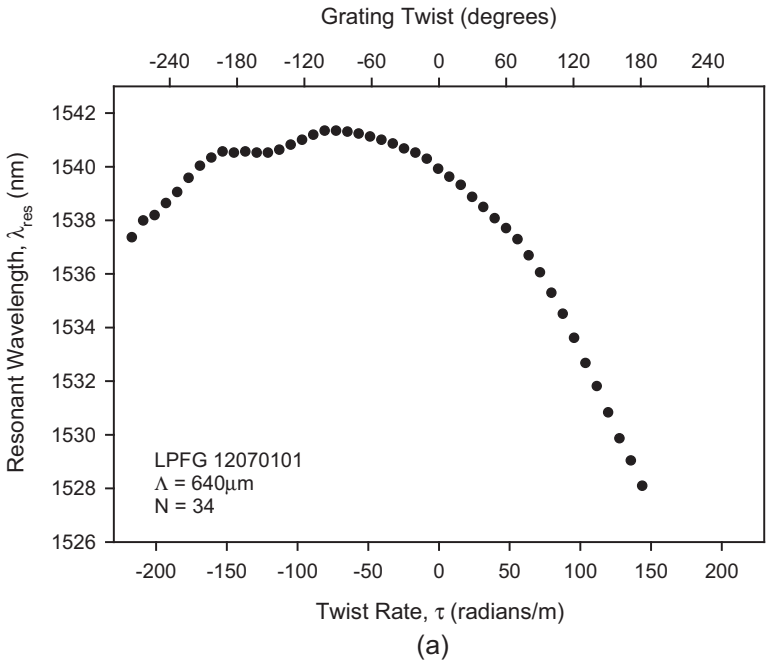

Figure 4.19: (a) Resonant wavelength versus twist rate for the same 640μm-period CO_2-laser-induced LPFG as in Fig. 4.18 (LPFG 12070101). (b) Peak transmission loss versus twist rate.

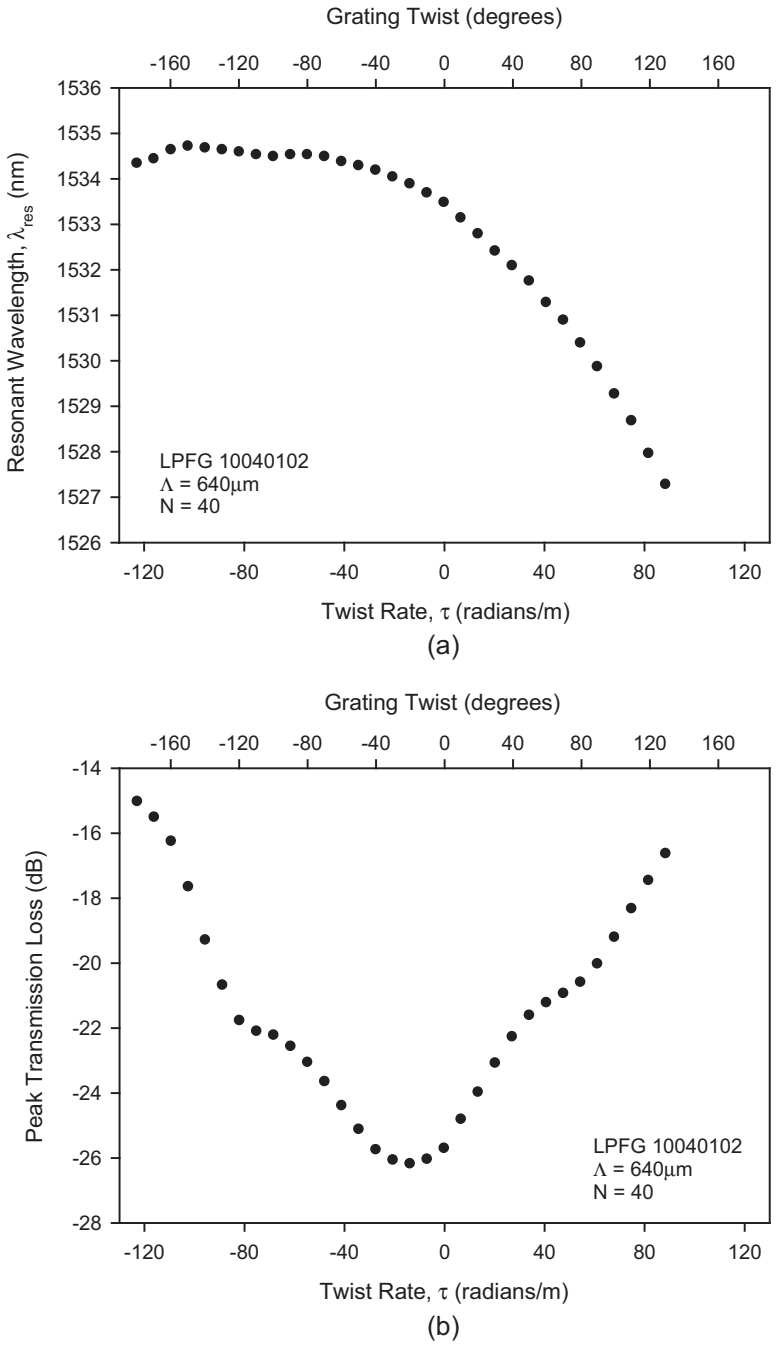

Figure 4.20: (a) Resonant wavelength versus twist rate of another 640μm-period CO_2-laser-induced LPFG (LPFG 10040102). (b) Peak transmission loss versus twist rate.

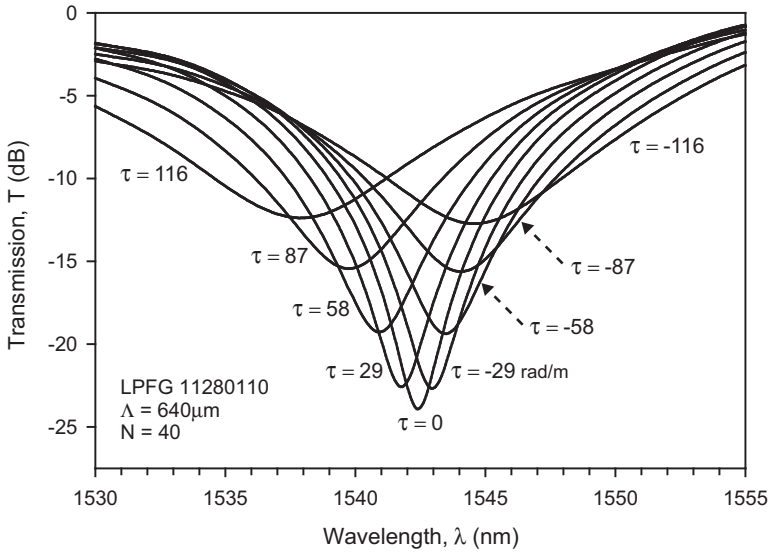

Figure 4.21: Select transmission spectra of another 640μm-period CO_2-laser-induced LPFG (LPFG 11280110) for various twist rates. The response of the grating to twist appears to be symmetric about the untwisted state.

In contrast to the consistent responses observed in other 640μm-period CO_2-laser-induced LPFGs when subjected to torsion, one of the tested gratings exhibited a unique response. Figure 4.21 shows several transmission spectra of the particular 640μm-period CO_2-laser-induced LPFG for several different twist rates. The change in attenuation with applied twist is clearly symmetric about the untwisted state; the change in attenuation at resonance are the same for absolute levels of torsion, though the direction of resonant shift still depends on the direction of twist. A symmetric response was observed only rarely while conducting all of the torsion response measurements and the large majority of 640μm-period gratings responded similarly when twisted.

4.2.3.2 Twist Response of Different Cladding Modes

Individual cladding modes can exhibit different sensitivities to torsion, meaning that the resonant wavelength and attenuation at resonance will change more quickly for certain cladding modes than for others. For instance, the shift in resonant wavelength of three different cladding modes in a UV-induced LPFG was found to be different for the same twist rate [91]. The variation in the sensitivity of different cladding modes in CO_2-laser-induced LPFGs was examined by measuring the torsion response of the primary cladding

mode (highest attenuation for an undermodulated condition) for two additional grating periods.

Figure 4.22 shows the measured transmission spectrum of a $565\mu m$-period CO_2-laser-induced LPFG for a number of different twist rates while Fig. 4.23 contains plots of the resonant wavelength shift and peak transmission loss versus twist rate for the same grating. Compared to the results obtained for the $640\mu m$-period CO_2-laser-induced LPFGs, the resonant wavelength of the $565\mu m$-period grating shifts more rapidly over a given twist range. No turn-around in the resonant wavelength shift direction is evident as CW twist increases, in contrast to observed response of the $640\mu m$-period CO_2-laser-induced LPFGs, though the rate of change in the shift does decrease as the twist rate approaches $-150 rad/m$. The rate decrease suggests that a reversal of shift direction might occur at a higher CW twist rate (which could not be verified because of fracture).

The resonant wavelength shift for applied torsion occurs even more rapidly in $597\mu m$-period CO_2-laser-induced LPFGs than in the $565\mu m$-period and $640\mu m$-period gratings. Figure 4.24 shows the measured transmission spectrum of a $597\mu m$-period CO_2-laser-induced LPFG over a range of twist rates while Fig. 4.25 shows the resonant wavelength shift and peak transmission loss versus twist rate for the same grating. There is no direct observation of a reversal of the resonant wavelength shift direction. However, the rate of change of the resonant wavelength is larger for CCW twist than CW twist, which is consistent with responses observed for $565\mu m$-period and $640\mu m$-period gratings. The trend is shown most clearly in Fig. 4.26, where the resonant wavelength shift (relative to the resonant wavelength in the untwisted state) versus twist rate is plotted for the $640\mu m$-, $597\mu m$-, and $565\mu m$-period CO_2-laser-induced LPFGs.

4.2.3.3 Discussion of Torsion Response

The twist direction dependence of the resonant wavelength shift is a characteristic feature of LPFGs written by one-sided exposure to CO_2 laser light; as a result of the linear birefringence present in the grating structure, twisting the fiber containing the LPFG produces complex forms of birefringence. Consider a CO_2-laser-induced LPFG subjected to twist

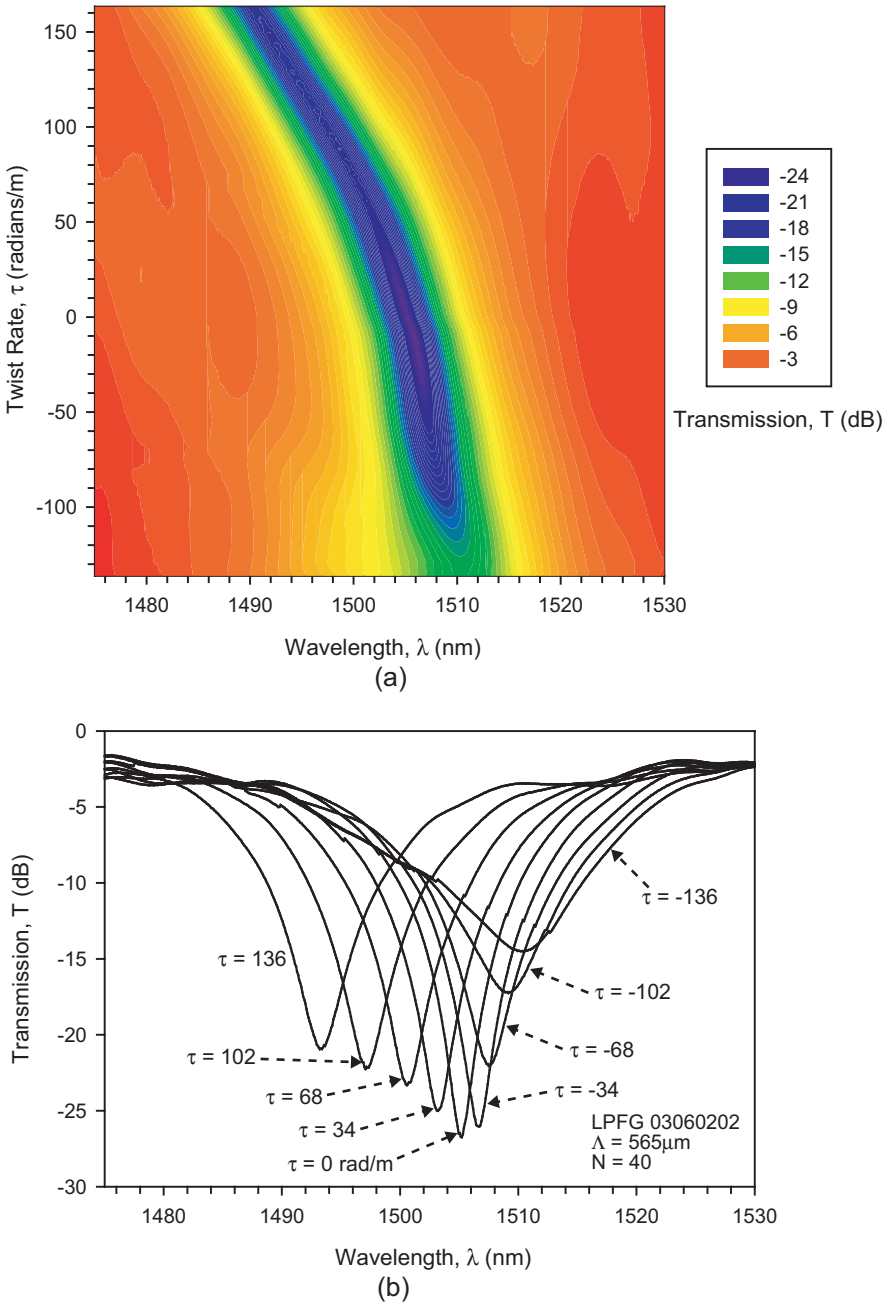

Figure 4.22: (a) Pseudocolor surface plot showing the change in the 565μm-period CO_2-laser-induced LPFG transmission spectrum for various levels of applied torsion (LPFG 03060202). (b) Selected transmission spectra of the same LPFG for several twist rates.

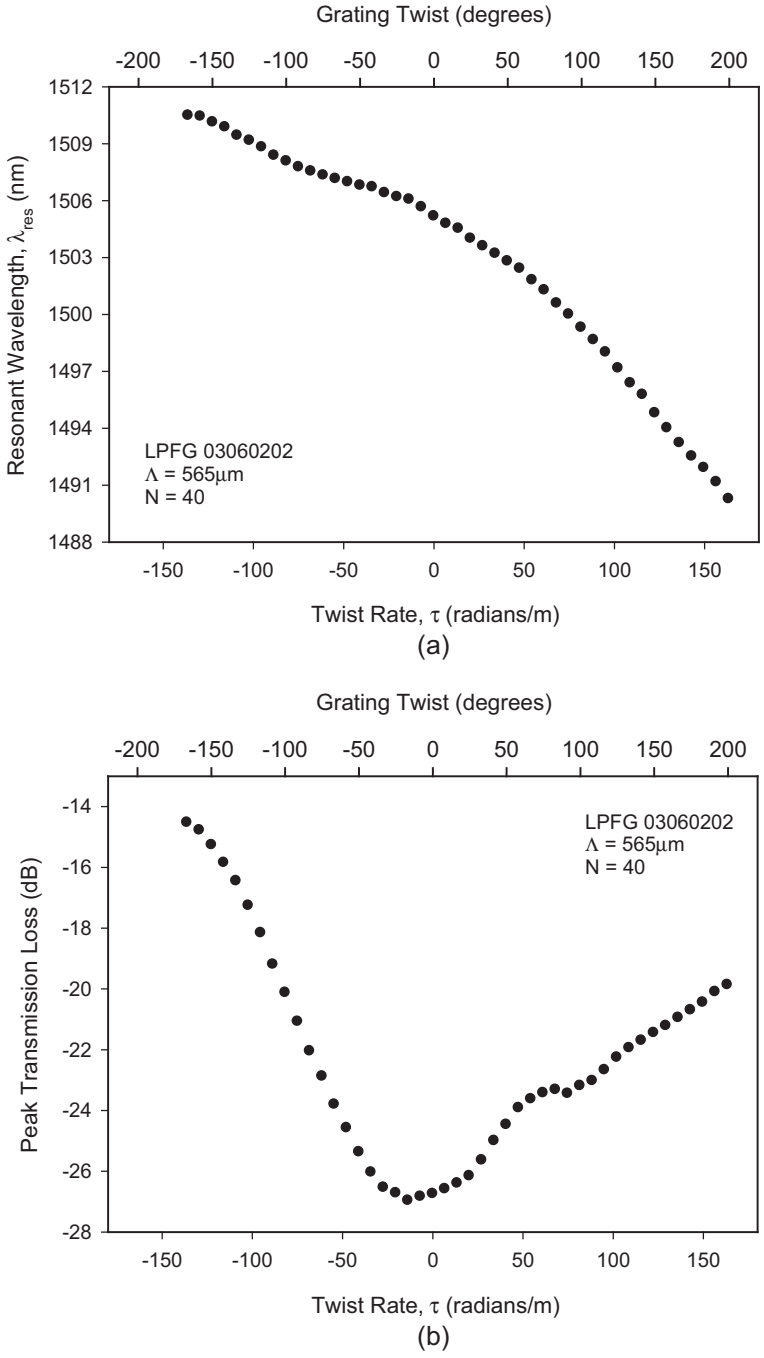

Figure 4.23: (a) Resonant wavelength versus twist rate of the same 565μm-period CO_2-laser-induced LPFG (LPFG 03060202). (b) Peak transmission loss versus twist rate.

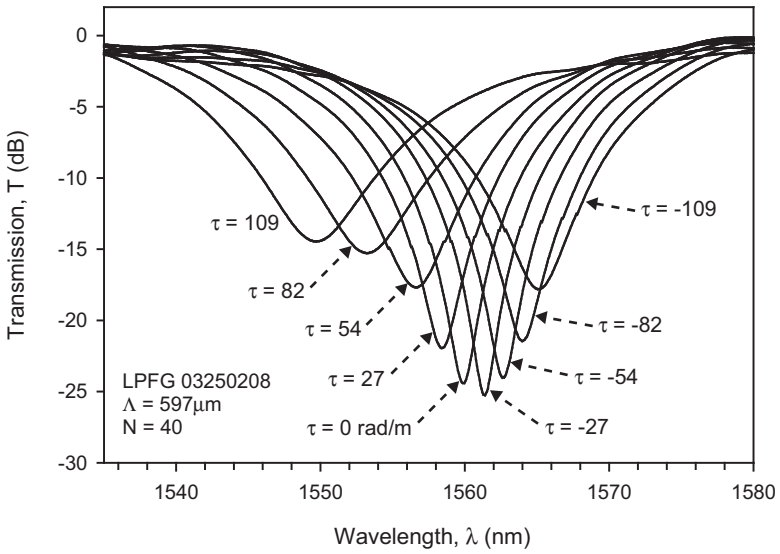

Figure 4.24: Selected transmission spectra of a 597μm-period CO_2-laser-induced LPFG for several twist rates (LPFG 03250208).

(Fig. 4.16). In the optical fiber and away from any grating periods, the condition of strong twist exists and circular birefringence dominates. This condition holds in the unexposed sections almost independent of the amount of twist applied since linear birefringence levels are very low. In the sections of the grating exposed to CO_2-laser-light, linear birefringence is present (see Chapter 3). The core-guided modes only experience circular birefringence as a result of the index asymmetry being limited primarily to the cladding, but the cladding modes experience a pattern of birefringence that produces complex polarization state evolution as the cladding modes travel through the CO_2-laser-induced LPFG. However, the polarization state evolution depends upon the amount of applied twist. Similar to the effect of torsion on optical fibers, three regimes of behavior exist. The interplay between the linear birefringence induced by one-sided exposure to CO_2-laser-light and twist-induced circular birefringence directly influences the effective indices experienced by modes in the LPFG and, hence, the mode resonant wavelength.

For low levels of twist, the twist-induced circular birefringence is still very low and the linear birefringence present in the CO_2-laser-induced LPFG dominates. The grating behaves normally as if it were not twisted. This regime exists only immediately around the untwisted state.

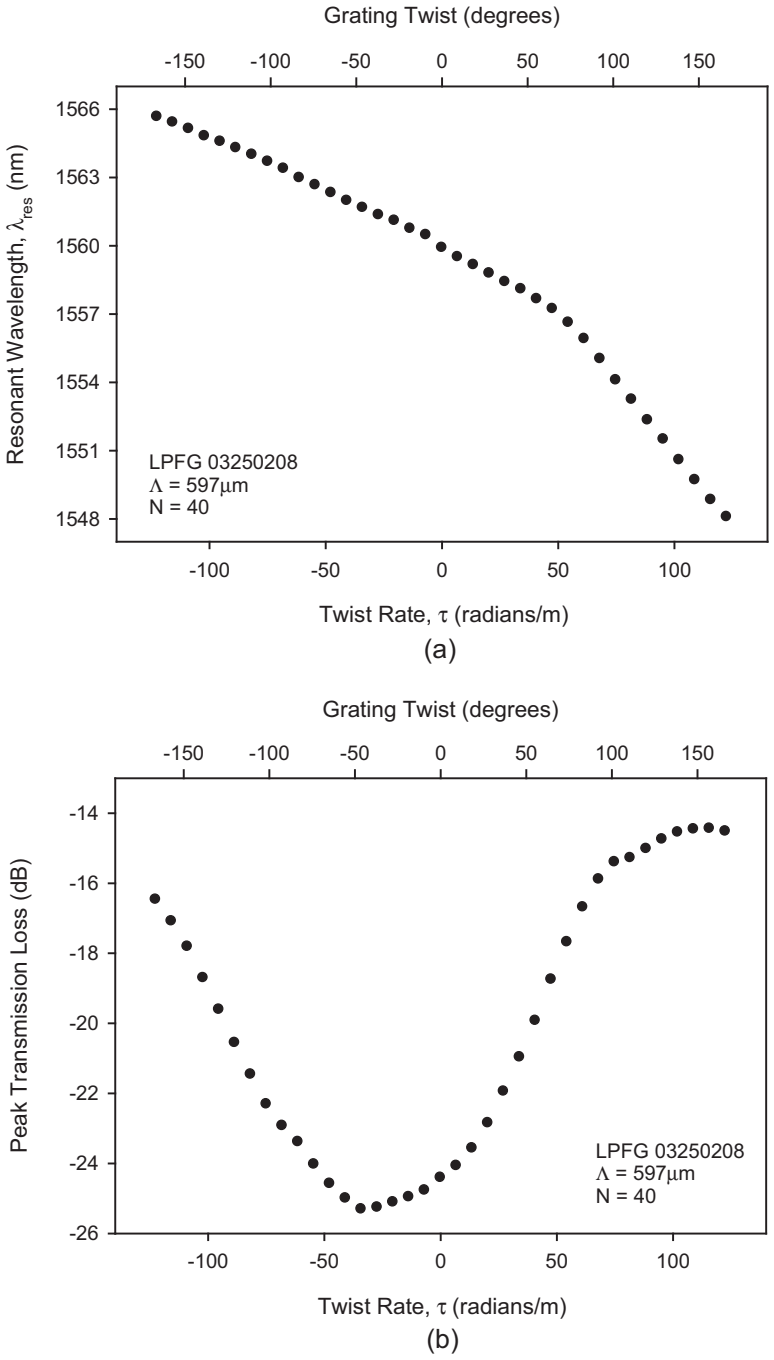

Figure 4.25: (a) Resonant wavelength versus twist rate of the same 597μm-period CO_2-laser-induced LPFG (LPFG 03250208). (b) Peak transmission loss versus twist rate.

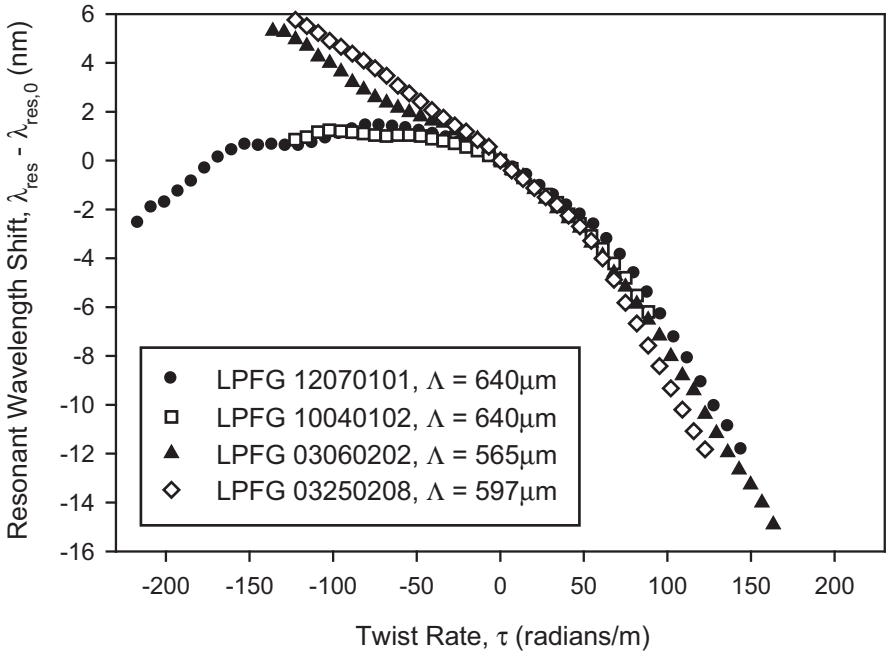

Figure 4.26: Resonant wavelength shift (relative to the untwisted state) for four different CO_2-laser-induced LPFGs.

As the twist rate increases, linear birefringence and circular birefringence approach the same level. The circular birefringence experienced by the core-guided modes and the elliptical birefringence experienced by the cladding-guided modes holds independent of the twist direction. However, if CCW twist is applied, the grating periods rotate correspondingly and right-rotating elliptical birefringence results. The opposite is correct for CW twist. In effect, torsion forces an alteration in polarization state evolution of core and cladding modes that changes both the effective indices and coupling coefficients. The effective-index difference [Eq. (3.1)], and therefore the resonant wavelength, increase for CCW twist and decrease for CW twist as a result of the different effective indices encountered by the modes for the two twist directions. This condition is similar to that of moderate twist in optical fibers.

Finally, for higher levels of twist applied to the CO_2-laser-induced LPFG, the circular birefringence becomes much larger than the linear birefringence. The grating would then begin to behave as if the linear birefringence was not present and the resonant wavelength shift becomes independent of the twist direction; this accounts for the reversal of shift

direction (now towards shorter wavelengths) observed in $640\mu m$-period CO_2-laser-induced LPFGs at higher CW twist rates. The explanation is consistent with the response of UV-induced LPFGs, which are known to shift to shorter wavelengths for both CCW and CW twist and contain relatively low levels of linear birefringence [92].

The qualitative explanation provided here, which follows from the SOP evolution argument by Wang *et al.* [87] that incorporates higher twist rates, neglects more complex issues such as the state evolution that occurs between the linearly birefringent periods. Finite deformation theory, nonlinear photoelasticity, and hybrid mode coupling theory, adopted by Ivanov *et al.* to model the effects of torsion on corrugated and UV-induced LPFGs, may also be important for CO_2-laser-induced LPFGs [91, 95].

The SOP evolution argument also does not clearly explain why the twist direction dependence of the resonant wavelength shift exists; there must be some inherent difference in the grating structure when the grating is twisted in opposite directions. One other type of LPFG, the helical LPFG, exhibits twist direction dependence of the resonant wavelength shift with applied torsion. This type of LPFG is fabricated in such a way as to produce a helical-type index modulation. Applying CCW or CW twist to a helical LPFG correspondingly increases or decreases the helical pitch of the grating and produces a dependence of the resonant wavelength shift on twist direction. It is certainly possible that CO_2-laser-induced LPFGs could possess an helical pattern intrinsic to the grating. What is not obvious, however, is why a helical-type pattern would be present in CO_2-laser-induced LPFGs and how such a structure would be induced given the particular fabrication apparatus/technique presented in Chapter 2. A complete cross-sectional and longitudinal (along the grating length) refractive-index profile of a CO_2-laser-induced LPFG is required to determine if a helical-type pattern exists.

Another characteristic of the change in CO_2-laser-induced LPFG transmission spectra with applied torsion is the increasing bandwidth (full-width at half-maximum) with increasing twist rate (independent of twist direction). Recent modeling of propagation and coupling constants of hybrid modes in twisted optical fibers indicates the reason for the increasing bandwidth [95].

4.3 Summary

In this chapter, the response of CO_2-laser-induced LPFGs to physical manipulation, in the form of applied flexure and applied torsion, has been examined. Expanding upon previous investigations of the flexure response of CO_2-laser-induced LPFGs, variable attenuation tuning and wavelength tuning in the $1550nm$ telecommunications wavelength band were demonstrated. A direct comparison of the flexure response of a CO_2-laser-induced LPFG and a more typical UV-induced LPFG was conducted. The large number of flexure tests conducted on LPFGs required the development of an automated testing system.

The torsion response of CO_2-laser-induced LPFGs was measured. As expected, the transmission spectra of CO_2-laser-induced LPFGs change as the gratings are twisted, with both the resonant wavelength and attenuation altered. Relatively complex response patterns were observed, with a twist-direction dependence of the resonant wavelength shift existing for lower twist rates but with twist-direction independence for higher twist rates.

The unique behavior of CO_2-laser-induced LPFGs when subjected to flexure and torsion is another consequence of the azimuthally asymmetric refractive-index profile. The twist direction dependence of the resonant wavelength shift and the dependence of the flexure response on axial rotational orientation would not occur with an azimuthally symmetric induced index change.

The change in CO_2-laser-induced LPFG transmission spectra in response to flexure and torsion have been examined in this chapter. Another major type of physical manipulation, axial tension, has not been discussed for two primary reasons: (1) any actual change in the transmission spectra (resonant wavelength shift and attenuation) for varying applied tension is much smaller than for applied flexure and torsion, and (2) the asymmetric refractive-index profile has little (or no) effect on the response of CO_2-laser-induced LPFGs to tension. Informal tension response tests conducted on a typical CO_2-laser-induced LPFG indicated that the grating behaves similarly to other LPFGs [96].

CHAPTER 5

APPLICATIONS

The azimuthally asymmetric refractive-index properties of carbon-dioxide-laser-induced long-period fiber gratings (CO_2-laser-induced LPFGs) make them particularly well suited for performing certain operations. Asymmetry present over the refractive-index profile of this type of LPFG can influence grating behavior in response to physical manipulation, as reported in the previous chapter. In addition, the effect of the asymmetry can be directly useful for certain applications. In this chapter, three distinct applications of CO_2-laser-induced LPFGs are examined: variable optical attenuation, optical tunable filtering, and optical fiber-to-waveguide coupling. Prototype variable optical attenuator (VOA) and optical tunable filter (OTF) devices, based on controlled flexure of CO_2-laser-induced LPFGs, are described in Sec. 5.1 while the optical fiber-to-waveguide coupler is discussed in Sec. 5.2. The significance of the azimuthal asymmetry on device performance in the application areas is discussed in each section.

5.1 Prototype Variable Optical Attenuators and Optical Tunable Filters

To achieve higher data rates in high-speed optical telecommunications networks, a number of operations that were previously performed in the electrical domain are now being performed in the optical domain [7]. Examples of such operations include switching, routing, and channel monitoring. Accomplishing these operations without optical to electrical signal conversion requires suitable all-optical devices. Two illustrative devices, variable optical attenuators and optical tunable filters, enable critical operations, including channel balancing, gain control, and channel dropping.

With the variable attenuation tuning (VAT) and wavelength tuning (WT) behavior observed by VanWiggeren *et al.* and that reported in Chapter 4, it is evident that controlled

flexure of CO_2-laser-induced LPFGs at certain axial rotational orientations could be used to create VOA and OTF devices. Use of CO_2-laser-induced LPFGs for VOAs and OTFs offers several advantages, including an all-fiber geometry, low fabrication costs, and low backreflection. In this section, prototype VOA and OTF devices developed using a piezoceramic bending actuator are described and example results from constructed devices are given. A more detailed description of prototype device assembly, testing, and performance is available in the literature [5, 6].

5.1.1 Prototype Concept

Development of prototype devices based on controlled flexure of CO_2-laser-induced LPFGs requires some form of actuator to perform bending operations. Thin, curved piezoceramic actuators were selected to serve as the flexure platforms of the prototype devices. The actuators, known as thin layer unimorph ferroelectric drivers and sensors (THUNDER), change curvature when different voltage levels are applied. The actuators are manufactured by Face International [97]. From an actuator's initial structural curvature (at zero volts), applying a positive voltage (top surface with respect to bottom surface) decreases the curvature (flattens), while applying a negative voltage increases the curvature. Advantages of the using THUNDER actuators to flex LPFGs include small size, low cost, and fast response time (in the millisecond regime).

Ultrasonic aluminum wire bonding was used to attach leads to the bottom and top surfaces of the actuators so that various voltage levels could be easily applied to the prototype devices. The actuators are secured to Plexiglass bases that provide electrical isolation, in addition to being lightweight and small. A section of optical fiber containing a CO_2-laser-induced LPFG, after being rotated to a suitable axial rotational orientation that produces VAT or WT, was positioned in the center of the top actuator surface and attached to the surface (on either side of the grating) with silicone adhesive.

A schematic diagram and a photograph of an assembled prototype device are shown in Fig. 5.1 and Fig. 5.2, respectively. For the particular THUNDER actuator model used in prototype development (TH 11-R), achievable curvatures range from $4.7m^{-1}$ (at $450V$) to

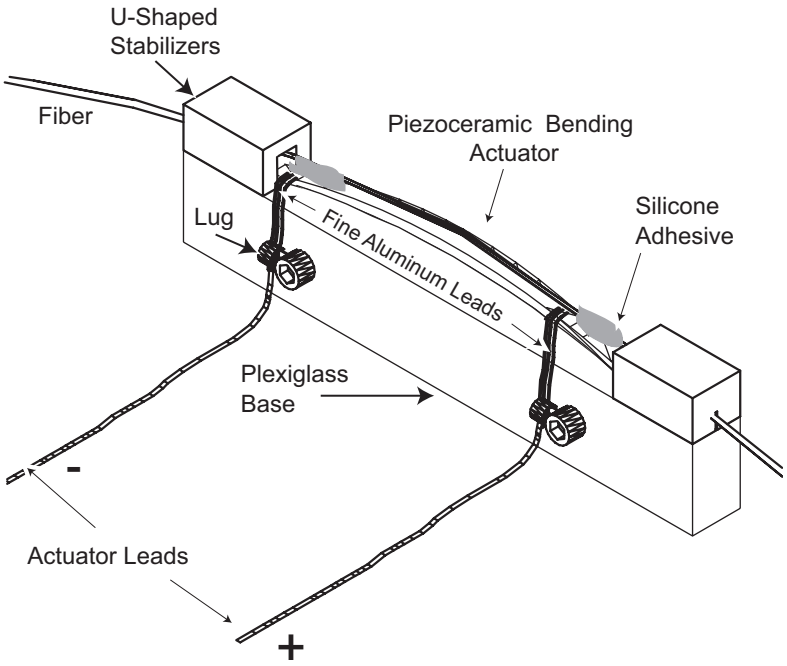

Figure 5.1: Diagram of an assembled prototype device. The external leads connect to lug screws in the Plexiglass base, to which the wire-bonded leads from the actuator also connect [5].

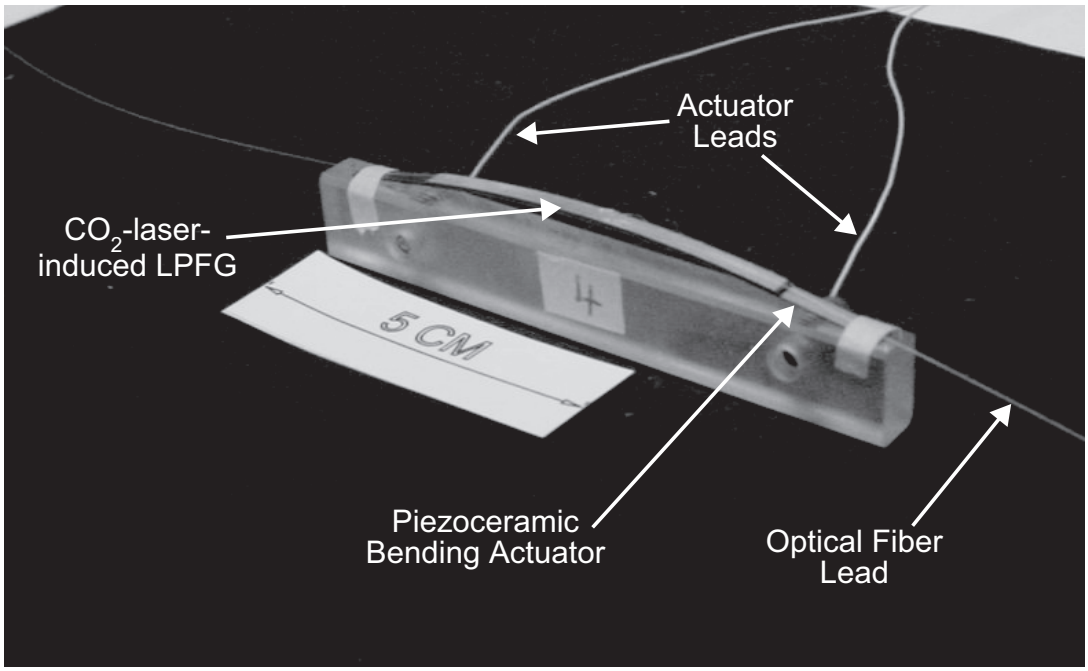

Figure 5.2: Photograph of an assembled prototype device. The CO_2-laser-induced LPFG is attached to the top surface of the bending actuator [6].

$7.4m^{-1}$ (at $-450V$) with a base curvature of $6.1m^{-1}$ (at $0V$). The small size of the devices ($76.2mm \times 2.54mm$) is evident from the photograph. Stabilizers, shown in the diagram but not in the photograph, were added to prevent undesirable lateral movements of the actuator during curvature changes.

5.1.2 Initial Testing for Prototype Development

Prior to assembling the prototype VOA and OTF devices, CO_2-laser-induced LPFGs displaying VAT and WT at the desired curvature levels needed to be identified. A number of LPFGs were tested using a variant of the automated flexure testing system described in Chapter 4. The variant testing system employed one of the THUNDER actuators to perform the bending instead of the plastic platform and linear stage. The pair of rotation stages was still used to test the gratings at different axial rotational orientations [5, 6].

Overmodulated $480\mu m$-period CO_2-laser-induced LPFGs exhibited VAT and WT at the higher actuator curvature levels during flexure response testing. All of the developed prototype devices used overmodulated $480\mu m$-period gratings [5].

5.1.3 Examples of Prototype Devices

An example of the transmission spectra from a prototype device developed to perform VOA at a constant wavelength is shown in Fig. 5.3. A variable attenuation range from $-4dB$ to $-17dB$ at a wavelength of $1393nm$ was achieved while varying the applied voltage from -450 to $150V$. The device possesses a broadband loss of $3dB$.

An example of the transmission spectra from a prototype device developed to perform as an OTF is shown in Fig. 5.4. Wavelength tuning occurs over $7nm$, from 1533 to $1540nm$, at an attenuation of $30dB$. The device also has a broadband loss of $3dB$ and a $20dB$ bandwidth of $3.1nm$. The applied voltage ranged from 0 to $300V$. Prototype devices possessing combined VOA and OTF behavior have also been developed [5, 6].

As discussed and demonstrated in Chapter 4, the azimuthally asymmetric refractive index profile present in CO_2-laser-induced LPFGs leads to VAT and WT behavior when the gratings are subjected to flexure. Simple flexure-based VOA and OTF devices could not be made using most other types of LPFGs.

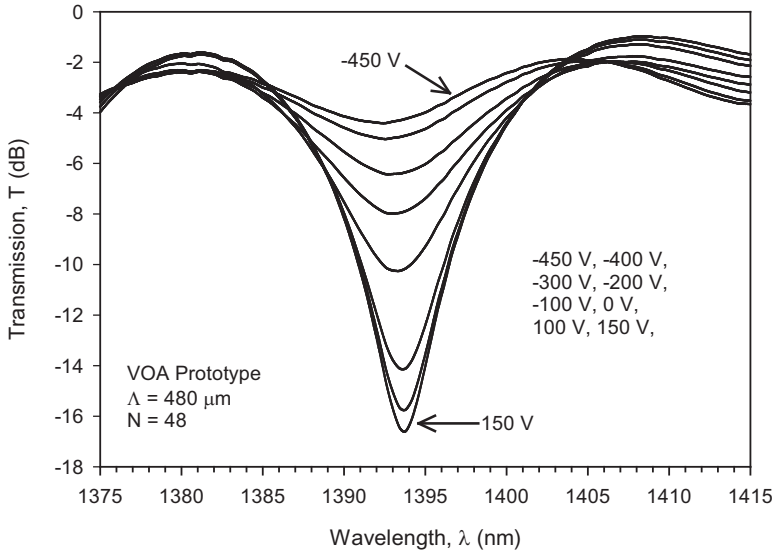

Figure 5.3: Transmission spectra at various applied voltage levels of a prototype CO_2-laser-induced LPFG VOA device (LPFG 11200204) [6].

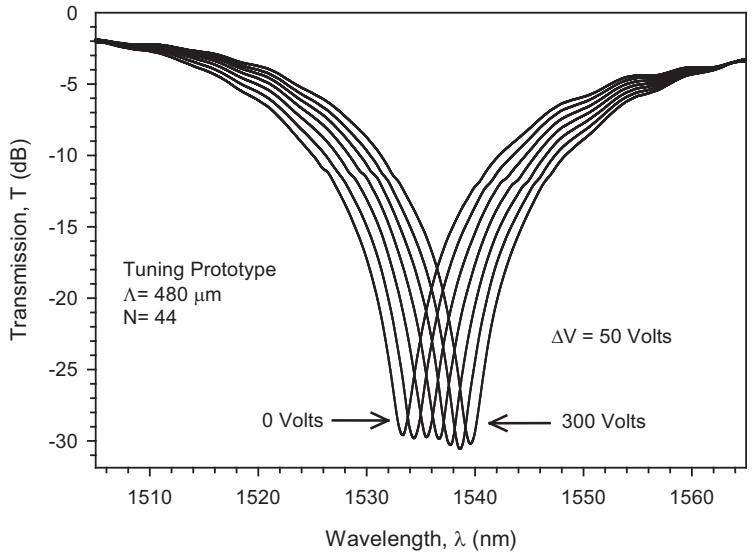

Figure 5.4: Transmission spectra at various applied voltage levels of a prototype CO_2-laser-induced LPFG OTF device (LPFG 07090208) [6].

5.2 Optical-Fiber-to-Waveguide Directional Coupler

Optical interconnects show significant promise for enabling high-speed input/output in future microelectronics systems. Applications of optical interconnects currently being developed include optical clock distribution and high-speed communication between systems [98–100]. Optical fibers are expected to play a role in chip-level and board-level optical interconnects. Efficient coupling of light from optical fibers to chip-level and board-level waveguides will be necessary.

A number of different configurations have been investigated for accomplishing the required fiber-to-waveguide coupling. High efficiency was achieved for fiber endface-to-waveguide coupling using D-shaped optical fiber positioned in specially designed alignment ways [101]. Compact nanotapers, functioning as mode converters, have been used to couple light from optical fibers to silicon waveguides and photonic crystals [102]. Diffractive optical elements (DOEs) can also be used to couple light emerging from fibers into waveguides [103]. While relatively high coupling efficiencies have been reported for nanotaper- and DOE-based couplers, most of the configurations mentioned still require precise alignment of the fiber endface and coupler device to avoid extraneous insertion losses. Most of the configurations also require additional or special fabrication steps to create the integrated coupling devices. There are several advantages to using a coupling device intrinsic to an optical fiber and which does not require access to fiber or waveguide endfaces. Such a coupler would be well suited for enabling direct optical fiber interconnects and for optical interconnect prototyping and research.

Fiber gratings are one type of intrinsic device that can be used for coupling light into and out of optical structures. It has been proposed that tilted fiber gratings be used to perform coupling [104]. In addition, LPFGs can be used. Typical LPFGs couple light from core-guided modes to cladding-guided modes near specific resonant wavelengths. The cladding mode coupling function of LPFGs can be used to couple light into other fibers or waveguides.

The index asymmetry present in CO_2-laser-induced LPFGs permits coupling to azimuthally asymmetric cladding modes [105] and such modes could produce preferential (directional) outcoupling. While preferential outcoupling has not been proven experimentally, an indication of the phenomenon is seen in Fig. 5.5. The line-profile of the cladding-mode intensity pattern suggests an asymmetric intensity pattern. However, the observed intensity pattern asymmetry may be due to inadvertent absorption or scattering by oil or debris (on the side or endface of the fiber) instead of following from the CO_2-laser-induced LPFG index profile. Experimental proof of directional coupling in CO_2-laser-induced LPFGs requires measurement of light emerging from the side of the fiber along the length of the grating region and around the circumference (azimuthal dependence). The required measurement would be similar to one conducted recently on FBGs [106].

With multiple LPFGs existing in a given optical fiber segment, light can even be coupled between different waveguides on separate boards [107]. Possible uses for CO_2-laser-induced LPFG-based couplers in optical interconnect systems are shown in Fig. 5.6.

With the potential advantages described, an LPFG-based fiber-to-waveguide coupler would be a useful device for optical interconnect systems. LPFG-based couplers have been demonstrated previously, but primarily for achieving coupling between two parallel fibers, for coupling between two fiber endfaces, and for coupling between a laser diode and a fiber (using a micro-lens) [32, 33, 108]. In this section, the first experimental demonstration of optical-fiber-to-waveguide coupling using a CO_2-laser-induced LPFG is presented. Many different formats for an LPFG-based coupler are possible, but the particular configuration presented here has the format shown in Fig. 5.7 and acts as a directional coupler. After briefly describing the coupler operation, fabrication, and characterization apparatus, the role of the LPFG in performing coupling is demonstrated and the wavelength-dependence of the coupling illustrated.

For the form of the CO_2-laser-induced LPFG-based fiber-to-waveguide coupler shown in Fig. 5.7, light in the core of the LPFG is coupled to a cladding mode and a portion of the light in the cladding mode is then coupled into the channel waveguide [109]. For the simple CO_2-laser-induced LPFGs considered here (Chapter 2) and because of the different

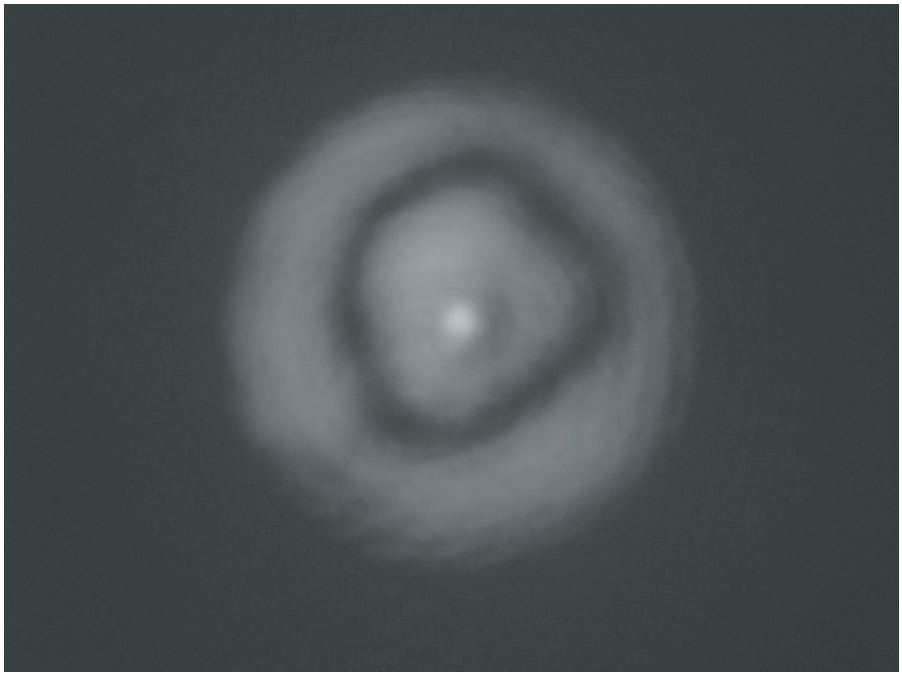

(a)

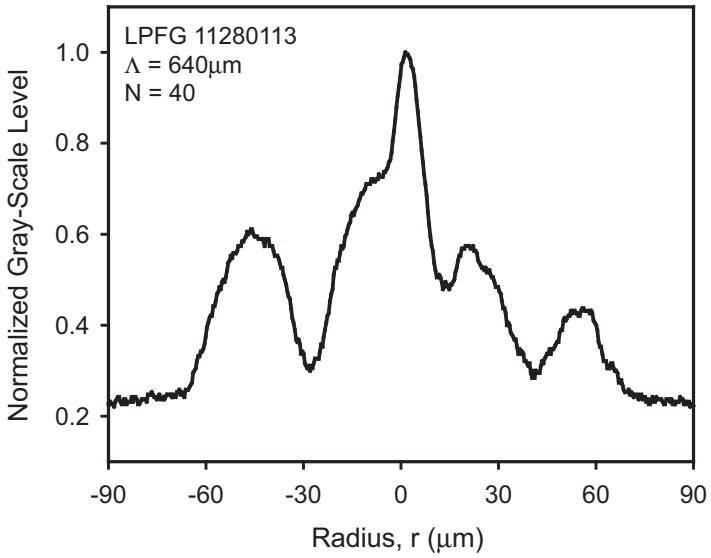

(b)

Figure 5.5: (a) Image of cladding mode emerging from a cleaved optical fiber endface (b) Horizontal line-profile of cladding mode taken through the center of the pattern. The wavelength of the laser source is $1543nm$

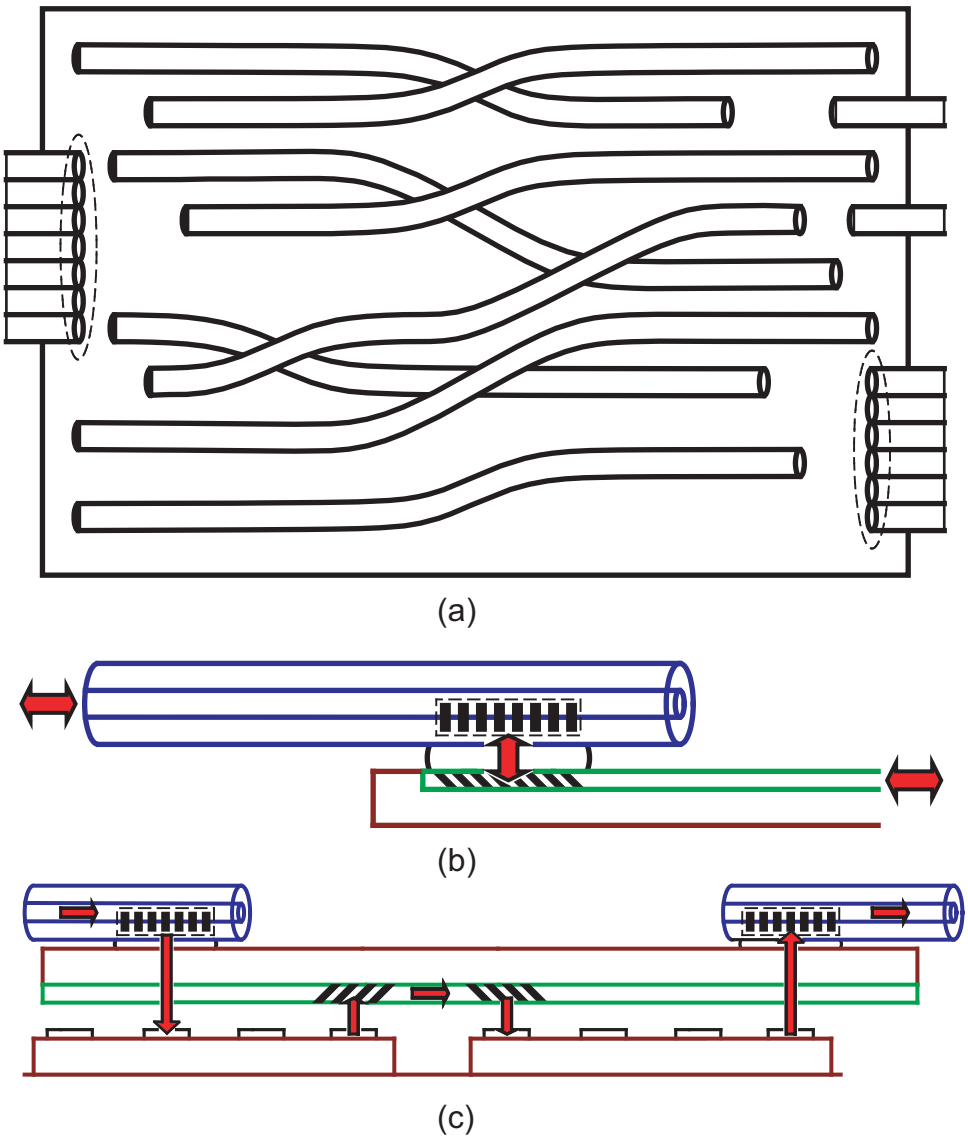

Figure 5.6: Potential uses for CO_2-laser-induced LPFG-based couplers in optical interconnects: (a) optical interconnect plane, (b) fiber-to-waveguide coupler (c) multi-chip coupling.

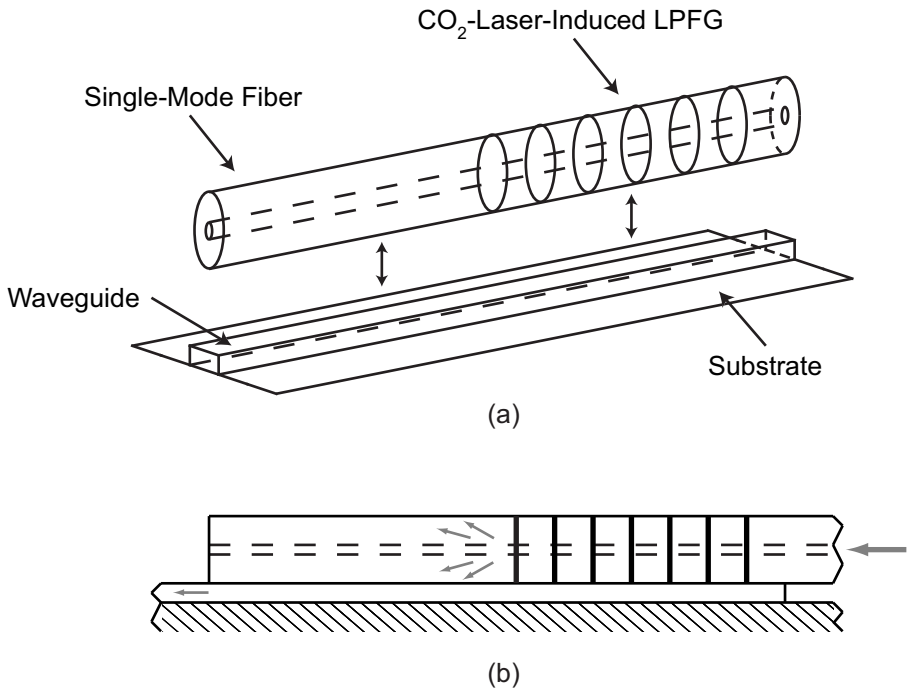

Figure 5.7: (a) Diagram of one possible type of LPFG-based fiber-to-waveguide coupler. (b) Side view showing coupling of light from fiber core to cladding. A portion of the cladding-guided light is then coupled into the channel waveguide. For this particular arrangement, the LPFG performs as a directional coupler.

dimensions and shape of the optical fiber and waveguide, only a small portion of the light from the cladding mode is coupled into the waveguide. Although the coupling efficiency is anticipated to be relatively low, a coupler of this form is simple to implement. The actual amount of light coupled to the waveguide depends upon the cladding-mode pattern, LPFG coupling strength, fiber/waveguide interaction length, and additional factors.

5.2.1 Simulations and Simulation Results

To examine the performance of the directional coupler shown in Fig. 5.7 and to evaluate potential waveguide dimensions and properties, a series of basic simulations of a portion of the coupler were conducted using the three-dimensional beam propagation method (BPM) [110, 111]. The BPM simulations were conducted using OptiBPM commercial software [112]. Based on the simulation results, the dimensions of the waveguide were selected so as to ensure light coupled into the waveguide from the LPFG/fiber could be observed with available instruments.

In conducting the simulations using BPM, a number of assumptions are made regarding the coupler components. The properties and dimensions of Corning SMF-28 single-mode optical fiber are used for representing the optical fiber in the simulation. The waveguide material is assumed to be polymer-based and the waveguides themselves are assumed to be fabricated on top of an oxide layer (grown on a silicon substrate) and surrounded by air. Similar waveguides are currently being used in optical interconnect research [113]. Most significantly, only the beam propagation along a portion of the fiber-waveguide interaction length is considered. Simulations were conducted for propagation over a $4mm$ length along the coupler after the last period of the LPFG. With this restriction, it is assumed that a well defined cladding mode exists at the end of the grating and the cladding mode of the optical fiber can serve as the input field for the simulation. Use of a cladding mode emerging from the LPFG as an input to the simulation, of course, does not take into account any coupling that occurs in the waveguide region where the grating is present. However, rather complex modeling is required to simulate correctly the grating/waveguide interaction. The primary purpose of the simulations was to verify expected waveguide behavior and to assist in selecting suitable waveguide dimensions to enable observation of coupled light for the experiments. As such, the assumptions made in conducting the simulations are appropriate.

A cross-section of the coupler, shown in Fig. 5.8, is the structure used for conducting the simulations. The simulation dimensions and properties are listed in Table 5.1 while the BPM computation parameters are given in Table 5.2. The input cladding mode, identified and calculated using the mode solver feature of the software, is launched into the optical fiber and propagates in the fiber alone for $100\mu m$ before the start of the waveguide and substrate.

BPM simulations were conducted for various waveguides heights, cladding mode shapes, and polarization states, as summarized in Table 5.3. Example simulation results are shown for the case of a $6\mu m$ waveguide height, an LP_{04} input cladding mode, and scalar polarization in Fig. 5.9, 5.10, and 5.11. To emphasize the light coupled into the waveguide, the field amplitude in each plot is truncated at a certain level. Example coupler simulation results are shown in Table 5.4.

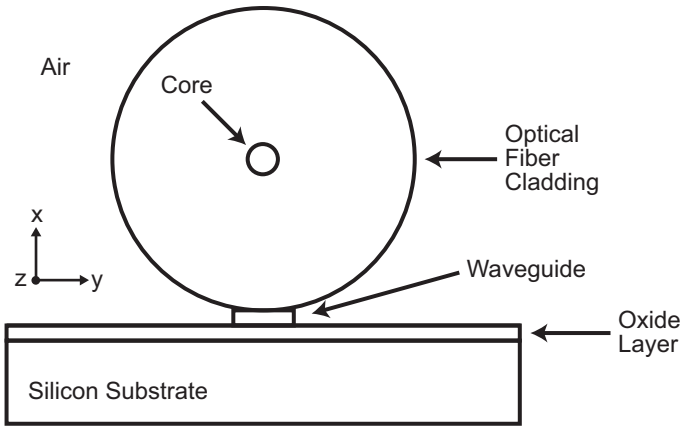

Figure 5.8: Optical-fiber-to-waveguide coupler simulation cross-section. The optical fiber and waveguide are assumed to be surrounded by air. The index matching gel (not shown) rests on top of the waveguide, has the same width as the waveguide, extends into the fiber cladding, and has the same refractive index as the cladding.

Table 5.1: Coupler Simulation Cross-Section Dimensions and Properties (for $\lambda = 1550nm$).

	Refractive Index	Length [μm]	Width [μm]	Height [μm]
Si Substrate	3.478	3900	300	98
SiO_2 Layer	1.458	3900	300	2
Polymer Waveguide	1.500	3900	25	variable
Index Matching Gel	1.458	3900	25	25
Optical Fiber Cladding	1.458	4000	125 (diameter)	-
Optical Fiber Core	1.4631	4000	8.3 (diameter)	-

Table 5.2: BPM Computation Parameters

Propagation Step	$3\mu m$
Mesh Size	3 points/μm
Wavelength	$1550nm$
Computation Dimensions	$4000 \times 300 \times 340\mu m$

Table 5.3: Parameters Varied During Coupler Simulations.

Waveguide Heights [μm]	2.5, 3.5, 6, 25
Cladding-Mode Patterns	LP_{01} (core-guided mode), LP_{02}, LP_{04}
Polarization	scalar, TE, TM

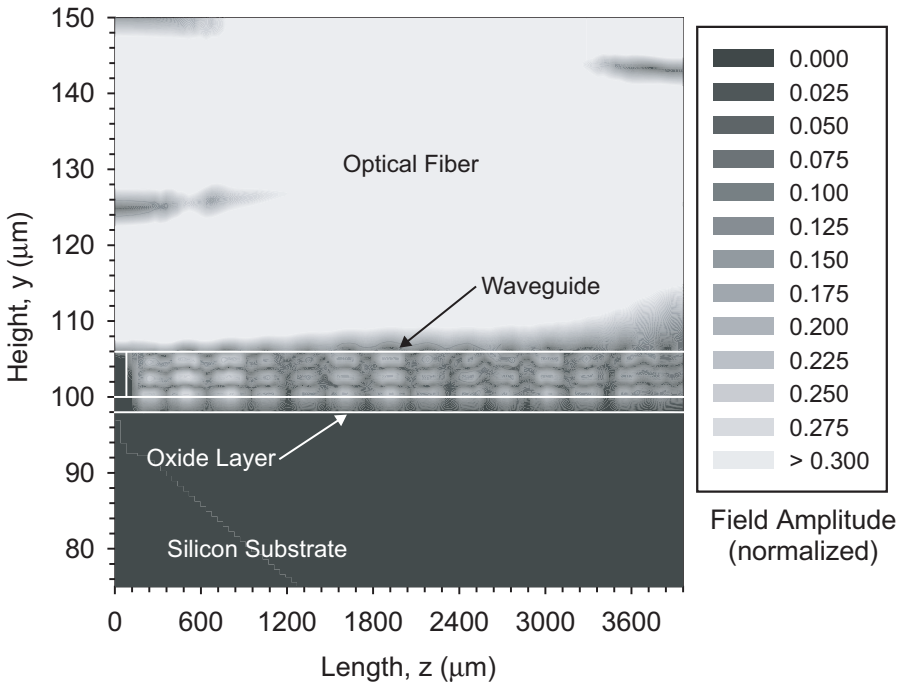

Figure 5.9: Example coupler simulation results for the yz-plane at $x = 0\mu m$ (vertical slice through the center).

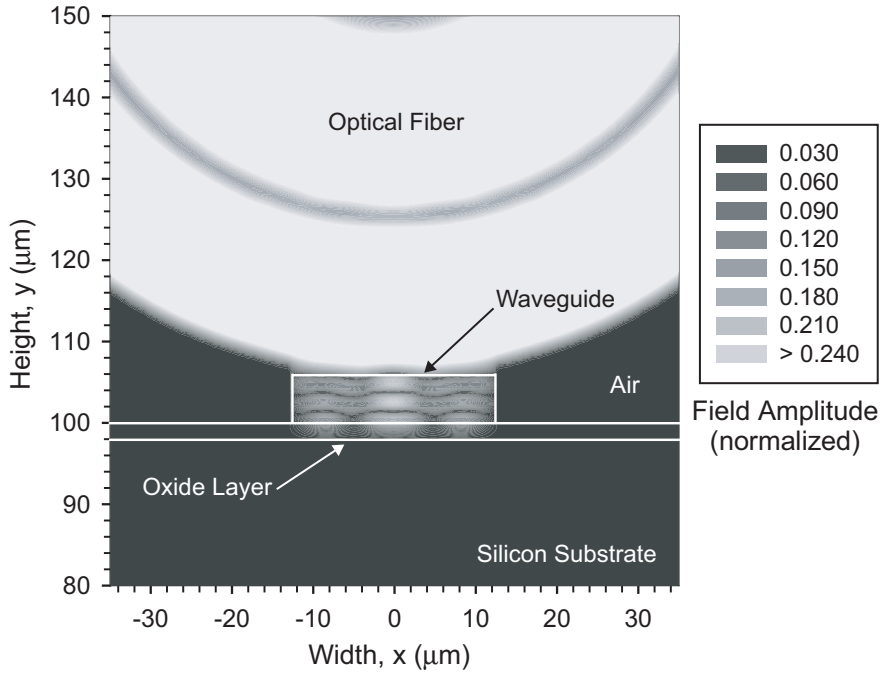

Figure 5.10: Example coupler simulation results for the xy-plane at $z = 444\mu m$ (longitudinal slice).

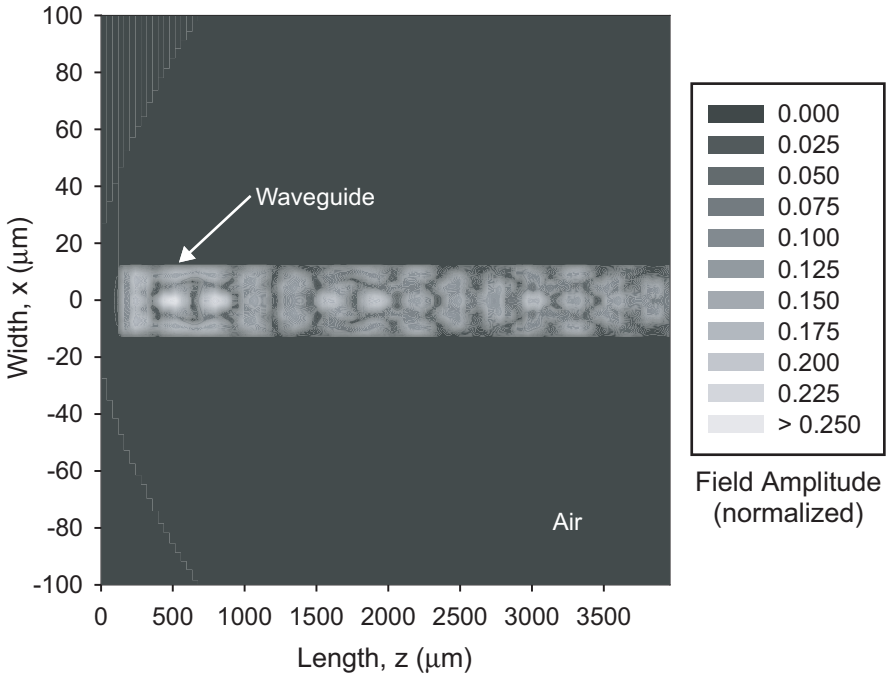

Figure 5.11: Example coupler simulation results for the xz-plane at $y = 103\mu m$ (horizontal slice through waveguide center).

Table 5.4: Example Coupler Simulation Results

Waveguide Height	Cladding-Mode Pattern	Field Amplitude in Waveguide Region	
$[\mu m]$	(effective index)	z = $2000\mu m$	z = $4000\mu m$
6	LP_{02} (1.45794437)	0.022	0.019
6	LP_{04} (1.45750568)	0.054	0.038
25	LP_{02} (1.45794437)	0.027	0.039

As expected, the overall level of light coupled into the waveguide is significantly lower than the light present in the optical fiber for the waveguide dimensions considered during simulation. Also, as can be predicted from planar slab waveguide theory, the taller height waveguides support more modes ($6\mu m$-tall waveguides support approximately the first three modes for the parameters given in Table 5.1). Several additional conclusions were reached after considering all of the various simulated cases:

1. No significant differences were observed in the amount of light coupled to the channel waveguide for scalar, transverse electric (TE), and transverse magnetic (TM) polarization cases,

2. More light was coupled into the waveguide for the LP_{04} cladding mode, most likely due to the mode's larger evanescent tail,

3. Two-layer waveguide (polymer waveguide in combination with the $2\mu m$-thick oxide layer) behavior occurs for shorter waveguide heights (less than $6\mu m$).

4. The amount of light coupled into the waveguide is too small to observe with an vidicon near-infrared (NIR) camera if coupling gel is not used. The low level of light coupled into the waveguide is due to the small interaction area (over the cross-section in the xy-plane) between the rectangular waveguide and the circular fiber. Detection of light coupled into the waveguide necessitates the use of index coupling gel.

After examining the simulation results, a height of $6\mu m$ was selected for the waveguides. The amount of light coupled into the waveguides for this height was thought to be sufficient for detection using a near-infrared camera and the same height is used in other optical interconnect research.

5.2.2 Coupler and Waveguide Fabrication

For the device demonstration, it is necessary to fabricate both the CO_2-laser-induced LPFG used to perform the coupling and the waveguide into which light is coupled. The coupler is designed to operate near a wavelength of $1550nm$ in order to utilize existing test and measurement instruments.

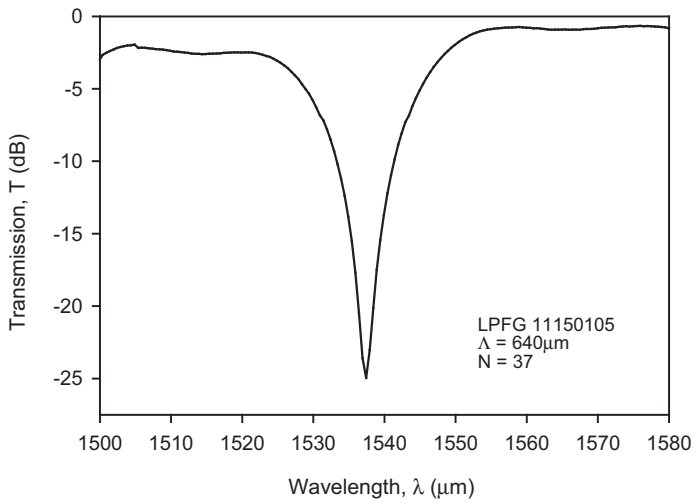

Figure 5.12: Transmission spectrum of CO_2-laser-induced LPFG used to perform coupling. The grating resonant wavelength in this region is near $1537nm$.

The CO_2-laser-induced LPFG has a period (Λ) of $640\mu m$ with 37 total periods. The combination of period spacing and number of periods yields an LPFG approximately $23.7mm$ in length. The optical fiber containing the LPFG is prepared for use by removing any buffer material on the fiber within $38mm$ from the first period of the grating. The fiber is then cleaved at the end of the uncoated section away from the grating (to facilitate positioning on the waveguide).

The waveguide into which light is coupled from the optical fiber is fabricated from Avatrel 2190P photopolymer [114] on top of a $2\mu m$ oxide layer grown on a silicon substrate [113]. Air serves as the cladding-layer of the waveguide (away from the optical fiber/waveguide interface) while the oxide layer on the silicon acts as the substrate-layer. The waveguide dimensions are $6\mu m$ high by $100\mu m$ wide, as shown in Fig. 5.13, with an overall length of $38mm$. At a wavelength of $1550nm$, the refractive index of the polymer is approximately 1.50 while that of the oxide layer is approximately 1.46. For the wavelength, waveguide dimensions, and refractive-index values given, the waveguide supports the first two to three modes in the vertical ($6\mu m$ height) direction and is multimodal in the horizontal direction. Thus, it is expected that profile of the light emerging from the waveguide endface will be primarily Gaussian-like along the vertical direction but will contain many nulls and peaks along the horizontal direction.

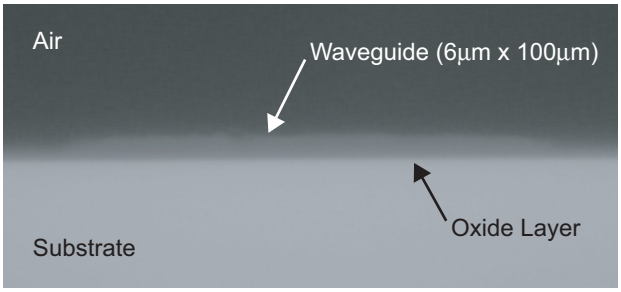

Figure 5.13: Reflected-light image of the cleaved waveguide endface region.

To prepare the waveguide for characterization, the substrate is cleaved to produce a smooth waveguide endface. The stripped section of the optical fiber is cleaned with isopropyl alcohol and lens tissues in order to remove any oil or debris. Several thin layers of black acrylic paint are applied to the cleaved endface of the optical fiber by touching the endface to a pool of the paint; the thin coating of paint prevents light that remains in the cladding mode (not coupled into the waveguide) from exiting the fiber and saturating the camera, as saturation prevents the lower levels of light emerging from the waveguide to be observed. The channel waveguide and optical fiber are then positioned in the coupler characterization apparatus.

5.2.3 Coupler Characterization Apparatus

To observe coupling of light from the optical fiber to the waveguide, the coupler is assembled on an optical fiber endface characterization apparatus. The waveguide is secured on top of a three-axis linear stage and the waveguide endface positioned at the focal plane of an endface inspection microscope (with a 20× objective), as shown in Fig. 5.14. The optical fiber containing the CO_2-laser-induced LPFG is inserted into a fiber positioner and then aligned over the waveguide with the aid of a long-working distance (LWD) microscope located over the substrate. Several images of the optical fiber lying on the waveguide, taken with a camera on the long-working distance microscope, are shown in Fig. 5.15. A small amount of index matching gel (with a refractive index of approximately 1.46) is applied to the bottom surface of the optical fiber over the entire $38mm$ length (to enhance coupling) before the fiber is lowered into contact with the waveguide. The optical fiber containing

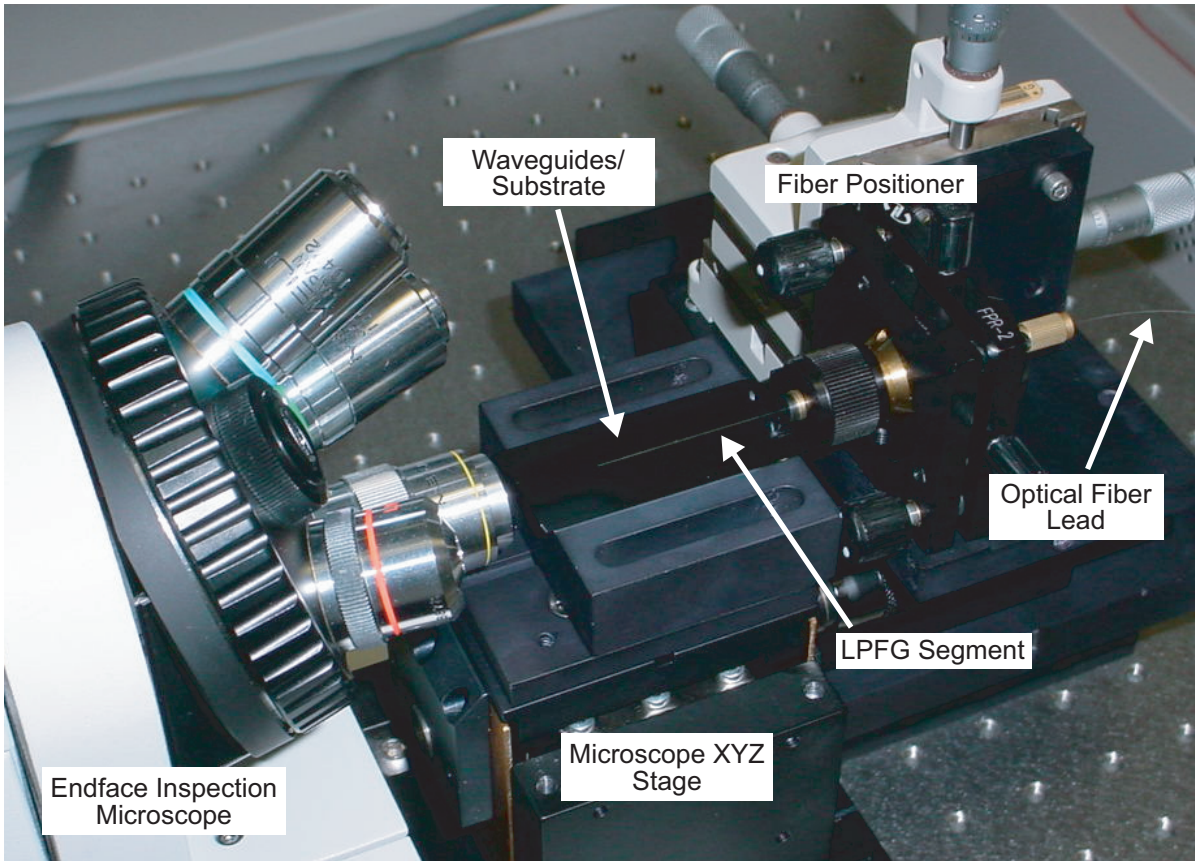

Figure 5.14: Photograph of the coupler characterization apparatus.

the LPFG and the waveguide are in contact (parallel) over most of the waveguide length, with the first period of the grating close to the start of the waveguide and the optical fiber ending $3mm$ before the waveguide endface.

With the coupler assembled on the characterization apparatus, a tunable laser source is connected to the optical fiber lead located away from the waveguide. Use of the tunable laser source enables the wavelength response of the coupler to be measured. The light from the laser is randomly polarized. Light emerging from the waveguide endface is observed using the endface inspection microscope in conjunction with a vidicon NIR camera. Images from the camera are captured using a frame-grabber card and stored for subsequent examination. Figure 5.16 shows a diagram of the overall characterization apparatus and an example of an image captured from the waveguide endface is given in Fig. 5.17.

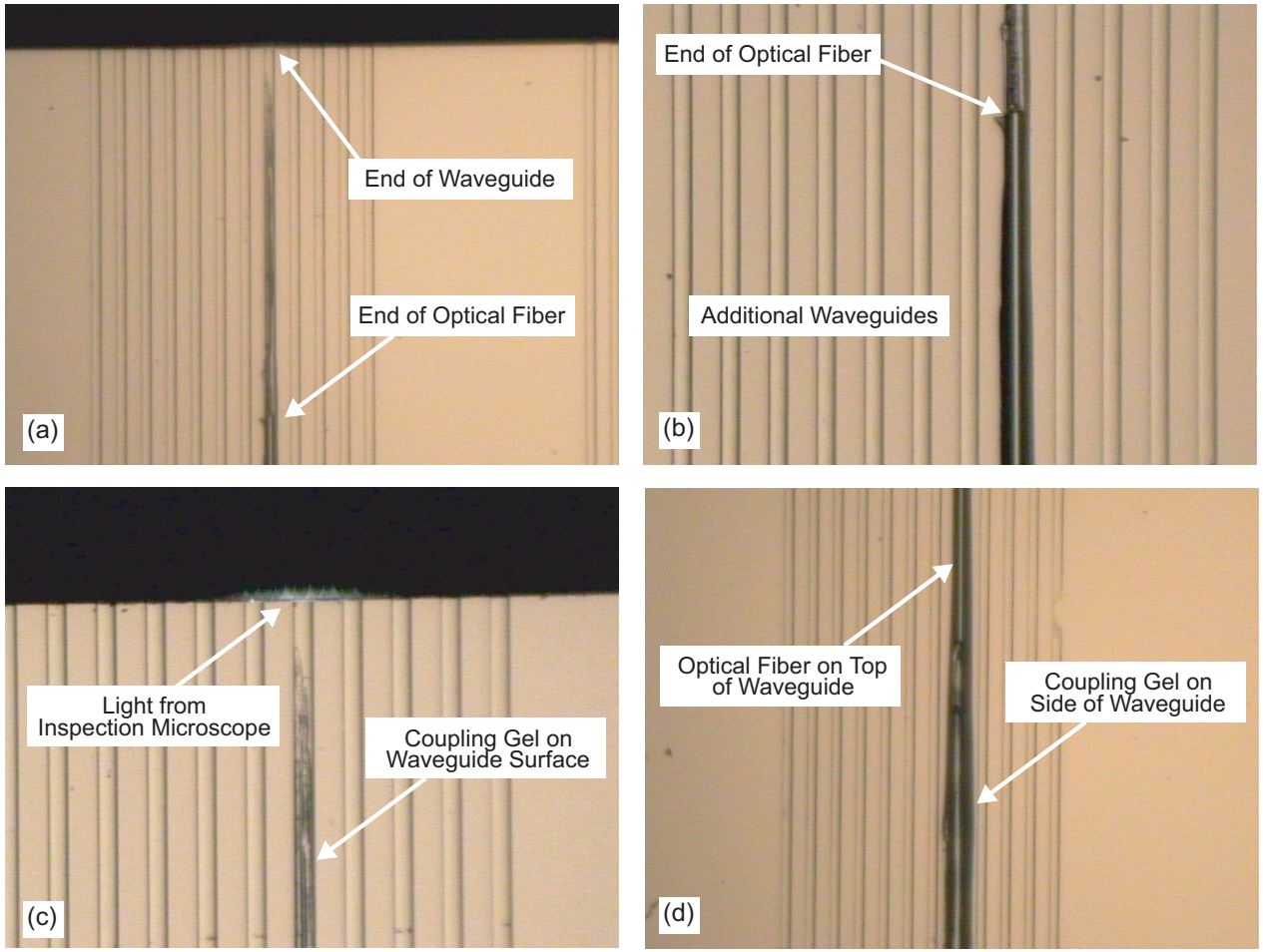

Figure 5.15: Images of the waveguide and optical fiber (coupler) taken from above with a long-working distance microscope/camera.

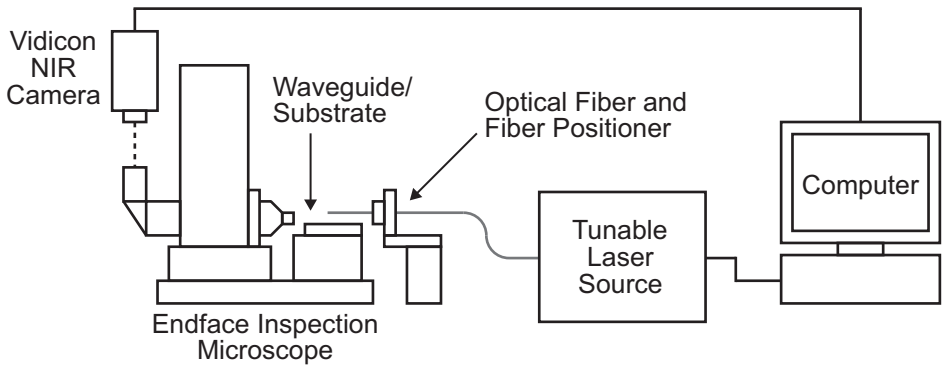

Figure 5.16: Diagram of the coupler characterization apparatus. The long-working distance microscope (positioned over the waveguides/substrate) is not shown.

5.2.4 Coupler Performance

To demonstrate the effect of the CO_2-laser-induced LPFG, the light emerging from the waveguide endface was observed for an optical fiber without an LPFG and for a fiber containing the LPFG [109]. Example resulting images of the waveguide region are shown in Fig. 5.18. No light is coupled into the channel waveguide for the optical fiber without an LPFG while light is clearly observed emerging from the waveguide endface for the fiber containing the CO_2-laser-induced LPFG, thus indicating that coupling occurs. The images are normalized to the peak observed gray-scale level after subtracting background light levels. From the comparison of the images in Fig. 5.18, it is evident the LPFG performs as a coupler. The coupling efficiency is estimated to be between 1% and 10% for this initial configuration.

Light observed in the LPFG case is also clearly confined to the $6\mu m$ high by $100\mu m$ wide waveguide region. As anticipated from slab waveguide theory, the light in the waveguide is highly multimodal in the horizontal direction but approaches single-mode operation in the vertical direction. Vertical and horizontal line-profiles from the waveguide endface region are shown in Fig. 5.19 and Fig. 5.20, respectively.

Attempts were made to observe any light coupled into the waveguide from the fiber for the case that coupling gel was not used. However, as discussed in the simulation section, any light coupled into the waveguide could not be observed with the available NIR camera.

The wavelength response of the LPFG-based optical-fiber-to-waveguide coupler was also

Figure 5.17: Image of light emerging from waveguide endface for a source wavelength of $1540nm$. The image is 640 by 480 pixels.

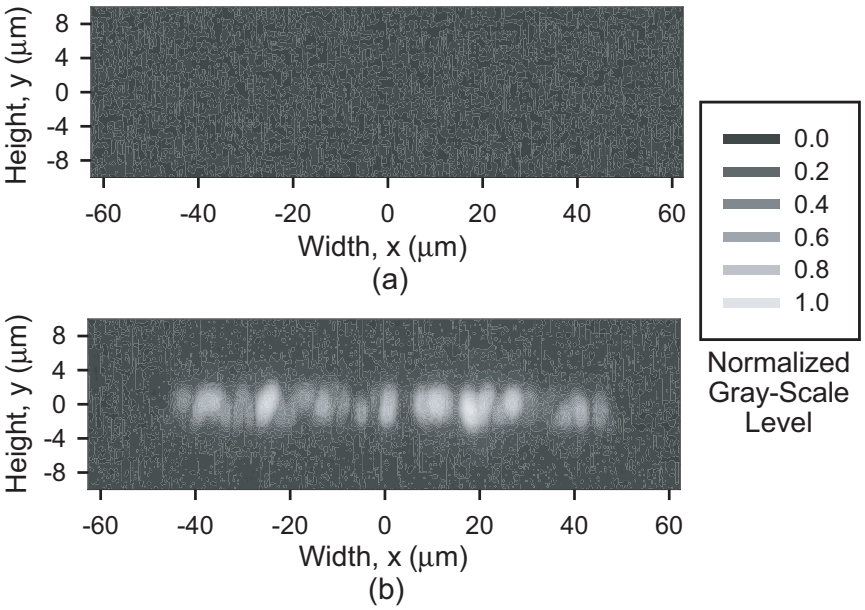

Figure 5.18: Light observed emerging from the waveguide endface for an optical fiber positioned on top of the waveguide (a) without an LPFG and (b) with a CO_2-laser-induced LPFG. The laser source wavelength is $1540nm$.

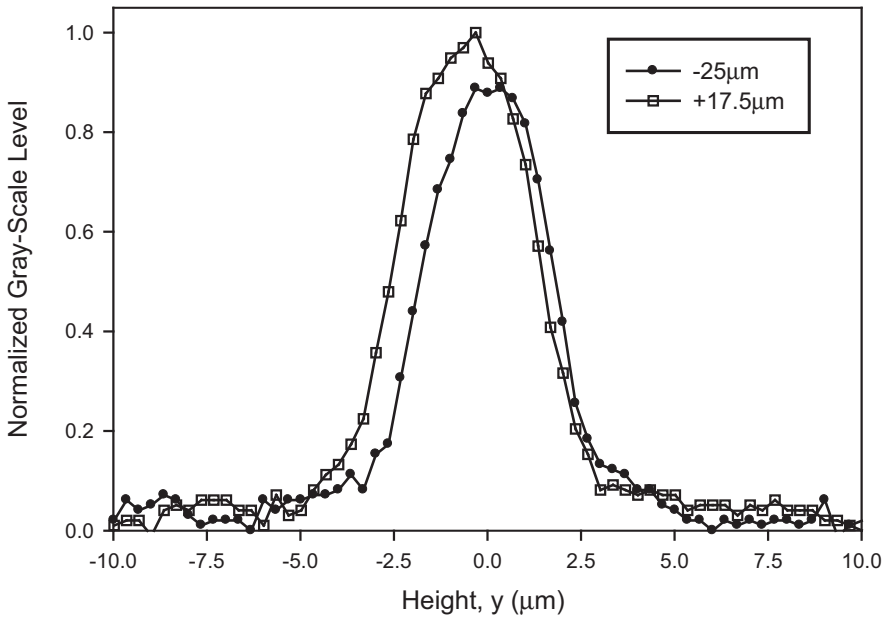

Figure 5.19: Line-profile plots of light in waveguide region [from Fig. 5.18(b)] along the vertical direction at two different horizontal locations.

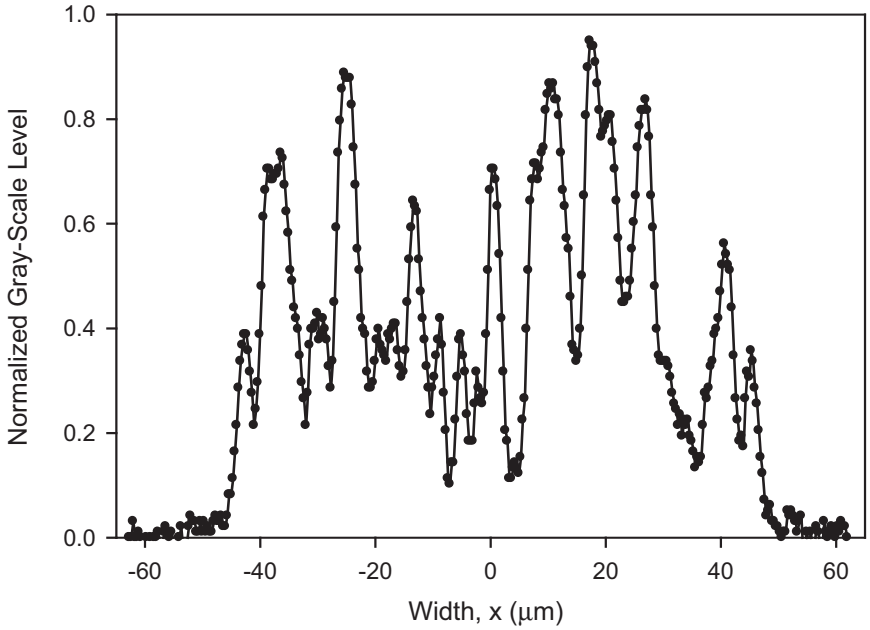

Figure 5.20: Line-profile plot of light in waveguide region [from Fig. 5.18(b)] along the horizontal direction through the center of the waveguide ($y = 0$).

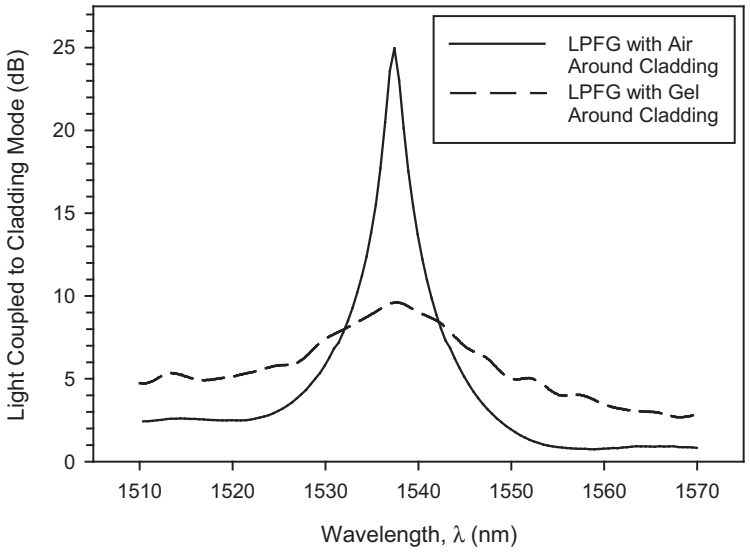

Figure 5.21: Cladding mode coupling spectra for a CO_2-laser-induced LPFG surrounded by air index matching gel (solid line versus dashed line). Broadening of the coupler bandwidth occurs due to the presence of gel on the LPFG

measured [109]. In considering the wavelength response of the coupler, it is necessary to examine the effect of the coupling gel on the CO_2-laser-induced LPFG transmission spectrum. The resonant wavelength and associated transmission characteristics (bandwidth, attenuation at resonance) for a given cladding mode of an LPFG change if the refractive index of the material surrounding the cladding changes [115]. An example of this effect is shown in Fig. 5.21, where the transmission spectrum near a particular cladding mode is plotted for the (typical) circumstance of air surrounding the fiber cladding in the grating region versus gel surrounding the cladding (LPFG on a waveguide). Significant broadening of the spectral bandwidth, along with a decrease in attenuation, occurs when the LPFG is coated with the gel. Thus, the wavelength response of the coupler follows the pattern shown in Fig. 5.21 for the LPFG coated with gel.

The normalized summation of image gray-scale values over the waveguide region for fourteen test wavelengths are plotted in Fig. 5.22, with example patterns for two of the wavelengths shown in Fig. 5.23. The light coupled into the waveguide from the LPFG decreases as the source wavelength changes away from the grating resonant wavelength, as follows the LPFG cladding mode coupling wavelength spectrum (also shown in Fig. 5.22). However, the light coupled to the waveguide does not decrease as rapidly as the spectrum

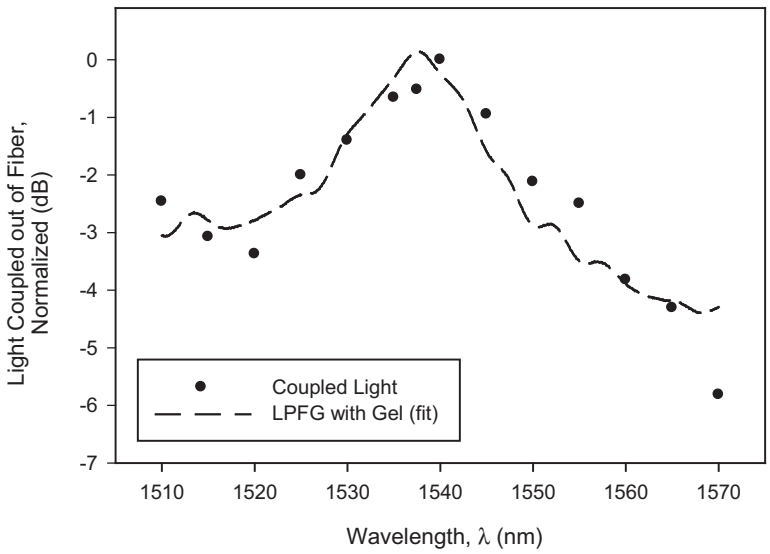

Figure 5.22: Normalized summation of image gray-scale values for each test wavelength over the waveguide region (solid circles) along with a fitted coupling spectrum for an LPFG surrounded by index matching gel (dashed line).

measured for the LPFG when surrounded by air. Broadening of the coupler bandwidth occurs due to the presence of the index matching gel on the surface of the fiber along the region containing the grating; the presence of the gel also explains the slight shift in resonant wavelength. The effect of the gel on the LPFG coupling spectrum is illustrated by the fitted cladding mode coupling curve in Fig. 5.22. The fitted coupling curve was obtained by adjusting the amplitude and bias of the associated curve from Fig. 5.21 using a least-squares approach. Also evident in the wavelength response measured for the coupler is the increase in light levels at shorter wavelengths (near $1510nm$). The increase is due to another cladding mode resonance present at a shorter wavelength.

5.3 Summary

In this chapter, devices for performing variable optical attenuation, optical tunable filtering, and optical-fiber-to-waveguide coupling using CO_2-laser-induced LPFGs have been described. Prototype variable optical attenuator and optical tunable filter devices based on controlled flexure of CO_2-laser-induced LPFGs were presented. The devices employ voltage-dependent piezoceramic bending actuators to perform flexure. Example tuning results for several devices were given.

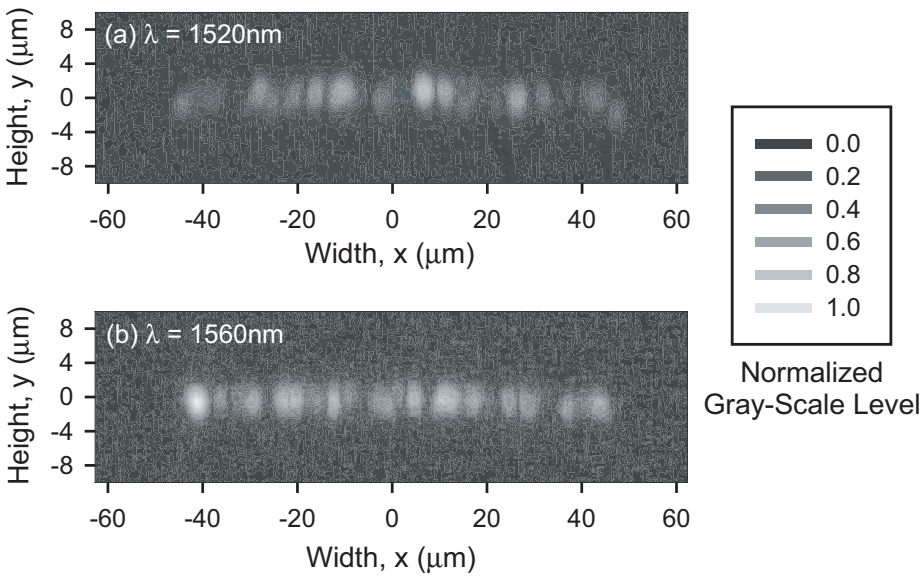

Figure 5.23: Light observed emerging from the waveguide endface for different source wavelengths: (a) $\lambda = 1520nm$ and (b) $\lambda = 1560nm$.

Optical-fiber-to-waveguide coupling using a CO_2-laser-induced LPFG has been demonstrated and the wavelength dependence of the coupler has been measured. The demonstrated device does not require access to fiber or waveguide endfaces to perform coupling and the observed wavelength-dependent coupling would be valuable for interconnect systems employing coarse wavelength-division multiplexing. The particular LPFG-based coupler demonstrated here performs directional coupling. Other implementations (such as incorporating a CO_2-laser-induced LPFG in a D-shaped optical fiber) may have additional efficiencies.

The devices discussed in the chapter and their associated applications highlight areas where the asymmetric refractive-index profile present in CO_2-laser-induced LPFGs confers certain advantages. In the case of optical tunable filters and variable optical attenuators based on flexure of CO_2-laser-induced LPFGs, the corresponding wavelength tuning and variable attenuation tuning are not possible without the asymmetry. For the coupler, the presence of the azimuthally asymmetric refractive-index profile could produce directional/preferential coupling. Bend sensing and polarization-dependent loss compensation are additional applications areas where such asymmetry may be beneficial.

CHAPTER 6

CROSS-SECTIONAL REFRACTIVE-INDEX PROFILE MEASUREMENTS

Some of the consequences arising from the azimuthally asymmetric refractive-index profile present in carbon-dioxide-laser-induced long-period fiber gratings (CO_2-laser-induced LPFGs) have been examined in the previous chapters. The impact of asymmetry on LPFG polarization-dependent transmission characteristics was examined in Chapter 3 while Chapter 4 discussed the impact of asymmetry on LPFG response to flexure and torsion. The asymmetry significantly influences the performance of CO_2-laser-induced LPFGs and can be used to create useful fiber-based devices like variable optical attenuators, optical tunable filters, and couplers, as seen in Chapter 5. To enhance and improve further the performance of such devices, it is necessary to model the effects of the index asymmetry. However, suitable modeling techniques, including modified coupled-mode theory, require accurate knowledge of the transverse cross-sectional refractive-index profile of the LPFGs before modeling can accurately reproduce and predict performance.

Numerous techniques exist for measuring refractive-index profiles of optical fibers and fiber devices. However, many of these techniques require the assumption that the fiber being profiled is azimuthally symmetric. For example, traditional transverse interferometric profiling, while non-destructive, assumes azimuthal symmetry when characterizing optical fibers [116, 117]. Similarly, index profiling using the focusing method yields accurate one-dimensional profiles only for azimuthally symmetric fibers [118]. A differential interference contrast-based profile measurement technique, as recently reported, also assumes symmetry [119]. The implicit assumption of azimuthal symmetry prevents these techniques from being used to characterize irregular, asymmetric index variations existing in the cross-sections of optical fibers.

Additional profiling techniques have been developed for characterizing asymmetry in

optical fiber index profiles. Etching combined with atomic force microscopy provides topographical detail over small regions, but quantitative interpretation requires calibration and the etching process is destructive [120, 121]. A variation on the refracted-near-field scanner can measure two-dimensional index profiles, but also requires access to an endface and is therefore destructive [122, 123]. Several basic (one-dimensional) profiling techniques have been combined with computed tomography to permit non-destructive measurement of asymmetric index profiles. Profiling of optical fibers in combination with tomography has been demonstrated using the focusing method, multidirectional scattering-pattern, and quantitative phase microscopy approaches [58, 124, 125]. While these combined techniques are effective for profiling typical optical fiber and are non-destructive, they can lack sufficient resolution to detect small, irregular variations in fiber profiles, such as those created by one-sided exposure to CO_2 laser light (typically on the level of $1x10^{-4}$ [2]). The ability of several example refractive-index profiling techniques to meet the criteria required for accurate profiling of CO_2-laser-induced LPFG are listed in Table 6.1. Considering the need to measure accurately small and irregular index variations present in CO_2-laser-induced LPFGs and the currently available profiling techniques, there is a need for a non-destructive measurement technique that permits high resolution, high accuracy measurements of small, asymmetric variations in the refractive-index profiles. The technique must be capable of measuring both small index variations and characterizing asymmetric index profiles.

This chapter describes efforts to measure the transverse cross-sectional refractive-index profile of CO_2-laser-induced LPFGs. A new profiling technique, microinterferometric optical phase tomography (MIOPT), was developed to address the special requirements of measuring small and asymmetric refractive-index differences, such as those present in CO_2-laser-induced LPFGs. The new technique is described in Sec. 6.1. Experimental validation of the new technique is achieved through measurements of both azimuthally asymmetric and symmetric optical fibers and the technique is then used to profile a CO_2-laser-induced LPFG. The profile measurements are presented in Sec. 6.2.

Table 6.1: Ability of Example Refractive-Index Profiling Techniques to Meet Requirements for Accurate Profiling of CO_2-Laser-Induced LPFGs

Refractive-Index Profiling Technique	Capable of Measuring Small Index Differences?	Capable of Measuring Asymmetric Index Profiles?
Refractive Near-Field [122]	No	Yes(?)
Quantitative Phase Microscopy [58]	No	Yes
Axial Interferometry [126, 127]	No	Yes(?)
Transverse Interferometry [128]	Yes	No

6.1 Development of a New Index Profiling Technique

In this section, the MIOPT technique is developed and its value in measuring small, asymmetric refractive-index differences (about $1x10^{-4}$) in the transverse cross-sectional profiles of LPFGs established [129]. The method combines microscopy-based fringe-field interferometry with parallel projection-based computed tomography to characterize refractive-index profiles. The theory relating interference measurements to the projection set required for tomographic reconstruction is given and numerical simulations are presented for three test index profiles that establish the technique's ability to characterize fiber with small and asymmetric index differences.

Interferometry and tomography have been combined for index profiling measurements of optical fibers in two previous efforts, neither of which focused primarily on detecting small and asymmetric index variations. The first effort involved characterizing graded-index waveguides that possessed known profile forms (power law) and in which significant ray refraction occured over sample cross-sections [130]. The significant levels of ray refraction can be attributed to relatively large refractive-index gradients present in graded-index fibers. The second effort, by Górski, involved profiling optical fibers under conditions of relatively large index differences (greater than 0.015) between fiber cladding and surrounding matching oil [131]. Under such conditions, it becomes difficult to characterize small index

changes over an entire cross-section due to, in part, enhanced diffraction effects. Simulations and measurements, using a bulk interferometer system, for a symmetric multi-mode optical fiber were conducted.

The measurement approach described in this section is concerned with characterizing small index variations (about $1\text{x}10^{-4}$) in small objects (about $125\mu m$ diameter). As such, a number of additions and alterations can be made to the combined interferometry and tomography methodology to enhance detection of small index variations. The presence of only small index differences over a cross-sectional profile allows the use of a ray-based, no deviation formulation that is compatible with established parallel projection computed tomography. Use of commercial interference microscopes to conduct measurements enables control and optimization of interference images to enhance detection of small index differences. Developed interference microscopes also reduce wavefront deviation and diffraction errors and can be easily adapted to perform automated measurements. In the tomography reconstruction process, the acquisition procedure and reconstruction algorithm can be altered to produce lower noise and enhance detection of small index differences. Numerical simulations with example optical fiber profiles demonstrate that is possible to characterize fibers with small, asymmetric index variations beginning from a set of interference images. The average error in the reconstructed profiles is less than 0.1% for three simulated profiles resulting from, in part, implementation of practices to enhance reconstruction accuracy.

The description of MIOPT begins with a discussion of the ray-based interpretation of the measurement process and includes details on what type of measurements must be conducted and how the information is interpreted and analyzed. Restrictions on using this measurement approach are also presented. Implementation of interference image analysis and tomographic reconstruction is presented along with specific methods for improving the detection of small index differences. The results of numerical simulations, used for testing and exploring the analysis portion of the technique, for three different optical fiber profiles are presented. Spatial and refractive-index resolution and accuracy issues are briefly addressed. This technique is suitable for characterizing the index profile asymmetry induced in CO_2-laser-induced LPFGs resulting from one-sided exposure to laser light.

6.1.1 MIOPT Theory

Computed tomography allows multi-dimensional profiling of irregular objects. Such profiling is accomplished through the measurement of a set of projections. For the type of profiling considered here, the projections must be related to the refractive-index values over the fiber transverse cross-section. This section discusses the relationship between measured interference images of optical fiber test objects, projections, computed tomography reconstruction and the general process for conducting non-destructive characterization. The ray-based approach used for developing the theory is valid for the small index differences considered here and also provides a clear physical understanding of the measurement process [132]. This section focuses on the theory relating the refractive-index profile to required projections, but additional details concerning computed tomography are presented in Appendix C.

In the context of measuring two-dimensional transverse cross-sectional refractive-index profiles of optical fibers and fiber devices using computed tomography, a set of one-dimensional projection measurements must be collected. An individual projection is a one-dimensional representation of an object that contains both intrinsic property and spatial information [133]. Collected projections are then used to reconstruct the two-dimensional transverse cross-sectional index profile. Three-dimensional measurements (addition of longitudinal direction) are achieved by stacking the two-dimensional reconstructed cross-sectional profiles. In the context of measuring refractive-index profiles, a projection is a line integral of the object's refractive index taken at a specific angle around the object and over its spatial extent. Such a projection can be interpreted as the optical path length over its spatial extent when the object is viewed at a particular angle. The concept of a projection is illustrated in Fig. 6.1, along with the notation used in discussing them. The d and L axes represent the rotated coordinate system of the projection and are related to the fixed coordinate system of the object (x and y axes) by the projection angle θ. In mathematical terms, a projection, $p(d, \theta)$, taken at a particular angle (θ) from the x-axis is

$$p(d, \theta) = \int_{-\infty}^{\infty} n(d, L)\, dL, \tag{6.1}$$

with $n(d, L)$ being the refractive-index profile of the object in the rotated coordinate system.

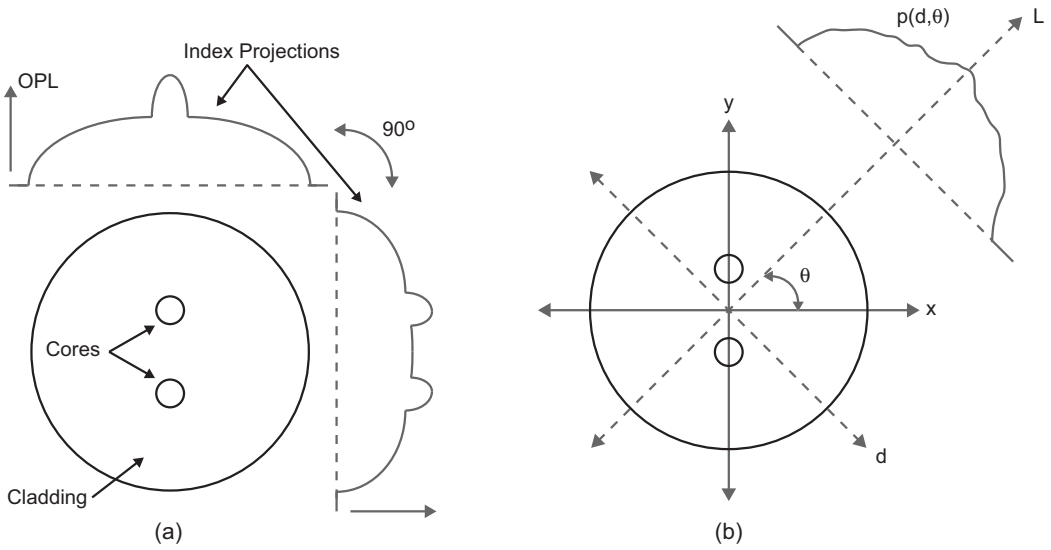

Figure 6.1: (a) Illustration of refractive index projections (optical path length) of a twin-core optical fiber taken 90° apart. (b) Relationship between the fixed coordinate system (x, y) of the optical fiber and the rotated coordinate system (d, L) of the projection, $p(d, \theta)$, at angle θ. The projections go to zero outside the spatial limits of the fiber cross-sections.

The profile $n(d, L)$ is related to $n(x, y)$ by a transformation involving the angle θ. In practice, the projection integral is not taken over infinity since objects have finite boundaries and the profile should go to zero at the boundaries.

In developing the theory, only parallel projections are considered for use in measuring two-dimensional profiles possessing small index differences. The assumption regarding parallel projections places a restriction on rays traveling through the test object, namely, that no refraction occurs. The absence of refraction implies that rays traveling through the sample cross-section will always be perpendicular to the d-axis in the rotated coordinate system at every projection angle. This restriction cannot be met even in the ideal case since some form of index difference always exists in optical fibers (at least at the core-cladding interface) and this leads to some rays being refracted. However, if the refractive index of the surrounding matching oil is closely matched to the sample cladding (within $1\text{x}10^{-3}$) in an interference microscope system, refraction at the outer boundaries is limited. Other measures can also be taken to limit refraction effects and will be discussed later. If proper practices are adopted, the parallel projection approximation for ray travel is valid for use in characterizing fiber samples with small index differences.

A set of projections consists of individual projection measurements taken at various angles around the test object. From a set of projections, the object refractive-index profile can be reconstructed from

$$n(x,y) = \int_0^{2\pi} d\theta \int_0^{\infty} P(\omega,\theta)\,\omega\, e^{i\,2\pi\,\omega\,d} d\omega, \tag{6.2}$$

with ω being the spatial frequency and $P(\omega,\theta)$ being the one-dimensional Fourier transform of the projection $p(d,\theta)$ [133].

The optical path length values required for the projection set can be determined by measuring phase, since the two are simply related by the free-space wavevector magnitude. Several different methods exist for measuring phase, but one of the most accurate involves interfering an optical wave that has passed through an object with a reference wave. Interference measurement schemes routinely detect optical path differences of less than $\lambda/100$ and thus can detect small changes in index for the same path length. Numerous techniques exist for generating interference images of phase objects, but static, fringe-field interferometry is considered in the present approach. While not possessing an index resolution better than that of other interference schemes [134], the resulting interference images are simple to interpret and are useful for illustrating the concepts presented. Almost any interference technique from which the phase can be determined quantitatively would suffice (including phase-shifting interferometry) [135, 136].

Figure 6.2 shows a ray passing through an optical fiber. The figure depicts a transverse cross-section of a typical single-mode optical fiber, but could easily represent another object or device with a more complicated profile. Only one ray is shown in the illustration; a collection of rays at points along the d-axis is necessary to obtain one projection at each angle θ. The following equations are developed for a ray passing perpendicularly (to the d-axis) through the object, as occurs in the rotated projection coordinate system and are correct for any angle. The mathematical relationship between the measured phase from the interferogram and the projection integral is developed below through examination of the accumulated phase of rays in the sample and reference arms of an interferometer.

The accumulated phase of a ray passing through the optical fiber in the sample arm of

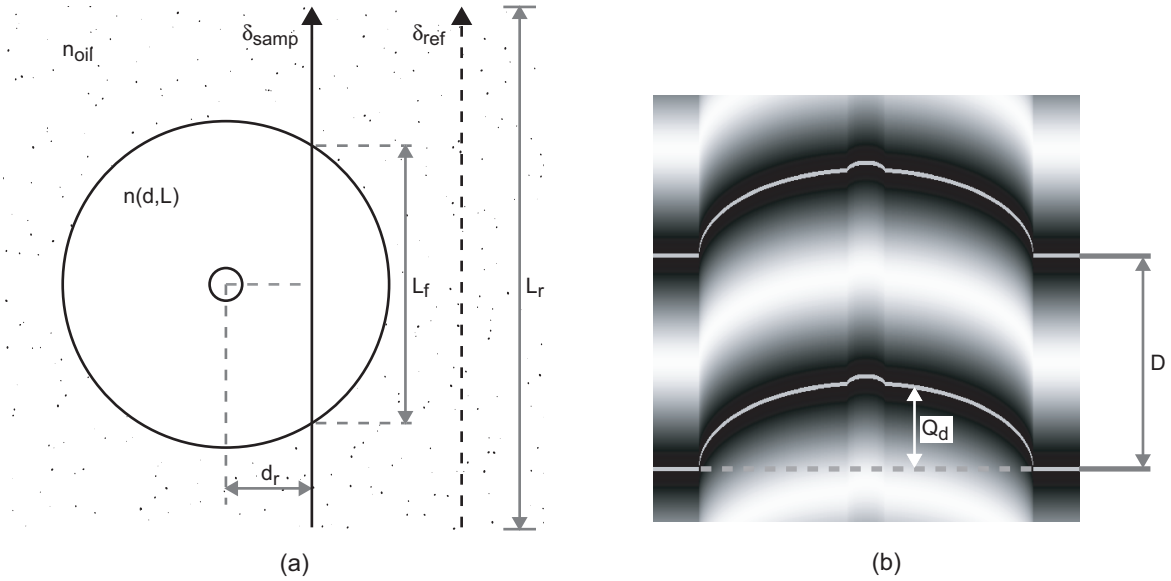

Figure 6.2: (a) Diagram of a typical ray passing through the optical fiber sample. The quantities d and L are the rotated coordinate system axes, $n(d, L)$ is the two-dimensional transverse refractive-index profile of the sample, n_{oil} is the index of the matching oil, δ_{ref} is the phase of a ray traveling through the oil in the reference arm, δ_{samp} is the accumulated phase of a ray traveling through the sample, d_r is the distance from the fiber core to the sample ray, L_f is the length of the sample the ray passes through, and L_r is an arbitrary reference length. (b) Example interference image of an optical fiber sample. D is the fringe separation distance and Q_d is the relative fringe shift.

the interferometer, δ_{samp}, is given by

$$\delta_{samp} = k_o n_{oil}[L_r - L_f] + k_o \int_{L_f} n(d, L) dL, \tag{6.3}$$

where k_o is the free-space wavevector magnitude, n_{oil} is the refractive index of the matching oil, L_r is the overall length of the interferometer path (in one arm), L_f is the length of the sample which the ray traverses (with $L_r > L_f$), and $n(d, L)$ is the two-dimensional refractive-index profile of the optical fiber sample in the rotated coordinate system. The accumulated phase of a ray in the reference arm of the interferometer, δ_{ref}, is simply

$$\delta_{ref} = k_o n_{oil} L_r = k_o n_{oil}[L_r - L_f] + k_o n_{oil} L_f. \tag{6.4}$$

In practice, only the short segment of L_r immediately around the sample (and its equivalent in the reference arm) needs to be considered since the remaining segments of the interferometer path are assumed to be identical for both the sample and reference arms.

As the waves in the two interferometer arms interfere, the phase differences between the sample and reference manifests itself as relative shifts in the minimum/maximum intensity peaks of the static interferogram. The phase difference between rays in the reference and sample beams that pass through the matching oil only possess a zero additional phase difference and their interference peaks serve as the baseline for calculating the phase shift due to the presence of the sample. The phase difference between reference rays and rays traveling through the sample are calculated by subtracting Eq. (6.3) and Eq. (6.4). This difference is interpreted as the relative phase shift ($\Delta\delta$), with

$$\Delta\delta = \delta_{samp} - \delta_{ref} = k_o n_{oil}[L_r - L_f] + k_o \int_{L_f} n(d, L) dL - k_o n_{oil}[L_r - L_f] - k_o n_{oil} L_f, \tag{6.5}$$

$$\Delta\delta = k_o \int_{L_f} n(d, L) dL - k_o n_{oil} L_f. \tag{6.6}$$

The resulting integral term in Eq. (6.6) is the projection required for directly implementing computed tomography reconstruction to retrieve the index profile. However, a different form of the integral is more conducive to performing the reconstruction. The alternative form can be derived by rewriting the n_{oil} term in Eq. (6.6) as

$$k_o n_{oil} L_f = k_o \int_{L_f} n_{oil}\, dL. \tag{6.7}$$

The integral term in Eq. (6.7) can then be substituted into Eq. (6.6) to yield

$$\Delta\delta = k_o \int_{L_f} n(d, L)dL - k_o \int_{L_f} n_{oil}dL = k_o \int_{L_f} [n(d, L) - n_{oil}]dL. \tag{6.8}$$

The integral term containing the difference between $n(d, L)$ and n_{oil} can be calculated directly from a recorded interference image and confers the advantage of eliminating the need to calculate L_f during analysis and reconstruction. Although the relative refractive index is now being reconstructed, simply adding the refractive index of the matching oil after the reconstruction process yields the desired sample refractive index, $n(x, y)$.

Calculating the relative refractive-index projection integral from interference image data requires measuring the relative fringe shift from the baseline fringes that do not pass through the sample and the fringe separation distance. The relative phase shift, $\Delta\delta$, at some distance, d_r, from the fiber core is calculated from the interferogram using

$$\Delta\delta = \frac{2\pi Q_d}{D}, \tag{6.9}$$

where Q_d is the distance from the baseline fringe reference and D is the separation distance between fringe minima (or maxima) that represents a 2π phase difference [116]. The two values are illustrated on the example interference image shown in Fig. 6.2.

Equating Eq. (6.8) and Eq. (6.9) and then rearranging gives the relative refractive-index projection integral in terms of the quantities measured from the interference images taken at each projection angle,

$$p_r(d, \theta) = \int_{L_f} [n(d, L) - n_{oil}]dL = \frac{2\pi Q_d}{k_o D} = \frac{Q_d}{D}\lambda_o, \tag{6.10}$$

where $p_r(d, \theta)$ is now the relative index projection. The ratio $\frac{Q_d}{D}$ represents the percent change in the fringe position from the fringe baseline. Since the physical path is the same, the integral also represents the optical path difference along the d-axis. A set of relative projections taken at various angles around the test object can be used to reconstruct the relative-index profile, from which the actual index profile can be determined by adding the matching oil refractive-index value. Equation (6.10) has a fundamental relationship to the corresponding equation used for determining the one-dimensional refractive-index profile in traditional transverse interferometric profiling [116].

From the analysis presented above, it is seen that the micro-interferometric optical phase tomography process consists of: (1) measuring interference images at a set of projection angles, (2) analyzing the images to extract the phase information, (3) converting the phase information into projection data, (4) collecting the analyzed projection data at all angles, (5) performing computed tomography reconstruction, and (6) adding the matching oil index to the reconstructed profile to retrieve the index profile $n(x, y)$.

6.1.2 Analysis Implementation

The general measurement procedure described in the previous section can be used for measuring the transverse cross-sectional refractive-index profiles of CO_2-laser-induced LPFGs. The procedure consists of acquiring interference images at many angles around a sample and analyzing the images in order to derive the projections required to perform reconstruction. Specific implementation of the fringe analysis and computed tomography reconstruction portions of the measurements procedure is discussed below, with the experimental configuration for recording interference images discussed in Sec. 6.2.

Implementation of the analysis portion of MIOPT can be split into two parts: interference fringe analysis and tomographic reconstruction. Splitting the analysis task into two parts allows for flexibility during reconstruction. For instance, the data resulting from analyzing interference images can be stored and a variety of reconstruction approaches independently attempted. The particular approaches selected for implementing fringe analysis and computed tomography reconstruction are discussed below. Both the interferogram analysis and the tomographic reconstruction algorithm were implemented discretely (as opposed to the continuous form presented in the previous section).

The static interferogram analysis technique selected for use employs a direct polynomial fitting routine based on parabolic approximation of fringe minima [134]. This approach has been used previously in other optical fiber index profiling systems and has the advantage of requiring only one interference image per projection for calculating the phase [128]. A threshold is first applied to the images to locate approximately the fringe minima. Data below the threshold level is retained for use in polynomial fitting. Each pixel column of an

interference image is treated as an individual ray for calculation purposes. Therefore, the fitting routine is used to identify fringe minima pixel locations along each column. Once the minima locations are known, the relative index projection can be calculated [using the right-hand side of Eq. (6.10)]. All images captured during measurement are analyzed to extract their phase, which is used to calculate the projection integrals. Following the calculations, the projection integrals are stored (as a sinogram [133]) for later use in the tomographic reconstruction program.

The second portion of the analysis procedure, tomographic reconstruction, was implemented using the filtered backprojection algorithm [133]. Again, a number of reconstruction algorithms exist, but the filtered backprojection algorithm is a well established technique in tomography that provides flexibility for optimizing the reconstruction process to increase accuracy. The projection integrals, derived from interference images taken at various angles, serve as the input to the algorithm. Basically, the algorithm involves taking the Fourier transform of each projection, applying a reconstruction filter to it, and then performing an inverse Fourier transform. The filtered projection is then back-projected to form a square matrix, the matrix is rotated by the corresponding projection angle (θ), and then added to previously processed back-projection matrices. More detail on the filtered backprojection algorithm is available in Appendix C. Object reconstruction is complete when all projections have been processed and the matching oil's index value is added.

The programs required for conducting fringe analysis and tomographic reconstruction were implemented using the MATLAB programming language [137]. Changes were specifically implemented in the programs to ensure high index resolution [129].

6.1.3 Measurement and Analysis Optimization for Characterizing Small Index Differences

Characterizing small asymmetric index differences in the refractive-index profiles of optical fibers and fiber devices requires consideration of the measurement procedures associated with fringe-field interferometry and tomography. Additions and alterations to the basic interferometry and tomography approaches can lower noise levels and enhance detection of small index differences. The methods for improving detection identified and discussed in

this section form a critical part of the MIOPT technique.

Use of a developed commercial interference microscope, as opposed to a bulk optic interferometer implementation [131], offers several advantages for conducting this type of measurement. Interference microscopes, such as the Mach-Zehnder transmitted-light system discussed below, are designed to have precise, stable optical elements that minimize wavefront distortion and maintain path balance and thereby increase interference image stability. Optical plates and wedges incorporated within the microscope permit precise adjustment of fringe spacing, orientation, and width. The ability to conduct precise adjustments means that fringe properties can be optimized for detecting small index differences. Spurious fringes and speckle noise are reduced by using a bright, bandpass-filtered mercury lamp instead of a laser-based illumination system (commonly employed in bulk systems).

Using an interference microscope to conduct measurements has the additional advantage of reducing refraction effects. As mentioned previously, optical fiber samples must be surrounded with an accurately known index matching oil whose refractive-index value is close to (but not equal to) that of the sample outer cladding. Matching the indices of the oil and cladding lowers the deviation of the rays at the surface boundaries [138]. Direct use of high magnification oil-immersion objectives ensures the matching criteria will be met and eliminates the need for microscope slides and cover slips that can introduce wavefront distortion. In situations where the index value of the cladding is not known, oils with different refractive indices can be tried until a suitable fringe field is observed. In addition to enabling precise matching, using an interference microscope corrects for some refraction effects when the system is properly focused on the center of the fiber [138]. Even with the two corrective measures suggested, samples such as graded-index and air-silica microstructure optical fiber would not meet the parallel projection criteria due to excessive ray refraction over their transverse cross-sections. However, since the emphasis of MIOPT is on measuring small perturbations in index profiles of commercial telecommunications fiber, refraction effects due to asymmetry are expected to be below those due to interfaces (oil/cladding and core/cladding). In cases of excessive refraction, a different form than parallel projections

may be adopted in describing ray paths through the sample (for example, a fan-beam projection [133]). Ray tracing offers one method for investigating whether a particular optical fiber sample would produce significant deviation [131, 138].

Consistent with the primary purpose of detecting small variations in refractive index, several portions of the measurement and analysis procedures can be changed within the reconstruction process to lower noise levels and subsequently improve detection of small variations in refractive index. Taking projections over a full 360°, taking additional projections, and employing various reconstruction filters all act to lower noise levels in certain regions of reconstructed objects. Taking projections 360° around the sample object, instead of over just 180°, increases averaging of noisy data and reduces asymmetric ringing effects [139]. Increasing the total number of projections (decreasing the angle between projections) also leads to increased averaging of noisy data [139]. Altering the reconstruction filter (part of the filtered backprojection algorithm) to introduce averaging and attenuation of higher frequencies lowers the noise level and improves the chances of detecting small variations within interior regions, but not near edges or sharp transitions [132, 133, 139]. Various effects of the type of filter used in reconstruction will be demonstrated through simulations.

By incorporating all of the additions and alterations discussed in this section into the MIOPT measurement process, the ability to detect small, asymmetric index changes is improved. The effect of some of these changes can be illustrated through numerical simulations.

6.1.4 Simulations and Simulation Results

A series of numerical simulations were conducted to evaluate the proposed measurement methodology, test the analysis programs, and to verify the ability to profile asymmetric objects such as CO_2-laser-induced LPFGs. Three optical fiber transverse cross-sections were numerically generated, from which interference images were created. The generated interference images served as simulated inputs to the fringe analysis and reconstruction programs. The specific details of interferogram analysis and tomographic reconstruction

implementation are given below, along with results for the three different types of simulated profiles. The method for generating the interference images using the MATLAB programming language is also given. The average error between the simulated and reconstructed refractive-index profiles was less than 0.1%, dependent on the type of reconstruction filter employed and any post-reconstruction image processing. The simulations verify that it is possible to reconstruct refractive-index profiles with small and asymmetric index variations from a set of measured interference images taken at various angles around a test object.

To begin the simulation process, a desired cross-sectional refractive-index profile of an optical fiber is generated as a 512×512 matrix, with the fiber surrounded by an index matching oil. The optical fiber index profile matrix is subtracted from another constant-valued (n_{oil}) matrix of the same dimensions and the result multiplied by the image pixel spacing (ΔL). The resultant matrix serves as the basis for calculating the phase used in generating the interference image for each projection angle. An example relative refractive-index profile is shown in Fig. 6.5. The difference matrix is then rotated by the current projection angle and its columns summed to generate an array containing the optical path difference due to the object. For all three simulations, projections were taken every 0.5^{o} around the generated profile (720 projections total for each simulation). The large number of projections reduces noise levels in the reconstructed image.

The interference images used for evaluating the tomographic process were generated using Kingslake's formulation, which is given by

$$I(p,q) = \{A + Bcos\,[k_o W(p,q)]\} + N(p,q), \tag{6.11}$$

where p and q are, respectively, the columns and rows of the image, $I(p,q)$ is the irradiance in the interferogram plane, A is the static bias, B is the fringe amplitude, $W(p,q)$ is the optical path difference, and $N(p,q)$ is the noise added to the interference image [140]. The irradiance, static bias, and amplitude are in terms of an 8-bit gray-scale (0-255), as would be captured from a typical CCD camera. The parameters used in generating the interference images for all three simulated cross-sections are given in Table 6.2. The optical path difference was calculated by first generating a matrix with the dimensions of the image

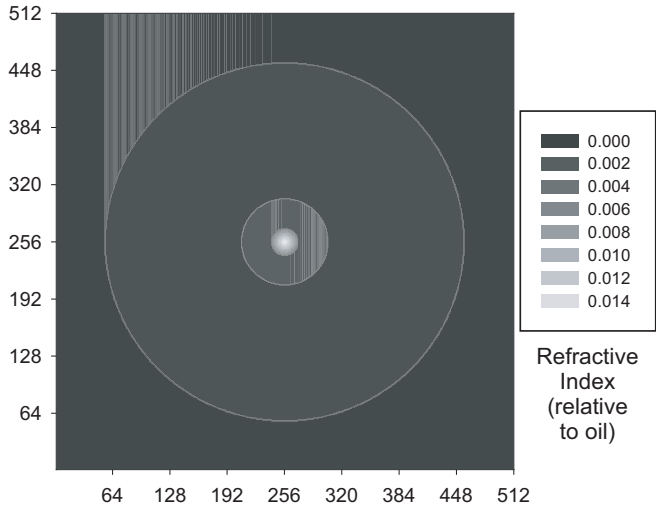

Figure 6.3: Gray-scale plot of a cross-sectional optical fiber refractive-index profile relative to the matching oil index. Simulated profiles, like this one, can be used for generating interference images and testing the fringe analysis reconstruction programs. This particular simulated profile is azimuthally symmetric and possesses outer cladding, inner cladding, and core regions.

and possessing a linear optical path variation along its columns but an optical path that is constant across its rows. This mimics the interference of two waves that are tilted with respect to each other to create carrier fringes. Another matrix, with the same dimensions as the carrier fringe matrix, is created with the projection optical path difference array (representing the phase effect of the sample) and is added to the carrier fringe matrix. After calculating the complete interference image, Gaussian noise is added that possesses a zero mean and standard deviation of σ_m [140, 141]. A noisy interference image is generated for each projection taken of the test index profile and saved in an image file format that would be the same as experimentally captured images. The entire set for a particular test profile served as the input to the fringe analysis program. A typical interference image, generated from the index profile in Fig. 6.3, is shown in Fig. 6.4.

Table 6.2: Parameters Used in Generating Simulated Interference Images

A	B	λ_o	μ	σ_m	ΔL
128	108	$546nm$	0	8	$312.5nm$

In generating the interference images, the parallel projection (no refraction) assumption

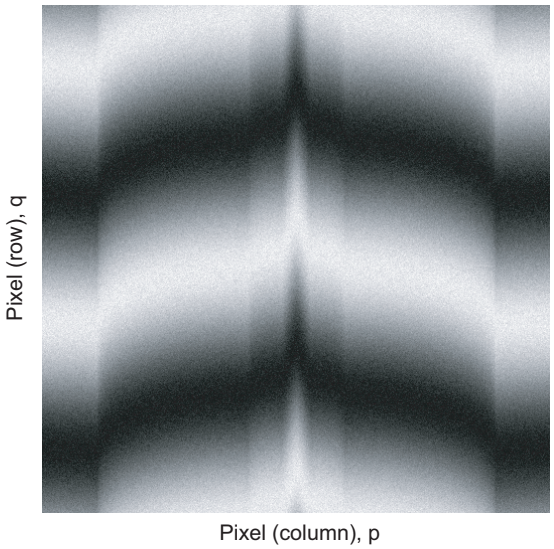

Figure 6.4: Example interference image generated using Eq. (6.11) from the test profile shown in Fig. 6.3. Since the profile is symmetric, all of the projections are identical (except for additive noise).

was followed. Therefore, any variations in the gray-scale intensity are due only to shifts in phase. It was also assumed that sample rotation occured exactly axially, implying that tilting and shifting of the sample cross-section center location (center of fiber core) is not a factor. In practice, tilting and shifting of sample objects in images can be compensated for if they are found to occur [142].

The first simulated profile was that of a azimuthally symmetric optical fiber with an inner cladding, an outer cladding, and a core, the same as that shown in Fig. 6.3. A symmetric profile was simulated initially to test the programs as it represents a simple, symmetric profile. The reconstructed object profile is shown in Fig. 6.5, after processing the simulated interference images using the interferogram analysis and reconstruction programs. The maximum error for the entire cross-section was 0.12% and the average error was 0.0014%. Specific results are shown in Fig. 6.6 for a line-section of the profile along its length at the center width. Figure 6.6 also shows the absolute difference between the test and reconstructed profiles. The reconstructed profile matches very closely the generated test profile. All profiles from Fig. 6.3 to Fig. 6.10 are plotted relative to the matching oil index to enhance illustration of index variations. Only the refractive-index value of the

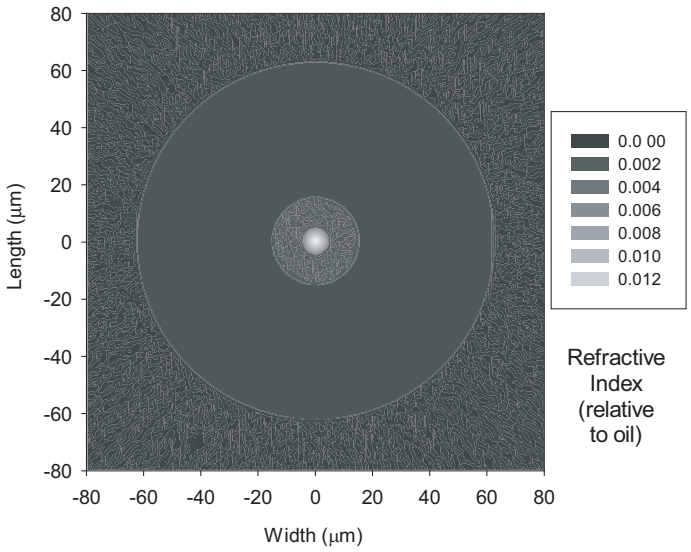

Figure 6.5: Gray-scale plot of the reconstructed index profile of the azimuthally symmetric optical fiber.

matching oil (1.4571) must be added to yield the absolute index profiles. A modified reconstruction filter (typical ramp-type combined with a Hanning) was used to enhance the accuracy in interior regions of the profile, with a corresponding decrease in accuracy near edges and sharp transitions [133, 139].

Next, a twin-core optical fiber was generated with a profile similar to that in the work by Barty *et al.* [58] and used as a simulated input. This fiber is not azimuthally symmetric, as can be seen in Fig. 6.7, and is therefore useful for evaluating the ability of the present method to characterize asymmetric objects. The reconstructed object profile is shown in Fig. 6.7(b). The maximum error for the entire cross-section was 0.21% and the average error was 0.052%. Specific results, following successful processing, are shown in Fig. 6.8(a) for a line-section of the profile along its length at the center width. Figure 6.8(b) shows the absolute difference between the test and reconstructed profiles. The error is larger over the entire profile for this reconstruction, in contrast to one shown in Fig. 6.6(b), because only the required ramp-type filter (unmodified) was used for the reconstruction. The error is larger, though more uniform, over the line-section and the core features are better preserved.

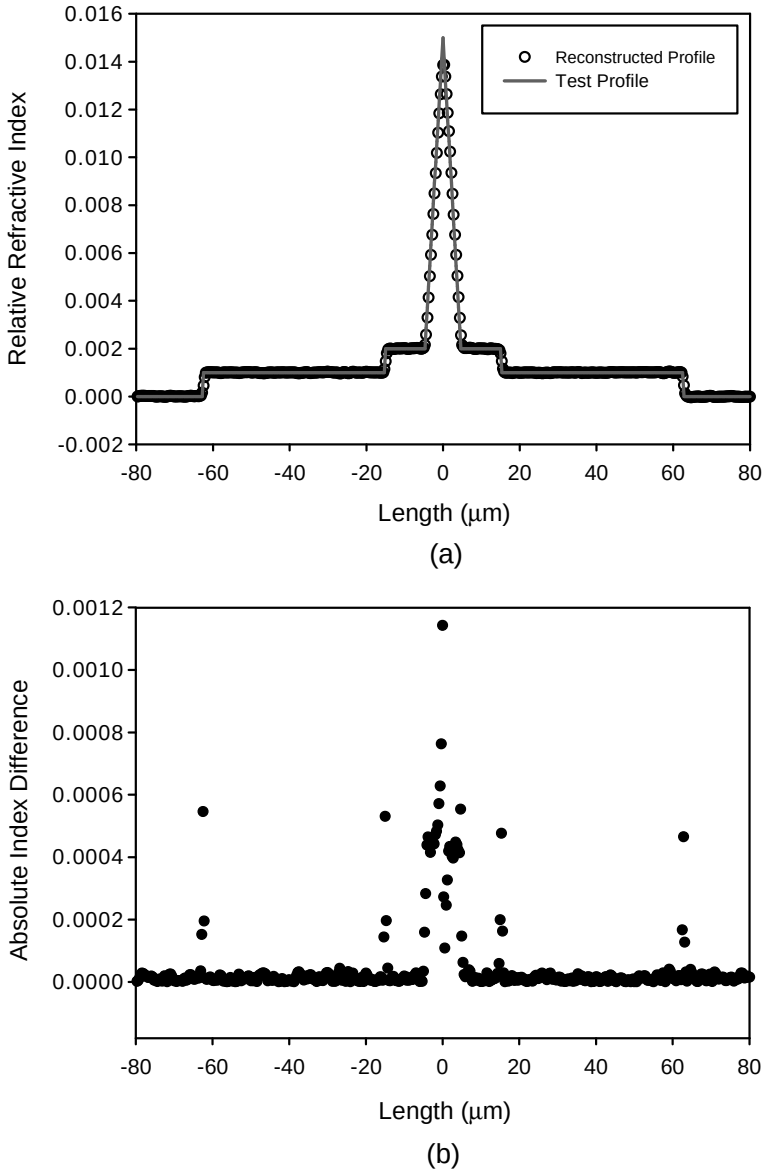

Figure 6.6: Symmetric optical fiber simulation results. (a) Comparison of test and reconstructed profiles taken along length at the center of the width. (b) Absolute index difference between test and reconstructed profiles shown in (a). The noise in the interior cladding regions is lower than that near the edges and in the core due to the use of a modified filter.

The third profile, an single-mode optical fiber with an exponential refractive index variation over the cross-section, is shown in Fig. 6.9. The index profile is circularly asymmetric and has one side of the cladding at a slightly higher index value than the other side ($1.5\text{x}10^{-4}$). The asymmetry in the profile is similar to that observed in optical fibers exposed to ultraviolet light, only applied over the entire cross-section. The exponential variation originates from one side and was calculated using an equation by Dossou *et al.*, only applied over the entire cross-section [68]. Optical fibers exposed to CO_2 laser light have approximately this form of small index asymmetry. The reconstructed object profile is shown in Fig. 6.9(b). The maximum error for the entire cross-section was 0.08% and the average error was 0.0012%. Specific results, following successful processing, are shown in Fig. 6.10(a) for a line-section of the profile along its length at the center width. Figure 6.10(b) shows the absolute difference between the test and reconstructed profiles. Since the exponential variation is concentrated predominantly within the cladding, a modified reconstruction filter (the same used for the symmetric profile simulation) was used to achieve lower error in the cladding regions.

The results of the simulations demonstrate that it is possible to reconstruct the index profiles of optical fibers with index asymmetry and small index differences by analyzing interference images taken at multiple angles and using computed tomography; this means the technique is suitable for measuring transverse cross-sectional refractive-index profiles of CO_2-laser-induced LPFGs. They also show how reconstruction can be changed to emphasize certain aspects (such as interior regions) by modifying the basic ramp-type reconstruction filter used in the filtered backprojection algorithm to attenuate selected spatial frequencies. Modifying the filter can be useful when attempting to profile fibers with small index variations in, for instance, the cladding region.

6.1.4.1 Resolution and Accuracy

High resolution and high accuracy, both in spatial and refractive-index terms, are two of the advantages offered by using microinterferometry to conduct profiling. The factors

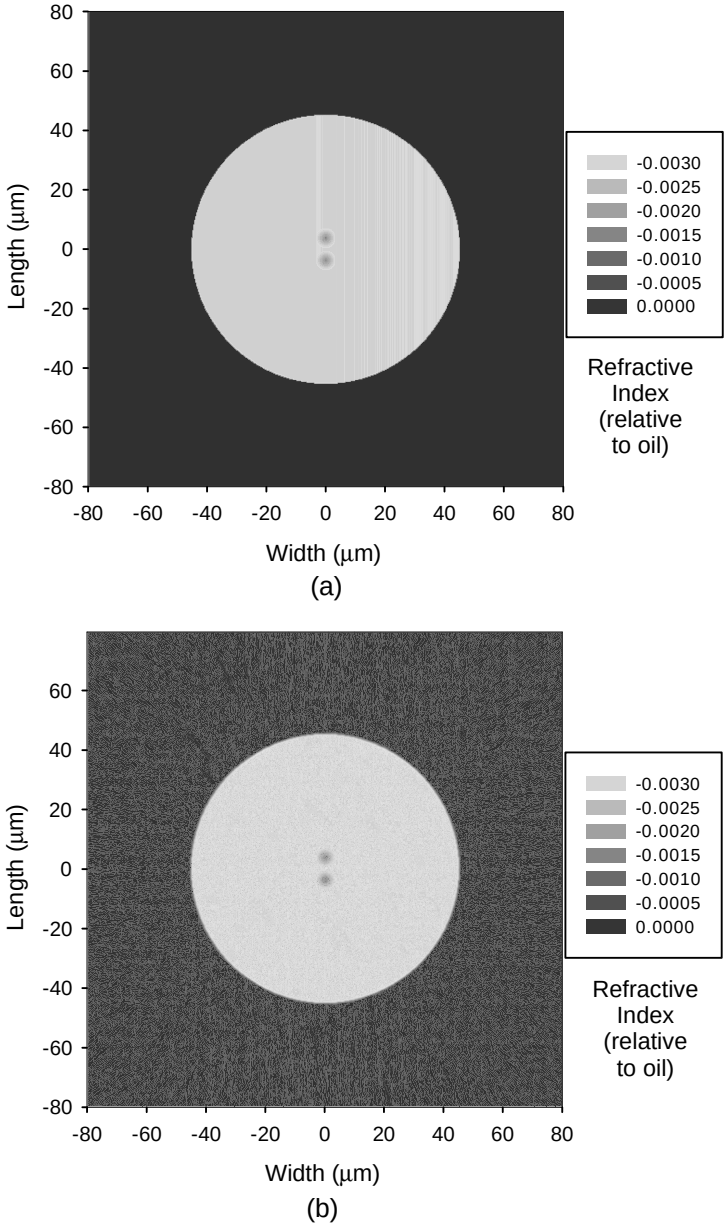

Figure 6.7: (a) Gray-scale plot of the generated cross-sectional refractive-index profile of a twin-core optical fiber relative to the matching oil index. The profile is not azimuthally symmetric due to the two offset (from center) cores. (b) Reconstructed index profile.

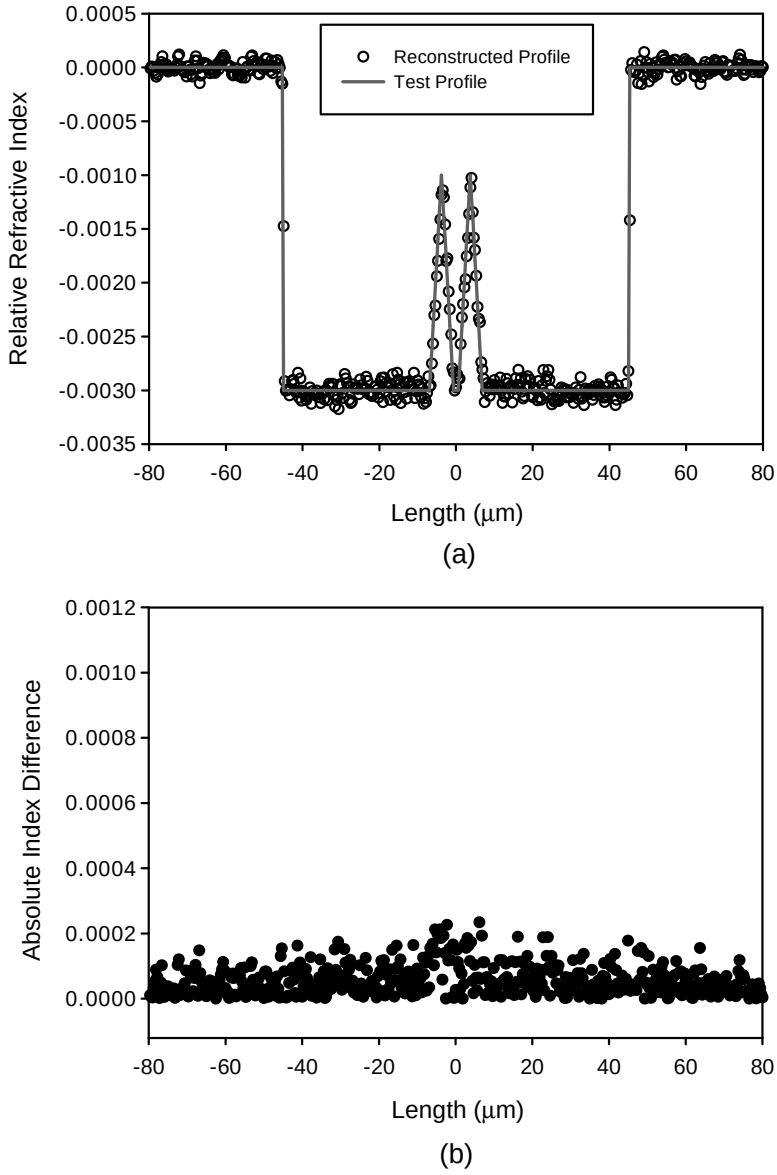

Figure 6.8: Twin-core optical fiber simulation results. (a) Comparison of test and reconstructed profiles taken along the length at the center of the width. (b) Absolute index difference between test and reconstructed profiles shown in (a). Noise levels are roughly similar in the cladding, cores, and near the edges since only the basic ramp-type filter was used.

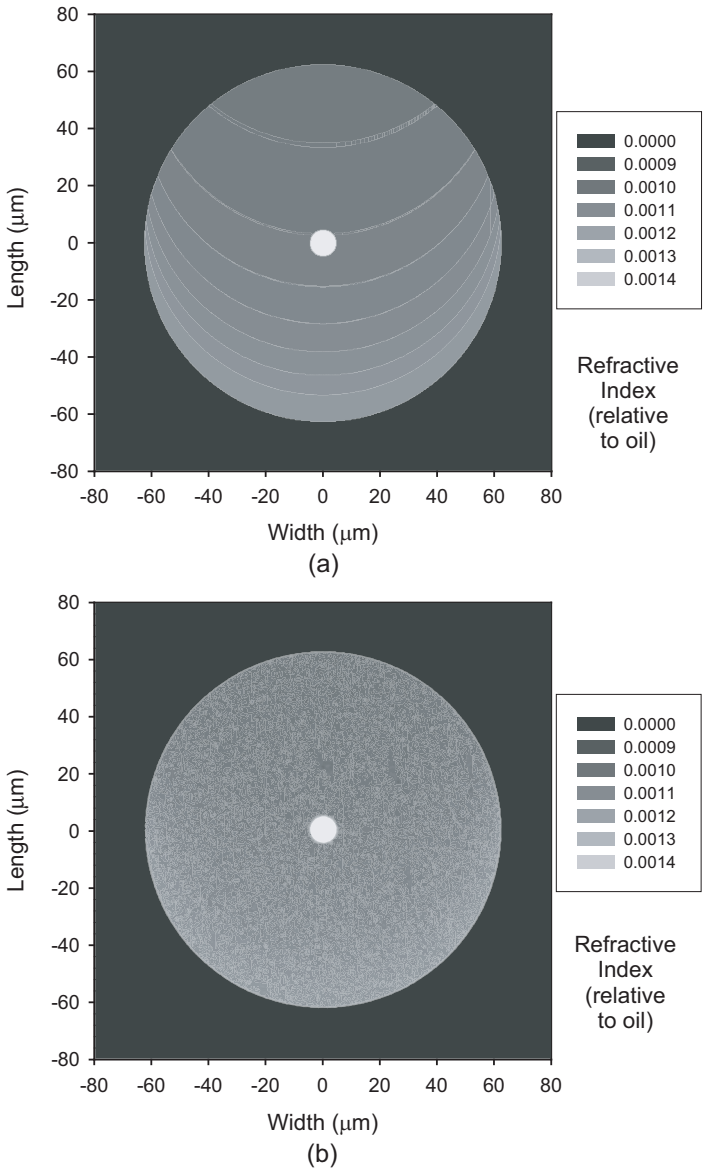

Figure 6.9: (a) Gray-scale plot of the generated cross-sectional refractive-index profile of a single-mode optical fiber relative to the matching oil index. (b) Reconstructed index profile. A shorter relative index range is used in order to highlight index variations in the cladding region (core features are not shown).

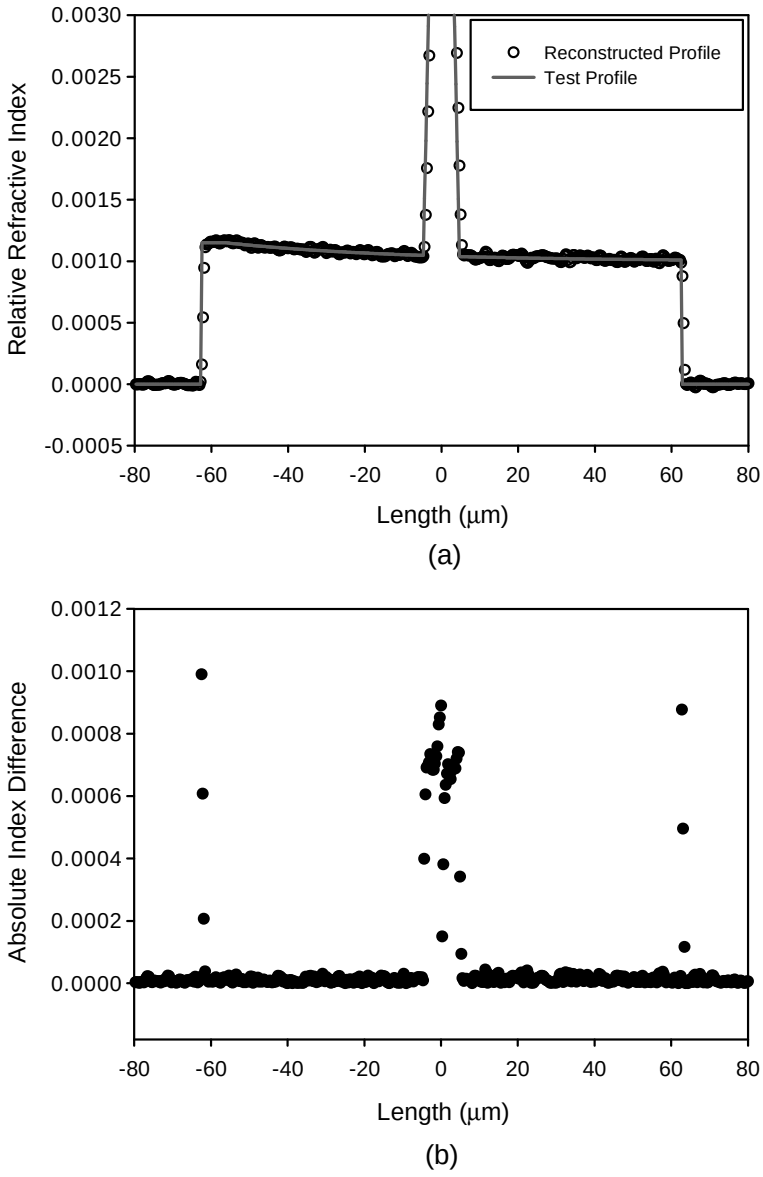

Figure 6.10: Asymmetric (exponential) profile optical fiber simulation results. (a) Comparison of test and reconstructed profiles taken along length at the center of the width. The exponential variation over the length is evident in the reconstructed profile. (b) Absolute index difference between test and reconstructed profiles shown in (a).

influencing resolution and accuracy are different for the refractive index and spatial domains; the issues are far more complicated for the index case.

Spatial resolution is determined by distinct factors in the transverse (cross-section) and axial directions. The transverse spatial resolution is set by a combination of the microscope's lateral resolving power and the equivalent pixel spacing of the CCD camera at a given magnification. For the Mach-Zehnder transmitted light microscope discussed in Sec. 6.2, the lateral resolvable power is approximately $0.5\mu m$ at $50\times$ magnification [143]. As an example, if the equivalent pixel spacing of a typical CCD camera at that magnification is approximately $0.6\mu m$, then the pixel spacing limits the transverse spatial resolution since it is the larger value. Axial spatial resolution is set by the fringe separation distance. In calculating the relative phase shift from interference images, the phase difference between fringe minima is assumed to be the same. The assumption is necessary to scale relative shifts to a known phase value (2π). For the assumption to be true, the transverse cross-sectional index profile must be constant along the axial direction. In the example interferogram shown in Fig. 6.4, the fringe separation distance is approximately $100\mu m$ and that value represents the axial spatial resolution limit. The fringe separation can be decreased to improve axial resolution, but only with an accompanying reduction in the ability to detect small changes in phase. The spatial resolution gained by using microinterferometry allows profiling of samples with more rapidly varying radial changes, as occur in dispersion-compensating fiber, than in typical optical fiber.

It should be noted that the restriction on axial spatial resolution is derived from the choice of fringe acquisition and analysis techniques. Implementation of other analysis techniques will yield improved axial spatial resolution. For example, phase-shifting (phase-sampling) interferometry (PSI) [135, 144] provides two-dimensional phase information, in contrast to the one-dimensional information obtained with static fringe-field interferometry. With PSI, a two-dimensional projection is obtained at each projection angle and the subsequent reconstruction produces a three-dimensional object. The transverse and axial spatial resolution are then equivalent.

Refractive-index resolution and accuracy are more complicated than their spatial equivalents. Noise levels in the reconstructed image depend not only on the smallest detectable fringe shift difference, but also on tomography reconstruction practices. The smallest detectable fringe shift difference is influenced by environmental factors, system noise, and the fringe analysis program. Factors influencing index resolution originating from computed tomography include the type of algorithm used for reconstruction, filters, the number of projections taken, and the number of samples per projection [139]. In addition, the accuracy of the reconstructed object can vary between different regions (interior versus edge) [131, 132, 139]. No models exist for predicting signal-to-noise ratio for a measurement approach like MIOPT, though simplified noise models are available for traditional (x-ray) computed tomography [139, 145]. Quantitative signal-to-noise ratio values are usually established through measurements of a uniform phantom [133]. Despite the complexity inherent in the process, the simulation results give a general idea of the noise arising from the analysis portion of the measurement process.

6.1.5 Summary

A new technique for measuring transverse cross-sectional refractive-index profiles of optical fiber and fiber devices has been presented. MIOPT combines fringe-field microinterferometry with computed tomography to characterize asymmetry present in cross-sectional profiles. Both the microinterferometry and tomography portions of the technique are specifically implemented so as to enhance reconstruction accuracy and resolution. The simulation results demonstrate that MIOPT is capable of profiling fibers and fiber devices that possess azimuthally asymmetric refractive-index profiles, including CO_2-laser-induced LPFGs.

6.2 Refractive-Index Profile Measurements

Through use of the developed MIOPT measurement technique, it is possible to measure accurately the transverse cross-sectional refractive-index profiles of CO_2-laser-induced LPFGs. Profiling measurements, conducted using MIOPT, of an azimuthally symmetric optical fiber [single-mode fiber (SMF)], an azimuthally asymmetric optical fiber [polarization-maintaining fiber (PMF)], and a CO_2-laser-induced LPFG are presented in this section.

The experimental apparatus for making the projection measurements, along with the actual measurement procedure, are also discussed.

6.2.1 Experimental Configuration, Procedure, and Issues

6.2.1.1 Experimental Configuration

A microinterferometer arrangement, and associated hardware, is necessary for obtaining interference images of optical fiber and fiber devices required for performing accurate reconstruction. While it is possible to construct an apparatus for conducting measurements from bulk optical elements, a suitable commercial interference microscope is available that can be used, with some modification, for conducting projection measurements.

The Mach-Zehnder two-objective, transmitted-light interference microscope, traditionally used for profiling symmetric optical fibers, is easily adapted to enable interference measurements at various projection angles [116, 146]. Adapting the microscope only requires the addition of a rotary stage and motion controller. A diagram of the overall experimental configuration is shown in Fig. 6.11. The measurement process, in this arrangement, is automated to reduce the amount of time required to take the large number of projections needed for low-noise reconstruction. The microscope (originally manufactured by Ernst Leitz GMBH, Wetzlar, Germany), is found in many fiber characterization laboratories since it is used for profiling azimuthally symmetric optical fiber.

A fiber sample positioner/rotator, shown in Fig. 6.12, was designed and fabricated to provide precise positioning and automated rotation of samples in the optical path of the interference microscope. The three manual linear axes and two manual tip-tilt axes are used to position the sample in the index matching oil so as to appear in the center of the CCD array. The motorized rotation stage is used to rotate the sample around the fiber longitudinal axis (axial rotational orientation) so that interference images can be captured at the necessarily large number of projections angles. The positioner/rotator assembly mounts on the interference microscope plate to provide a stable platform for any samples. A prepared fiber sample, secured in the small-bore of a needle, is attached to the rotation stage through a mating plate and needle hub adapter.

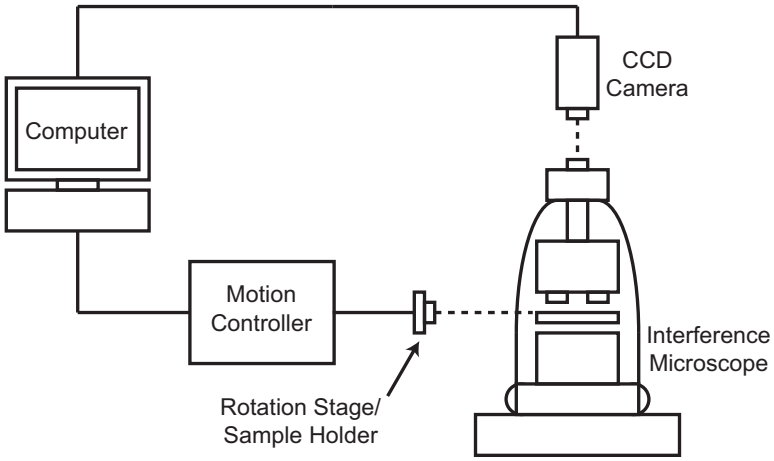

Figure 6.11: Experimental configuration for measuring interference images of an optical fiber test object at various projection angles. An optical fiber sample, secured in the holder, can be rotated about its axis to enable interference images to be recorded at any angle. The measurement system is automated by incorporating a motion controller and a computer-controlled camera.

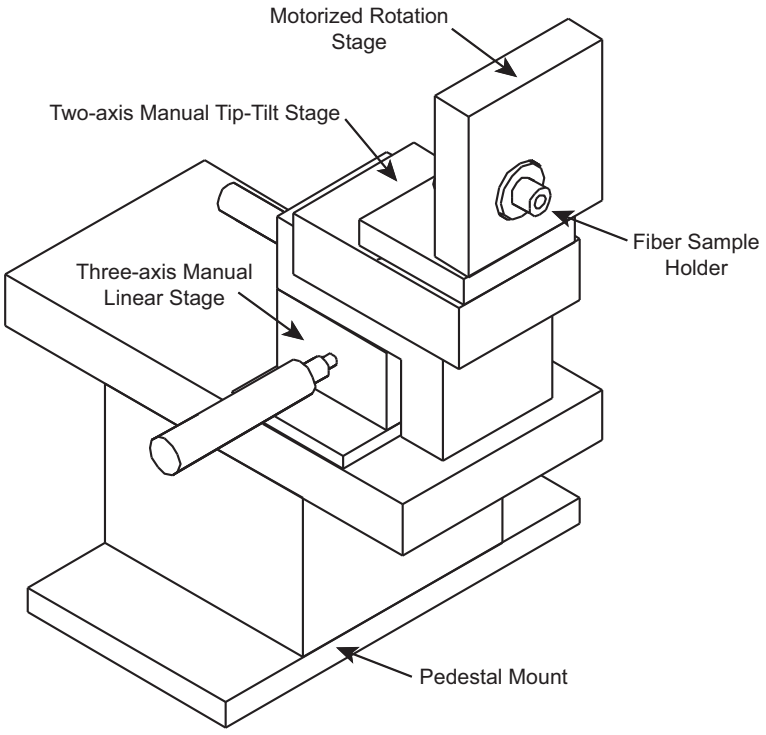

Figure 6.12: Diagram of the fiber sample positioner/rotator for use in refractive-index profiling. The three linear axes and two tip-tilt axes align the sample in the center of the interferometer measurement area and correct wobble or offset during rotation. The sample can then be rotated about its longitudinal axis so interference images can be captured at the required projection angles.

6.2.1.2 Sample Preparation

Prior to acquiring the interference images using the interference microscope, the fiber samples to be profiled are cleaned and mounted in a holder. An approximately $25mm$ section of buffer near the fiber region of interest is removed chemically (using a gel containing methylene chloride) and the region is then cleaned with isopropyl alcohol and lens tissue paper. A segment of the fiber still containing the buffer near the stripped region is inserted into a small-bore (25-gauge, $25.4mm$ long) needle until the start of the stripped section is at the tip of the needle. The needle containing the fiber sample is positioned under a standard optical reflection microscope so that the tip of the needle is in the microscope field-of-view. A small amount of epoxy is then applied, using a syringe, to the tip of the needle so that the fiber remains stationary during the testing that follows. Prior to any measurement, the fiber segment extending beyond the needle tip is cut to a suitable length (approximately $15mm$) and carefully cleaned again (using lens tissue paper, isopropyl alcohol, and compressed air) to ensure no dirt or oil remain on the fiber surface. In the case of CO_2-laser-induced LPFG samples, preparation for mounting requires removal of any orientation tabs added after fabrication and cleaning removes the black marks that indicate the first and last grating periods.

6.2.1.3 Measurement Procedure

A diagram of the MIOPT measurement procedure is shown in Fig. 6.13. After final sample preparation, the needle containing the sample is secured to the rotation stage (using the hub adapter) and the entire positioner assembly is moved toward the interference microscope until the tip of the fiber sample penetrates the pool of index matching oil surrounding the sample-arm immersion objective. With the reference arm of the interferometer blocked (thus producing an intensity image by preventing interference), the linear and tip-tilt stages are adjusted until the sample (in the oil) is positioned so as to appear in the center of the CCD array and in-focus. An example of an in-focus fiber sample is shown in Fig. 6.14. Only the fiber cladding and core edges can be (barely) discerned in the when the fiber sample is in focus; this is due to the index matching oil having a nearly identical index value to that

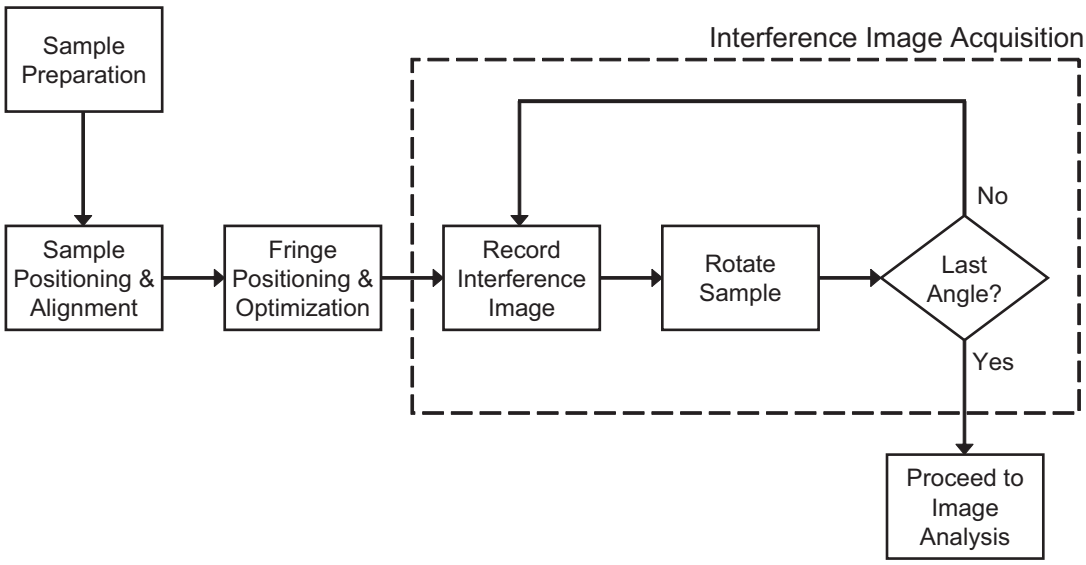

Figure 6.13: Block diagram of MIOPT measurement procedure.

of the fiber cladding. The closeness of the matching oil and cladding index values reduces focusing effects and is required in order to obtain accurate profiles near sample edges.

Following initial sample positioning, the reference arm of the interferometer is unblocked and the resulting interference pattern is adjusted to produce relatively high-visibility fringe patterns with the desirable number of fringe maxima/minima within the CCD array detection area. Adjustments are also made to ensure that the fringes run perpendicular to the fiber sample longitudinal axis and that the two fringes used to derive the index projection are fully contained within the image. The positions of the fringe minima along the fiber sample longitudinal axis are also adjusted to ensure that the minima are away from the edges of the image. An example fringe-field interference pattern captured with the 1.3 megapixel and 12-bit depth scientific-grade CCD camera is shown in Fig. 6.15.

Once the sample is correctly positioned and a suitable fringe-field is obtained, the actual profile measurement can be conducted. An image of the resulting fringe-field interference pattern on the CCD array is captured and stored for later processing. Each stored image is an average of 32 images, with image averaging conducted in order to reduce noise. An example of an acquired interference image containing an optical fiber sample is given in Fig. 6.16. The sample is then rotated (by $\Delta\theta$) to the next projection angle. The process is

(a)

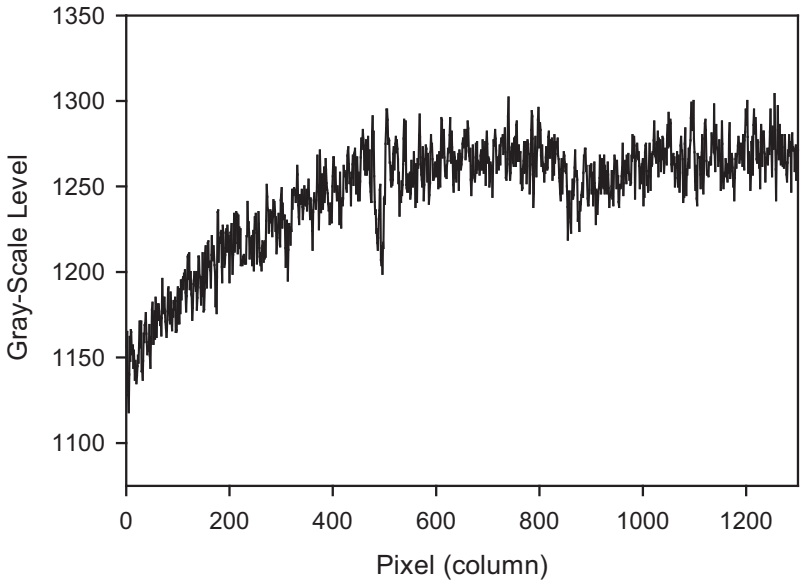

(b)

Figure 6.14: (a) Gray-scale level (intensity) image of a fiber sample in focus. The image is 1030×1300 pixels. (b) Line plot of the center pixel row (515) across all of the column pixels from the image in (a). While there is a general intensity variation over the image, focusing effects due to cladding/matching oil index mismatch are minimal.

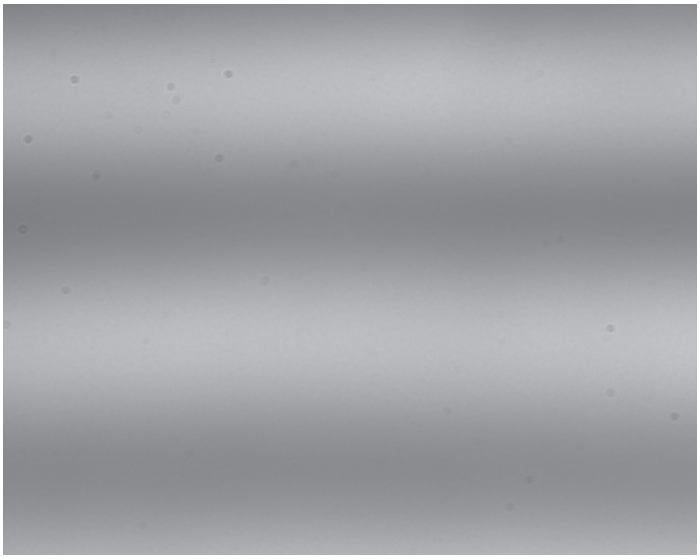

Figure 6.15: Example fringe-field interference image captured with the CCD camera. No fiber sample is present in this image, as reflected by the straight fringe minima (darkest regions).

repeated until the sample is rotated over a full 360°. Image acquisition, storage, and sample rotation are controlled through a single custom LabVIEW program [52]. Periodically, acquisition is temporarily halted and the microscope focus is adjusted to ensure the sample remains correctly focused. The adjustment is necessary due to the sample wobbling and/or precessing during rotation.

Following acquisition of the required interference images at all of the projection angles, the index projections can be calculated and the profile reconstructed. A diagram of the analysis procedure is shown in Fig. 6.17.

6.2.1.4 Measurement and Analysis Issues

While recording images used to reconstruct the profiles presented in the next two sections, several issues emerged that impact the accuracy and resolution of the reconstructed profiles. The three issues with the most significant impact on the results are: (1) the effect of sample wobble and precession resulting from rotation, (2) temperature fluctuation, and (3) the difference between index matching oil and cladding. Potential solutions to these issues, being necessary to improve MIOPT profiling, are discussed in Chapter 7.

Computed tomography reconstruction requires that all of the acquired projections share

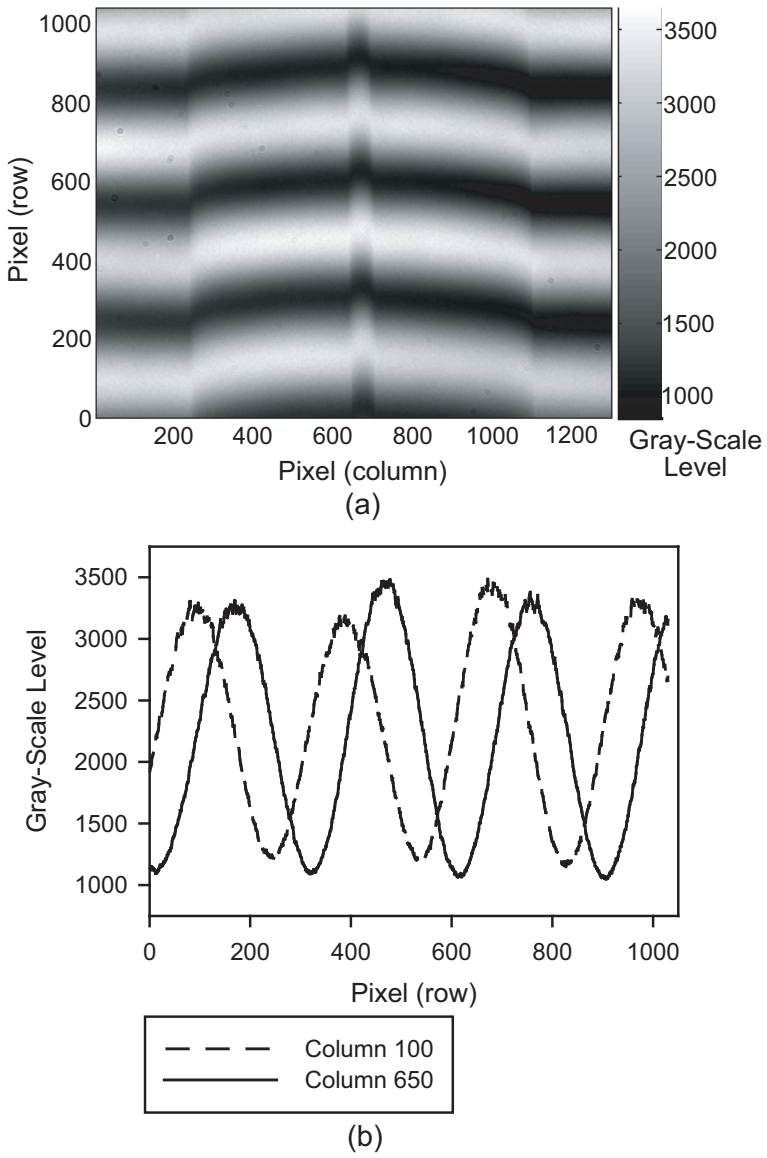

Figure 6.16: (a) Example interference image of an optical fiber sample. (b) Example line-plots along the vertical direction from the interference image shown in (a). Column 100 is in the fringe baseline (outside the fiber) while column 650 is near the center of the fiber. The fringe visibility is approximately 50%.

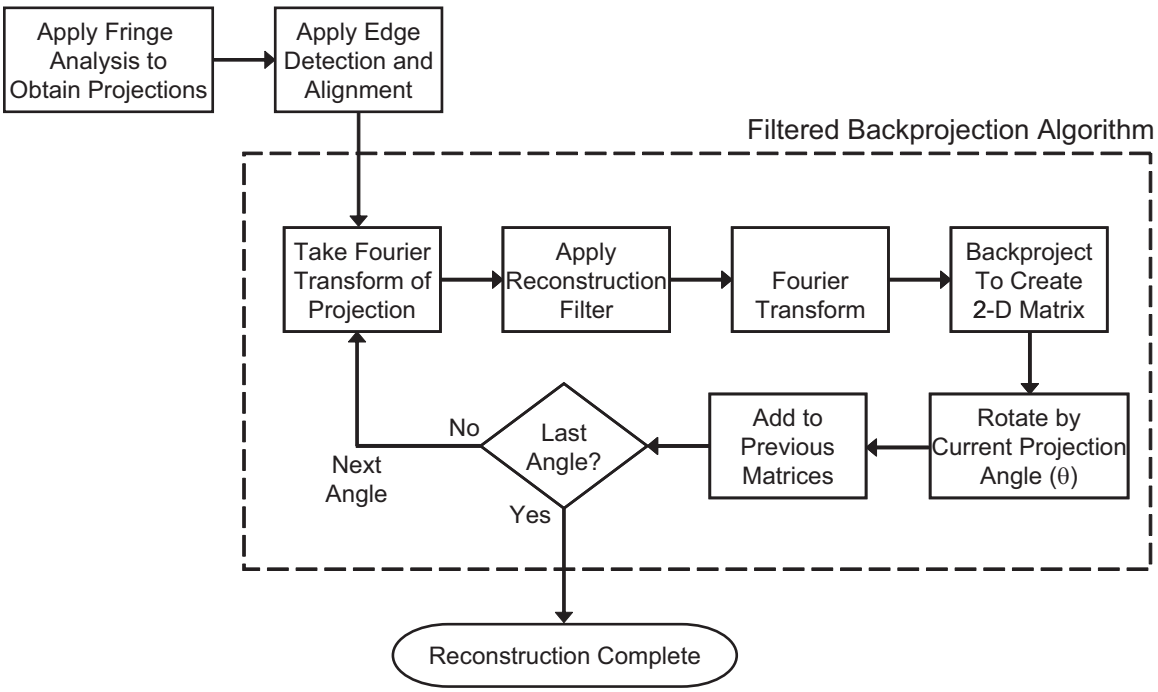

Figure 6.17: Block diagram of MIOPT analysis procedure.

a common spatial origin. The required common origin for each projection is violated if sample wobble and/or precession occurs as the sample is rotated through various projection angles. Sample movement is difficult to avoid in MIOPT because the sample must be rotated (as the interferometer cannot be) and the sample holder and positioner are not mounted directly to the microscope stage. Significant shifts in the origin of the projection yield distorted reconstructed profiles, while only small shifts primarily produce blurring and averaging. Some of the shifts can be corrected by identifying the edges of the sample and aligning all of the collected projections to common edges, though the process assumes a perfectly circular cross-section (a reasonable assumption for fiber samples). An example of the results of alignment is given in Fig. 6.18, with a sinogram (sequential stacking of all projections) shown before and after the process. Edge detection and alignment offers restricted accuracy due to noise, debris, or focusing effects present in the interference image and the limited efficacy of the particular edge detection routine that is employed.

Temperature fluctuation during measurement alters the absolute levels of projections, though not necessarily their shape. The primary effect of temperature fluctuation is to

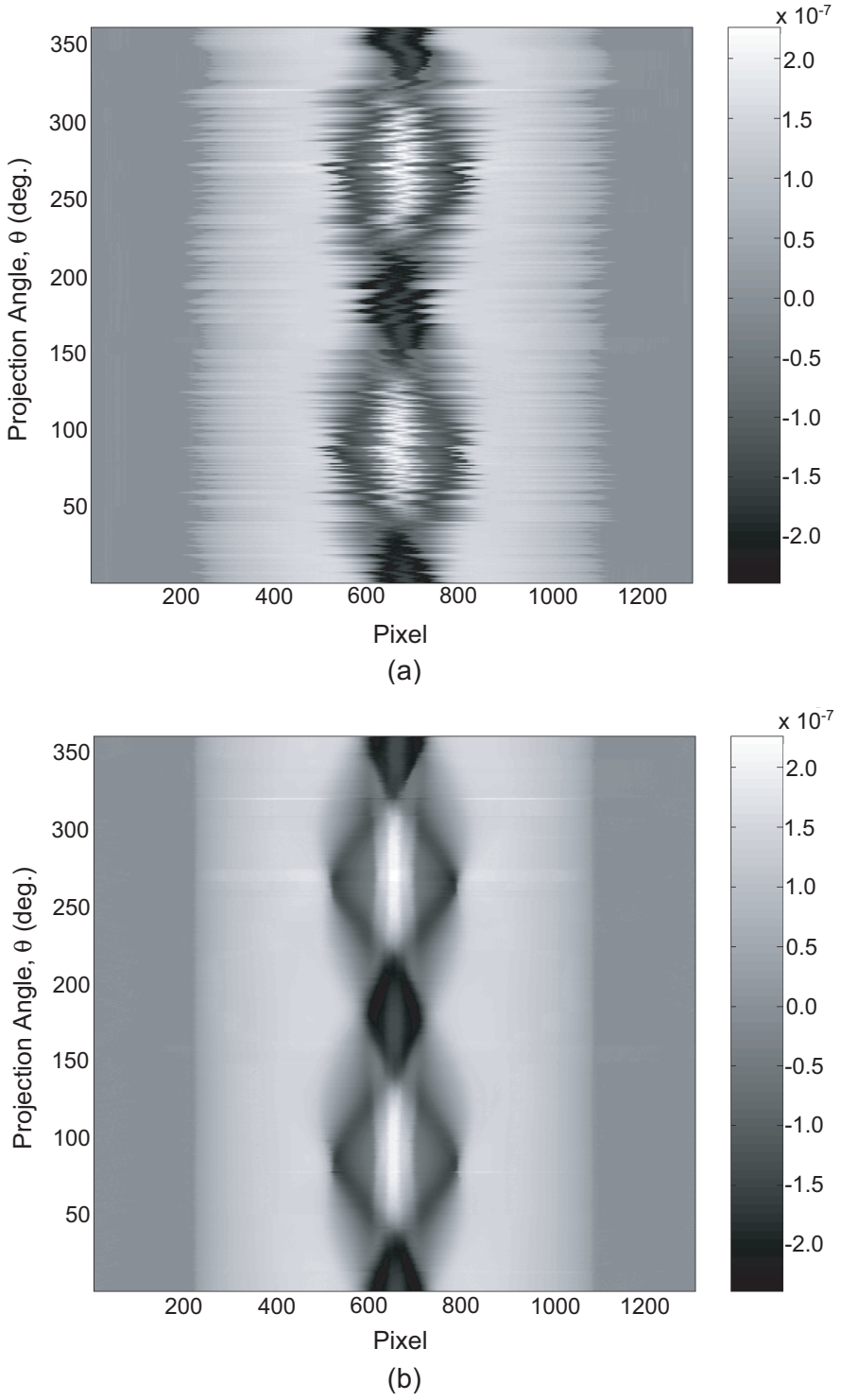

Figure 6.18: Example of projection edge detection and alignment: (a) Sinogram before alignment and (b) Sinogram after alignment. A reconstruction conducted using the projections shown in (a) produces a severely distorted profile.

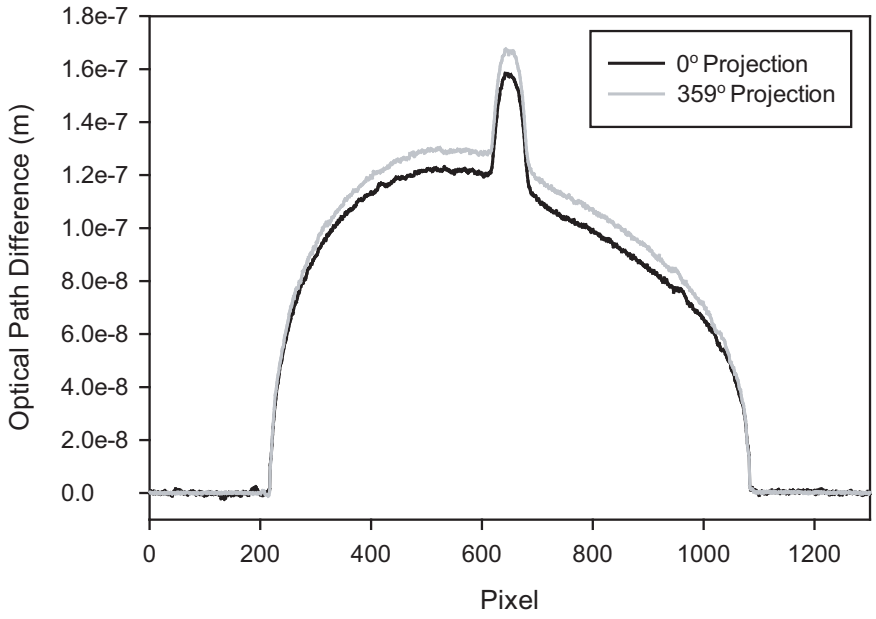

Figure 6.19: Example of the effect of temperature fluctuation during projection acquisition. The two relative index projections should be very similar, since they are only 1° apart, but the temperature change that occurred between their acquisition contributes to the dissimilarity.

change the refractive-index value of the matching oil. As can be ascertained from Eq. (6.8), the absolute levels of the relative index projections at each point change linearly with index oil changes. For correct profile reconstruction, the relative index projections must be comparable and this requires the index value of the matching oil to be constant throughout the measurement. An example of the effect of temperature fluctuation is shown in Fig. 6.19. The possibility of correcting for matching oil index variations in post-processing of the projections is limited to cases of azimuthally symmetric samples and any attempted correction certainly impacts accuracy.

Any difference between the refractive-index value of the matching oil and the index of the fiber cladding region does introduce errors, primarily near the oil/cladding and core/cladding interfaces. This issue has been examined in depth by Górski and others [131] and must be considered when profiling asymmetric fiber samples.

6.2.2 Experimental Verification of Technique

To verify that MIOPT is suitable for profiling optical fiber and CO_2-laser-induced LPFG samples, it is necessary to conduct measurements for several example fiber profiles. Measured refractive-index profiles are presented below for two different optical fiber samples [147]. One sample possesses an azimuthally asymmetric cross-sectional profile while the other possesses a symmetric profile and, therefore, both types are useful for evaluating the technique. The measured experimental results demonstrate the ability of MIOPT to profile both azimuthally asymmetric and symmetric optical fiber.

Both of the profiles were reconstructed from 360 interference images taken every 1^{o} around the samples and processed using a modified reconstruction filter [129, 139]. Examples of the interference images recorded during measurement are shown in Fig. 6.20. The reconstructed profiles are shown relative to the surrounding refractive index of the matching oil used during measurement $[n(x, y) - n_{\text{oil}}]$. Based on the two index profiles measured by MIOPT, the estimated spatial resolution is $0.5\mu m$ while the index resolution is estimated to be below (better than) 5×10^{-5}. After processing of the SMF interference images (azimuthally symmetric case), it was necessary to correct for a slight ambient temperature variation that occurred during measurement (additive shift).

6.2.2.1 Azimuthally Symmetric Optical Fiber

MIOPT can also be used to profile optical fibers with azimuthally symmetric cross-sectional refractive-index profiles. Although tomography is not required for profiling symmetric objects, its application can lower overall noise levels and potentially reveal index irregularities and other unintended nonuniformities. As an example, a measurement of a standard telecommunications single-mode optical fiber was conducted, with the resulting reconstructed index profile shown in Fig. 6.21. The cladding and core diameters in the reconstructed profile closely match the SMF's specified values ($125\mu m$ and $8.2\mu m$, respectively). As expected of typical SMF, the profile is azimuthally symmetric.

Figure 6.22(a) shows the vertical line-profile of the relative refractive index through the center of the reconstructed profile. As a comparison to a common one-dimensional profiling

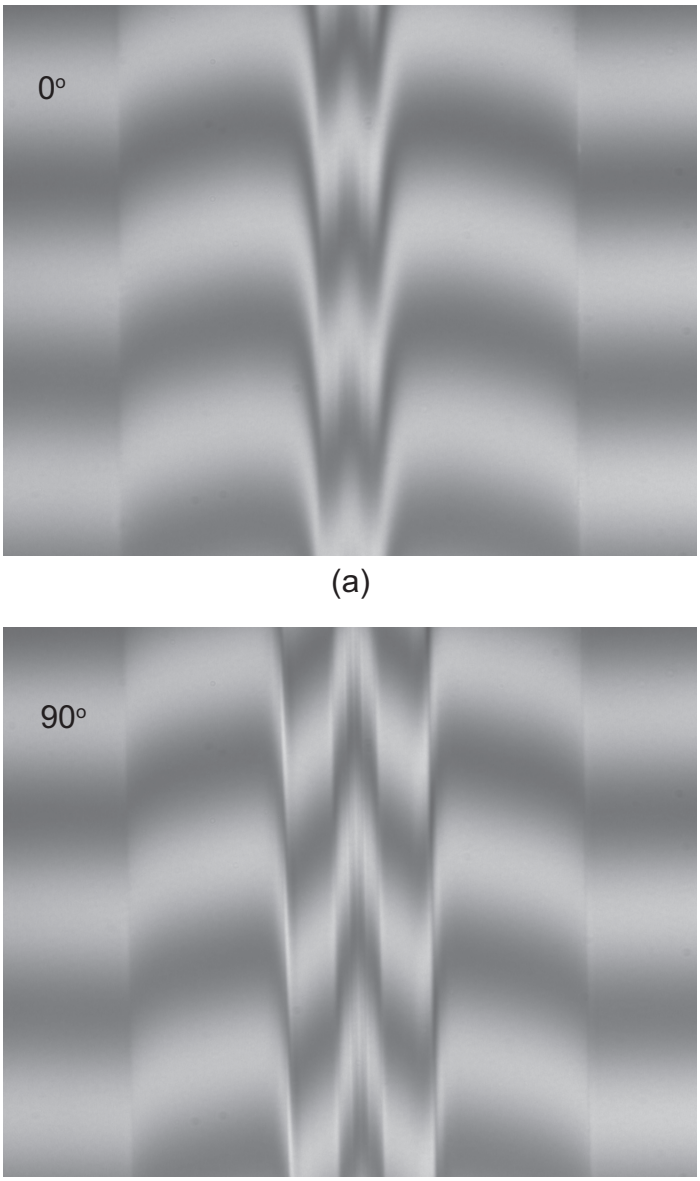

Figure 6.20: Example interference images recorded for the azimuthally asymmetric fiber (bow-tie type PMF) at two different projection angles: (a) $\theta = 0^{\circ}$ and (b) $\theta = 90^{\circ}$.

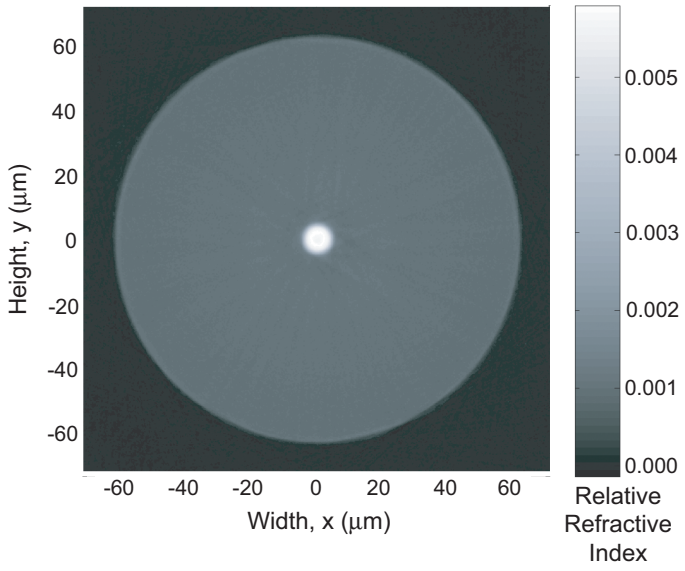

Figure 6.21: Reconstructed relative refractive-index profile of a Corning SMF-28 optical fiber.

technique, transverse interferometric profiling [116, 148], the profile shown in Fig. 6.22(b) was calculated from the last interference image of the set used in the MIOPT reconstruction. The two profiles are similar, though the line-profile taken from the MIOPT reconstruction does possess lower noise levels. Wobble of sample during measurement contributes to blurring and averaging across the profile, but with the most impact in the core region.

6.2.2.2 Azimuthally Asymmetric Optical Fiber

The reconstructed cross-sectional refractive-index profile of the bow-tie type PMF is shown in Fig. 6.23. The bow-tie shape of the stress-producing region is evident in the profile. Noise in the profile is relatively low and the typical tomographic starring effect, while present, is minor; the low levels of both result from practices implemented in MIOPT during measurement and reconstruction, as discussed in Sec. 6.1 [129]. The cladding diameter in the reconstructed profile closely matches the PMF's specified value ($125\mu m$). Also, the portion of the cladding away from the bow-tie region is uniform. The quantitative features present in the reconstructed profile agree well with the qualitative features observed in the dark-field reflected-light image of a polished endface of the PMF shown in Fig. 6.23(b) (taken with a microscope at 50× magnification). Particularly evident in both the profile

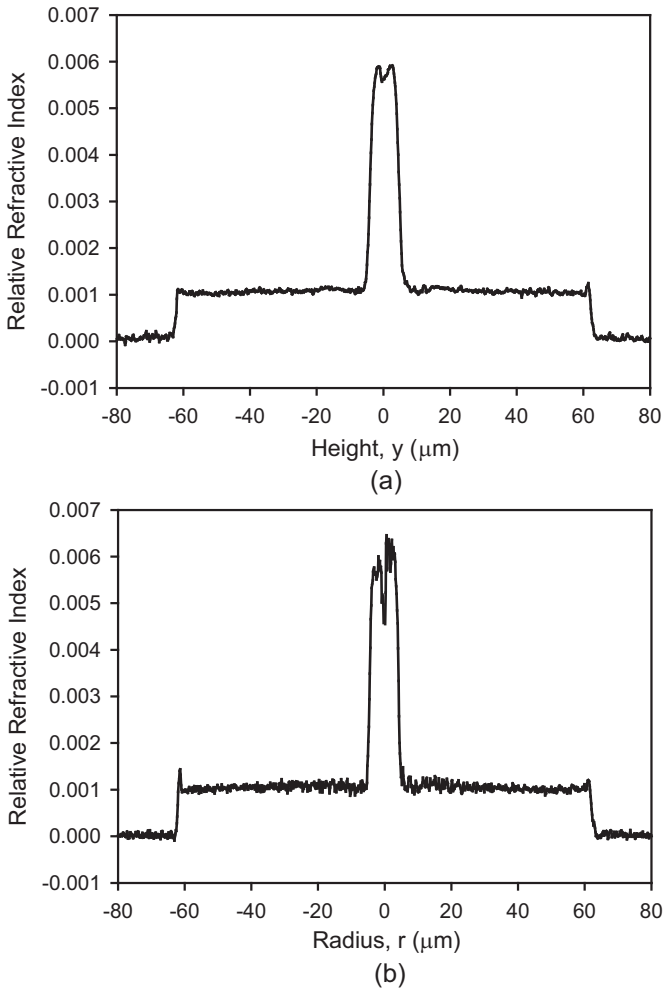

Figure 6.22: (a) Vertical line-profile taken through the center of the reconstructed profile of the Corning SMF-28 fiber $[n(0, y) - n_{\text{oil}}]$. (b) One-dimensional profile calculated using transverse interferometry which assumes azimuthal symmetry.

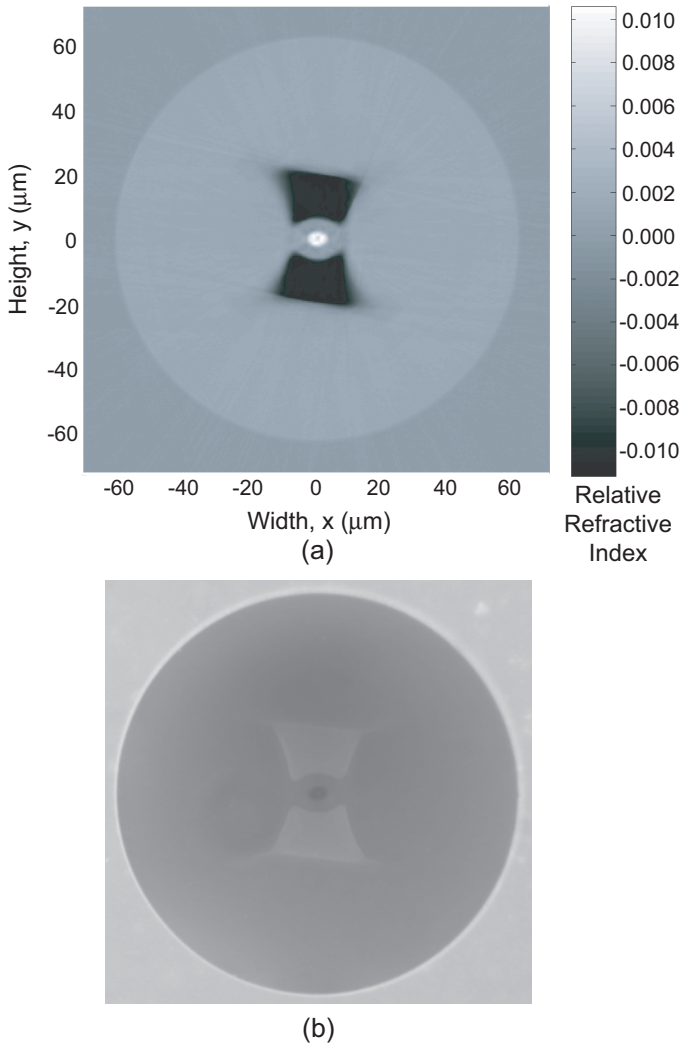

Figure 6.23: (a) Reconstructed relative refractive-index profile of a bow-tie type PMF. (b) Dark-field reflected-light image of the PMF endface. Structural features present in both the reconstructed profile and the endface image agree closely.

and image is the slant of the outer edges of the bow-tie region and the distortion at the corners.

Figure 6.24(a) shows the vertical line-profile taken through the center of the reconstructed profile while Fig. 6.24(b) shows the equivalent horizontal line-profile. Features of the core region are evident, including the center dip and overall ellipticity. The variations present in the lower index stress-producing region is apparent in the vertical line-profile.

The two profiles shown in Fig. 6.21 and Fig. 6.23 represent the first nondestructive

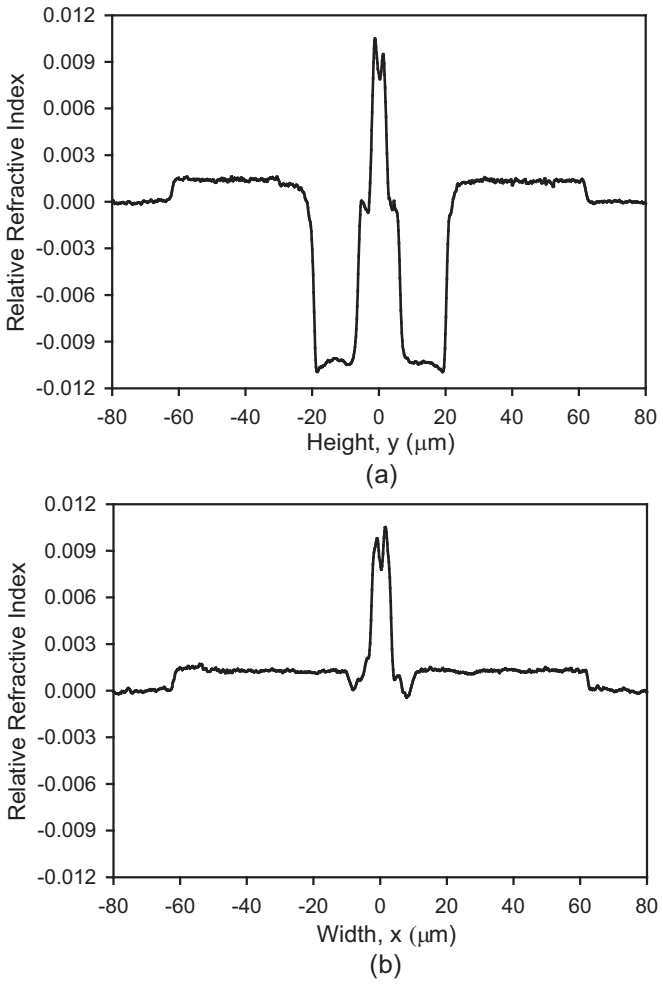

Figure 6.24: (a) Vertical line-profile taken through the center of the reconstructed profile of the PMF $[n(0, y) - n_{\text{oil}}]$. (b) Horizontal line-profile taken through the center of the reconstructed profile of the PMF $[n(x, 0) - n_{\text{oil}}]$.

measurements of optical fiber refractive-index profiles obtained using MIOPT. The example measured profiles demonstrate experimentally the ability of MIOPT to profile both azimuthally asymmetric and symmetric optical fibers or fiber devices. Thus, the technique is suitable for characterizing samples such as optical fiber exposed to CO_2 laser light. Based on the two index profiles measured by MIOPT, the estimated spatial resolution is $0.5\mu m$ while the index resolution is estimated to be below (better than) 5×10^{-5}. The resolution values of the technique are estimated and depend upon many factors (CCD array size, resolving power, beam deflection, source wavelength, *etc.*)

6.2.3 Optical Fiber Exposed to CO_2-Laser Light

Following the successful verification of the MIOPT technique's ability to profile fiber samples with azimuthal asymmetry, several segments of fiber exposed to CO_2 laser light were profiled. Measured profiles for three different samples are given below. The reconstructed profiles illustrate clearly the asymmetry present in the exposed fiber.

Individual periods of CO_2-laser-induced LPFGs form suitable samples for use in profiling fiber exposed to CO_2 laser light. Three fiber sections were prepared from different CO_2-laser-induced LPFGs and mounted in needles following the steps listed in Sec. 6.2.1. The portion of fiber extending beyond the needle tip contained several grating periods from a single LPFG. During mounting, the side of the fiber exposed to CO_2 laser light was unknown. Therefore, the exposed side possesses an arbitrary angular orientation relative to the projection angle.

After inserting and aligning a given sample in the interference microscope, the longitudinal position of the sample (along the fiber axis) was adjusted until a single period was contained within the interference image. By isolating a single grating period between two fringes in an interference image, the average cross-sectional refractive-index profile was obtained using MIOPT. Since the periods along the length of the sample could not be located from an intensity image, it was necessary to use the interference fringes to locate the periods. While translating the sample along its longitudinal axis (relative to the static interference image), the individual grating periods pass through the fringes and thus modify the fringe

patterns. By monitoring the change in the fringes during sample translation, a single grating period was isolated and positioned between the two fringes used for calculating the associated projection. Figure 6.25 shows an intensity image and an interference image of a single period of an LPFG.

Adjustment and positioning of the fringe spacing was necessary to ensure that the same fringe shift was present in the two adjacent fringes used for calculating the projection; having identical adjacent fringes is a requirement for using static fringe-field interferometry in MIOPT profiling. Due to limitations on pattern adjustment and sample positioning, adjacent fringes are not perfectly identical, however, they typically vary by less than $\pm 5\%$. An example of the small difference existing between two adjacent fringes is given in Fig. 6.26. The fringe separation for this particular case is approximately $45\mu m$, but the fringe separation can be varied to accommodate different samples.

For each sample, a set of interference images was collected for the various projection angles. The images were then processed to yield the required projections. Due to sample wobble, edge detection and alignment was implemented prior to reconstruction to ensure all projections shared a common origin. A sinogram of one of the samples is shown in Fig. 6.27.

Using the projections obtained from the interference images, the associated profiles were reconstructed. The two-dimensional reconstructed cross-section of one period of an overmodulated CO_2-laser-induced LPFG is given in Fig. 6.28. This profile was reconstructed from the 360 projections shown in Fig. 6.27. A vertical line-profile taken through the center of the reconstructed profile is shown in Fig. 6.29(a) while Fig. 6.29(b) shows the equivalent horizontal line-profile. The cross-sectional refractive-index profile is clearly azimuthally asymmetric, with one side of the cross-section possessing a higher index than the opposite side. The profile partly resembles the contour plot of intensity in an optical fiber exposed to CO_2 laser light (Fig. 1.3).

The reconstructed profiles of individual periods from two undermodulated CO_2-laser-induced LPFGs are shown in Fig. 6.30 and Fig. 6.31. Each profile was reconstructed from only 180 projections; starring effects are more pronounced due to the reduced number of projections used for reconstruction. The profile shown in Fig. 6.30 more closely resembles

(a)

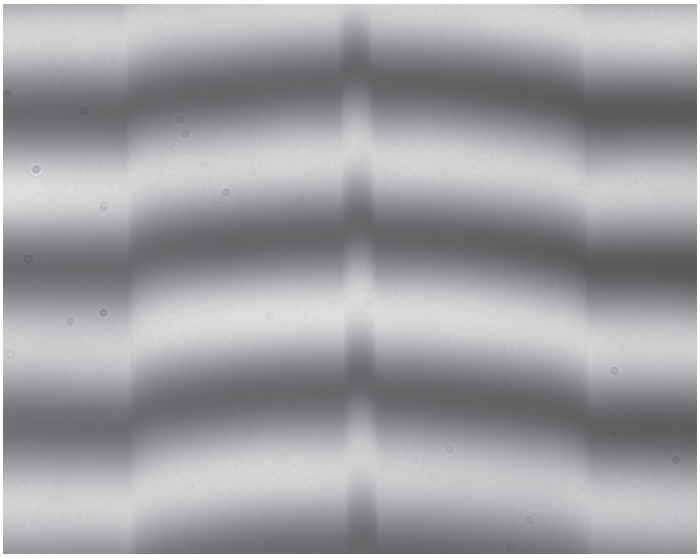

(b)

Figure 6.25: (a) Gray-scale level (intensity) image of a segment of optical fiber exposed to CO_2 laser-light. (b) Fringe-field interference image of the same segment as in (a). The images are 1030×1300 pixels.

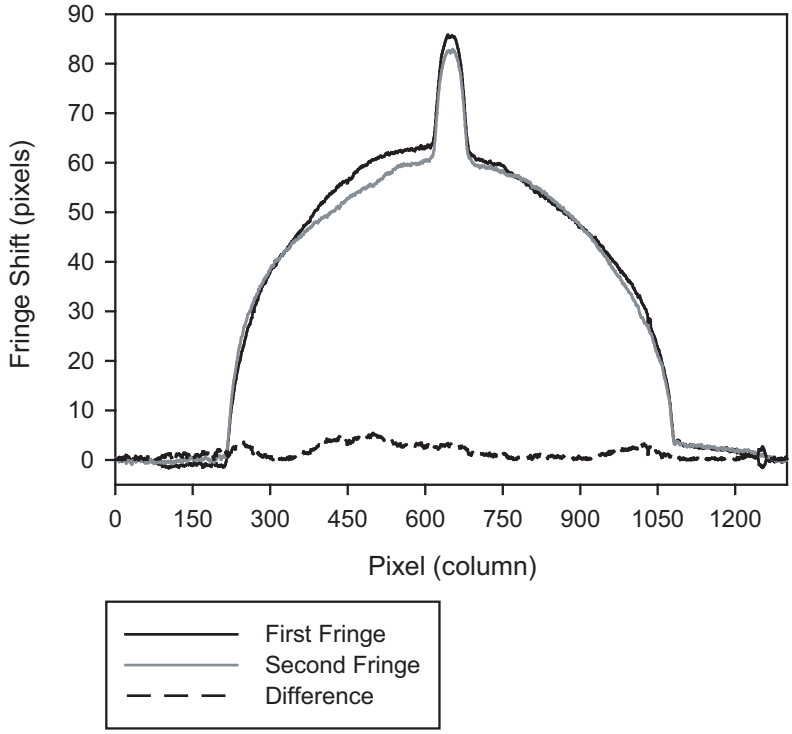

Figure 6.26: Fringe shift as derived from an interference image for two fringes used to calculate the projection. The shift is similar for the two fringes, as is required for implementing MIOPT.

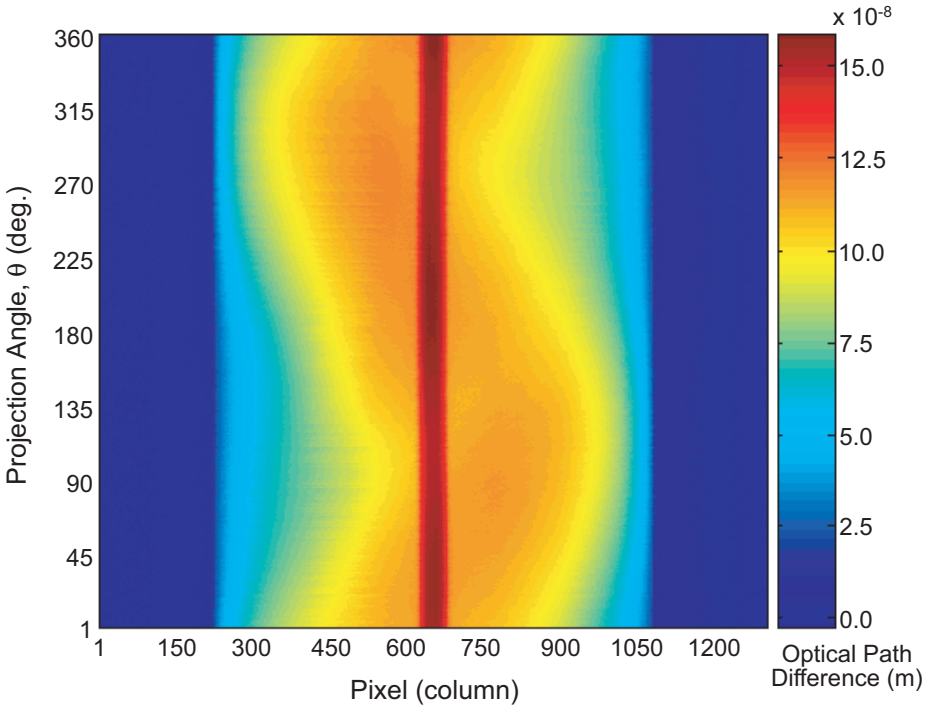

Figure 6.27: Collection of index projections over all of the projection angles (sinogram) for a one period of an overmodulated CO_2-laser-induced LPFG (LPFG 08210205).

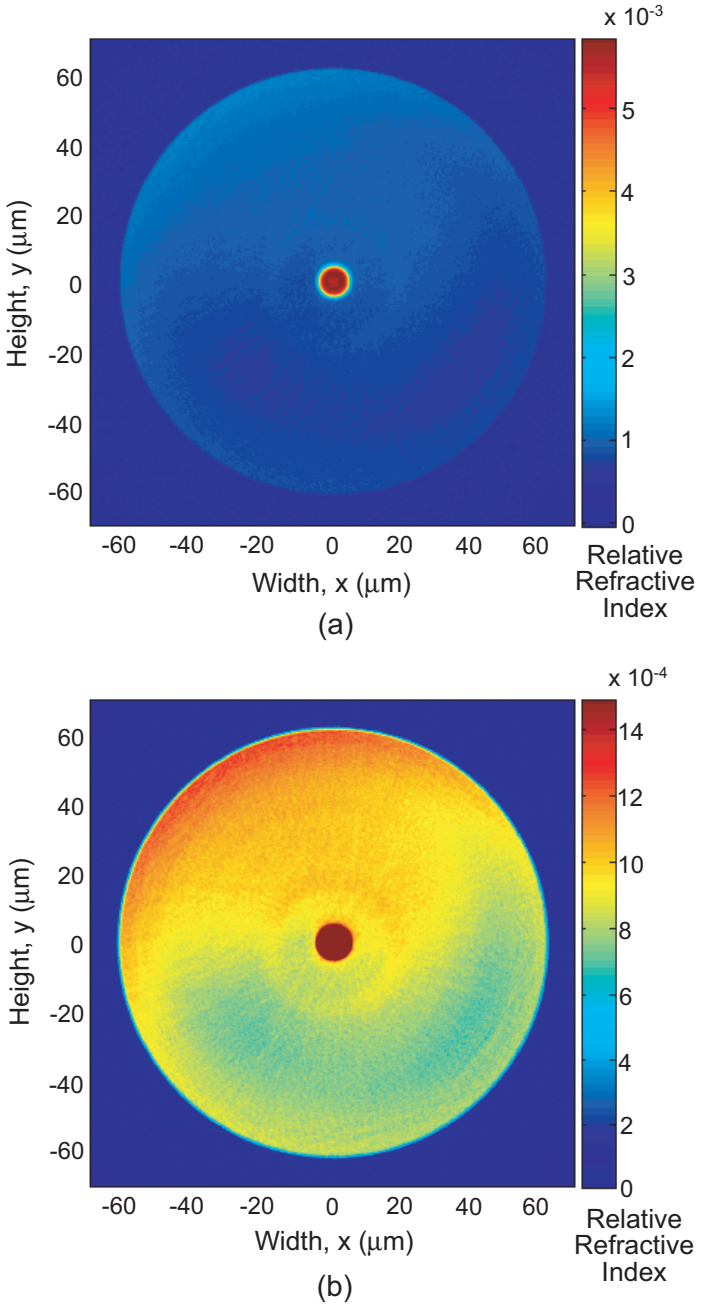

Figure 6.28: Reconstructed relative refractive-index profile $[n(x, y) - n_{\text{oil}}]$ of one period of an overmodulated CO_2-laser-induced LPFG (LPFG 08210205). (a) Full-scale pseudocolor surface plot. (b) Reduced-scale pseudocolor surface plot emphasizing the variation in the cladding region.

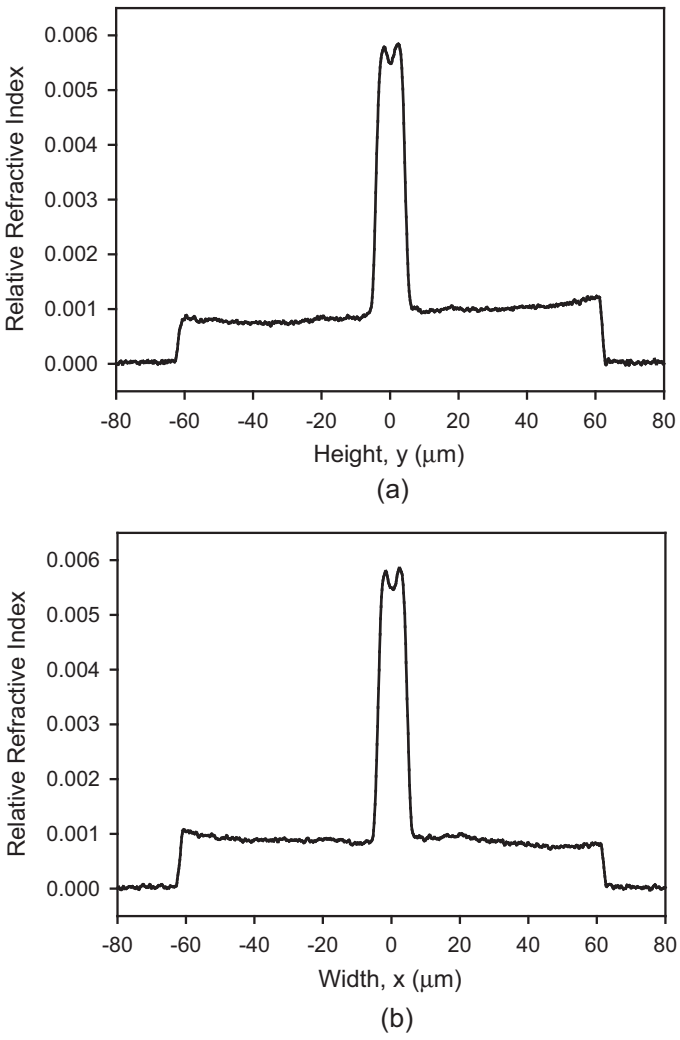

Figure 6.29: (a) Vertical line-profile $[n(0, y) - n_{\text{oil}}]$ taken through the center of the reconstructed profile given in Fig. 6.28. (b) Horizontal line-profile $[n(x, 0) - n_{\text{oil}}]$ taken through the center of the same reconstructed profile.

that of the overmodulated LPFG [Fig. 6.28], though both of the profiles of the undermodulated LPFG periods exhibit azimuthal asymmetry.

6.3 Summary

Before conducting further investigations into the characteristics, applications, and properties of CO_2-laser-induced LPFGs, accurate measurements of the asymmetric refractive-index profile induced by one-sided exposure to CO_2 laser light are required. The lack of any suitable existing technique motivated the development of a new refractive-index profiling technique. The capabilities of the MIOPT profiling technique were verified through simulations and measurements of several optical fiber samples.

Three profiles of optical fiber exposed to CO_2 laser light were measured. All three of the profiles clearly exhibit azimuthal asymmetry, with one side of the cross-section possessing a higher refractive index than the opposite side. The measured profiles can be used to model, among various characteristics, the guided-mode transmission spectra of CO_2-laser-induced LFPGs using modified-coupled mode theory [105].

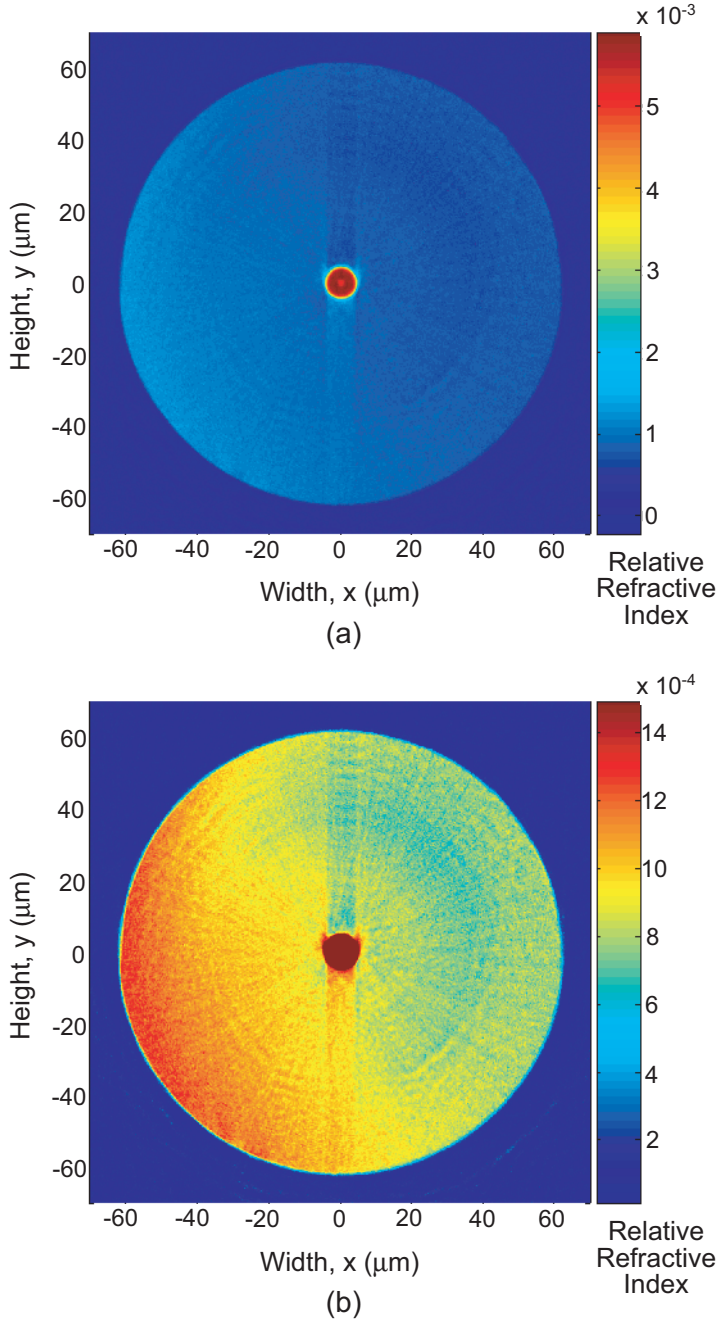

Figure 6.30: Reconstructed relative refractive-index profile $[n(x, y) - n_{\text{oil}}]$ of one period of an undermodulated CO_2-laser-induced LPFG (LPFG 02270208). (a) Full-scale pseudocolor surface plot. (b) Reduced-scale pseudocolor surface plot emphasizing the variation in the cladding.

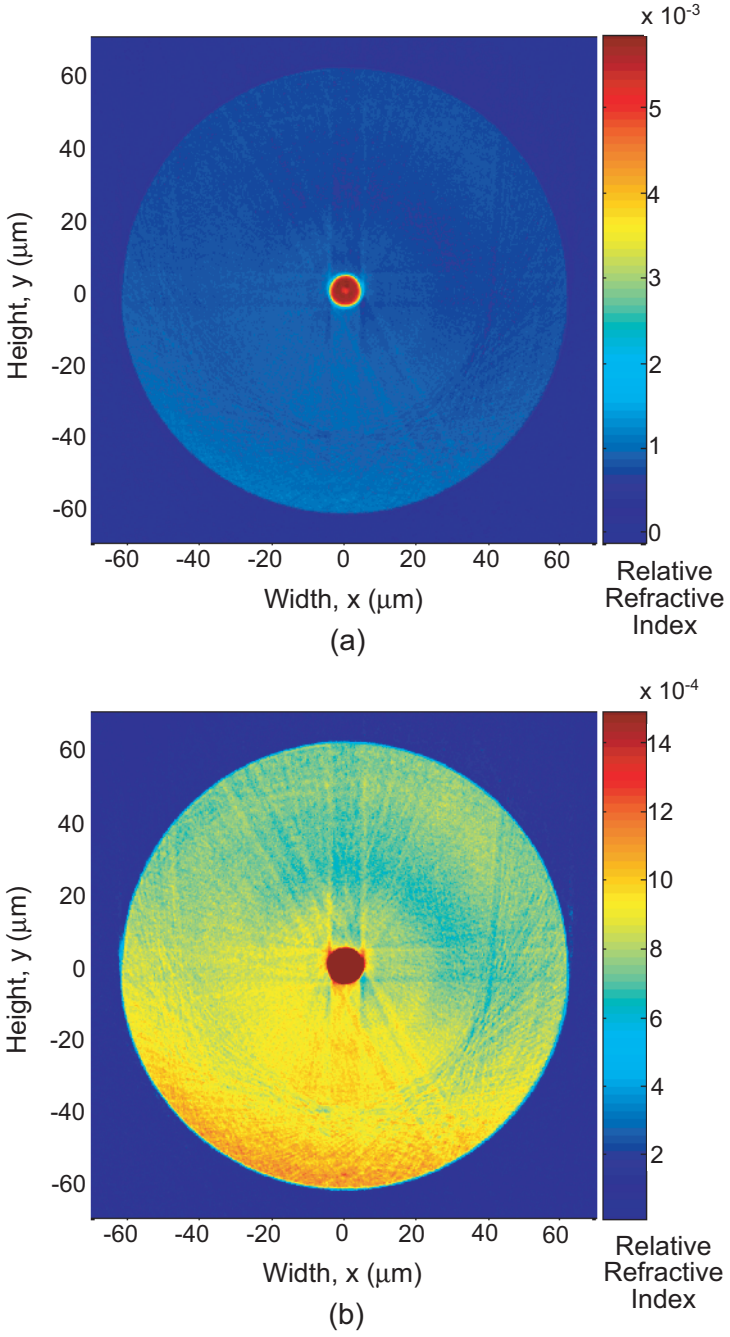

Figure 6.31: Reconstructed relative refractive-index profile $[n(x, y) - n_{\text{oil}}]$ of one period of an undermodulated CO_2-laser-induced LPFG (LPFG 03250201). (a) Full-scale pseudocolor surface plot. (b) Reduced-scale pseudocolor surface plot emphasizing the variation in the cladding.

CHAPTER 7

CONCLUSIONS

In this thesis, the characteristics, applications, and properties of carbon-dioxide-laser-induced long-period fiber gratings (CO_2-laser-induced LPFGs) have been examined in terms of the influence of the asymmetric refractive-index profile present in these gratings. The principal themes examined in the previous chapters are summarized below.

7.1 Summary of Results

7.1.1 Fabrication

The fabrication apparatus and procedure for writing CO_2-laser-induced LPFGs were discussed and the one-sided nature of the exposure emphasized. Fabrication variability was considered and improvement in the fabrication yield was demonstrated, thus allowing LPFGs with specific transmission characteristics to be obtained rapidly. Various transmission spectra for two categories of CO_2-laser-induced LPFGs, delineated based on the evolution of their transmission spectra during fabrication, were presented.

7.1.2 Polarization-Dependent Transmission Characteristics

The impact of the asymmetric index change on the polarization-dependent transmission characteristics of CO_2-laser-induced LPFGs was investigated. Two significant polarization-dependent characteristics, polarization-dependent loss and polarization mode dispersion, were examined.

The theory of polarization-dependent loss in LPFGs was extended to include CO_2-laser-induced LPFGs, along with other types of less traditional LPFGs. Detailed measurements comparing the polarization-dependent loss and polarization-dependent transmission spectra of UV-induced and CO_2-laser-induced LPFGs illustrate the influence of the asymmetry present in the latter type of LPFG. Estimates of modal birefringence, as derived from the polarization-dependent transmission spectra, establish the relative effects of the asymmetric

refractive-index profile in the two types of LPFGs.

The first measurement of polarization mode dispersion in CO_2-laser-induced LPFGs was presented. The measurement of device polarization mode dispersion required implementation of a suitable measurement technique in order to circumvent interference by device polarization-dependent loss. Measured differential group delay values in CO_2-laser-induced LPFGs are comparable to the low levels present in UV-induced LPFGs, in contrast to the relatively higher polarization-dependent loss levels in CO_2-laser-induced LPFGs.

7.1.3 Response to Physical Manipulation

The response of CO_2-laser-induced LPFGs to physical manipulation was investigated, with the important areas of applied flexure and applied torsion examined specifically.

Building upon previous research on the response of CO_2-laser-induced LPFGs to flexure, the first observations of variable attenuation tuning and wavelength tuning in the important $1550nm$ telecommunications wavelength band with applied flexure were reported. The first direct comparison of the flexure response of a more traditional LPFG (UV-induced) and a CO_2-laser-induced LPFG was conducted. An automated flexure testing system was designed to enable rapid and accurate flexure testing of a large number of LPFGs.

The response of CO_2-laser-induced LPFGs to applied torsion was investigated. A distinct twist-direction dependence of the resonant wavelength shift with applied torsion was observed for twists less than 180^o around the initial untwisted state. For cumulative twists larger than 180^o, the resonant wavelength shifts in the same direction independent of the twist direction. Peak attenuation generally decreases with increasing twist rate, with the exception of the region around the untwisted state. The explanation for the resonant wavelength shift behavior centers on the interplay between linear birefringence associated with the induced asymmetric index profile and twist-induced circular birefringence with circular birefringence dominating over linear birefringence as the applied twist rate increases.

7.1.4 Applications

The first prototype variable optical attenuator and optical tunable filter devices based on controlled flexure of CO_2-laser-induced LPFGs were developed and their operation demonstrated. Flexure of the CO_2-laser-induced LPFGs used in the prototype devices is accomplished by varying voltage levels applied to piezoceramic bending actuators. Example transmission spectra of variable optical attenuator and optical tunable filter devices, for various applied voltage levels, were given.

The concept of CO_2-laser-induced LPFG-based optical-fiber-to-waveguide couplers was introduced. The operation of a CO_2-laser-induced LPFG-based directional coupling was demonstrated and the wavelength dependence of the coupler established. The performance of the coupler was consistent with simplified beam propagation method simulations.

7.1.5 Refractive-Index Profile Measurements

The first cross-sectional refractive-index profiles of optical fiber exposed to CO_2 laser light have been presented. The form of the asymmetry induced by one-sided exposure to CO_2 laser light is clearly evident in the profiles: the index in the cladding is higher on one side than on the other and decreases slowly as the cross-section is traversed.

A new refractive-index profiling technique was developed that possesses sufficient resolution and accuracy, for both refractive index and spatial dimensions, for profiling fiber samples with azimuthally asymmetric refractive-index variations. The capabilities of the new profiling technique were verified through simulations and measurements of azimuthally symmetric and asymmetric optical fibers.

7.2 Future Research

A significant amount of research concerning CO_2-laser-induced LPFGs has appeared in the literature since Davis *et al.* first reported fabricating such gratings and additional topics were presented in this thesis. However, there is no doubt that many avenues of research remain that require further investigation. Several areas for potential future research on CO_2-laser-induced LPFGs are delineated in the sections that follow.

7.2.1 Fabrication

There are at least two closely linked issues concerning fabrication that require further investigation: fabrication mechanisms and fabrication variability. The usefulness of CO_2-laser-induced LPFGs for applications can be, in part, hampered by the inability to fabricate large numbers of gratings with similar transmission characteristics both rapidly and efficiently. This reason alone is sufficient motivation to identify the causes of, and subsequently eliminate, fabrication variablity.

However, successful elimination of fabrication variability requires a fundamental understanding of the mechanisms that induce a refractive-index change in the optical fiber when exposed to CO_2 laser light. A comprehensive understanding of the fabrication mechanisms will allow the more significant factors contributing to the index change to be identified and investigated. For example, is convective air flow near the surface of the fiber during exposure important or can it be neglected? How significant is any change in the fiber position relative to the incident laser beam? On what sort of time scales does the fiber reach steady-state temperature and, if it does reach a constant temperature over the cross-section, why does the induced index asymmetry exist? Currently, it is not clear which factors are more significant in creating the index change and which can be ignored. Some form of guidance is necessary if fabrication variability is to be eliminated and the lack of a through understanding of the fabrication mechanisms precludes addressing the variability issue.

Several different thermodynamic models have been suggested to account for the index change upon exposure to CO_2 laser light, but no comprehensive model (or explanation) exists. The lack of a comprehensive model follows from a variety of reasons, but can be partly attributed to the lack of experimental evidence with which to test and verify existing or proposed models. Temperature measurements of the optical fiber during exposure to CO_2 laser light are necessary. In conjunction with the temperature measurements, changes in residual stress and refractive index in the exposed region must be recorded. The tools now exist for accomplishing the latter, but any form of non-contact temperature measurement is complicated by the lasing wavelength and the small object dimensions. Additional problems plague any investigation, including the uncertainty in glass material properties

(such as emissivity) in the CO_2 laser wavelength range, which makes predictive modeling inaccurate. All of these issues, and potentially others, must be addressed before a comprehensive explanation and model of the fabrication mechanisms can be derived. Recent work by Jiang and Woodward offers a possible basis for examining and modeling the exposure process [149].

Another fabrication-related area that should be considered for future research is tailoring the asymmetry present in the refractive-index profile. Control of the exact form of asymmetry provides another means for shaping device performance. As an example, the elimination of the asymmetry reduces polarization-dependent transmission effects. Successful tailoring of profiles, however, requires reducing fabrication variability and fully understanding fabrication mechanisms. Models to predict performance for various profiles are also required.

7.2.2 Modeling

Further insight into the effects of azimuthal asymmetry on CO_2-laser-induced LPFG optical characteristics requires that appropriate models be developed. The same holds for improving performance in various applications. A first step towards developing the necessary models would be to use modified-coupled mode theory (modified-CMT) [105] to investigate the basic transmission characteristics of CO_2-laser-induced LPFGs. The refractive-index profile measurements presented at the end of Chapter 6 provide a good portion of the information required to conduct modified-CMT-based transmission spectrum modeling. From such modeling, the evolution of the grating transmission spectra during fabrication can be understood and predicted. Also, the transmission spectrum and cladding modes excited for a given period spacing could be determined more accurately.

Modeling basic transmission spectra of CO_2-laser-induced LPFGs using modified-CMT is only one option of many to pursue; response-prediction models for physical manipulation would also be useful. A model for predicting grating response to flexure could aid in the design and improvement of VOA and OTF devices. Similarly, more complex models and simulations for predicting the behavior of the CO_2-laser-induced LPFG-based fiber-to-waveguide couplers are required.

7.2.3 Response to Torsion

To date, the dependence of the resonant wavelength shift in CO_2-laser-induced LPFGs on the twist direction has not been analyzed quantitatively. The combination of linear birefringence and circular birefringence within the grating structure makes any direct analytical analysis difficult. However, determination of the effective index experienced by the cladding modes for various twist rates (and directions) is one place to begin an in-depth examination since the effective indices of the core and cladding modes partly determine the resonant wavelength. The right- or left-rotary elliptical polarization state evolution of the cladding modes as they travel through a twisted CO_2-laser-induced LPFG certainly impacts the resulting effective index. If the actual SOP of light at each point along the length of the LPFG can be calculated for some incident polarization state, then the effective index at that point can also be calculated. Taking the average of the effective indices at each point over the length of the grating then yields the average effective index experienced by the cladding mode. A related approach is used to predict the resonant wavelength of twist-induced virtual LPFGs (Sec. 4.2) [93].

7.2.4 Optical-Fiber-to-Waveguide Coupler

The CO_2-laser-induced LPFG-based fiber-to-waveguide coupler concept presented in Chapter 5 offers several potential advantages over other coupling devices. However, a large amount of research remains to be undertaken before the full potential of a CO_2-laser-induced LPFG-based coupler is realized. As was mentioned, modeling of the coupler performance is needed. Other potential areas of research are listed below.

1. Quantitative measurements of coupling efficiency need to be conducted. While LPFG-based fiber-to-waveguide coupling was successfully demonstrated, the actual coupling efficiency remains to be established. Coupling efficiency measurements in this case are complicated by the experimental arrangement; the coupler is assembled on an endface inspection microscope and standard optical power detectors cannot be easily positioned in front of the waveguide endface. The coupler characterization apparatus will need to be modified to accommodate efficiency measurements. An alternative

is to design the coupler to operate at visible wavelengths where a scientific-grade CCD camera can then (potentially) be used to calculate the power emerging from the waveguide endface.

2. Different forms of couplers to achieve higher coupling efficiencies should be investigated. The coupler examined in Chapter 5 performs as a directional coupler and is most suitable for multiple-drop (tap) communications (with several LPFGs existing in a single fiber). The efficiency of that type of coupler can be considered low when compared to other types of couplers; certain applications require far higher coupling efficiencies. Given the potential advantages of CO_2-laser-induced LPFG-based couplers, it is worth investigating other possible forms for accomplishing coupling. One alternative form involves fabricating the CO_2-laser-induced LPFGs in a D-shaped optical fiber [150]. With the flat portion of the fiber in contact with the top surface of the waveguide, significantly higher coupling efficiencies could be reached.

3. Possible preferential coupling associated with the asymmetric refractive-index profiles should be examined. One potential advantage of using CO_2-laser-induced LPFGs for performing coupling is the preferential out-coupling from the fiber cladding. Observations of the cladding modes emerging from CO_2-laser-induced LPFGs at a cleaved fiber endface revealed potential asymmetries in the cladding mode, which points to the possibility of preferential out-coupling. To establish whether such out-coupling exists requires an experiment to be conducted that is similar in form to one performed recently on a FBG, where light emerging from the fiber cladding from radiation modes was measured along the length of the FBG [106]. Characterization at various axial rotational orientations would need to be added to that experimental arrangement.

4. The polarization-dependence of coupling requires examination. As was established in Chapter 3, the amount of light coupled to a cladding mode depends on the polarization state of the light incident on the grating. From this observation, it can be expected that the coupling is also polarization dependent.

7.2.5 Refractive-Index Profile Measurements

MIOPT is a promising profiling technique, as is evident from measurements of the asymmetric refractive-index profiles of optical fiber exposed to CO_2-laser-light. Further research and development is required before the full potential of the technique's ability to profile CO_2-laser-induced LPFGs and other fiber is realized.

1. Refinement of the measurement apparatus is required in order to produce more accurate profiles. As discussed in Chapter 6, a number of issues concerning the measurement apparatus impact the resulting profiles. Critical to reducing the effects of ambient temperature variation is control of the matching oil refractive-index value. Setting the oil index value is most easily accomplished through control of the oil temperature. Additionally, control of the oil temperature also provides another degree-of-freedom for establishing optimum fringe patterns and ensuring the same value for comparing profile measurements to each other. Eliminating sample wobble and/or precession in the microscope field-of-view during rotation is required to improve resolution and accuracy; eliminating sample movement would also remove the need for edge detection and alignment during reconstruction. However, it is possible that sample movement can not be completely eliminated. In that case, techniques currently under investigation in medical imaging to correct for patient motion during computed tomography imaging should be examined and applied (if appropriate). More advanced edge detection techniques or other forms of fringe-field interferometry could also be employed. Though a portion of the measurement process is already automated, further refinements could reduce the measurement time significantly (in conjunction with removing/reducing sample movement). One potential improvement is the implementation of digital signal processing-based image analysis to permit real-time projection viewing, error detection/correction, and faster reconstruction. A host of more minor issues (more accurate equivalent pixel spacing, coding efficiency, image noise reduction) need to be addressed.

2. Quantitative measurements of the absolute resolution and accuracy, in both spatial

and refractive index terms, of the MIOPT technique are needed. The accuracy and resolution of the technique have been only estimated from the profiles presented in Chapter 6. Traditionally, such a determination would be established through profile measurement and reconstruction of some standard or phantom. However, no standard of sufficient accuracy exists and there is no other profiling technique that can characterize a standard to the necessary accuracy so that that standard can then be used in the evaluation of other profiling techniques. One possible approach is to profile a small-diameter multi-bore capillary tube whose bores are filled with a variety of refractive-index matching liquids. The index values of the liquids can be established independently with high-precision and thus provide suitable reference points. A similar approach was taken by Park *et al.* while examining off-focusing and beam-deflection effects in residual stress profiling of optical fiber [138].

3. Closely related to the issues of resolution and accuracy is the assumption of undeviated projections. By nature of possessing azimuthally asymmetric profiles, it is inevitable that ray-refraction occurs and it is important to examine the effects of refraction in detail. A starting place for investigating the issue is provided by Górski and by Wu *et al.* [131, 151]. There is a need to model ray-deviation/wave-front deformation for several typical fiber profiles (polarization-maintaining fiber, single-mode fiber, *etc.*)

4. The effect of the sequential fringe-spacing on axial spatial resolution should be examined. Alternatively, the implementation of phase-shifting interferometry (PSI) [152] will provide substantially better axial spatial resolution. PSI produces a two-dimensional phase map projection at each angle instead of the one-dimensional phase projection obtained using static fringe-field interferometry. Reconstruction with two-dimensional projections yields a three-dimensional volume and eliminates the axial spatial resolution limitation. In addition, PSI offers better phase resolution than static fringe-field interferometry. PSI was applied successfully to profiling of optical fibers conducted using a commercial microinterferometer employing a Wollaston prism [135].

With a fully developed profiling technique, additional measurements should be conducted on a variety of CO_2-laser-induced LPFGs. Both undermodulated and overmodulated gratings need to be studied. Profiles of both exposed and unexposed sections of an LPFG should be obtained. Profiles obtained for a wide variety of CO_2-laser-induced LPFGs will yield an idea of the level of variablity both within a grating and between gratings while enabling more precise modeling.

In addition, the refractive-index profile measurements of CO_2-laser-induced LPFGs should be examined in conjunction with stress profile measurements. The combination of the two techniques permits a comprehensive examination of issues such as fabrication mechanisms and fabrication variability. Stress profiles can be obtained using a variation of MIOPT, where two profiles are collected using a polarizer/analyzer pair and the profiles are then subtracted. One profile is obtained with the pair aligned along the sample longitudinal axis and the other is obtained with the pair aligned perpendicular to the longitudinal axis. Subtracting the index profiles yields an absolute birefringence profile, from which the stress can be calculated. Other birefringence measurement techniques, such as the two-wave-plate compensator method, could also be used as they typically offer better axial spatial resolution [153].

7.3 Concluding Remarks

The discussions and investigations presented in this thesis demonstrate the impact of the asymmetric refractive-index change on CO_2-laser-induced LPFG performance. CO_2-laser-induced LPFGs occupy a middle ground between other types of LPFGs; their profiles are more asymmetric than those of UV-induced LPFGs but the asymmetry is not so large as to produce the polarizer-like behavior observed in LPFGs fabricated in polarization-maintaining fiber. The absolute level of asymmetry in the CO_2-laser-induced LPFG cross-sectional profile is not large, but the effects of the asymmetry can be magnified due to its presence within the grating structure. This point is illustrated most clearly in comparing the results of the polarization-dependent loss and polarization mode dispersion investigations. The asymmetry induced by one-sided exposure to CO_2 laser light offers an additional

degree-of-freedom to tailor grating response and behavior but can also produce additional, and perhaps undesirable, side-effects. The salient point to consider is that the azimuthal asymmetry present in CO_2-laser-induced LPFG offers many advantages but also entails inherent trade-offs that must be evaluated on an application-by-application basis.

APPENDIX A

CO_2-LASER-INDUCED LPFG PARAMETERS

The fabrication parameters of all of the CO_2-laser-induced LPFGs used throughout this thesis are listed in Table A.1. The definitions of the parameters (Λ, N, n, and so forth) are given in Table 2.3. All of the gratings were fabricated with laser light at a wavelength of $10.59\mu m$. The number of exposures per period (n) was not recorded during fabrication for LPFG 11200204 (used in the prototype development). In the table below, the heading *Polarization* refers to the polarization state of the light incident on the fiber during fabrication [transverse-magnetic (TM) or transverse electric (TE) linearly polarized (LP)].

Table A.1: CO_2-Laser-Induced LPFG Fabrication Parameters

LPFG Designation	Λ $[\mu m]$	N	n	T_t $[ms]$	T_p $[ms]$	P $[W]$	Polarization
10040102	640	40	1	265	265	0.781	TM LP
11150105	640	37	1	400	400	0.910	TE LP
11280110	640	40	160	50	36	0.854	TE LP
11280113	640	40	160	50	36	0.860	TE LP
11300108	640	40	160	50	36.5	0.853	TE LP
12070101	640	34	160	50	36.5	0.853	TE LP
02270208	597	38	160	50	37	0.882	TE LP
03060202	565	40	160	50	37	0.879	TE LP
03060212	640	43	160	50	37	0.878	TE LP
03250201	597	36	160	50	37	0.880	TE LP
03250206	597	40	160	50	37	0.881	TE LP
03250208	597	41	160	50	37	0.880	TE LP
04230206	650	40	320	50	37	0.888	TE LP
07090208	480	44	120	50	37	0.946	TE LP
08210205	597	36	80	50	37	0.938	TE LP
09090207	597	40	240	50	37	0.948	TE LP
11200204	480	48	?	50	37	0.934	TE LP

APPENDIX B

QUALITATIVE TECHNIQUE FOR ORIENTATION IDENTIFICATION

With the asymmetric refractive-index change present in CO_2-laser-induced LPFGs, a need exists to identify the axial rotational orientation of the fiber relative to the incident laser beam to assist in analyzing the results of various investigations into the effect of the asymmetry. Reflected Nomarski differential interference contrast (DIC) microscopy [154] is a simple and rapid method for identifying the fiber orientation during exposure. The method presented here is an extension of the process described by Montarou and Gaylord [155, 156].

Example images captured while using the technique to examine a CO_2-laser-induced LPFG are shown in Fig. B.1, with several images of a grating period taken at various axial rotational orientations (angles around the fiber longitudinal axis). The images were taken using an Olympus BX-60 microscope with a 10× brightfield-darkfield-polarized (BDP) objective, a modified Wollaston prism [155], and a crossed polarizer/analyzer pair. The LPFG is secured between two rotation stages and placed in the microscope field of view with only air surrounding the fiber. The modified Wollaston prism is adjusted until good color contrast is obtained between the exposed and un-exposed section of fiber. Images are captured at various angles after the fiber is rotated about its longitudinal axis.

The azimuthally asymmetric refractive index change is clearly indicated by the changing colors of the grating period over the full angular range. Contamination (oil or debris) of the surface of the fiber can be seen in the 270° image, but does not appear to affect the results. The image taken at 0°, with the two-color change (pink-blue), corresponds to side of the fiber facing the laser during exposure being downward (into the page). The image taken at 180°, with no evident color change, corresponds to the incident side of the fiber being upward (out of the page). The two images showing a strong, single color change (pink or

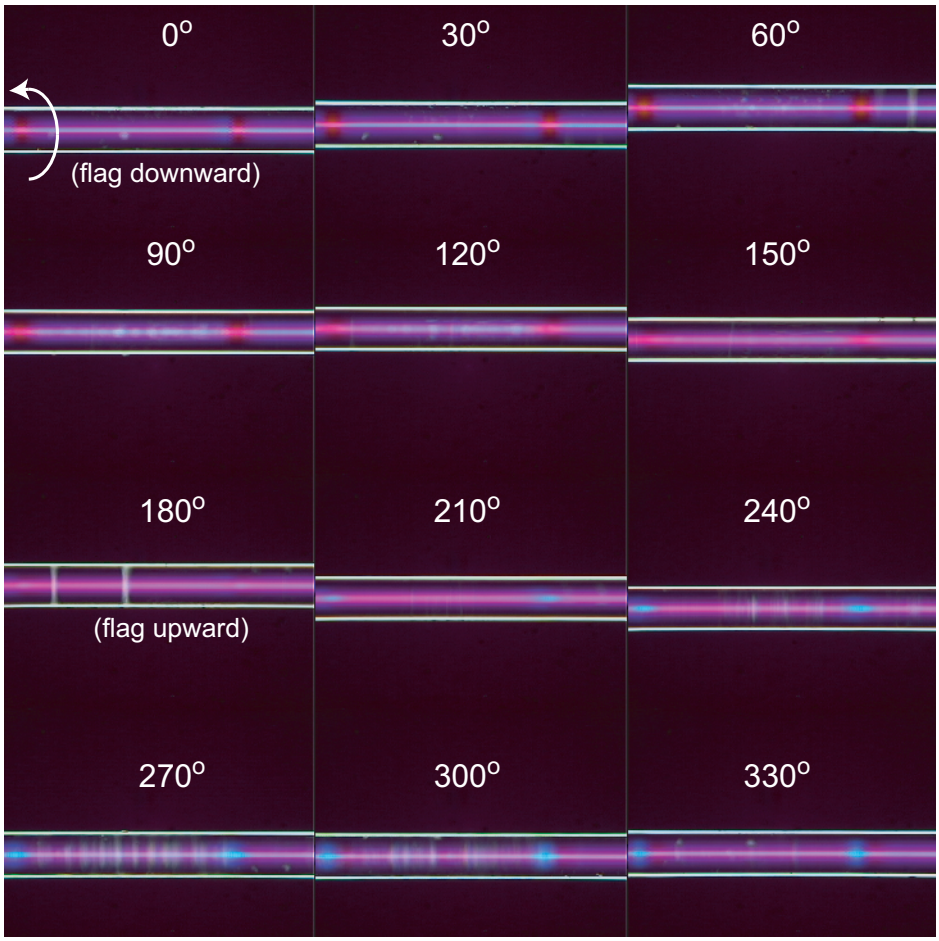

Figure B.1: Reflected Nomarski differential interference contrast images of a CO_2-laser-induced LPFG (LPFG 11300108) at different axial rotational orientations. The arrow indicates the direction of rotation. The asymmetry of the induced refractive-index change is indicated by the color changes that occur with rotation.

blue, 90° and 270°) indicate the incident side of the fiber is on the left or right side (parallel to plane of the page). In this case, the tab orientation is an accurate indicator of the fiber orientation relative to the incident laser beam.

Observing the changes in color with rotation verifies that the induced refractive-index change is non-uniform over the fiber transverse cross-section. The changes also correlate with which side of the fiber was facing the laser during fabrication. In similar observations of an UV-induced LPFG, no color change was evident when the grating was rotated about its longitudinal axis. Observing no color change with rotation indicates the LPFG has a relatively uniform (azimuthally symmetric) refractive-index profile.

Reflected Nomarski DIC is a useful and rapid technique for identifying precisely the axial rotational orientation of a CO_2-laser-induced LPFG during fabrication relative to the incident laser beam. The technique can also be used to identify variation in the induced refractive-index change along the length of the grating. Along similar lines, the cross-sectional refractive-index profile of a graded-index multi-mode fiber was measured recently using a related transmitted-light DIC technique [119].

APPENDIX C

COMPUTED TOMOGRAPHY PRINCIPLES

A brief overview of the principles of computed tomography (CT) reconstruction is presented in this appendix. The overview provides further explanation of some of the central concepts discussed in Chapter 6. The overview follows the discussions in Chapter 3 of *Computed Tomography* [133], in Chapter 1 of *Principles of Medical Imaging* [157], and in Chapter 7 of *Radiological Imaging* [145]. The mathematical notation used in *Computed Tomography* is primarily adopted for presenting the reconstruction process [133], with a few notational changes implemented to match the equations presented in Chapter 6 of the thesis. Frequency domain-based CT is employed in MIOPT, though other approaches (such as algebraic reconstruction) would be suitable as well.

Fourier Slice Theorem

The Fourier Slice Theorem encompasses the fundamental concepts of frequency domain-based CT reconstruction and relates the Fourier transform of projections through a two-dimensional object to the two-dimensional Fourier transform of the object. A short derivation of the theorem follows.

Consider a two-dimensional object described by the function $f(x, y)$, with the x-axis and y-axis at a fixed orientation relative to the object. For the objects considered in this thesis, $f(x, y)$ represents the two-dimensional refractive-index cross-sectional profile, $n(x, y)$, of an optical fiber sample (the typical fiber cylindrical coordinate system representation of the refractive-index profile, $n(r, \phi)$, is related to $n(x, y)$ by a simple coordinate transformation). The two-dimensional Fourier transform of the object described by $f(x, y)$, $F(u, v)$, is given by

$$F(u, v) = \int_{-\infty}^{\infty} \int_{-\infty}^{\infty} f(x, y)\, e^{-i2\pi(xu+yv)} \mathrm{d}x\, \mathrm{d}y \tag{C.1}$$

where u is the spatial frequency along the x-axis direction and v is the spatial frequency

along the y-axis direction.

The object can be referenced using a different set of coordinates, (d, L), that share the same origin as the previous coordinates, but that can be rotated about that origin. The fixed (x, y) coordinates are related to the rotating (d, L) coordinates through the angle θ that the L-axis makes with the x-axis, as illustrated in Fig. 6.1. In the rotating coordinate system the object can be described by $f(d, L)$ with

$$d = xcos\theta + ysin\theta, \tag{C.2}$$

$$L = -xsin\theta + ycos\theta. \tag{C.3}$$

A projection, $p(d, \theta)$, can be taken of the two-dimensional object at an angle θ. The projection is the line integral of the rotated-coordinate function $[f(d, L)]$ over the length of the d-axis and with the line integral taken along the L-axis.

$$p(d, \theta) = \int_{-\infty}^{\infty} f(d, L)\, \mathrm{d}L. \tag{C.4}$$

The coordinate d represents the distance from the projection ray to the coordinate system origin for each angle θ. In practice, the function goes to zero outside the outer limits of the function and the integral is, therefore, not taken over infinity.

The 1-D Fourier transform of the projection, $P(\omega, \theta)$, can be taken with respect to the coordinate variable d to obtain

$$P(\omega, \theta) = \int_{-\infty}^{\infty} p(d, \theta) e^{-i2\pi\omega d} \mathrm{d}d = \int_{-\infty}^{\infty} \int_{-\infty}^{\infty} f(d, L) \mathrm{d}L\, e^{-i2\pi\omega d} \mathrm{d}d. \tag{C.5}$$

with ω being the spatial frequency along the d-axis direction.

The Fourier transform of the projection is in terms of the rotated-coordinate system (and therefore directly related to the projection angle θ) but can be related to the fixed coordinates (x, y) by direct transformation. The transformation can then be substituted into the Fourier transform of the projection to obtain

$$P(\omega, \theta) = \int_{-\infty}^{\infty} \int_{-\infty}^{\infty} f(x, y)\, e^{-i2\pi\omega(xcos\theta + ysin\theta)} \mathrm{d}x\, \mathrm{d}y. \tag{C.6}$$

Examination of the integral portions of Eq. (C.1) and Eq. (C.6) reveals that they share a similar form. If we let $u = \omega cos\theta$ and $v = \omega sin\theta$ then

$$F(\omega cos\theta, \omega sin\theta) = P(\omega, \theta) \tag{C.7}$$

Equation (C.7) dictates that the one-dimensional Fourier transform of the projection taken at an angle θ is equal to the two-dimensional Fourier transform of the object along a line passing through the origin that makes an angle θ with the u frequency axis. The Fourier transform of the projection, in effect, samples the frequencies in a polar form as opposed to the traditional rectangular form of the two-dimensional Fourier transform. Projections taken at adjacent angles, say $\theta \pm \Delta\theta$, bound the projection taken at angle θ in the frequency domain. Without interpolation, each projection occupies a pie-shaped wedge in the frequency domain of the two-dimensional Fourier transform of the object [133]. This is the central concept of the Fourier Slice Theorem and is the basis of frequency-domain CT reconstruction.

If enough projections of the object are taken over a full 360°, then the two-dimensional Fourier transform of the object can be constructed (with interpolation). By taking the inverse two-dimensional Fourier transform of the sampled frequency space, the original two-dimensional object is reconstructed. Profiles of three-dimensional objects $[f(x, y, z)]$ are obtained by stacking two-dimensional profiles taken at sequential locations along the z-axis.

Filtered Backprojection Reconstruction

While reconstruction of the object from the two-dimensional Fourier transform is possible, the frequencies in the polar coordinates must be mapped to rectangular coordinates before taking the inverse transform. This requires interpolation in the frequency domain, which can be problematic and leads to distortions in the reconstructed object. An alternative method for implementing the Fourier Slice Theorem is the filtered backprojection algorithm. A partial derivation of the algorithm is given below [133].

The inverse two-dimensional Fourier transform of the object, in terms of the rectangular spatial frequency coordinates (u, v), is

$$f(x, y) = \int_{-\infty}^{\infty} \int_{-\infty}^{\infty} F(u, v) e^{i2\pi(ux+vy)} \mathrm{d}u \, \mathrm{d}v. \tag{C.8}$$

The two-dimensional Fourier transform of the object can be converted to polar coordinates using the relationships

$$u = \omega cos\theta, \tag{C.9}$$

$$v = \omega sin\theta, \tag{C.10}$$

$$\mathrm{d}u\,\mathrm{d}v = \omega\,\mathrm{d}\omega\,\mathrm{d}\theta. \tag{C.11}$$

Substituting the above relationships into the inverse two-dimensional Fourier transform of the object given by Eq. (C.8) yields

$$f(x,y) = \int_0^{2\pi} \mathrm{d}\theta \int_0^{\infty} F(\omega cos\theta, \omega sin\theta)\, e^{i2\pi\omega(xcos\theta + ysin\theta)}\, \omega\,\mathrm{d}\omega. \tag{C.12}$$

The projection Fourier transform can be substituted for the term in Eq. (C.12) [by Eq. (C.7)] and cast with reference to the rotated coordinate system

$$f(x,y) = \int_0^{2\pi} \mathrm{d}\theta \int_0^{\infty} P(\omega,\theta)\, \omega\, e^{i2\pi\omega d}\mathrm{d}\omega. \tag{C.13}$$

The term $P(\omega,\theta)\omega$ represents the Fourier transform of the projection at angle θ multiplied by a ramp-type (frequency-domain) filter. The term's inverse Fourier transform is called the filtered projection, $g(d,\theta)$,

$$g(d,\theta) = g(xcos\theta + ysin\theta) = \int_{-\infty}^{\infty} P(\omega,\theta)\, \omega\, e^{i2\pi\omega(xcos\theta + ysin\theta)}\,\mathrm{d}\omega. \tag{C.14}$$

The two-dimensional inverse Fourier transform given in Eq. (C.13) is now rewritten as

$$f(x,y) = \int_0^{2\pi} g(xcos\theta + ysin\theta)\,\mathrm{d}\theta. \tag{C.15}$$

Equation (C.15) states that the value of the object at the coordinates (x,y) is the integral sum over 360° of all of the filtered projections that pass through that point. An alternative interpretation is to consider the smearing backwards of each projection in the data set at the projection angle (hence the designation backprojection). The two-dimensional reconstructed object is then the sum of the all of the rotated, filtered, and backprojected projections at each point divided by an appropriate scaling factor (π/number of projections).

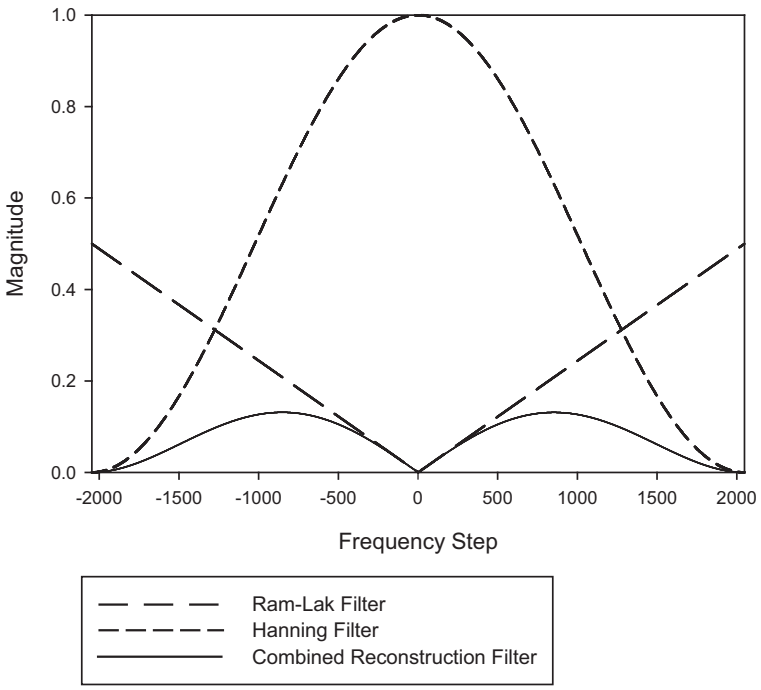

Figure C.1: Magnitude of the traditional Ram-Lak filter, a common Hanning filter, and the combination of the two that produces the filter used in reconstruction.

The formulas presented above are for the continuous spatial representation only. The actual algorithms must be implemented using their discrete versions and unique issues associated with such forms must be addressed (zero-padding, interperiod interference, periodic versus aperiodic convolution, FFTs, and so forth).

The discrete representation of the ramp-type filter used in the algorithm is commonly referred to as the Ram-Lak filter [145]. As discussed in Chapter 6, the reconstruction filter can be modified, for example, by combining the Ram-Lak filter with a more common filter-type such as Hanning [139]. Figure C.1 shows the magnitude of the Ram-Lak filter, the magnitude of the Hanning filter, and the magnitude of the combined reconstruction filter sometimes employed in the filtered backprojection algorithm. The combined filter used in reconstruction significantly attenuates higher spatial frequencies. In reconstructing actual fiber cross-sectional profiles, however, the type of reconstruction filter employed in the algorithm had little impact due to the more dominant averaging effect arising from sample movement.

REFERENCES

[1] G. D. VanWiggeren, T. K. Gaylord, D. D. Davis, E. Anemogiannis, B. D. Garrett, M. I. Braiwish, and E. N. Glytsis, "Axial rotation dependence of resonances in curved CO_2-laser-induced long-period fibre gratings," *Electron. Lett.*, vol. 36, pp. 1354–1355, Aug. 3, 2000.

[2] D. Davis, *Long-Period Fiber Gratings Fabricated with Focused CO_2 Laser Pulses*. PhD thesis, Georgia Institute of Technology, May 1999.

[3] G. D. VanWiggeren, T. K. Gaylord, D. D. Davis, M. I. Braiwish, E. N. Glytsis, and E. Anemogiannis, "Tuning, attenuating, and switching by controlled flexure of long-period fiber gratings," *Opt. Lett.*, vol. 26, pp. 61–63, Jan. 15, 2001.

[4] E. N. Glytsis, "Scattering by a dielectric (or lossy dielectric) cylinder," 2001.

[5] M. I. Braiwish, "Fabrication and packaging of carbon-dioxide-laser-induced long-period fiber grating devices," Master's thesis, Georgia Institute of Technology, Mar. 2003.

[6] M. I. Braiwish, B. L. Bachim, and T. K. Gaylord, "Prototype CO_2 laser-induced long-period fiber grating variable optical attenuators and optical tunable filters," *Appl. Opt.*, vol. 43, pp. 1789–1793, Mar. 20, 2004.

[7] L. Eldada, "Optical communication components," *Rev. Sci. Instr.*, vol. 75, pp. 575–593, Mar. 2004.

[8] E. Udd, ed., *Fiber Optic Sensors: An Introduction for Scientists and Engineers*. New York: John Wiley and Sons, 1991.

[9] B. Culshaw, "Optical fiber sensor technologies: Opportunities and-perhaps-pitfalls," *J. Lightwave Technol.*, vol. 22, pp. 39–50, Jan. 2004.

[10] U. Willer, C. Bohling, and W. Schade, "Using laser spectroscopy and fiber optic sensors to monitor volcanoes," *Opt. Photon. News*, vol. 15, pp. 18–23, Mar. 2004.

[11] A. Othonos and K. Kalli, *Fiber Bragg Gratings: Fundamentals and Applications in Telecommunications and Sensing*. Boston: Artech House, 1999.

[12] A. M. Vengsarkar, P. J. Lemaire, J. B. Judkins, V. Bhatia, T. Erdogan, and J. E. Sipe, "Long-period fiber gratings as band-rejection filters," *J. Lightwave Technol.*, vol. 14, pp. 58–65, Jan. 1996.

[13] Q. Li, C.-H. Lin, A. A. Au, and H. P. Lee, "Compact all-fibre on-line power monitor via core-to-cladding mode coupling," *Electron. Lett.*, vol. 38, pp. 1013–1015, Aug. 29, 2002.

[14] D. B. Stegall and T. Erdogan, "Dispersion control with use of long-period fiber gratings," *J. Opt. Soc. Am. A*, vol. 17, pp. 304–312, Feb. 2000.

[15] D. D. Davis, T. K. Gaylord, E. N. Glytsis, S. G. Kosinski, S. C. Mettler, and A. M. Vengsarkar, "Long-period fibre grating fabrication with focused CO_2 laser pulses," *Electron. Lett.*, vol. 34, pp. 302–303, Feb. 5, 1998.

[16] T. Erdogan, "Fiber grating spectra," *J. Lightwave Technol.*, vol. 15, pp. 1277–1294, Aug. 1997.

[17] A. Yariv, "Coupled-mode theory for guided-wave optics," *IEEE J. Quantum Electron.*, vol. QE-9, pp. 919–933, Sep. 1973.

[18] T. Erdogan, "Cladding-mode resonances in short- and long- period fiber grating filters," *J. Opt. Soc. Am. A*, vol. 14, pp. 1760–1773, Aug. 1997.

[19] A. M. Vengsarkar, J. R. Pedrazzani, J. B. Judkins, and P. J. Lemaire, "Long-period fiber-grating-based gain equalizers," *Opt. Lett.*, vol. 21, pp. 336–338, Mar. 1, 1996.

[20] P. F. Wysocki, J. B. Judkins, R. P. Espindola, M. Andrejco, and A. M. Vengsarkar, "Broad-band erbium-doped fiber amplifier flattened beyond 40 nm using long-period fiber grating filter," *IEEE Photon. Technol. Lett.*, vol. 9, pp. 1343–1345, Oct. 1997.

[21] V. Bhatia, "Applications of long-period gratings to single and multi-parameter sensing," *Opt. Express*, vol. 4, pp. 457–466, May 24, 1999.

[22] S. G. Kosinksi and A. M. Vengsarkar, "Splicer-based long-period fiber gratings," in *Optical Fiber Communication Conference*, (Washington, D.C.), pp. 278–279, Optical Society of America, Feb. 1998.

[23] Y. Kondo, K. Nouchi, T. Mitsuyu, M. Watanabe, P. G. Kazansky, and K. Hirao, "Fabrication of long-period fiber gratings by focused irradiation of infrared femtosecond laser pulses," *Opt. Lett.*, vol. 24, pp. 646–648, May 15, 1999.

[24] M. Fujimaki, Y. Ohki, J. L. Brebner, and S. Roorda, "Fabrication of long-period optical fiber gratings by use of ion implantation," *Opt. Lett.*, vol. 25, pp. 88–89, Jan. 15, 2000.

[25] Y. Jeong, B. Yang, B. Lee, H. S. Seo, S. Choi, and K. Oh, "Electrically controllable long-period liquid crystal fiber gratings," *IEEE Photon. Technol. Lett.*, vol. 12, pp. 519–521, May 2000.

[26] S. Savin, J. F. Digonnet, G. S. Kino, and H. J. Shaw, "Tunable mechanically induced long-period fiber gratings," *Opt. Lett.*, vol. 25, pp. 710–712, May 15, 2000.

[27] X. Shu, L. Zhang, and I. B. and, "Sensitivity characteristics of long-period fiber gratings," *J. Lightwave Technol.*, vol. 20, pp. 255–266, Feb. 2002.

[28] S. W. James and R. P. Tatam, "Optical fibre long-period grating sensors: Characteristics and applications," *Meas. Sci. Technol.*, vol. 14, pp. R49–R61, May 2003.

[29] X. Chen, K. Zhou, and I. Bennion, "Optical chemsensors utilizing long-period fiber gratings UV-inscribed in D-fiber with enhanced sensitivity through cladding etching," *IEEE Photon. Technol. Lett.*, vol. 16, pp. 1352–1354, May 2004.

[30] T. Allsop, R. Reeves, D. J. Webb, I. Bennion, and R. Neal, "A high sensitivity refractometer based upon a long period grating Mach-Zehnder interferometer," *Rev. Sci. Instr.*, vol. 73, pp. 1702–1705, Apr. 2002.

[31] V. E. Perlin and H. G. Winful, "Nonlinear pulse switching using long-period fiber gratings," *J. Lightwave Technol.*, vol. 18, pp. 329–333, Mar. 2000.

[32] K. S. Chiang, Y. Liu, M. N. Ng, and S. Li, "Coupling between two parallel long-period fibre gratings," *Electron. Lett.*, vol. 36, pp. 1408–1409, Aug. 3, 2000.

[33] W. T. Chen and L. A. Wang, "Laser-to-fiber coupling scheme by utilizing a lensed fiber integrated with a long-period fiber grating," *IEEE Photon. Technol. Lett.*, vol. 12, pp. 501–503, May 2000.

[34] A. S. Kurkov, M. Douay, O. Duhem, B. Leleu, J. F. Henninot, J. F. Bayon, and L. Rivoallan, "Long-period fibre grating as a wavelength selective polarisation element," *Electron. Lett.*, vol. 33, pp. 616–617, Mar. 27, 1997.

[35] U.-C. Paek and Y. Chung, "Fabrication of long-period fiber gratings with a CO_2 laser," in *OECC/IOOC Conference Incorporating ACOFT*, pp. 106–109, July 2001.

[36] Y.-J. Rao, Y.-P. Wang, Z.-L. Ran, T. Zhu, and B.-M. Yu, "Characteristics of novel long-period fibre gratings written by focused high-frequency CO_2 laser pulses," in *Passive Components and Transmission Systems*, vol. 4581, SPIE, Nov. 2001.

[37] G. Kakarantazas, T. E. Dimmick, T. A. Birks, R. L. Roux, and P. S. J. Russell, "Miniature all-fiber devices based on CO_2 laser microstructuring of tapered fibers," *Opt. Lett.*, vol. 26, pp. 1137–1139, Aug. 1, 2001.

[38] A. J. C. Grellier, N. K. Zayer, and C. N. Pannell, "Heat transfer modelling in CO_2 laser processing of optical fibres," *Opt. Comm.*, vol. 152, pp. 324–328, July 1, 1998.

[39] K. Morishita, S. F. Yuan, Y. Miyake, and T. Fujihara, "Refractive index variations and long-period fiber gratings made by the glass structure change," *IECIE Trans. Electron.*, vol. E86-C, pp. 1749–1758, Aug. 2003.

[40] B. H. Kim, T.-J. Ahn, D. Y. Kim, B. H. Lee, Y. Chung, U.-C. Paek, and W.-T. Han, "Residual stress relaxation in the core of optical fiber by CO_2 laser irradiation," *Opt. Lett.*, vol. 26, pp. 1657–1659, Nov. 1, 2001.

[41] B. H. Kim, T.-J. Ahn, D. Y. Kim, B. H. Lee, Y. Chung, U.-C. Paek, and W.-T. Han, "Effect of CO_2 laser radtiation on the refractive-index change in optical fibers," *Appl. Opt.*, vol. 41, pp. 3809–3815, July 1, 2002.

[42] A. D. Yablon, M. F. Yan, P. Wisk, F. V. DiMarcello, J. W. Fleming, W. A. Reed, E. M. Monberg, D. J. DiGiovanni, J. Jaspara, and M. E. Lines, "Refractive index perturbations in optical fibers resulting from frozen-in viscoelasticity," *Appl. Phys. Lett.*, vol. 84, pp. 19–21, Jan. 5, 2004.

[43] A. D. Yablon, M. F. Yan, D. J. DiGiovanni, M. E. Lines, S. L. Jones, D. N. Ridgway, G. A. Sandels, I. A. White, P. Wisk, F. V. DiMarcello, E. M. Monberg, and J. Jaspara, "Frozen-in viscoelasticity for novel beam expanders and high-power connectors," *J. Lightwave Technol.*, vol. 22, pp. 16–23, Jan. 2004.

[44] Y. Park, U.-C. Paek, S. Han, B.-H. Kim, C.-S. Kim, and D. Y. Kim, "Inelastic frozen-in stress in optical fibers," *Opt. Comm.*, vol. 242, pp. 431–436, Dec. 8, 2004.

[45] L. Drozin, P.-Y. Fonjallaz, and L. Stensland, "Long-period fibre gratings written by CO_2 exposure of H_2-loaded, standard fibres," *Electron. Lett.*, vol. 36, pp. 742–744, Apr. 13, 2000.

[46] D. D. Davis, T. K. Gaylord, and S. C. Mettler, "CO_2 laser-induced long-period fibre gratings: Spectral characteristics, cladding modes and polarisation independence," *Electron. Lett.*, vol. 34, pp. 1416–1417, July 9, 1998.

[47] H. S. Ryu, Y. Park, S. T. Oh, Y. Chung, and D. Y. Kim, "Effect of asymmetric stress relaxation on the polarization-dependent transmission characteristics of a CO_2 laser-written long-period fiber grating," *Opt. Lett.*, vol. 28, pp. 155–157, Feb. 1, 2003.

[48] S. T. Oh, W. T. Han, U. C. Paek, and Y. Chung, "Azimuthally symmetric long-period fiber gratings fabricated with CO_2 laser," *Mircowave Opt. Technol. Lett.*, vol. 41, pp. 188–190, May 5, 2004.

[49] Y.-J. Rao, Y.-P. Wang, Z.-L. Ran, and T. Zhu, "Novel fiber-optic sensors based on long-period fiber gratings written by high-frequency CO_2 laser pulses," *J. Lightwave Technol.*, vol. 21, pp. 1320–1327, May 2003.

[50] D. A. González, J. L. Arce-Diego, A. Cobo, and J. M. López-Higuera, "Spectral modelling of curved long-period fibre gratings," *Meas. Sci. Technol.*, vol. 12, pp. 786–792, July 2001.

[51] Y.-P. Wang, Y.-J. Rao, Z.-L. Ran, T. Zhu, and A.-Z. Hu, "A novel tunable gain equalizer based on a long-period fiber grating written by high-frequency CO_2 laser pulses," *IEEE Photon. Technol. Lett.*, vol. 15, pp. 251–253, Feb. 2003.

[52] National Instruments Corp., Austin, Texas.

[53] H. R. Philipp, "The infrared optical properties of SiO_2 and SiO_2 layers on silicon," *J. Appl. Phys.*, vol. 50, pp. 1053–1057, Feb. 1979.

[54] Y. Feiner and U. P. Oppenheim, "Measurements of optical constants of absorbing materials in the infrared," *Infrared Phys.*, vol. 33, no. 4, pp. 289–292, 1992.

[55] E. A. Wood, *Crystals and Light: An Introduction to Optical Crystallography.* New York: Dover Publications, second ed., 1977.

[56] B. L. Bachim and T. K. Gaylord, "Polarization-dependent loss and birefringence in long-period fiber gratings," *Appl. Opt.*, vol. 42, pp. 6816–6823, Dec. 1, 2003.

[57] Y. Ishii, K. Shima, S. Okude, K. Nishide, and A. Wada, "PDL suppression on long-period fiber gratings by azimuthally isotropic exposure," *IEICE Trans. Electron.*, vol. E85-C, pp. 934–939, Apr. 2002.

[58] A. Barty, K. A. Nugent, A. Roberts, and D. Paganin, "Quantitative phase tomography," *Opt. Comm.*, vol. 175, pp. 329–336, Mar. 1, 2000.

[59] T. Erdogan and V. Mizrahi, "Characterization of UV-induced birefringence in photosensitive Ge-doped silica optical fibers," *J. Opt. Soc. Am. B*, vol. 11, pp. 2100–2105, Oct. 1994.

[60] A. M. Vengsarkar, Q. Zhong, D. Inniss, W. A. Reed, P. J. Lemaire, and S. G. Kosinski, "Birefringence reduction in side-written photoinduced fiber devices by a dual-exposure method," *Opt. Lett.*, vol. 19, pp. 1260–1262, Aug. 15, 1994.

[61] J. A. Buck, *Fundamentals of Optical Fibers*. New York: John Wiley & Sons, 1995.

[62] D. Chowdhury and D. Wilcox, "Comparison between optical fiber birefringence induced by stress anisotropy and geometric deformation," *IEEE J. Select. Topics Quantum Electron.*, vol. 6, pp. 227–232, Mar. 2000.

[63] I. P. Kaminow, "Polarization in optical fibers," *J. Quantum Electron.*, vol. QE-17, pp. 15–22, Jan. 1981.

[64] Y. Zhu, E. Simova, P. Berini, and C. P. Grover, "A comparison of wavelength dependent polarization dependent loss measurements in fiber gratings," *IEEE Trans. Instrument. Meas.*, vol. 49, pp. 1231–1239, June 2000.

[65] G. S. Smith, *An Introduction to Classical Electromagnetic Radiation*. New York: Cambridge University Press, 1997.

[66] B. H. Lee, J. Cheong, and U. C. Paek, "Spectral polarization-dependent loss of cascaded long-period fiber gratings," *Opt. Lett.*, vol. 27, pp. 1096–1098, July 1, 2002.

[67] P. I. D. C. Reyes and P. S. Westbrook, "Tunable PDL of twisted-tilted fiber gratings," *IEEE Photon. Technol. Lett.*, vol. 15, pp. 828–830, June 2003.

[68] K. Dossou, S. LaRochelle, and M. Fontaine, "Numerical analysis of the contribution of the transverse asymmetry in the photo-induced index change profile to the birefringence of optical fiber," *J. Lightwave Technol.*, vol. 20, pp. 1463–1470, Aug. 2002.

[69] P. Hernday, "PMD posts a speed limit for high-speed fiber networks," *Laser Focus World*, vol. 37, pp. 171–178, Jan. 2001.

[70] E. Rudkevich and F. Y. Pan, "Understanding polarization-mode dispersion," *Laser Foucs World, suppl. issue*, pp. 39–42, June 2000.

[71] B. L. Heffner and P. R. Hernday, "Measurement of polarization-mode dispersion," *Hewlett-Packard J.*, pp. 27–33, Feb. 1995.

[72] B. L. Heffner, "Automated measurement of polarization mode dispersion using Jones matrix eigenanalysis," *IEEE Photon. Technol. Lett.*, vol. 4, pp. 1066–1069, Sep. 1992.

[73] A. Eyal and M. Tur, "Measurement of polarization mode dispersion in systems having polarization dependent loss or gain," *IEEE Photon. Technol. Lett.*, vol. 9, pp. 1256–1258, Sep. 1997.

[74] R. M. A. Azzam and N. M. Bashara, "Polarization transfer function of an optical system as a bilinear transformation," *J. Opt. Soc. Am.*, vol. 62, pp. 222–229, Feb. 1972.

[75] Hewlett Packard, *User's/Reference Guide HP8509A/B*, 08509-90016 ed., 1994.

[76] H. Sunnerud, M. Karlsson, C. Xie, and P. A. Andrekson, "Polarization-mode dispersion in high-speed fiber-optic transmission systems," *J. Lightwave Technol.*, vol. 20, pp. 2204–2219, Dec. 2002.

[77] S. J. Savory and F. P. Payne, "Pulse propagation in fibers with polarization-mode dispersion," *J. Lightwave Technol.*, vol. 19, pp. 350–357, Mar. 2001.

[78] L. R. Chen, S. D. Benjamin, P. W. E. Smith, and J. E. Sipe, "Ultrashort pulse reflection from fiber gratings: A numerical investigation," *J. Lightwave Technol.*, vol. 15, pp. 1503–1512, Aug. 1997.

[79] J. N. Kutz, B. J. Eggleton, J. B. Stark, and R. E. Slusher, "Nonlinear pulse propagation in long-period fiber gratings: Theory and experiment," *IEEE J. Selected Topics Quantum Electron.*, vol. 3, pp. 1232–1245, Oct. 1997.

[80] B. L. Bachim and T. K. Gaylord, "Automated flexure testing of axially rotated optical fiber gratings," *Rev. Sci. Instr.*, vol. 73, pp. 3454–3457, Oct. 2002.

[81] H. J. Patrick, C. C. Chang, and S. T. Vohra, "Long period fibre gratings for structural bend sensing," *Electron. Lett.*, vol. 34, pp. 1773–1775, Sep. 3, 1998.

[82] B. L. Bachim, M. I. Braiwish, T. K. Gaylord, E. N. Glytsis, V. Grubsky, and W. Morey, "Spectral characteristics of flexed long-period fiber gratings fabricated using UV and CO_2 lasers," in *Optical Society of America Annual Meeting Program*, p. 125, Oct. 2002.

[83] B. L. Bachim, M. I. Braiwish, D. D. Davis, T. K. Gaylord, E. N. Glytsis, and S. C. Mettler, "Variable attenuation and wavelength tuning of flexed CO_2-laser-fabricated long-period fiber gratings in 1550nm wavelength range," in *Optical Society of America Annual Meeting Program*, p. 52, Oct. 2002.

[84] S. Y. Kim, S. Y. Yoon, M. S. Kim, and K. H. Kwack, "Birefringence reduction in long period fiber gratings by the fiber-twist method," in *Conference on Lasers and Electro-Optics*, (Washington, D.C.), pp. 576–577, Optical Society of America, May 2000.

[85] L. A. Wang, C. Y. Lin, and G. W. Chern, "A torsion sensor made of a corrugated long period fibre grating," *Meas. Sci. Technol.*, vol. 12, pp. 793–799, July 2001.

[86] Y. P. Wang, Y. J. Rao, A. Z. Hu, X. K. Zeng, Z. L. Ran, and T. Zhu, "A novel fiber-optic torsion sensor based on a CO_2-laser-induced long-period fiber grating," in *Optical Fiber Senors Conference*, (Piscataway, NJ), pp. 147–150, IEEE, May 2002.

[87] Y.-P. Wang, Y.-J. Rao, and J.-P. Chen, "Torsion characteristics of long-period fiber gratings induced by high-frequency CO_2-laser pulses," *J. Opt. Soc. Amer. B*, vol. 22, pp. 1167–1172, June 2005.

[88] R. C. Hibbeler, *Mechanics of Materials*. Upper Saddle River, New Jersey: Prentice Hall, third ed., 1997.

[89] R. Ulrich and A. Simon, "Polarization optics of twisted single-mode fibers," *Appl. Opt*, vol. 18, pp. 2241–2251, July 1, 1979.

[90] C. N. Alexeyev, A. V. Volyar, and M. A. Yavorsky, "Vortex-preserving weakly guiding anisotropic twisted fibres," *J. Opt. A: Pure Appl. Opt.*, vol. 6, pp. S162–S165, 2004.

[91] O. V. Ivanov and L. A. Wang, "Wavelength shifts of cladding-mode resonance in corrugated long-period fiber gratings under torsion," *Appl. Opt.*, vol. 42, pp. 2264–2272, May 1, 2003.

[92] D. A. González, C. Jáuregui, A. Quintela, F. J. Madruga, P. Marquez, and J. M. López-Higuera, "Torsion-induced effects on uv-long period fiber gratings," in *Second European Workshop on Optical Fibre Sensors* (J. M. López-Higuera and B. Culshaw, eds.), vol. 5502, pp. 192–195, SPIE, 2004.

[93] C. Jáuregui and J. M. López-Higuera, "Virtual long-period gratings," *Opt. Lett.*, vol. 30, pp. 14–16, Jan. 1, 2005.

[94] H. S. Park, S. Lee, C. S. Kim, J. H. Kim, U. C. Paek, and Y. Chung, "A novel method of removing optical fiber coating with hot air stream," in *Optical Fiber Communication Conference and the International Conference on Integrated Optics and Optical Fiber Communication*, (Washington, D.C.), pp. 371–373, Optical Society of America, 1999.

[95] O. V. Ivanov, "Propagation and coupling of hybrid modes in twisted fibers," *J. Opt. Soc. Amer. A*, vol. 22, pp. 716–723, Apr. 2005.

[96] L. Qin, Z. X. Wang, Q. Y. Wang, H. P. Li, W. Zheng, Y. S. Zhang, and D. S. Gao, "Compact temperature-compensating package for long-period fiber gratings," *Optical Materials*, vol. 14, pp. 239–242, May 2000.

[97] Face International Corp., Norfolk, Virginia.

[98] D. A. B. Miller, "Rationale and challenges for optical interconncets to electronics chips," *Proc. IEEE*, vol. 88, pp. 728–749, June 2000.

[99] N. M. Jokerst, T. K. Gaylord, E. N. Glytsis, M. A. Brooke, S. Cho, T. Nonaka, T. Suzuki, D. L. Geddis, J. Shin, R. A. Villalaz, J. Hall, A. Chellapa, and M. Vrazel, "Planar lightwave integrated circuits with embedded actives for board and substrate level optical signal distribution," *IEEE Trans. Adv. Packaging*, vol. 27, pp. 376–385, May 2004.

[100] C. Choi, L. Lin, Y. Liu, L. Wang, D. Haas, J. Magera, and R. T. Chen, "Flexible optical waveguide film fabrications and optoelectronic devices integration for fully embedded board-level optical interconnects," *J. Lightwave Technol.*, vol. 22, pp. 2168–2176, Sep. 2004.

[101] T. S. Barry, D. L. Rode, and R. R. Krchnavek, "Highly-efficient coupling between single-mode fiber and polymer optical waveguides," *IEEE Trans. Components, Packaging, and Manufacturing Technol. Part B: Advanced Packaging*, vol. 20, pp. 225–228, Aug. 1997.

[102] V. R. Almeida, R. R. Panepucci, and M. Lipson, "Nanotaper for compact mode conversion," *Opt. Lett.*, vol. 28, pp. 1302–1304, Aug. 1, 2003.

[103] S. Lu, Y.-B. Yan, D.-E. Yi, G.-F. Jin, and M.-X. Wu, "Integrated diffractive optical mode converter for fiber-to-waveguide coupling," *Opt. Laser Technol.*, vol. 35, pp. 369–373, July 2003.

[104] G. Meltz, W. W. Morey, and W. H. Glenn, "In-fibre bragg grating tap," in *Digest of Conference on Optical Fiber Communication*, (Washington, DC), p. 24, Optical Society of America, 1990.

[105] E. Anemogiannis, E. N. Glytsis, and T. K. Gaylord, "Transmission characteristics of long-period fiber gratings having arbitrary azimuthal/radial refractive index variations," *J. Lightwave Technol.*, vol. 21, pp. 218–227, Jan. 2003.

[106] R. R. J. Maier, J. S. Barton, and J. D. C. Jones, "Fiber Bragg Grating location by a side-scatter technique based on cladding-mode coupling," *Appl. Opt.*, vol. 43, pp. 3310–3314, June 1, 2004.

[107] T. K. Gaylord and B. L. Bachim, "Optical interconnects in microelectronics based on azimuthally asymmetric long-period fiber grating couplers," Dec. 18, 2003. GTRC ID 3069.

[108] Y. Li and T. Erdogan, "Cladding-mode assisted fiber-to-fiber and fiber-to-free space coupling," *Opt. Comm.*, vol. 183, pp. 377–388, Sep. 2000.

[109] B. L. Bachim, O. O. Ogunsola, and T. K. Gaylord, "Optical-fiber-to-waveguide coupling using carbon-dioxide-laser-induced long-period fiber gratings," *Opt. Lett.*, 2005. Accepted for publication.

[110] J. M. Jarem and P. P. Banerjee, *Computational Methods for Electromagnetic and Optical Systems*. New York: Marcel Dekker, 2000.

[111] W.-Y. Su, G.-W. Chen, and L. A. Wang, "Analysis of cladding-mode couplings for a lensed fiber integrated with a long-period fiber grating by use of the beam-propagation method," *Appl. Opt.*, vol. 41, pp. 6576–6584, Nov. 1, 2002.

[112] Optiwave Corp., Ottawa, Canada.

[113] A. V. Mulé, *Volume Grating Coupler-Based Optical Intereconnect Technologies for Polylithic Gigascale Integration*. PhD thesis, Georgia Institute of Technology, Jan. 2004.

[114] Promerus LLC, Brecksville, Ohio.

[115] H. J. Patrick, A. D. Kersey, and F. Bucholtz, "Analysis of the response of long period fiber gratings to external index of refraction," *J. Lightwave Technol.*, vol. 16, pp. 1606–1612, Sep. 1998.

[116] L. M. Boggs, H. M. Presby, and D. Marcuse, "Rapid automatic index profiling of whole-fiber samples: Part 1," *Bell Sys. Tech. J.*, vol. 58, pp. 867–882, Apr. 1979.

[117] D. Marcuse and H. M. Presby, "Focusing method for nondestructive measurement of optical fiber index profiles," *Appl. Opt.*, vol. 18, pp. 14–22, Jan. 1, 1979.

[118] Y. Kokubun and K. Iga, "Precise measurement of the refractive index profile of optical fibers by a nondestructive interference method," *Trans. IECE Japan*, vol. E60, pp. 702–707, Dec. 1977.

[119] Z. Liu, X. Dong, Q. Chen, C. Yin, Y. Xu, and Y. Zheng, "Nondestructive measurement of an optical fiber refractive-index profile by a transmitted-light differential interference contact microscope," *Appl. Opt.*, vol. 43, pp. 1485–1492, Mar. 1, 2004.

[120] Q. Zhong and D. Inniss, "Characterization of the lightguiding structure of optical fibers by atomic force microscopy," *J. Lightwave Technol.*, vol. 12, pp. 1517–1523, Sep. 1994.

[121] S. T. Huntington, P. Mulvaney, A. Roberts, K. A. Nugent, and M. Bazylenko, "Atomic force microscopy for the determination of refractive index profiles of optical fibers and waveguides: A quantitative study," *J. Appl. Phys.*, vol. 82, pp. 2730–2734, Sep. 15, 1997.

[122] N. H. Fontaine and M. Young, "Two-dimensional index profiling of fibers and waveguides," *Appl. Opt.*, vol. 38, pp. 6836–6844, Nov. 20, 1999.

[123] P. Oberson, B. Gisin, B. Huttner, and N. Gisin, "Refracted near-field measurements on refractive index and geometry of silica-on-silicon integrated optical waveguides," *Appl. Opt.*, vol. 37, pp. 7268–7272, Nov. 1998.

[124] K. Toga, N. Amano, and K.-I. Noda, "Microscopic computer tomography measurement of nonaxisymmetrically distributed optical fiber refractive index," *J. Lightwave Technol.*, vol. 6, pp. 73–79, Jan. 1988.

[125] T. Okoshi and M. Nishimura, "Measurement of axially nonsymmetrical refractive-index distribution of a single-mode fiber by a multidirectional scattering-pattern method," *J. Lightwave Technol.*, vol. 1, pp. 9–14, Jan. 1983.

[126] D. Gloge, I. P. Kaminow, and H. P. Presby, "Profile dispersion in multimode fibres: Measurement and analysis," *Electron. Lett.*, vol. 11, pp. 469–471, Sep. 18, 1975.

[127] C. A. Burrus and R. D. Stanley, "Viewing refractive-index profiles and small-scale inhomogeneities in glass optical fibers: Some techniques," *Appl. Opt.*, vol. 13, pp. 2365–2369, Oct. 1974.

[128] D. Marcuse and H. Presby, "Index profile measurements of fibres and their evaluation," *Proc. IEEE*, vol. 68, pp. 666–688, June 1980.

[129] B. L. Bachim and T. K. Gaylord, "Microinterferometric optical phase tomography for measuring small, asymmetric refractive-index difference in the profiles of optical fibers and fiber devices," *Appl. Opt.*, vol. 44, pp. 316–327, Jan. 20, 2005.

[130] N. Barakat, H. A. El-Hennawi, E. A. El-Ghafar, H. El-Ghandoor, R. Hassan, and F. El-Diasty, "Three-dimensional refractive index profile of a grin optical waveguide using multiple beam interference fringes," *Opt. Comm.*, vol. 191, pp. 39–47, May 1, 2001.

[131] W. Górski, "The influence of diffraction in mircointerferometry and microtomography of optical fibers," *Opt. Lasers Engineering*, vol. 41, pp. 563–583, 2004.

[132] W. Górski and M. Kujawińska, "Three-dimensional reconstruction of refractive index inhomogeneities in optical phase elements," *Opt. Lasers Engineering*, vol. 38, pp. 373–385, Dec. 2002.

[133] J. Hsieh, *Computed Tomography: Principles, Design, Artifacts, and Recent Advances.* Bellingham, Washington: SPIE Press, 2003.

[134] J. Schwider, "Advanced evaluation techniques in interferomtery," in *Progress in Optics* (E. Wolf, ed.), vol. 28, ch. 4, pp. 271–359, New York: Elsevier, 1990.

[135] M. Sochacka, "Optical fiber profiling by phase-stepping transverse interferometry," *J. Lightwave Technol.*, vol. 12, pp. 19–23, Jan. 1994.

[136] B. V. Dorrio and J. L. Fernández, "Phase-evaluation methods in whole-field optical measurement techniques," *Meas. Sci. Technol.*, vol. 10, pp. R33–R55, Mar. 1999.

[137] Mathworks Inc., Natick, Massachusetts.

[138] Y. Park, S. Choi, U. C. Paek, K. Oh, and D. Y. Kim, "Measurement method for profiling the residual stress of an optical fiber: Detailed analysis of off-focusing and beam-deflection effects," *Appl. Opt.*, vol. 42, pp. 1182–1190, Mar. 1, 2003.

[139] D. A. Viskoe and G. W. Donohoe, "Optimal computed tomography data acquisition techniques and filter selection for detection of small density variations," *IEEE Trans. Instr. Meas.*, vol. 45, pp. 70–76, Feb. 1996.

[140] S. Vázquez-Montiel, J. J. Sánchez-Escobar, and O. Fuentes, "Obtaining the phase of an interferogram by use of an evolution strategy: Part 1," *Appl. Opt.*, vol. 41, pp. 3448–3452, June 10, 2002.

[141] S. J. Sangwine and R. E. N. Home, eds., *The Colour Image Processing Handbook*, ch. 8, pp. 149–162. New York: Chapman and Hall, 1998.

[142] A. Barty, *Quantitative Phase-Amplitude Microscopy.* PhD thesis, University of Melbourne, Parkville, Victoria, Australia, Feb. 2000.

[143] Ernst Leitz GMBH, Wetzlar, Germany, *Transmitted-Light Interference Microscope Instructions*, 1971.

[144] K. Creath, "Phase-measurement interferometry techniques," in *Progress in Optics* (E. Wolf, ed.), vol. 26, ch. 5, pp. 349–393, New York: Elsevier, 1988.

[145] H. H. Barrett and W. Swindell, *Radiological Imaging: The Theory of Image Formation, Detection, and Processing*, vol. 2. New York: Academic Press, 1981.

[146] M. Pluta, *Advanced Light Microscopy Vol. 3: Measuring Techniques.* New York: Elsevier, 1993.

[147] B. L. Bachim, T. K. Gaylord, and S. C. Mettler, "Refractive-index profiling of azimuthally asymmetric optical fibers by microinterferometric optical phase tomography," *Opt. Lett.*, vol. 30, pp. 1126–1128, May 15, 2005.

[148] H. M. Presby, D. Marcuse, H. W. Astle, and L. M. Boggs, "Rapid automatic index profiling of whole-fiber samples: Part 2," *Bell Sys. Tech. J.*, vol. 58, pp. 882–902, Apr. 1979.

[149] H. Jiang and P. Woodward, "Methodology of generic modeling as applied to energy coupling of CO_2 laser material interaction," *Opt. Lasers Engineering*, vol. 43, pp. 19–31, 2005.

[150] R. B. Dyott, *Elliptical Fiber Waveguides*. Boston: Artech House, 1995.

[151] Z. Z. Wu, H. Davis, and S. K. Batra, "Correct ray-tracing analysis for interference microscopy of fibres," *Proc. R. Soc. Lond. A*, vol. 450, pp. 23–36, Jul. 8, 1995.

[152] G. Lai and T. Yatagai, "Generalized phase-shifting interferometry," *J. Opt. Soc. Am. A*, vol. 8, pp. 822–827, May 1991.

[153] C. C. Montarou and T. K. Gaylord, "Two-wave-plate compensator method for single-point retardation measurements," *Appl. Opt.*, vol. 43, pp. 6580–6595, Dec. 20, 2004.

[154] M. Pluta, *Advanced Light Microscopy Vol. 2: Specialized Methods*. New York: Elsevier, 1993.

[155] C. C. Montarou and T. K. Gaylord, "Analysis and design of modified Wollaston prisms," *Appl. Opt.*, vol. 38, pp. 6604–6616, Nov. 1, 1999.

[156] C. C. Montarou and T. K. Gaylord, "Analysis of transversely illuminated optical fibers," in *Optical Society of America Annual Meeting Program*, p. 62, Oct. 2000.

[157] K. K. Shung, M. B. Smith, and B. Tsui, *Principles of Medical Imaging*. New York: Academic Press, 1992.

VITA

Brent L. Bachim was born in 1978 in Fort Worth, Texas. Prior to attending Georgia Insitute of Technology, he received his Bachelor of Science in Engineering from Texas Christian University in 2000. Brent has been the recipient of the Barry M. Goldwater Scholarship, the National Science Foundation Graduate Research Fellowship, and the Georgia Tech Institute Fellowship. He is a member of the Insitute of Electrical and Electronics Enigneers, the Optical Society of America, and Sigma Xi.